Modeling and optimization of a low noise transceiver for cochlear implants application

Umberto Cerasani

UNIVERSITE NICE – SOPHIA ANTIPOLIS

UFR SCIENCES

En collaboration avec l'Ecole Doctorale des Sciences et des Techniques de l'Information et de la Communication (EDSTIC) et le Laboratoire d'Electronique, Antennes et Télécommunications (LEAT)

T H E S E

Pour obtenir le titre de Docteur en Sciences

de l'Université Nice – Sophia Antipolis

présentée et soutenue par

Umberto Cerasani

Modeling and Optimization of a low noise transceiver for cochlear implants application

Thèse dirigée par Gilles Jacquemod et William Tatinian

soutenue le 12 Septembre 2014

Ph. D thesis

Title: MODELING AND OPTIMIZATION OF A LOW POWER TRANSCEIVER FOR COCHLEAR IMPLANTS

AUTHOR: Umberto Cerasani

SUPERVISORS: William Tatinian, Gilles Jacquemod

PROJECT PERIOD: September 2010 – April 2014

APPENDICES: Annexes A-C
"Cochlear Implants estimation film" available at http://youtu.be/x5o4jeTZt5M

PUBLICATIONS ACCEPTED:

- "Matlab/Simulink modeling of RF microphone for cochlear implant application", U. Cerasani, Y.Vaiairello, G.Jacquemod, Y. LeDuc, SAME Ubooth, September 2011, Sophia Antipolis (FRANCE)
- "Modélisation et optimisation d'une chaine d'émission réception très faible consommation pour implants cochléaires », U. Cerasani, W. Tatinian, Y. Vaiarello, G.Jacquemod, GDR SOC SIP, June 2012, Paris (FRANCE)
- « Modeling and optimization of a low noise RF transmitter for cochlear implants application", U. Cerasani, W. Tatinian, Y. Vaiarello, G. Jacquemod, IEEE DCIS, November 2012, Avignon (FRANCE)
- "Comparison of receiver architecture in terms of power consumption and Noise Figure for cochlear implants application", U. Cerasani, W. Tatinian, P. Ndungidi, F. Dualibe, C. Valderrama, ICONS, February 2014, Nice (FRANCE)
- "Implementation of phase noise theories for transient simulations", U. Cerasani, W. Tatinian, Forum SAME, October 2012, Sophia Antipolis (FRANCE)
- "Audio signal reconstruction for a damaged cochlea model", U. Cerasani, W. Tatinian, DATE, March 2013, Grenoble (FRANCE)
- "Electrical analog of the organ of Corti stimulated by the cochlear implant electrodes", U. Cerasani, W. Tatinian, CENTRIC, October 2013 ,Venice (ITALY)
- "Study of cochlear implants electrodes stimulation based on the physics of the ear for audio signal integrity improvement", U. Cerasani, W. Tatinian, CENTRIC, October 2013 ,Venice (ITALY)

- “Modeling of the organ of Corti Stimulated by Cochlear Implant Electrodes and electrodes potential definition based on their part inside the cochlea”, U. Cerasani, W. Tatinian, International Journal On Advances in Life Sciences, v 6 n 1&2 2014

PUBLICATIONS SUBMITTED:

- “Rapid phase noise simulation for diverses oscillator topologies, based on simplification of Hajimiri and Lee phase noise description”, U. Cerasani, W. Tatinian, Y. Vaiarello, IEEE Electronics Letters, 2014
- “Multi domain modeling of the cochlea: from Basilar Membrane stimulation to Spiral Ganglion cells depolarization”, U. Cerasani, W. Tatinian, Neuroscience, Elsevier Journal, 2014
- “Auditory nerve spike train mathematical modeling including various sources of neuronal noise”, U. Cerasani, W. Tatinian, Computational Neuroscience, Elsevier Journal, 2014
- “New electric system analog of Action Potential propagation with equivalent wave dynamics”, U. Cerasani, W. Tatinian, IEEE Communications Magazine, 2014

NUMBER OF PAGES: 288

JURY: Olivier Romain
Luc Hebrard
Carlos Valderrama
Fahd Benadbeljelil
William Tatinian
Gilles Jacquemod

ABSTRACT

Cochlear implants are used by severely deaf people for partial hearing sensation. The improvement of this electronic device may lead to better neurostimulation resulting in increase sound perception. Cochlear implants are separated into two parts, one inserted surgically inside the patient' s skull and the other part outside the body, behind the ear. An external microphone registers the sounds which are processed by a Digital Signal Processing Unit before their wireless transmission to the receiver which will select the right electrode to stimulate, depending on the external sound frequency.

Implanted people often complain of aesthetical issues, due to the voluminous part of the implant. As current trends in electronic aim to make chips smaller and less consuming, a redesign of the implant may be of interest to tackle this problem. In the work presented by Y. Viarello and used as basis for the receiver implant design, a new type of emitter was proposed, encapsulating a RF transmitter, a battery and a microphone. The RF choice was preferred to the coil antenna communication for space saving. This new type of external part of the implant was planned to be inserted inside the ear canal, rendering it almost unnoticeable. However due to the very reduced space of the ear canal and the low power supply of the embedded battery, the Digital Signal Processing unit was encapsulated inside the receiver, requiring a complete receiver electrical architecture restudy.

Behavioral modeling of the external part of the cochlear implant was first performed using the software Matlab®. Then the propagation channel was modeled using electrical analogy of the biological tissues. Noise extraction of the propagation channel was performed in order to obtain the specifications for the RF receiver.

Based on the RF transmitter specifications and noise propagation channel theoretical results, three types of suitable RF receiver architectures were discussed and compared in term of power consumption and Noise Figure. The retained architecture was then implemented in Matlab® in order to obtain an overall transceiver testing. Worst parameters extraction was performed defining the blocks to optimize. As the receiver is implanted inside the patient's skull, extended testing of the overall RF circuitry is of great significance.

Two types of signal modulation are performed in the transmitter part: a Pulse Width Modulation (PWM), followed by an On Off Keying (OOK) modulation to send the signal in RF. Both modulations required an oscillator, making the study of phase noise of importance for LF signal recovery as well as ISM frequency band enclosure. The theoretical review of phase noise theories presented by Leeson and by Hajimiri and Lee was accomplished before proposing a new unifying model linking both theories. This model, currently under development, may further facilitate phase noise computation. Computing timing jitter from phase noise, permitted extended testing of the accuracy of the overall transceiver and mainly defined the maximum precision that could be expected with the PWM using this particular architecture and ring oscillator .

The major ameliorations that can be made on cochlear implants to improve their hearing efficiency are mainly related to the electrode array inserted inside the cochlea. The limited number of electrodes, which is by far lower

ABSTRACT

than the number of nerve fibers present inside the cochlea, makes the stimulation of the auditory nerve very approximate. The precise understanding and modeling of the different part of the ear resulting in nerve fibers stimulation is proposed in this document. The mechanical model of the external and middle ear followed by the Basilar Membrane variations associated with an external sound wave was extracted from various models. Then a new mechanical equivalent of the organ of Corti and stereocilia displacement was developed and confirmed by physical experiments results available on literature. The hair cells depolarization associated with the stereocilia movement was also computed and the synapse between the HC and nerve fibers was mathematically modeled, in order to obtain the electrical stimulus of the auditory nerve associated with a random sound stimulus. Furthermore a new analog model of the nerve fiber information propagation was realized in order to obtain a realistic electrical analogy with nerve fiber depolarization propagation.

Based on impedance spectroscopy biological tissue characterization, we proposed a new electrical analogy of the system composed of the electrodes inserted inside the cochlea. This electrical analogy permitted theoretical results extraction defining the maximum battery duration as well as the minimum power required for an electrode to stimulate the surrounding nerve fibers. Then a topographic map based on the threshold of hearing function and on the spiral ganglion cells repartition inside the cochlea was proposed in order to stimulate differently the nerve fibers depending on their position inside the cochlea, to obtain a sound perception closer to the one reached by an healthy ear. A new algorithm based on an adapted Fourier Transform for the electrodes selection based on the sound wave frequency was discussed with poor theoretical expectancy. A similar principle using the same mathematical background was developed in order to develop hypothesis on how deaf people using cochlear implants can perceive sounds.

The different works performed which cover a large spectrum of physical disciplines, aimed to improve the implants sound restoration, justifying many independent researches.

RESUME

Les implants cochléaires permettent aux personnes atteintes de surdité profonde de percevoir des sons. Toutefois les sons restitués grâce à l'implant cochléaire sont souvent différents des sons originaux. L'amélioration de l'implant, grâce à une neurostimulation plus sélective par exemple, pourrait résulter en une meilleure qualité des sons perçus. Les implants cochléaires se divisent en deux parties, la première insérée chirurgicalement dans la boîte crânienne des patients implantés et la seconde qui se place à l'extérieur du corps, derrière l'oreille. Un microphone externe enregistre les sons qui sont transformés par une unité de calcul digitale avant leur transmission sans fil vers le bloc de réception qui sélectionne les électrodes à stimuler en fonction de la fréquence du son.

Les patients implantés sont souvent dérangés par la partie externe de l'implant, très encombrante. La miniaturisation des circuits électroniques devenant toujours plus petits et consommant de moins en moins d'énergie, a permis le développement d'un nouveau type d'implant tel que proposé par exemple par Y. Vaiarello. Dans ce nouveau type d'implant, la partie externe serait réduite et se placerait dans le canal auditif du patient. Nous avons utilisé ce nouvel émetteur (composé d'un module Radio Fréquence (RF), une batterie et un microphone) afin de créer un récepteur complémentaire dont l'architecture et le cahier des charges seraient grandement dictés par la composition de l'émetteur. Toutefois à cause de la place réduite dans le canal auditif et de la faible batterie insérée dans la partie externe de l'implant, l'unité de calcul digitale devra donc être placée dans la partie chirurgicalement implanté (interne) de celui-ci, aboutissant à une nouvelle étude complète de l'architecture électrique de l'implant.

La modélisation comportementale de la partie externe de l'implant a été réalisée avec le logiciel Matlab®. L'étude du canal de transmission et sa modélisation utilisant des modèles électriques de tissus biologiques a été ensuite effectuée ainsi que l'étude du niveau de bruit introduit par le canal. Ceci a permis la définition complète du cahier des charges du récepteur RF.

En utilisant les spécifications de l'émetteur RF et les résultats théoriques obtenus liés à la modélisation du canal, trois types d'architectures diverses pour le récepteur ont été comparés en terme de puissance consommée et de facteur de bruit. L'architecture retenue a été implémenté en Matlab® afin de modéliser la chaîne de réception complète. Cette modélisation a permis l'extraction théorique des paramètres critiques ainsi que l'évaluation des blocs à optimiser. Le test approfondi du récepteur est capital considérant la difficulté d'extraction de celui-ci une fois implanté.

Deux types de modulations différentes sont réalisés à l'émission : une modulation PWM ainsi qu'une modulation OOK, la dernière permettant d'envoyer le signal en RF. Chacune de ces deux modulations nécessite un oscillateur. L'étude et la restriction du bruit de phase est donc de grande importance afin de garantir une précision suffisante pour la modulation PWM et de ne pas émettre hors de la bande ISM sélectionnée. La description de deux théories très utilisées décrivant le bruit de phase (la théorie de Leeson et le modèle d'Hajimiri et Lee) est proposée et un nouveau modèle unifiant ces deux théories a été extrait. Ce modèle, qui est toujours en cours de développement, pourrait permettre de faciliter le calcul du bruit de phase pour divers oscillateurs. L'extraction du jitter à partir du bruit de phase et son impact sur le transmetteur complet, a restreint la précision maximale du signal PWM.

RESUME

L'amélioration principale qui pourrait être effectuée sur les implants cochléaires pour augmenter la reconstitution du signal sonore, concerne le fil contenant les électrodes qui est inséré à l'intérieur de la cochlée. Le nombre limité d'électrodes qui est très largement inférieur au nombre de terminaisons nerveuses présentes dans la cochlée, aboutit à une restitution du signal sonore approximative. La compréhension précise et la modélisation des différentes parties de l'oreille humaine qui conduisent à la stimulation des terminaisons nerveuses ont été effectuées. Le modèle mécanique de l'oreille externe et de l'oreille moyenne ainsi que la vibration de la membrane basilaire (due à la perception d'un son externe) ont été extraits de différents modèles disponibles et assemblés. Par la suite nous avons développé un nouveau modèle mécanique de l'organe de Corti et du déplacement des stéréociles, que nous avons validé à l'aide de données provenant d'expériences physiques caractérisant ces deux différentes parties. La dépolarisation des cellules ciliées suites au mouvement de la membrane basilaire a été calculée et la modélisation mathématique de la synapse entre les cellules ciliées et les fibres nerveuses a été réalisée, afin d'obtenir le stimulus électrique relatif à un son perçu quelconque. De plus un nouveau modèle analogique décrivant la propagation de l'information nerveuse a été développé et pourrait permettre une étude complémentaire des connections neuronales.

En se basant sur la spectroscopie d'impédance électrochimique des tissus biologiques, nous avons créé un modèle électrique du fil d'électrodes inséré dans la cochlée. Ce modèle électrique a permis de définir de manière théorique la durée estimée de la batterie ainsi que la puissance minimale requise pour stimuler les cellules nerveuses autour de chacune des électrodes.

Ensuite nous avons créé une carte topographique des cellules ganglions spirales dans la cochlée que nous avons modifié par l'inclusion de la fonction du seuil d'audition afin de stimuler de manière différente les nerfs présents dans la cochlée en fonction de leur position dans cette dernière. L'utilisation de cette carte topographique modifiée pourrait aboutir à une perception des sons plus proches d'une oreille saine. Un nouvel algorithme concernant la sélection des électrodes à stimuler en fonction de la fréquence du son perçu et utilisant la Transformée de Fourier Discrète, est proposé. Celui-ci pourrait permettre une meilleure répartition de l'énergie sur l'ensemble des électrodes. Toutefois l'amélioration de la perception des sons qui pourrait être apportée par cet algorithme est hautement spéculative. En utilisant un développement mathématique similaire, nous avons également tenté de reproduire les sons que pourraient percevoir les personnes utilisant un implant cochléaire.

Les différents travaux réalisés et décrits dans ce document couvrent un large éventail de disciplines physiques et les différentes recherches menées ont pour but l'amélioration globale des implants cochléaires.

PREFACE

"Every great advance in science has issued from a new audacity of imagination." ~John Dewey, *The Quest for Certainty*, 1929

"Nature composes some of her loveliest poems for the microscope and the telescope." ~Theodore Roszak, Where the Wasteland Ends, 1972

"Science is simply common sense at its best." ~Thomas Huxley

"There is two possible outcomes: if the result confirms the hypothesis, then you have made a measurement. If the result is contrary to the hypothesis then you have made a discovery." ~Enrico Fermi

"In questions of science, the authority of a thousand is not worth the humble reasoning of a single individual." ~Galileo Galilei

"Science, my boy, is made up of mistakes, but they are mistakes which it is useful to make, because they lead little by little to the truth." ~Jules Verne, *Journey to the Center of the Earth*

"The scientist is not a person who gives the right answers, he's one who asks the right questions." ~Claude Lévi-Strauss, *Le Cru et le cuit*, 1964

"Science, in the very act of solving problems, creates more of them." ~Abraham Flexner, Universities, 1930

ACKNOWLEDGEMENTS

First, I give thanks to God for protection and ability to do work, may God always bless us.

My deepest gratitude for the help and support is presented to the following persons who have contributed to make this study successful:

I would like to thank my parents and my family for their endless love, encouragement and for being a continuous source of inspiration.

Next I would like to thank my supervisors, Gilles Jacquemod and William Tatinian for the benefic support throughout the difficulties encountered. I would like to sincerely acknowledge William Tatinian for his invaluably constructive criticism, friendly advice and confidence in me.

I would like to extend my gratitude toward Jacques Noel for allowing me to follow electrophysiological courses which were of precious importance and remarkably pleasant.

I have truly appreciated all the kindness, constant help and technical support of all the LEAT members.

TABLE OF CONTENT

LIST OF ACRONYMS

Acronym	Definition
AC	Alternating Current
ACE	Advanced Combination Encoder
AGC	Automated Gain Control
AIS	Asynchronous Interleaved Stimuation
AM	Amplitude Modulation
AMKA	chain-a myosin kinase
AMPA	Alpha-Amino-3-Hydroxy-5-Methyl-4-Isoxazolepropionic Acid
AMPAR	Alpha-Amino-3-Hydroxy-5-Methyl-4-Isoxazolepropionic Acid Receptor
AMS	Analog Mixed Signals
AP	Action Potential
ASK	Amplitude Shift Keying
ATP	Adenosine Triphosphate
ATPases	Adenylpyrophosphatases
BER	Bit Error Rate
BM	Basilar Membrane
BSIM	Berkeley Short-channel IGFET Model
BSP	Biomedical Signal Processors

Acronym	Definition
BW	Bandwidth
CAP	Compound Action Potential
CI	Cochlear Implant
dB	Decibel
DC	Direct Current
DFT	Discrete Fourier Transform
DNA	Deoxyribonucleic Acid
DSP	Digital Signal Processing
EAS	Electrodes array associated with Acoustic Stimulation
eCAP	evoked Compound Action Potential
ECoG	ElectroCorticoGraphy
EEG	ElectroEncephaloGraphy
FIR	Finite Impulse Response
FOM	Figure Of Merit
FSK	Frequency Shift Keying
FT	Fourier Transform
GABA	Gamma Aminobutyric Acid
HC	Hair Cell
IFA	Integrated F Antenna
IHC	Inner Hair Cell
IIP2	2^{nd}order Input Inter modulation Product
IIP3	3^{rd}order Input Inter modulation Product
IIR	Infinite Impulse Response
ISD	Inter Spike Delay
ISM	Industrial Scientific Medical

Acronym	Definition
LNA	Low Noise Amplifier
LSB	Least Significant Bit
MS	Mixed Signals
NF	Noise Figure
NMDA	N-Methyl-D-Aspartic acid
OHC	Outer Hair Cell
OOK	On Off Keying
PLL	Phase Locked Loop
PMW	Pulse Width Modulation
PSS	Periodic Steady State
RF	Radio Frequency
STFT	Short Time Fourier Transform
SNR	Signal to Noise Ratio
SPEAK	Spectral Peak
SR	Slew Rate
TM	Tectorial Membrane
UWB	Ultra Wide Band
V&V	Verification & Validation
VCO	Voltage Controlled Oscillator
VGA	Variable Gain Amplifier
VHDL	VHSIC Hardware Description Language

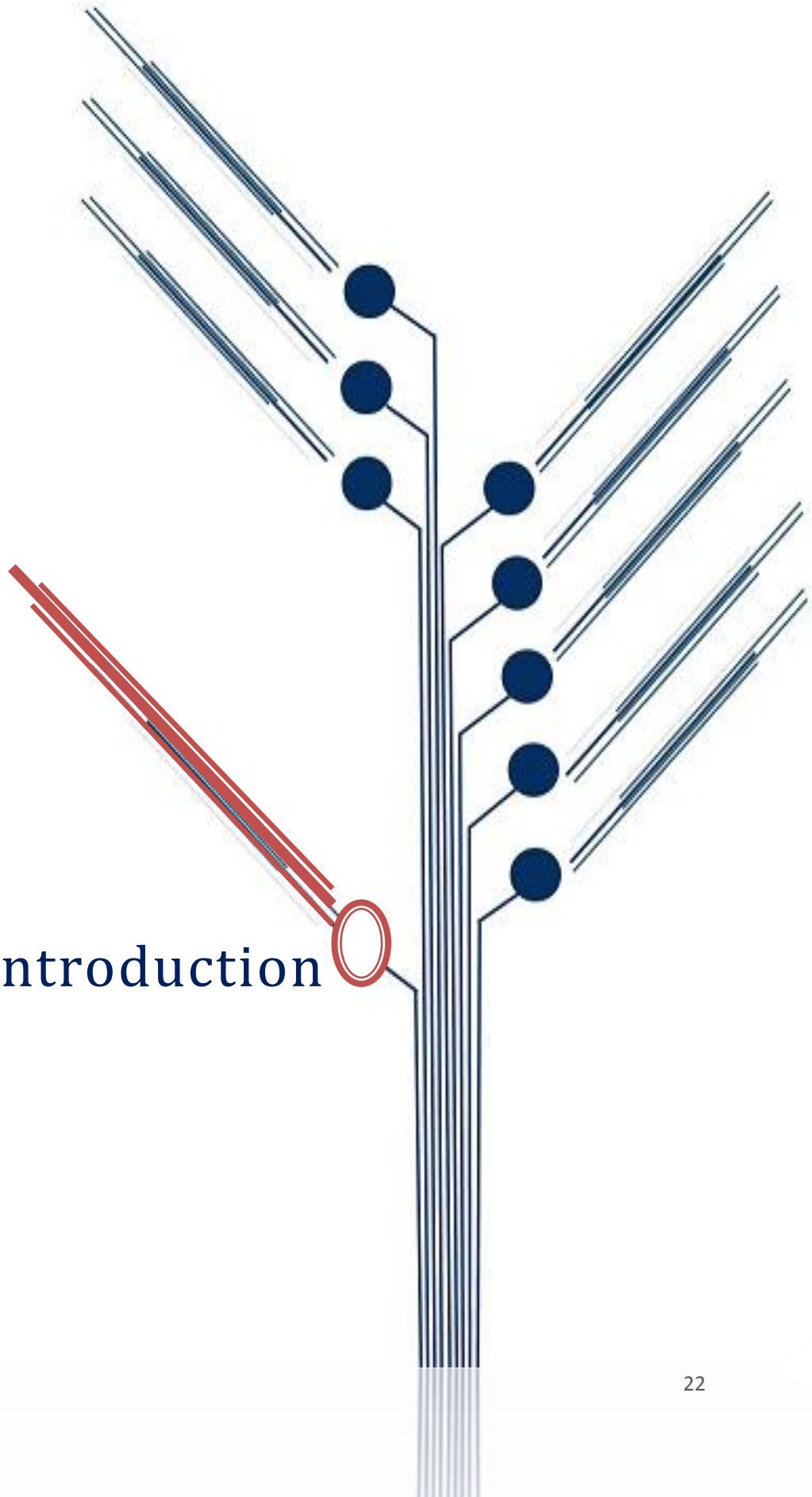

General Introduction

A. General introduction of biomedical engineering

Communication and communicating devices are today the leading words in industry as well as in our society. Long distances are not a challenge anymore for communication as structures were especially created to relay the signal such as antennas or satellites. Furthermore even for close communications, signals are transmitted more and more in a wireless way for convenience and simplicity. Wireless systems are nowadays ubiquitous all around us: cell phones, WI-FI, wireless sensors, RFID are some examples. Research on wireless system has increased incredibly during the last decades making them more efficient, more autonomous and easier to use.

Moreover biomedical engineering has recently emerged as a discipline mixing engineering fields such as mechanical engineering, electrical engineering, chemical engineering, etc. in order to cope medical challenges or to create medical devices. The creation of reliable medical sensors (for medical imaging or biological quantities detectors for instance) as well as the creation of embedded systems to cure illnesses such as peacemakers or cochlear implants are major applications of bioelectrical engineering.

B. Introduction to cochlear implant

Cochlear Implants (CIs) are neuro stimulating devices used to remedy partial or complete hearing loss. After decades of research, persons with hearing disabilities using CIs are able to communicate and to enjoy music or to follow a telephone conversation. Top performers cochlear implantees with present-day can obtain very high scores in diverse tests of hearing capacity such as speech recognition such as Consonant-Nucleus-Consonant words (50% of recognition achieved by top performers), recognition of sentences (around 90% achieved by top performers), recognition of syllabus in various tests such as developed in [1] (around 95% for top performers, very close to control patients with a healthy ear). These current results are encouraging and are proof of an almost complete restoration of hearing, for speech recognition at least, in a previously total deafened ear [1]. In addition as stated in [2], for most implanted patient speech recognition is mainly influenced by the audio signal (80% of speech recognition is achieved using only auditory indications, 40% using only lip reading and 90% using both), certifying better communication for implantees.

Various parameters poorly quantified are also involved in hearing restoration such as the time of deafness, the cause of deafness, the survival rate of Spiral Ganglion Cells (SGC), the age of implantation, the proximity of the electrodes array with the modiolus (during surgical insertion of the electrode array)or even the intelligence of the patient, maybe indicating better brain plasticity[3].

Furthermore the time involved for hearing restoration process in cochlear implantees is influenced by the age of implantation [4] and reaches a plateau after several months. As an example, the cortical response to brief speech sounds is within the normal range after 9 months in early implanted patients (around 3 years old) but only after one and a half year for late implanted patients (implantation around 12 years old) [1].

CIs allow direct stimulation of the auditory fibers with an electrodes array designed to reproduce the stimulus that would be generated by a healthy cochlea (FIGURE 1). In a functioning ear, when a sound wave strikes the eardrum, movement of the ossicles results in a liquid wave propagation inside the cochlea and stimulation of only a precise area depending on sound wave frequency. Complex mechanisms are involved (reviewed in Chapter III and Chapter IV) to finally produce auditory nerve fibers stimulation allowing sound perception. In the majority of patients, deafness is attributed to cochlea defects (cf. Section I.F).

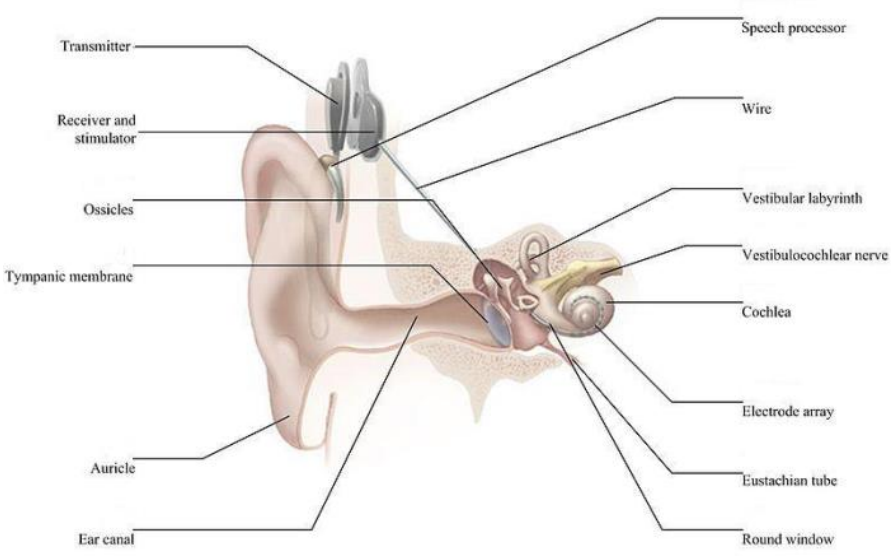

FIGURE 1: EAR ANATOMY AND COCHLEAR IMPLANT (ATTRIBUTED TO [5])

To do so, an external part of the hearing devices is located within the outer ear and contains a microphone that captures the acoustic waves and transforms them into an electrical signal. A Data

Processing Unit (DSP) subsequently creates the right stimulus for the electrodes array. Then, this signal is up-converted from baseband (audio signal from 20Hz to 20kHz) to the transmit frequency defined by the chosen ISM standard (13,56MHz, 433MHz, 866MHz or 2.45GHz). In the vast majority of cochlear implants, a transmitter coil antenna is preferred to send data to the receiver which is embedded inside the human body. Avoiding direct connection between the transmitter and the receiver is nowadays the solution retained by all the cochlear implants manufacturing companies to avoid infection risk. Several decades ago, CIs with a simple wire connection between these two parts (percutaneous connection) were commercially available [6]. The occurrence of infection may have motivated the withdrawal of single block cochlear implants, to prefer the use of two blocks, one external and the other inside the body, with an electromagnetic transmission between those. However electromagnetic transmission or wireless systems are not entirely safe. In fact the conclusions of the Bioinitiative report validated by the European Environment Agency [7] stated that WIFI waves can cause headaches, loss of concentrations, cardiac problems and even cancer (brain cancer, thyroid cancer and others neoplasms). Other documents [8, 9] have indicated possible protein conformation change, alterations in binding ligands to cell surface receptors and enhanced attraction between cells.

The danger of wireless systems are still controversial, hence extreme caution is advised for the use of such technology near the brain. Furthermore, the human body is mainly composed of water (70-80% depending on age). As the absorption coefficient of water at 2.45GHz is around 1m (cf Figure 2, attributed to [10]), all the brain may be affected by this wireless transmission.

New ways of transmission (light, vibrations) could be investigated to create safer CIs (outside the scope of this document).

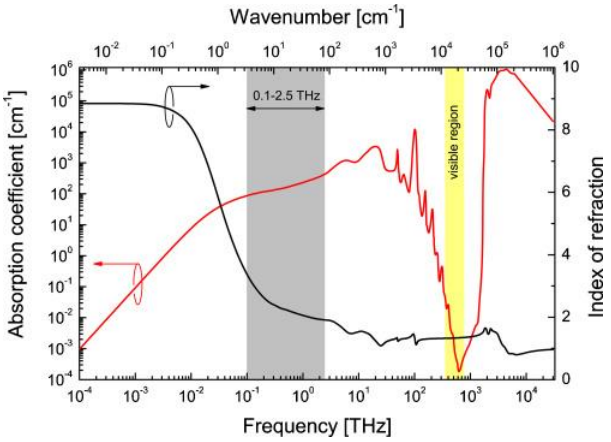

FIGURE 2: ABSORPTION COEFFICIENT OF WATER OVER FREQUENCIES (EXTRACTED FROM[10])

The corresponding receiver is located within the patient's head, close to the skull. It is composed of a demodulator and a set of electrodes, called the electrodes array. The electrodes array is driven by electrical signals resulting in stimulation of the auditory nerve fibers [11, 12].It is surgically inserted inside the scala tympani of the cochlea (Figure 3). The insertion depth of the electrodes array inside the cochlea (scala tympani) is around 25mm which is insufficient to stimulate all the cochlea nerve fibers since the cochlea measures approximately 35mm, resulting in inability of Cochlear Implant to stimulate low frequencies (explain in details in Section I.C).

Furthermore there are also safety concerns about cochlear surgery. Very low rate of abandoned procedures are achieved (less than 1%) but about 5% of the operations were followed by some forms of complications [13]. Major complications require a revision surgery as it may be the case in persistent ear infection, meningitis, facial nerve damage or repositioning of the electrode array but these complications are rare events [13].

As CIs performances are also dependent on the correct placement of the electrodes array inside the cochlea, incorrect positioning of the implant may result in poor language recognition. Hence correct insertion of the implant, with deep insertion and proximity to the modiolus is of capital importance. Delicate insertion surgery is required to avoid supplemental damage to the intra-cochlea structure [14].

As the technology is evolving very fast, CI replacement is advised after several years for better hearing sensation. However implant replacement is not the main preoccupation of manufacturing companies and the very elevated cost of the implant and surgery may discourage various users for system upgrade. A partial solution proposed in [14] could be to make the electrodes array detachable from the internal electronics to avoid cochlea surgery and damages. However to the author's personal belief, electrodes array future improvements would be the major reason for more accurate hearing in CIs users. New electrodes array are being investigated such as intramodiolar implants or functional nanoparticules coating the electrode pads for neurites growth toward the implant for very precise nerve fibers stimulation [1, 15].

Not all deaf people are candidate to CIs insertion. There are several criteria for acceptance such as profound bilateral sensorineural hearing loss or severe impairment of speech discrimination and recognition performance [16]. Besides the hearing improvement brought by CIs may greatly reside on the brain plasticity for adaptation to these new stimuli as well as the preservation of auditory nerve fibers and central nervous pathway neurons, explaining the better results obtained when the

device is inserted in very young patients or in patients who just become deaf (the main non genetic causes of deafness are presented in [17]).

Despites the incredible advantages brought to cochlear implantees, there is yet much room for improvement. At present, the reconstructed signal is not the same as the original sound due to the fact that the number of active channels is limited (around 8 depending on the type of CIs as explained in Section I.B) resulting in signal distortion. This explains the need of prolonged (re)learning process after patients implantation in order for them to ear and pronounce words correctly. As previously noted, any improvement especially in the electrodes array may be significant for patient hearing sensitivity. Electrodes array containing 30 electrodes [18] or nerve stimulation using light [19], hence very accurate, are also currently under study.

C. Undiscernible cochlear implants

Despite the disturbances associated with the electronics such as noise perception, battery lifetime, poor or no music perception as example, cochlear implantees often complains of various issues as reported in [20], such as electromagnetic perturbations near cell phones, esthetical issues or inconvenient external part for external activities. In order to tackle these secondary issues, new types of implants are being developed. Several years ago, the University of Melbourne research team proposed a Totally Integrated Cochlear Implant (TIKI) and phase I clinical trial results are available in [21]. Similar system was developed at Pittsburgh Ear Associates [22]

Other CIs manufacturing companies such as MXM® chose to lower aesthetic discomfort due to the voluminous shape of the external part of the cochlear implant. One of these prototypes (MicrA) proposed an architecture reorganization to insert the DSP (which is the most ample block) inside the receiver. In this work, presented in [23], the transmitter is inserted inside the auditory canal, sending RF waves (allowing reduced antenna size) to the receiver inside the patient' s skull. As the auditory canal space is limited, the DSP is now integrated on receiver, forcing electrical architecture reworking (this system is recalled in Figure 3).

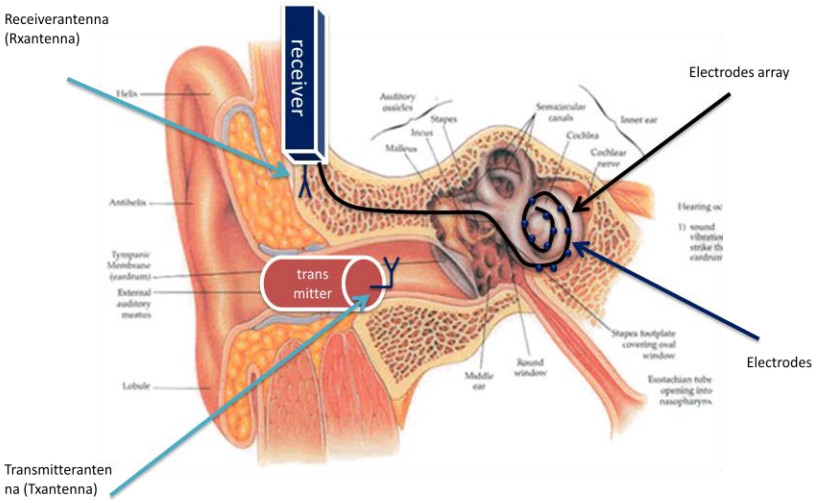

FIGURE 3: DEVELOPED COCHLEAR IMPLANT WITHIN EAR [24] (BACKGROUND EAR DRAWING ATTRIBUTED TO[25])

The transmitter architecture selected in [23], is based on a Pulse Width Modulation (PWM) encoding before sending the signal to the Industrial Scientific and Medical (ISM) band using an On Off Keying (OOK) modulation. This architecture selection was justified in [24]. The OOK modulation was preferred due to low power consumption but resulted in high noise sensitivity degrading the Bit Error Rate (BER) ratio. To ensure encapsulation of the antenna, the modulating frequency was 2.45GHz, however suffering of high attenuation as the propagating middle is human tissue. Finally the PWM was selected offering many advantages such as low integration surface, no need of numerical part and low power consumption. However the computational velocity and resolution were impacted (further discussion in Section V.C defining theoretically the maximum resolution reached by this type of system embedded in the auditory canal).

The work presented by Y. Vaiarello [23] is used as basis for the receiver specifications and receiver architecture selection as well as for the modeling of the overall CI system.

D. Main challenge in the field and project main goals

To create a suitable receiver to the work performed by Y. Vaiarello [23] in our laboratory, allowing a complete prototype of the presented less noticeable CI, the behavioral modeling of the transmitter and the propagation channel were first completed to obtain specifications for the receiver. Architecture choice of the receiver was considered before the electrical design of the

selected one. Behavioral modeling of the receiver blocks was performed to obtain the entire electrical system modeling to study parameters influence and to deduct system optimizations.

Phase noise influence on signal integrity was also studied, especially the influence of the low frequency oscillator. As we performed time simulations, conversion from phase noise to timing jitter was reviewed and integrated to the block model of the low frequency oscillator used for PWM signal creation.

As already introduced, the electrodes array and its interface with the nerve fiber are the elements involved in sound restitution accuracy. Any improvements in this stimulation may greatly increase the hearing perception.

In deaf patients, nerve response may be registered using back telemetry. Their hearing responses following sound wave detection are often evaluated in terms of evoked Compound Action Potential (eCAP) which characterizes the auditory nerve activity. A complete multi-disciplinary model from eardrum displacement to eCAP production has been developed.

To the author's best knowledge, such a heterogeneous model including the external and middle ear structures, connecting sound frequency and amplitude with the vibrations of the Basilar Membrane (BM), including the organ of Corti mechanical model and ultimately stimulating auditory nerve fibers, was not available until now. Synapses functioning and nerve fibers membrane voltage depolarization propagation were reviewed in that purpose.

This multi-disciplinary model may bring new insights, especially if validated by case measurements, to link special nerve responses with ear pathologies.

In addition, the deep understanding of the hearing mechanism may be of great importance to improve CI nerve stimulation and hearing restitution.

There is constant research ongoing to find new algorithms for improving sound perception in implanted patients. These improvements aim to recreate the illusions of a continuous and precise cochlea stimulation whereas the electrodes array constituting the cochlear implants are partly stimulating the cochlea. Using signal processing theory, we proposed new algorithms that may bring greater sound perception for deaf people. These algorithms are however waiting to be implemented in cochlear implants processing unit, for physical testing.

As already introduced, the nerve fiber electrode interface is central to hearing reconstitution. The accuracy of sound reproduction by cochlear implants is mainly dependent on this interface. Consequently, the precise understanding and modeling of this interface as well as new solutions for its improvement may be the main factors for cochlear implants ameliorations.

Cochlear implants often require extended learning process in order for deaf people to understand words and correctly express themselves as the sound they perceived is disturbed. Creating profiled learning exercises may hence diminish the learning time. In that intent it may be interesting to estimate or reproduce the sound perceived by deaf people using cochlear implants.

The previous points were investigated and we proposed new solutions to tackle these difficulties.

Besides they are also numerous issues that are not covered in this document and may improve the hearing sensitivity in implanted people: increasing battery duration allowing reduced battery reloading frequency, decreasing the noise brought by the electronic device and resulting in constant low level sound perturbations.

E. Technical choices

For biomedical implant more than any other application, foreseeing the behavior of electrical device *in situ* is of capital importance as failing to do so would immediately result in implanted patient discomfort. On top of that, the low power aspect of implanted electronics often leads to unusually poor designs in terms of performances compared to classical designs. Modeling of such designs for extended testing purpose is hence required.

The overall model is composed of an RF part, an analog one, a digital one and physical models of hearing stimulation. For modeling purposes, two main systems were considered: the Mixed Signals (MS) system (RF/analog/digital) and the heterogeneous system (mixed signals system/physical model of the hearing process).

1. Mixed signals system

MS languages may be used for the description of such system due to the presence of an analog part and a digital part. The different simulation frequencies needed for the analog part simulation and for the digital part simulation are still nowadays problematic [26].In fact at present time, SPICE simulators translate electrical circuits into matrices (using Kirchhoff' s circuits laws) and solve them at frequencies much higher than the working frequency (2.45GHz in our case) whereas DSP are working at frequencies often much smaller (around 100MHz), hence resulting in very long simulation time of the digital part. To decrease the simulation time of a MS System, various solutions exist such as partionning [27] or dynamic delay creation [28].

A solution often retained is the behavioral description of analog blocks [29].Avoiding a transistor level simulator for such a system can lead to significant saves in terms of CPU time and makes it possible to perform a fast architecture exploration and to find out which electrical parameters are of particular importance to device functioning. This MS system simulation is limited to time domain simulation only and require blocks design and testing before MS model creation.

VHDL AMS, Verilog A and SystemC AMS are currently the most popular MS languages used, ensuring high accuracy, integrating a large level of abstraction and reducing simulation time. At higher level of abstraction, Matlab/Simuling® simulation can be used for architectural exploration. Simulink® has an inbuilt analog toolset giving simulation results often as accurate as the ones obtained by SPICE simulations [30]. However the increase in simulation time is consequent compared to other MS tools which makes it unpopular at present.

2. Heterogeneous system

The modeling of the complete hearing process was performed connecting various models. As far as the author knows, no other accurate hearing model with external hear modeling, physics of the cochlea integration, mechanical modeling of the organ of Corti and mathematical modeling of nerve fibers transmission was developed.

The electrical stimulation of the organ of Corti by the electrodes array was theoretically developed to connect the electrical stimulation with the nerve fibers stimulation. We choose Matlab/Simulink® environment to model such an heterogeneous system providing advantages such as high level modeling (mathematical modeling), graphic function for visualizing data, data reading made easy from different inputs (USB key or various ports for instance).To improve portability, to refine the behavioral description and add noise sources, it was decided to create our own behavioral models (for the electrical blocks) instead of using existing ones. From this perspective, we created these models discarding Matlab® existing functions except for the *Gaussian noise generator* and the *waveread* function which can be found in other languages.

To implement the cochlea movement following sound perception or nerve fiber transmission, Maple Sotware® was used as it allows symbolic mathematical calculus.

The design of the electrical blocks (such as VCO or LNA) and their results extraction, previously accomplished before their behavioral modeling, was done in SPICE.

F. Modeling guidelines

For the blocks modeling, several rules were followed in order to ensure efficient model creation, to reduce simulation time and to increase results accuracy:

- Behavioral modeling of the blocks was preferred to structure modeling. In that intent equations were favored than precisely describing the internal architecture [31].
- Although the corresponding physical effects were studied, it was not necessary to model the behavior of the blocks outside their normal working range, a warning message was acceptable [31].
- Refining the model should be made only for significant parameters to optimize simulation time.
- For MS modeling, the models should take into account the perturbations of the load and the source.
- No digital noise coupling or substrate noise injection were considered.
- Parasitic effects were found insignificant (cf Section I.C.6) when comparing circuit measurements with circuit design performances hence they were neglected.

G. Verification and Validation

Testing process goal is to discover defects in the model created: blocks behavior may be incorrect or not in accordance with the specifications. To ensure that the modeling was correct, we used a similar approach to Verification and Validation (V&V) principle [32-34].

V&V ensures that the models are correct with a certain degree of confidence. The verification of each electrical block model was mainly done by single unit testing, where each block was considered as a black box. The comparison of this testing with results from SPICE simulation for diverse input cases ensured that the model was conformed to specifications.

Model creation may be disconnected from real world and often very restricted to narrow case representation. The validation of model is hence of primary importance. In the V&V procedure, the validation is often done after the model has been verified, and is used to demonstrate that the model fulfills its intended function [35]. Modeling main goal is to extend the testing of the real system as well as to make predictions about future events [33]. The validation of MS modeling was

achieved by comparison of the results from physical testing and by statistical analysis (as explained in Chapter I and II).

Furthermore there is a complementary work to validate the model: which are the particular cases where the model is validated (in accordance to physical measurements)? How can model re-use in other cases be performed? Our model validation of the complete hearing process was only targeting the healthy cochlea models.

H. Thesis outlines

This document is subdivided into 5 main Chapters. Chapter 1 focuses on model development for the transmitter and for the propagation channel. As the propagation channel is composed of biologic tissues, review of human tissue modeling theory is presented.

Chapter 2 explains the architecture selection motivation for the receiver followed by the electrical SPICE design of three different receiver architectures. The testing process of the overall system was carried out and could permit to recognize the restricting parameters for eventual block optimization. Then phase noise modeling was introduced and converted into timing jitter. The timing jitter inclusion into the low frequency oscillator model used for PWM creation permitted to extract the maximum precision envisaged. Besides phase noise restriction in the ring oscillator used for OOK modulation was necessary to respect the ISM radio bands specifications.

The creation of a heterogeneous model for the hearing process, starting from the sound reception to nerve fibers stimulation, is proposed in Chapter 3, for a healthy ear. Mechanical model of the outer ear and of the organ of Corti associated with nerve fibers stimulation by neurotransmitters at synapses were defined in order to express the auditory nerve response as a function of the sound wave input. To theoretically test the validity of our hypothesis, two sound waves of 300 Hz and 600 Hz respectively with 50 dB of magnitude were used as input and the subsequent results were discussed.

Chapter 4 discusses the nerve fibers information propagation (also called Action Potential (AP) propagation) spatial and time properties. A new analog model of action potential propagation was created with same wavelength, velocity and frequency as experimental ones. Then spikes trains were introduced before reviewing the current electrophysiological techniques to record nerve fibers activity.

Finally Chapter 5 describes the electrical model of the organ of Corti, created from anatomical study. Organ of Corti and electrodes interface was theoretically studied and an electrical analog of such a system was realized. The theoretical results obtained from this model may permit to define battery sizing of the cochlear implant, electrode stimulation type or minimal spacing size between electrodes.

A topographic map which indicates the afferent nerve fibers repartition inside the cochlea weighted by the cochlea sensitivity toward certain frequencies was created. This map may be used to increase cochlear implants sound perception. Applying the Discrete Fourier Transform (DFT) formula to only the frequencies stimulated by the electrodes, permitted a new algorithm proposition for electrodes selection. In addition this adapted Fourier transform was also used to estimate the sound sensitivity in deaf people using cochlear implants.

State of the art and technical background review was performed in each chapter separately rather than gathered into a single section. This choice was the most convenient, as the prerequisites and physical fields covered were often different and chapter specific.

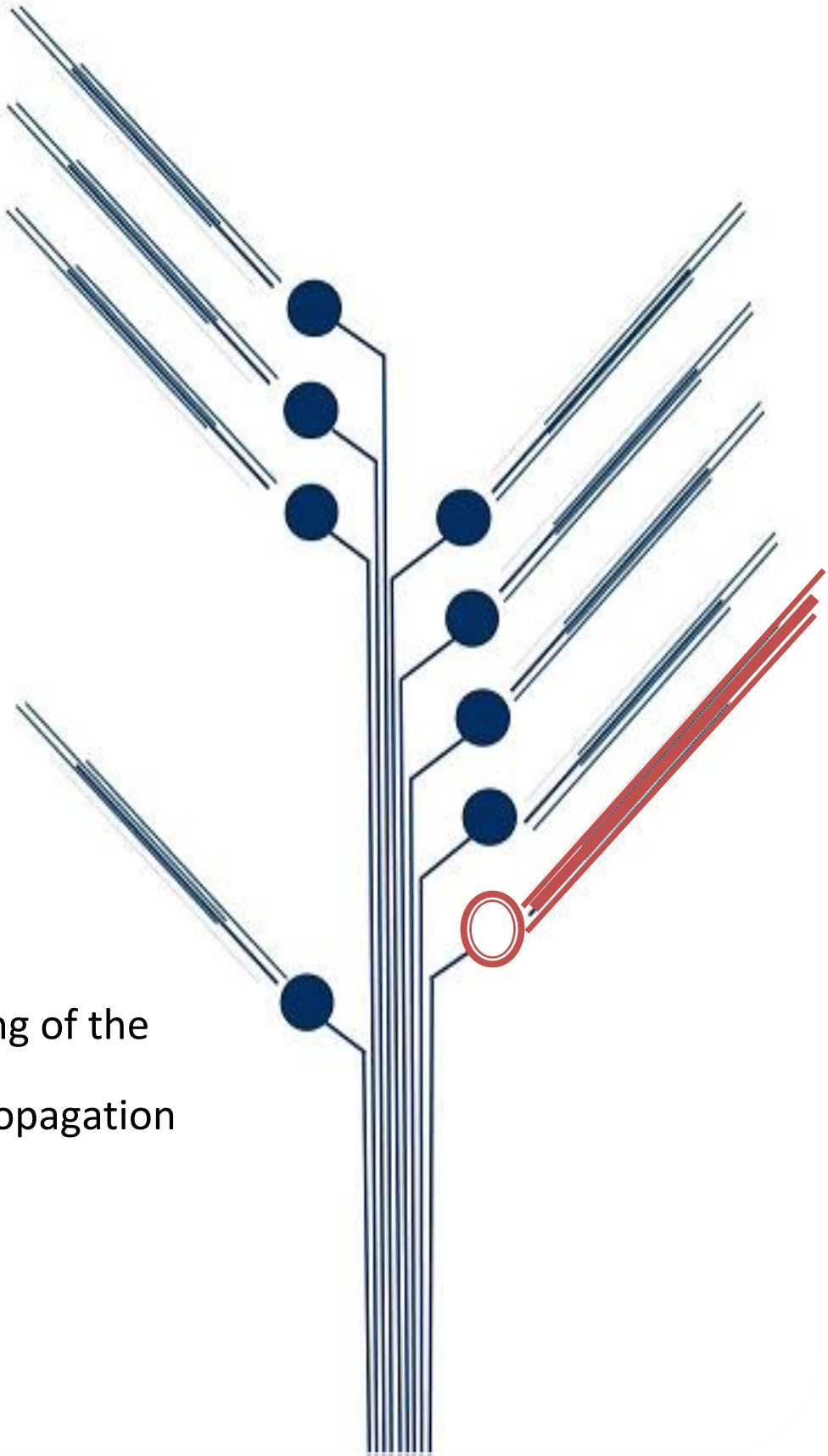

Chapter I:

Behavioral modeling of the transmitter and propagation channel study

A. Opening notifications

As the transmitter was available from the start, the modeling efforts were concentrated on this part. In this chapter the emitter architecture is presented, then each analog and RF block (and their corresponding behavioral models) that we created for this work are described more in detail. The encountered modeling and design bottlenecks are emphasized and the results are compared to SPICE simulations for block design optimization purpose. The maximum theoretical precision of the Pulse Width Modulation (PWM) signal (cf Section I.C) is discussed based on the ISM frequency band specifications and from prototype measurements.

Finally, the physical model of human tissues we implemented is presented to characterize the propagation channel and to obtain realistic receiver specifications.

B. Transmitter architecture

The architecture considered for modeling is described in Figure 4. It consists of a 2.45GHz OOK transmitter and the associated receiver.

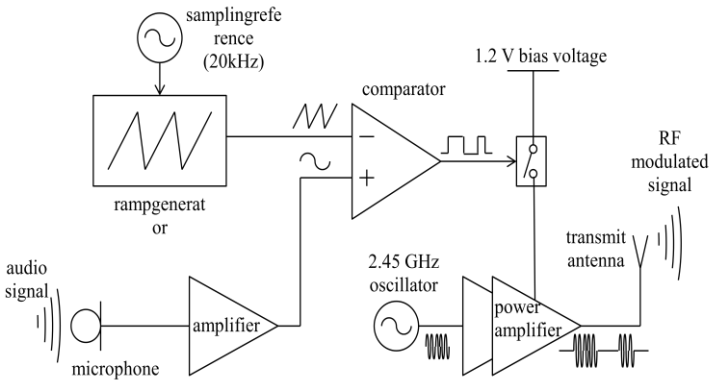

FIGURE 4: TRANSMITTER ARCHITECTURE

The transmitter gathers of a 2.45GHz oscillator generating a sine voltage which is amplified to the maximal allowed power in the ISM band and PWM. The modulating signal's duty cycle is determined according to the amplitude of the audio signal. The ramp block receives a rising edge from the

sampling reference clock which is approximately one thousand times higher than the sampling frequency of the microphone allowing to reach a maximal theoretical resolution of 10 bits at 20kHz [24]. The determination of the maximum number of bits reached by the PWM are one of the goals of the modeling and are discussed in the Section I.C.6 and II.D. The shape of the signals of relevance are given in Figure 5.

An example of ideal simulation, without noise nor distortion is given in Figure 5, where the different voltages represented are plotted as a function of time. In the top window, the output voltages of the low frequency amplifier (sine), ramp (triangle) and comparator (rectangle) are superimposed. In the bottom window, the RF signal (2.45 GHz carrier modulated with a PWM signal) is presented.

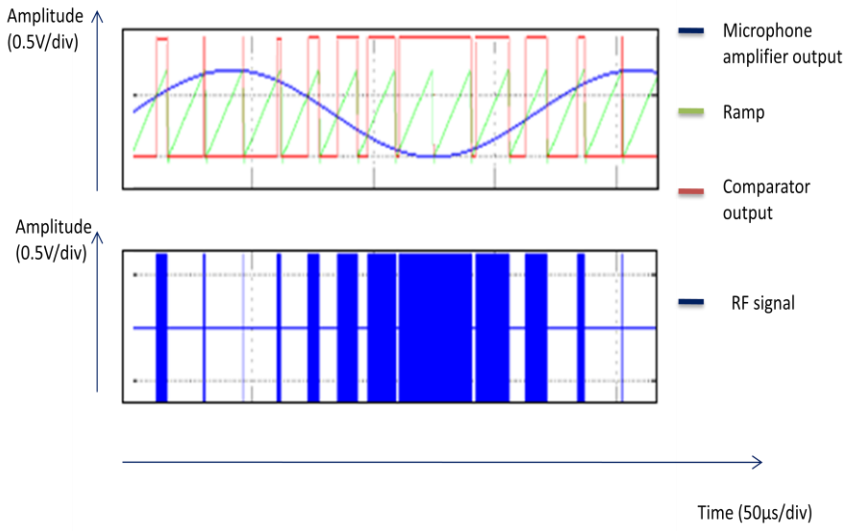

FIGURE 5: TRANSIENT IDEAL SIMULINK® SIMULATION. TOP : AMPLIFIER, RAMP AND COMPARATOR OUTPUT, BOTTOM : RF SIGNAL.

C. Model implementation

1. Baseband module implementation

The implementation in Matlab/Simulink® (displayed in Figure 6) was graphically very close to the electrical architecture, allowing a fine tuning of each block. In this way, corruption of these blocks with non linearities or noise perturbations was made easier as well as new implementation in case of architecture redesign.

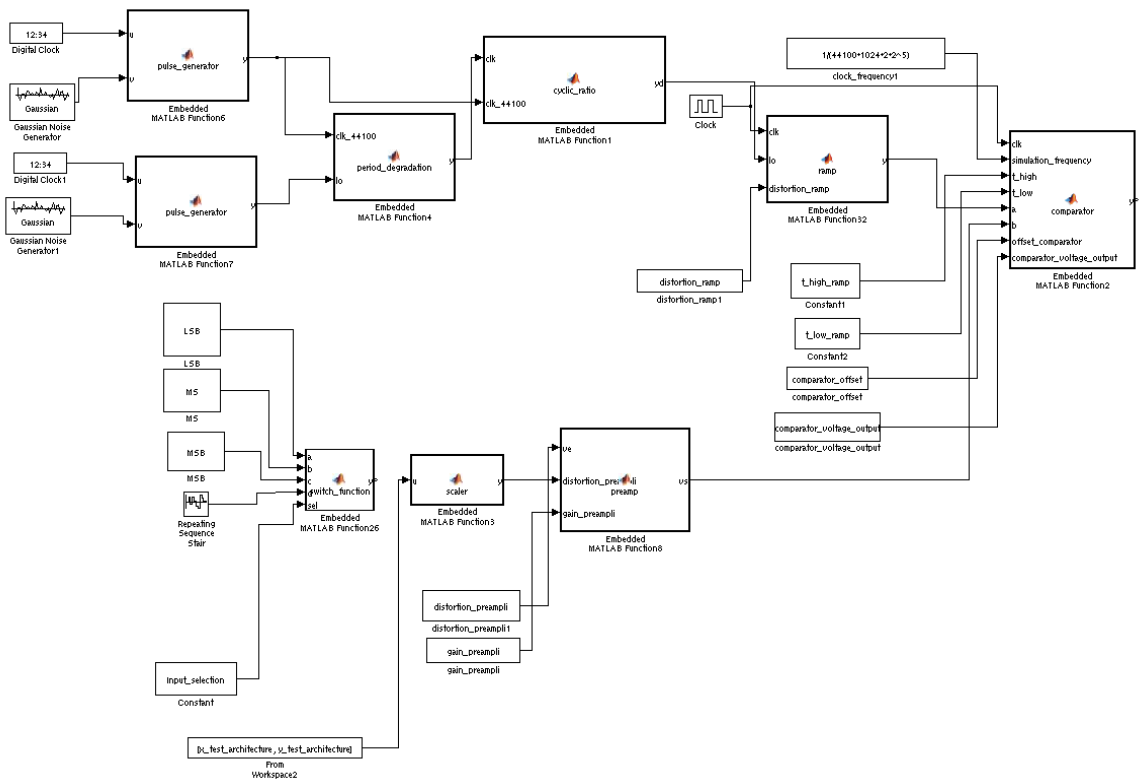

FIGURE 6: BASEBAND MODULE DESCRIPTION IN SIMULINK® ENVIRONMENT (THE BLOCKS WERE CREATED USING MATLAB® CODE)

For the first system simulation, the number of bits associated with the PWM encoding (N_{PWM}) has to be defined. The PWM upper limit depends on the product of the microphone frequency and the PWM Least Significant Bit (LSB) which should be enclosed in the ISM frequency range of the selected ISM band [2.4GHz;2.5GHz]. The maximum baseband frequency should be lesser than two times the selected ISM frequency range to respect the Shannon theorem [36, 37], which established the upper limit of N_{PWM}.

EQ. 1

$$f_{microphone} * \left(2^{(N_{PWM}+1)}\right) < \frac{(50) * 10^6}{2}$$

$$\Rightarrow exp^{((N_{PWM}+1)*ln2)} < \frac{50 * 10^6}{f_{microphone}}$$

$$\Rightarrow N_{PWM} < \frac{\left(ln\left(\frac{50*10^6}{f_{microphone}}\right)\right)}{ln(2)} - 1$$

$$\Rightarrow N_{PWM} \leq 10$$

where $f_{microphone}$ is the maximal microphone frequency and was equal to 20kHz for the microphone used.Furthermore to permit efficient filtering, the PWM signal frequency band, defined by the Least Significant Bit (LSB) should be significantly lower than the selected ISM band frequency range. Therefore the N_{PWM} value selected for subsequent testing was 8 bits (further refined in Section II.C and II.D)

2. Cyclic Ratio block and Oscillators description

a) Voltage Controlled Oscillators (VCO)

Jitter and phase noise limitations are of particular importance in this architecture since a high jitter on the low frequency oscillator irremediably causes demodulated signal distortion and high phase noise on the local oscillator results in spectral leakage outside the allowed frequency band.

In this Section, we did not study the influence of phase noise, resulting in a unsophisticated modeling of the oscillators. The study of oscillator perturbations on the signal integrity were studied in Section II.E, in terms of phase noise characteristics to determine statistical parameters for time domain simulation. Mathematical models were developed in Section II.E, to study jitter influence on the signal integrity. These models were mainly statistical, discarding their use in temporal simulations since the temporal simulation may characterize statistical effects only if repeated a significant number of times, which obviously would lead to a significant increase in simulation time. In this case, temporal models for oscillators included in the transmitter models brought no significant advantages than considering jitter inclusion independently of the other blocks.

The proposed architecture is composed by an initial PWM followed by an OOK modulation thus two oscillators working at different frequencies were required. The low frequency oscillator with a central frequency of 20kHz associated to the PWM ramp generator was critical for the system accuracy and the high frequency oscillator working with a central frequency of 2.45GHz had to be confined in the 2.4 – 2.5 GHz ISM band.

Furthermore anticipating eq. 30, presented in Section II.G.1 (which indicates that phase noise is inversely proportional to the consumed power and this characteristic is of interest for further optimization of the transmitter),the power budgeting of each block set a maximal phase noise value and thus a maximal carrier frequency shift within the ISM band (cf Section II.E).

b) Cyclic Ratio generation block

The cyclic ratio module has two clock generators as inputs:

- The first clock generator (clk_1) has a frequency of 20kHz which corresponds to the sampling frequency of the signal coming from the microphone. 20kHz is therefore the maximum frequency allowed between two consecutive frames.
- The second clock generator (clk_2) has a frequency of $20000 * (2^{(N_{PWM}+1)})$ where N_{PWM} is the maximum number of bits that will compose the PWM signal. As discussed above, N_{PWM} is fixed to 8. This clock generator should not be confused with the carrier oscillator (f_{osc}) used for the OOK modulation

The cyclic ratio generator creates a clock signal having a frequency of 20 kHz and with a clock ratio of $\frac{1}{2^{(N+1)}}$. The cyclic ratio algorithm is summarized by the flowchart exhibited in Figure 7.

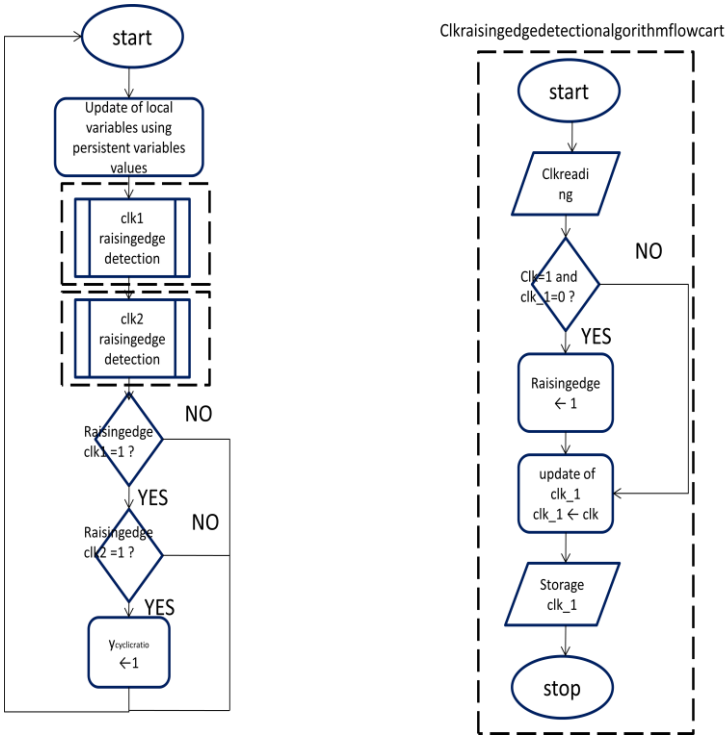

FIGURE 7: FLOWCHART OF THE ALGORITHMS USED FOR THE CYCLIC RATIO CREATION (LEFT) AND FLOWCHART OF THE RAISING EDGE DETECTOR (RIGHT)

where $y_{cyclicratio}$ is the output of the cyclic ratio block. Remembering that clk_1 is the variable associated with the first oscillator(having a frequency of 20kHz) and clk_2 is a variable associated with the second oscillator(with a frequency of $20000 * 2^{(8)}$), clk_1 is the previous state associated with the local variable clk in the raising edge detection

For the cyclic ratio generator algorithm, first the reading of persistent variables and then the update of local variables is made in order to load variable contents between two program executions (clk_1, clk_2).Then one raising edge detector linked to the faster clock $clk_2$and also a second raising edge detector which identified the raising edge of the second clock signal clk_1, were employed. The principle of this algorithm is straightforward: an output signal of time length equal to $\frac{1}{20000*2^{(8)}}$ is created each time the two raising edge detectors are equal to 1.

The raising edge detection was performed using a simplistic algorithm which used a buffer to store the value of an external clock (clk). The current value of clk and the previous state value (clk_1) were compared (the output raised to 1 when clk=1 and clk_1=0).

The time variations of clk_1, clk_2 and the created ramp reset signal (also named local oscillator) are indicated in Figure 8.

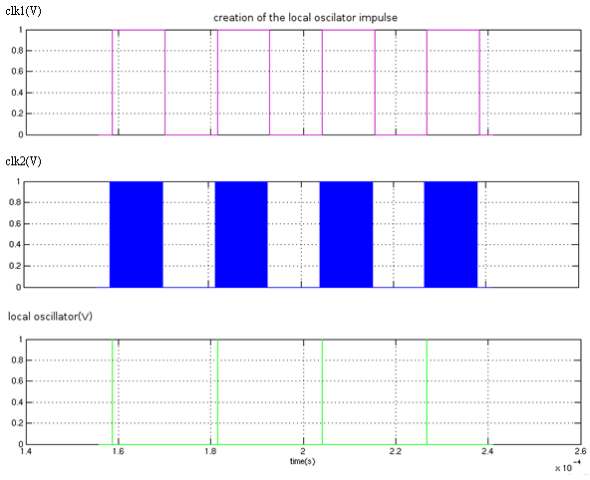

FIGURE 8: LOW FREQUENCY (LOCAL) OSCILLATOR PULSE CREATION BY THE CYCLIC RATIO BLOCK USING TWO OTHER OSCILLATORS

3. Power Amplifier

The mathematical model ofthe Power Amplifier (PA) can be found in [38, 39] and is usually described by eq. 2:

$$v_s(t) = a_1 v_e(t) + a_2 {v_e}^2 + a_3 {v_e}^3 \qquad \text{EQ. 2}$$

where $v_e(t)$ is the input voltage, $v_s(t)$ the output voltage, and a_1, a_2, a_3 scalar coefficients which depend on the 1 dB compression point (P1DB) and the Intermodulation Products of the second and third order (IIP2, IIP3) as described in [40-43]. The corresponding powers are then derived from eq. 2 according to the circuit input and output impedances. The PA mathematical model was limited to the third order time description but can be further extended as expressed in [44, 45] if needed.

However as the a_3 coefficient is negative to account for saturation effects, using only eq. 2 would lead to a v_s decrease if v_e was higher than a specific value v_{max}. Consequently, in the PA model construction, the local maximum of eq. 2 is used to switch equations for v_s description (cf eq. 3).

$$v_s(t) = \begin{cases} a_1 v_e(t) + a_2 v_e(t)^2 + a_3 v_e(t)^3 \; if \; v_e \leq v_{max} \\ v_s(t) + a_1 \, v_e(t) \qquad if \; v_e > v_{max} \end{cases} \qquad \text{EQ. 3}$$

The time where $v_e = v_{max}$ is reached (t_p) can easily be computed from the previous equation. The transfer expression for $v_e > v_{max}$ has to be modeled in order to correctly simulate input signals in the saturation region of the PA.

The modeled characteristic is compared to actual SPICE simulation in Figure 9.

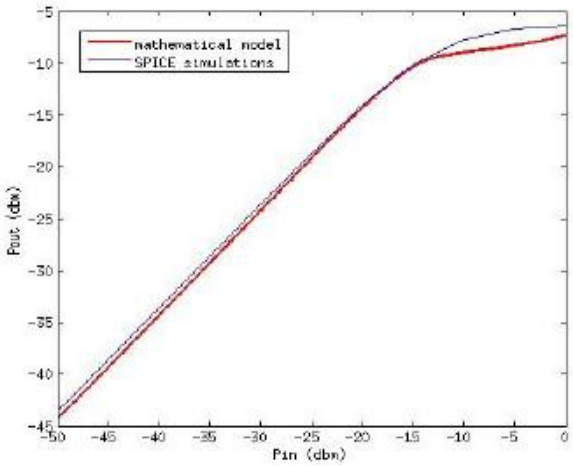

FIGURE 9: COMPARISON BETWEEN THE POWER GAIN CURVES FROM MATHEMATICAL MODELING AND SPICE SIMULATIONS

The PA model also includes noise corruption. The added PA noise (N_a) was supposed to be white noise because 1/f noise can be neglected around the working frequency (2.45GHz). The added noise is described by the Noise Factor (F), given by eq. 4:

$$F = \frac{N_a + GN_i}{GN_i}$$ EQ. 4

where N_a is the PA added noise,G the power gain and N_i the input noise. N_a and N_i were obtained using a SPICE Periodic Noise analysis on the PA only or on the PWM output block respectively. Only the output noise was take into account. G was obtained by a Periodic Steady State (PSS) analysis in Cadence. Other analysis may be used to extract those parameters (Scattering Parameters (SP) analysis for power gain, direct noise analysis for output noises floor,...)

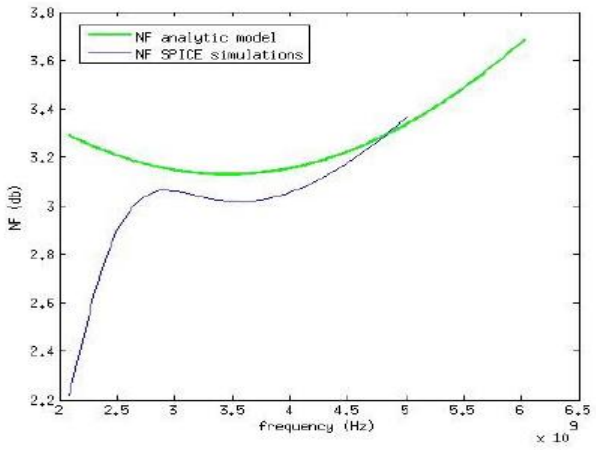

FIGURE 10: COMPARISONS BETWEEN THE MATHEMATICAL NF MODELING SIMULATIONS AND SPICE NF SIMULATION OF THE PA

Figure 10 presents the comparison between the Noise Figure (NF) from analytical model and electrical simulations. The NF simulated shape was not perfectly following the SPICE simulated NF since the equations implemented for NF modelling were standard equations to ease the computations, however the difference was very small (less than 1dB) between the NF values. Furthermore this parameter is not of critical importance because the PA is placed at the end of the transmitter and, according to Friss Formula [46].

Figure 11 shows the block diagram of the PA model. For modelling purpose, two PA were associated, one modelling the ON state of the PA and the other the OFF state. In this model the gain Kp_{OFF} of the OFF state was set to zero to decrease the simulation time. However this approximation is inexact as the real measurements made on the CMOS prototype (cf Section I.C.6) showed that during the OFF state of the PWM a few signal flowed from the PA input to the output at the working frequency due to parasitic capacitance.

The 2.45 GHz Voltage Controlled Oscillator (VCO) signal was applied to the respective PA inputs. The PA outputs were controlled by PWM and $\overline{PWM}$. Finally white noise corruption (N_a) was added in the PA model.

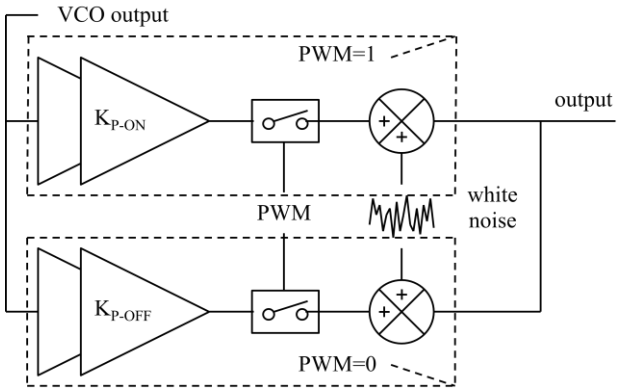

FIGURE 11: BLOCK DIAGRAM OF THE PA MODEL WITH NOISE CORRUPTION

The errors between the SPICE simulations and the mathematical models may arise from the low power design which causes huge non linearities, just partly taken into account in this modelling work, to reduce simulation time.

4. Ramp creation

The PWM signal was obtained using a ramp block generator which was compared to the input signal (wave sound from the microphone). A pulse is generated at a frequency of 20kHz and resets the ramp. Shorter is this pulse time length, greater is the accuracy that can be reached by the PWM.

The entire ramp can be constructed adding both the raising and the falling part equation selected by associated window functions (eq. 5)

$$s(t) = s_1(t)\prod\nolimits_{raising}(t) + s_2\prod\nolimits_{falling}(t) \qquad \text{EQ. 5}$$

where $\Pi_{raising}$ is a window function equal to 1 only when the ramp is raising and $\Pi_{falling}$ the opposite window function; s_1 and s_2 are obtained using polynomial extraction functions of the raising region of the ramp and the falling region of the ramp respectively.

Inaccuracies between the analytical model and the SPICE simulations shown in Figure 12 results from low level rank polynomial modeling. There is a maximum error between the 2 curves that can reach high values in the falling part and is much more limited, around 3%, in the rising part. The rank of polynomial extraction directly impacts the simulation time, however modeling the exact transient shape of falling part of the ramp is not critical because the signal distortion is due to the raising part of the ramp only. The falling part mainly impacts the data rate, meaning that only the fall time is of relevance independently of the transient model accuracy.

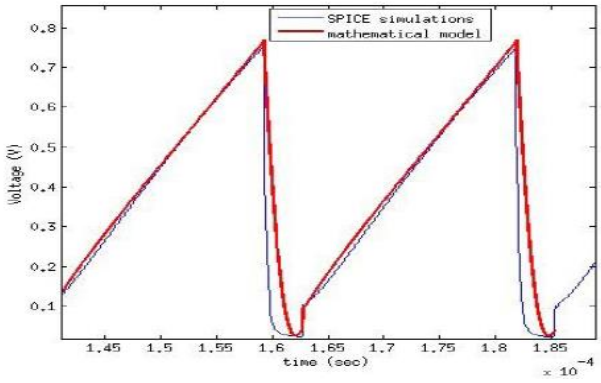

FIGURE 12: RAMP OBTAINED BY TRANSIENT SIMULATIONS BETWEEN THE ELECTRICAL DESIGN AND ANALYTICAL MODEL

5. Comparator modeling

The comparator is central to PWM modeling as it compares the input with a temporal ramp signal, yielding in a time length modulation. The comparator model includes constant distortion and offset perturbation as well as maximum rate change limitation of the output voltage, i.e. SlewRate (SR), extracted from SPICE simulations (by feeding the comparator input with a square function and computing the maximum output slope).

The mathematical comparator model without distortion is presented in eq. 6:

$$y = \begin{cases} 1 \ if \ v_{in} \geq v_{ref} + v_{offset} \\ 0 \quad otherwise \end{cases} \qquad \text{EQ. 6}$$

where y is the comparator output, v_{in} and v_{ref} are the comparator input signals and v_{offset} is the voltage offset defined by SPICE simulations as the minimum v_{ref} voltage (when v_{in} voltage is set to 0V) required for a comparator steady-state variation.

Both comparator input signals are analog, they are hence corrupted by noise especially high frequency noise. Filtering of the input signals with a digital filter like a Moving Average (MA) filter is required first before every comparison with constant slope (eq. 7):

$$v_f(n) = MA\,[v_{in}(n)] = \frac{1}{M}\sum_{1}^{M} v_{in}(n) \qquad \text{EQ. 7}$$

where n is the current sample, v_{in} is the input signal of the filter, v_f is the filtered signal and M a scalar coefficient.

The MA filter was not used to filter physical analog signals but used only for modeling purpose and no hardware implementation was done. The value of M was fixed at 32 samples that allowed sufficient accuracy for comparison of the input slope with the comparator SR obtained with SPICE simulations. Applying the MA filter to both input derivatives was required to obtain the slope of the input signals with reduced noise corruption, as presented in Figure 13:

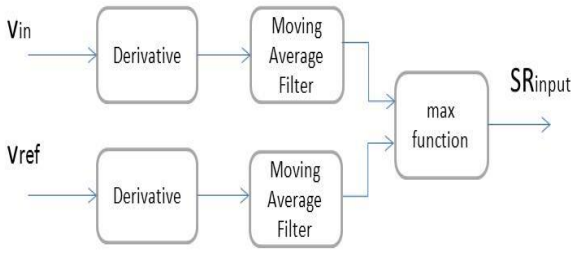

FIGURE 13: *BLOCK DIAGRAM FOR INPUT SR COMPUTATION*

where SR_{input} is the maximum SR of the signals feeding the comparator.

The output SR (SR_{output}) of the comparator is computed after the comparison of the input signals SR (SR_{input}) with the fixed SR obtained by SPICE simulations (SR_{SPICE}) (representing the SR of the comparator alone). If the slope of the input signals is greater than the SR obtained with SPICE simulations during the raising part of the comparator model, the slope of the output is limited to the comparator SR (as shown in eq. 8). If the slope of the input signal is lower than the SPICE obtained SR, the input slope can be conserved as the comparator maximum switching velocity is not reached. Inverse relations are obtained for the falling part of the comparator model.

$$SR_{output} = \begin{cases} SR_{input} & if\ SR_{input} < SR_{SPICE} \\ SR_{SPICE} & otherwise \end{cases} \qquad \text{EQ. 8}$$

SR_{output} is used to define the comparator output (eq. 9):

$$y_{SR}(n) = y(n-1) + SR_{output} \quad \text{EQ. 9}$$

where y_{SR} is the output of the comparator corrupted by the SR, SR_{SPICE} is the SR given by SPICE simulations.

eq. 9 is only valid for the raising part of the comparator model (i.e. $v_{in}>v_{ref}$). The SR creation block incorporates different SR for the raising part and the falling part of the comparator output, obtained from electrical simulations.

It should be noted that in the second version of the chip (MicRA v2), the practical SR of the comparator obtained by electrical simulations was few volts per nanosecond that is totally neglectful compared to the phase noise of the 20kHz oscillator (this oscillator is corrupting the PWM signal and hence the signal time length).

This block was simulated and the results were similar to SPICE simulations (not reported in this document).

6. System modeling validation

Transient simulations of the analytical model were compared with transient electrical measurements and presented in Figure 14.

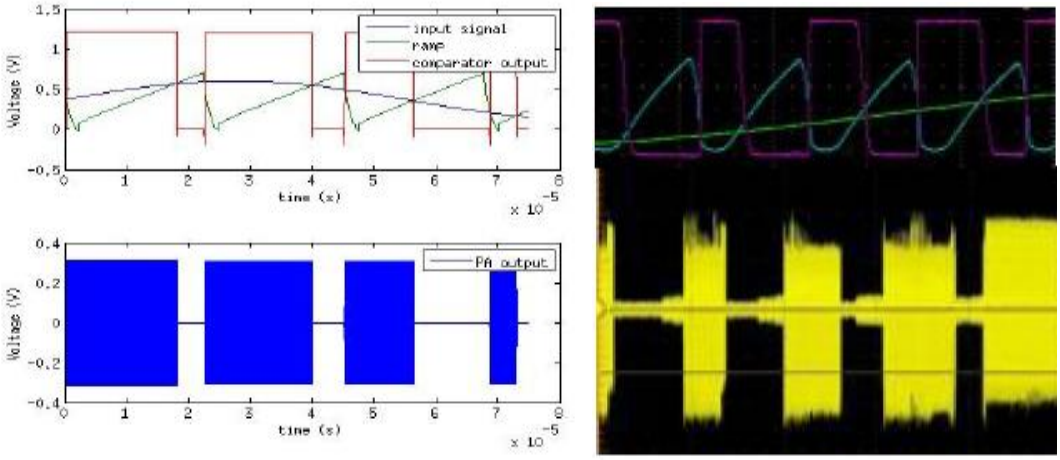

FIGURE 14: MATLAB® TRANSIENT SIMULATIONS OF THE OVERALL SYSTEM (LEFT FIGURE). MEASUREMENTS ON A 130 NM CMOS PROTOTYPE (RIGHT FIGURE) (FROM [24])

The general shape of the signals obtained by mathematical modeling or direct measurement on MicRA prototype was similar. The differences between the system modeling simulations and the measurements may be explained by the creation of the models which were made based on transistor-level description (SPICE) simulations and not directly on measurements, as they were not available when the models were created. Indeed SPICE simulations show also some differences with measurements.

As seen on Figure 14, there is a residual noise when the power amplifier is turned off but this noise can be reduced by PA subsequent optimized design. Nevertheless it can be noticed that the P_{on} over P_{off} ratio is high enough not to introduce demodulation error if using a threshold detection on the receiver.

The critical parameter for this application is the duty cycle which is close to SPICE extracted duty cycle, rather than to the measured one. The accuracy of the duty cycle is lower than 0.25% which ensures 8-bits precision for the PWM signal (remembering that 8 bits precision is the theoretical maximum accuracy than can reach the PWM for ISM specifications respect). This value was however not precisely verified as no extended tests to determine the duty cycle of the prototype as well as the ISM band inclusion verification were performed.

In addition, mathematical modeling exhibited simulation times about 15 times lower than SPICE netlisting while allowing to reach a relatively good transmit signal estimation.

D. Propagation channel modeling

1. Models of biological tissues

Dielectric materials conductivity and permittivity expressions related to Maxwell's equations development are reminded in Annex A.

The electric analog of biological tissues over frequencies available in literature are restricted to the interval between few hertz and few hundred giga Hertz as frequencies above may harm tissues (ionizing radiations). The most intuitive model is the Fricke model (recalled in Figure 15) which represents biomedical tissues as only a resistance at low frequencies (the current is passing through the extracellular space) or by a capacitance and another impedance in serial (in high frequency, the current is crossing the cells represented by a capacitance, which models the cell membrane (the

passage of ions and electrons through cell membrane is very highly controlled by the cell), and another resistance which models the intracellular space).

However this model is not in adequacy with impedance measurements (impedance spectroscopy of biological tissues) of various tissue types; the biological tissue permittivity shows generally several steps like decrease over frequencies and the conductivity increases in a steps like manner over the frequencies. The Fricke model is not modeling those discontinuities in the frequency response of permittivity or conductivity. The Debye model is based on the mathematical description of the frequency response. This model describes the permittivity frequency response similar to a filter frequency description response with consecutive low pass filter (each one with a different cutoff frequency), resulting in a step like frequency response. The initial Debye model, mathematically described by eq. 10, is based on a first order frequency response [47].

$$\epsilon_{Debye} = \epsilon_{high} + \frac{\epsilon_{low} - \epsilon_{high}}{1 + j\omega\tau} \qquad \text{EQ. } 10$$

where $\mathcal{E}$ is the complex permittivity, $\mathcal{E}_{low}$ is the static permittivity measured and $\mathcal{E}_{high}$ is the observed permittivity at a very high frequency, ω is the pulsation and τ is the time constant associated with a relaxation phenomenon (practically defined using the cutoff frequency of the tissue measured impedance over frequencies).

The Debye model was further improved adding the static middle conductivity ($j \frac{\sigma_s}{\omega\epsilon_0}$) and may integrate different relaxation phenomenon (with different cutoff frequencies) to precisely suit the mathematical frequency response. The mathematical description of this model can be found in [47] (cf eq. 11), and can be split into real part ($\mathcal{E}'$) and imaginary part (σ_{eff} also called σ').

$$\epsilon_{Debye} = \epsilon_{high} - j\frac{\sigma_s}{\omega\epsilon_0} + \frac{\Delta\epsilon_1}{1 + j\omega\tau_1} + \frac{\Delta\epsilon_2}{1 + j\omega\tau_2} + \frac{\Delta\epsilon_3}{1 + j\omega\tau_3} \qquad \text{EQ. } 11$$

where τ_i are the time constant for the different relaxation phenomenon and $\Delta\mathcal{E}_i$ are the permittivity difference of each permittivity intervals as indicated in Figure 15(redrawn from [47]).

Although describing the general shape of the permittivity response, many materials show an non Debye behavior with asymmetric loss tangent [48, 49]. To obtain a better fit with measurements Cole *et al.*[47]included a distribution parameter α. The Cole model is purely mathematical and is reminded in eq. 12

$$\epsilon_{Cole} = \epsilon_{high} - j\frac{\sigma_s}{\omega\epsilon_0} + \frac{\Delta\epsilon_1}{1+(j\omega\tau_1)^{1-\alpha}} \quad \text{EQ. 12}$$

Defining Z as the complex impedance given by the ratio of the complex voltage form over the complex current form such as $Z = Z' - jZ''$ and the complex permittivity as $\epsilon = \epsilon' - j\epsilon'' = \frac{1}{jC_0\omega Z}$ where C_0 is the vacuum capacitance given by $C_0 = \frac{\epsilon_0 A}{h}$ (A is the area of cross section and h is the thickness of the material), the relations between the complex impedance and the complex permittivity can be extracted [50](eq. 13):

$$\epsilon' = \frac{1}{\omega A\epsilon_0}\left[\frac{Z''}{Z'^2 + Z''^2}\right] \quad \text{EQ. 13}$$

$$and\ \epsilon'' = \frac{1}{\omega A\epsilon_0}\left[\frac{Z'}{Z'^2 + Z''^2}\right]$$

After inverting the relations, the general expression of Z can be expressed using first orders electrical system leading to the electrical analog model presented in Figure 15.

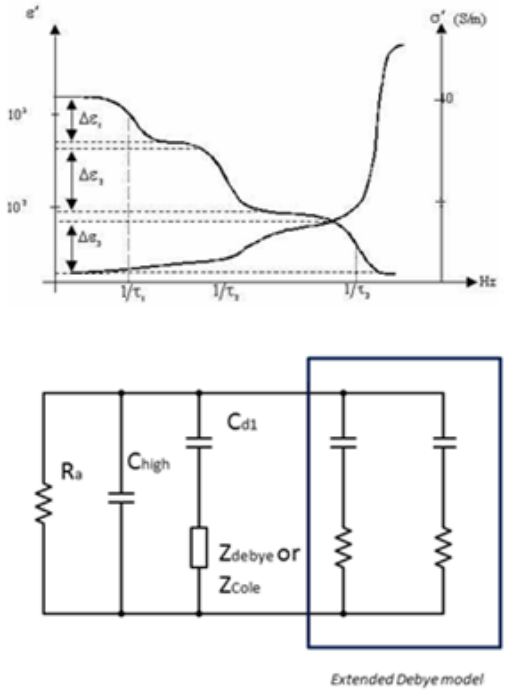

FIGURE 15: (ABOVE) PERMITTIVITY AND CONDUCTIVITY RESPONSES OVER FREQUENCY IN MUSCLE ATTRIBUTED TO [47]. (BELOW) DEBYE OR COLE ELECTRIC MODEL OF TISSUE ATTRIBUTED TO [47]

$$R_a = \frac{k}{\sigma_t} Z_{Debye} = \frac{k\tau}{\varepsilon_0 \left(\varepsilon_{low} - \varepsilon_{high}\right)} Z_{Cole} = \frac{k\tau_0 (j\omega\tau)^{-\alpha}}{\varepsilon_0 \left(\varepsilon_{low} - \varepsilon_{high}\right)} \qquad \text{EQ. 14}$$

$$C_{high} = \frac{\varepsilon_0 \varepsilon_{high}}{k} C_d = C_{low} - C_{high} = \frac{\varepsilon_0 \left(\varepsilon_{low} - \varepsilon_{high}\right)}{k}$$

where k is a geometric parameter. Above formulas were extracted from[47].

As indicated in [51], the complex permittivity of an heterogeneous material may be expressed as the sum of each atomic complex permittivity weighted by their respective concentrations (if several conditions are verified), expressed in eq. 15

$$\epsilon = \rho_1 \epsilon_1 + \rho_2 \epsilon_2 + \ldots \qquad \text{EQ. 15}$$

where ρ_i are the concentrations of the various elements and $\mathcal{E}_i$ are the complex permittivity of each element.

To the author personal interpretation, the biological tissue permittivity which has a step like frequency response may correspond to the addition of the most significant ionic permittivity responses (the ones of Na+, K+, Cl^- for instance) over frequency. If this hypothesis were true, it might have explained the theoretical limits of the impedance spectroscopy technique, as different biological tissue with close ionic tissue distribution may have the same frequency impedance response.

For this work purposes, the complete electric model of biological tissue behavior over frequencies was not required as only electrical model at low frequency (below 20 KHz for the stimulation of the cochlea by electrodes study) and around 2.45 GHz (for transmission canal noise study) was necessary. In order to increase the simulation time, the model considered was a resistance in parallel with a capacitance where the resistance value was computed using the $\mathcal{E}''$ value at the desired frequency and the capacitance value was computed using the $\mathcal{E}'$ value at the desired frequency. It should be notified that the permittivity frequency responses are tissue dependent. The impedance implementation was made using a cylindrical resistance model and the capacitance implementation was made using a parallel plate capacitors which formula are reminded in eq. 16

$$R = \frac{1}{\sigma'} * \frac{l}{S} \qquad and \qquad C = \mathcal{E}_0 \mathcal{E} \frac{A}{h} \qquad \text{EQ. 16}$$

where σ' is the total electrical conductivity, l is the length and S is the cross sectional area. $\mathcal{E}$ the relative permeability, A the area of the plates and h the distance separating the two plates.

a)

b)

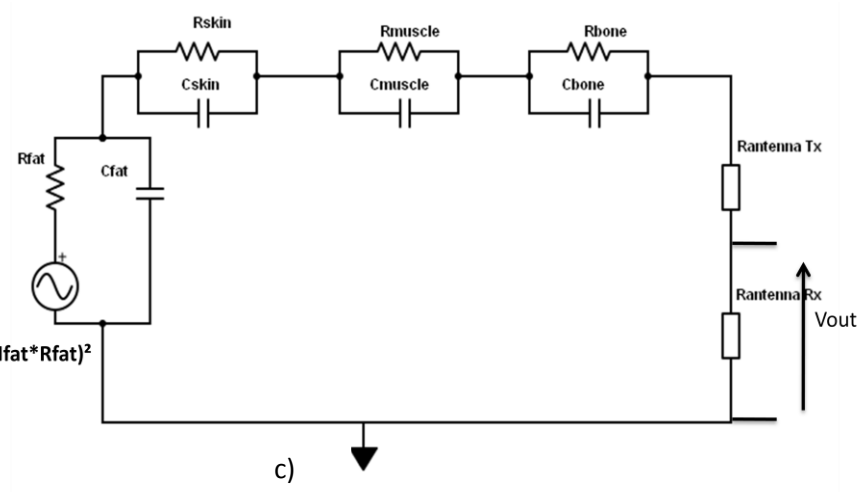

c)

FIGURE 16: SIMPLIFIED MODEL OF THE PROPAGATION CHANNEL (FROM [24]) (A) AND ITS ELECTRIC ANALOG CORRESPONDING MODEL (WITH CURRENT NOISE SOURCES GENERATORS REPRESENTING THE JONHSON-NYQUIST NOISE IN BOTH RESISTORS AND CAPACITORS) (B). ELECTRIC ANALOG USED FOR NOISE POWER ASSOCIATED WITH FAT TISSUE (AS IT IS THE MAIN CONTRIBUTING NOISE IN TISSUES) NOISE ESTIMATION (C)

The propagation channel simplified model and its electrical analog are presented in Figure 16. This model is a simplified 3 dimensional model accounting only for direct propagation between the transmitter antenna (Tx) and the receiver antenna (Rx). In real world, multi paths or other distortions may exist and may provoke results far from the ones predicted. The model is composed of a thin layer of skin, bone and cartilage and a thick layer of fat and the dimensions are indicated in Figure 16. The resistance and capacitance values were computed from the values of the relative permeability and electrical conductivity for human tissues which were found in [52, 53].The electrical components values are indicated in Table 1.

TABLE 1: VALUES OF THE COMPONENTS USED FOR THE ELECTRICAL ANALOG OF THE PROPAGATION CHANNEL (CONDUCTIVITY MEASUREMENTS FROM [52]AND FROM [53])

	Skin	Cartilage	Fat	Bone
ε' (2.45GHz)	42	74	4.2	11.5
σ (S/m) (2.45GHz)	1.1	0.9	0.7	32
C (F)	21n	9 n	61 p	5.7 n
R (Ω)	0.4	20	216	0.12

2. Propagation channel noise estimation

In biological tissues, major influencing noise are: thermal noise which is mathematically described as white noise, 1/f noise which is associated with ion entry inside the cells, shot noise which is often negligible and background electric fields in nerve or muscle tissues [54]. Because the RF frequency is very high compared to the membrane channels frequency dynamics and because we neglect the nervous or muscular cells in our model (cf Figure 16), we considered only the perturbations introduced by the thermal noise.

In the electrical model of the propagation channel illustrated in Figure 16, thermal noise is associated with temperature carrier agitations (called Jonhson-Nyquist noise) and is generated mainly by resistances in our model, regardless of any applied voltage [55]. The noise current generated by a resistor is expressed by eq. 17 [56]

$$\overline{I_{WN}}^2 = \frac{4\,k\,T\,B}{R} \qquad \text{EQ. 17}$$

where $\overline{I_{WN}}^2$ is the current variance in the frequency band B (equal to 100MHz in the selected ISM band), k the Boltzmann constant, T the absolute temperature in Kelvin and R the resistance generating the Johnson-Nyquist noise. Dielectric properties measurements performed on various biological tissues state that the thermal noise power is around 1µV/sqrt(Ω) at 300 Kelvins [8], confirming the results obtained from eq. 17.

Using the formula in Figure 16 and voltage division principle in this circuit permitted to express the noise contribution of each resistance (representing a particular tissue). Then considering uncorrelated noise sources (which may not entirely be true), the propagation channel noise Power Spectral Density (PSD) was equal to the sum of each resistance noise PSD. The total PSD of the noise in this propagation channel was found equal to -121dBm. Running noise analysis in Cadence® gave the same noise power estimation.

The noise power of the RF oscillator concatenated to the propagation channel was evaluated using SPICE noise analysis. The estimated noise power at the end of these two blocks was -95dBm.

This value still has to be confirmed by measurements and represent a minimal estimation since other noise sources in biological tissues have been discarded. If so, the noise power may be too close to the signal received (only 8 dB separating them as indicated in Section I.B, without the inclusion of the noise added by the PWM blocks of the transmitter). In consequence, an architecture reworking or even another transmission way should be evaluated.

E. Transmitter and receiver antennas characteristics

The transmitter antenna is a dipole antenna with a central balun and no ground plane, a length of 5.3mm and a width of 3.25mm, with 35 meanders and a spacing of 100µm between each meanders, allowing a measured maximum total gain of -13.9 dB [57].The antenna was printed on a substrate using the Integrated Passive Devices (IPD) technology to decrease the substrate losses and ensure better antenna characterization (decreasing interference due to cables used for measures)[58].

The receiver antenna should exhibit a reduced size, a proper radiation pattern to avoid radiations into the brain and sufficient gain. For such small antenna dimension and these overall constraints, direct antenna types reuse may be challenging. In [59], an Integrated F Antenna (IFA) was used in this context. For the receiver antenna, a custom design antenna might give better results.

It should be emphasized that in [24] and [58], the propagation channel length is estimated at 4cm and the antenna were supposed closely attached to the transmitter (Tx antenna) or to the receiver (Rx antenna). However as indicated in Section I.D, noise power inside this propagation channel is very closed to the received signal power. To increase the received Signal to Noise Ratio (SNR) and because antennas gains are further limited by other constraints, the distance between both antenna should be reduced (bringing the Rx antenna closer to the Tx antenna with the help of a biocompatible wire linking the Receiver and the Rx antenna). This simple solution needs further analysis as it may not be feasible or results in a difficult surgery insertion procedure.

F. Closure remarks

As a first emitter prototype was available, we decided to create behavioral models of the various blocks for extended testing purpose. Besides the receiver embedded a DSP unit to run cochlear implants speech algorithms, making the overall system a mixed system. Based on these considerations and because these models will be reused for heterogeneous electrophysiological simulations (latter described in Chapter III-IV) Matlab/Simuling environment was chosen.

The power consumption of the entire transmitter was already available from the works produced by Y. Vaiarello.

The theoretical restriction of the PWM signal accuracy was discussed based on ISM frequency band rang (100MHz) which was limited to 8 bits for a sampling frequency of 20kHz in the ideal case. This data rate will further be decreased by phase noise (developed in the next Chapter) and noise in the propagation channel.

This later noise was studied based on electrical modeling of human tissue by mean of the implementation of Cole and Cole impedance model and permitted the creation of a power budget for complete receiver specifications defined in the next Chapter.

G. Work published

- Matlab/Simulink modeling of RF microphone for cochlear implant application, U. Cerasani, Y.Vaiairello, G.Jacquemod, Y. LeDuc, SAME Ubooth, September 2011, Sophia Antipolis (FRANCE)

- Modélisation et optimisation d'une chaine d'émission réception très faibleconsommation pour implants cochléaires, U. Cerasani, W. Tatinian, Y. Vaiarello, G.Jacquemod, GDR SOC SIP, June 2012, Paris (FRANCE)
- Modeling and optimization of a low noise RF transmitter for cochlear implants application, U. Cerasani, W. Tatinian, Y. Vaiarello, G. Jacquemod, IEEE DCIS, November 2012, Avignon (FRANCE)

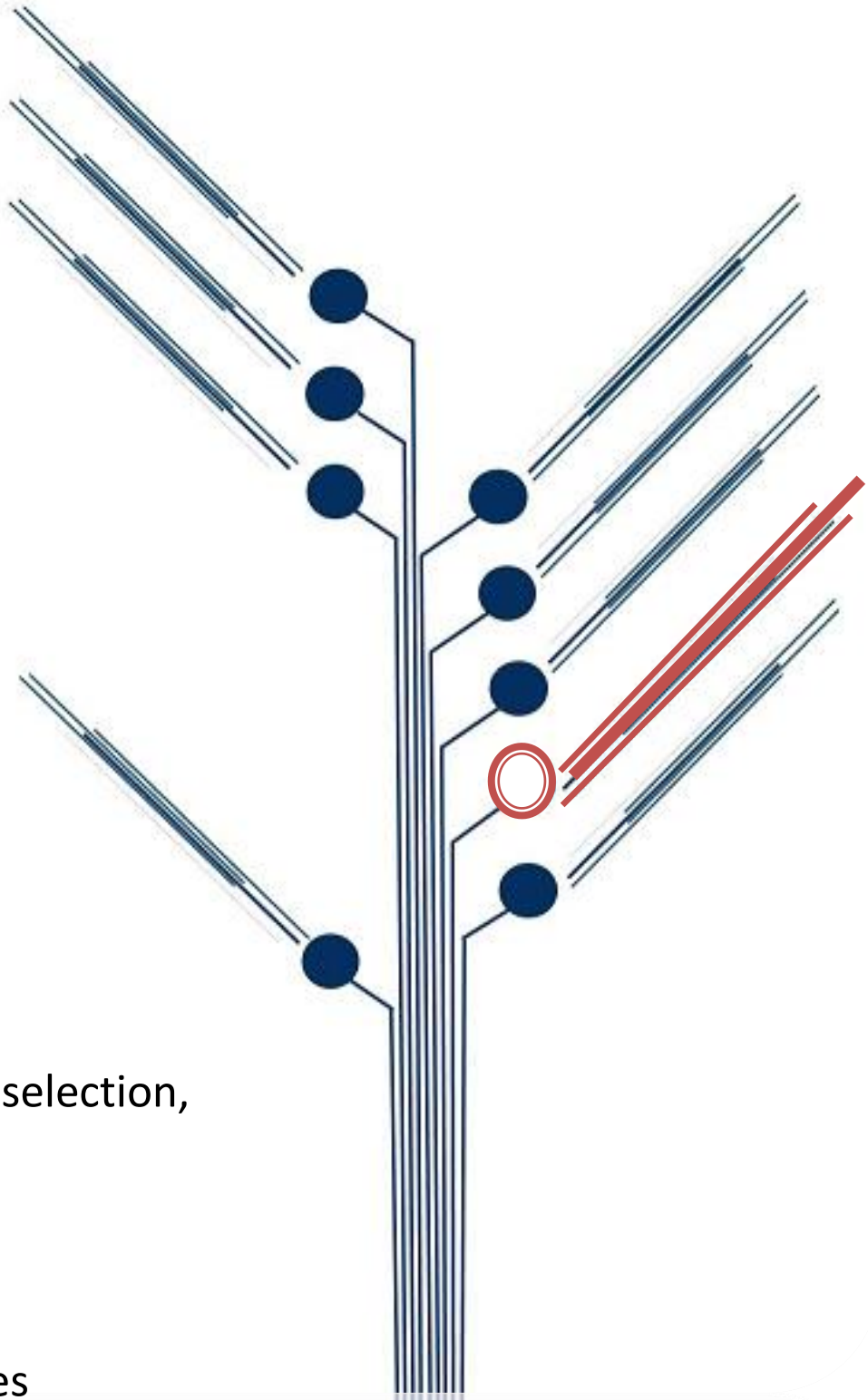

Chapter II:

Receiver architecture selection, behavioral modeling and overall RF chain optimization guidelines

A. Opening notifications

Change in patients request for aesthetic considerations has led to new CIs architecture specifications most particularly regarding overall power consumption. According to previous work done in our laboratory [23], the DSP that was initially located in the emitter, can be integrated in the receiver. This architecture change reduces the emitter consumption but on the other hand implies finding a fitting receiver architecture.

In this Chapter, the receiver chain architecture study and design for new type of cochlear implants is presented. We proposed three possible receiver architectures which were compared in terms of power consumption and noise figure, both of fundamental importance in biomedical embedded systems. SPICE simulations of these architectures were carried out and transient results were presented for the solution retained. Furthermore optimization of the LNA using mathematical computations that was done in collaboration with Mons University microelectronics research team is presented, increasing the entire receiver performances.

Then the behavioral modeling of the receiver architecture was performed and added to the transmitter and propagation channel models. This overall system modeling permitted to extract the parameters impacting the transceiver output signal integrity and hence the blocks that required optimization.

In addition it was found that phase noise is of first importance as it can alter both the baseband (PWM) and the RF (OOK) signals. For modeling considerations we proposed a new theoretical model for phase noise extraction based on simplification of Hajimiri and Lee theory.

After introducing timing jitter mathematical description, the conversion to phase noise into timing jitter was performed using different methodologies for the two oscillators of the transmitter chain. Phase noise Power Spectral Density of the oscillator utilized for the PWM signal creation resulted in timing jitter value not suitable with the previously found PWM precision.

B. Receiver chain OOK demodulation architecture

1. Receiver architecture

The communication channel between the transmit- and the receive antenna is presented in Section I.D, resulting in an added noise in the propagation channel alone of -121dBm using the maximal authorized emitted power in the ISM band (20dBm), the attenuation in human tissue with corresponding dielectric constants, the ISM bandwidth (100MHz) and assuming a white noise distribution. The estimated power losses through the channel and antenna was estimated by Y. Vaiarello [24] and was around -87dBm. This fixes the LNA sensitivity and is used as basis for the receiver specifications and architecture selection.

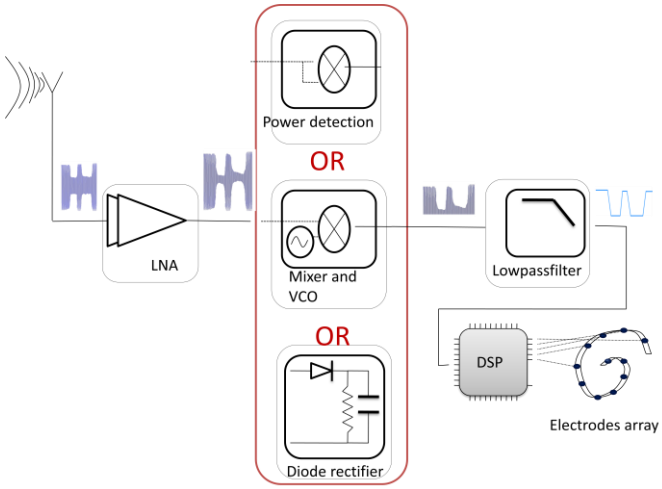

FIGURE 17: RECEIVER ARCHITECTURE OVERVIEW, WITH SIGNAL OUTPUTS IN COLOR

The selected architecture for the receiver includes a LNA followed by an amplitude demodulation stage and a digital signal processing unit controlling the electrodes array which is implanted inside the patient's cochlea.

The power consumption and distribution in commercially available CI is estimated in Section II.B.3. The total electronic consumption should be lowered as possible to increase battery lifetime.

Most particularly, a high consumption would lead to an increase of the battery reload frequency which is inconvenient for the patients. Because of low power constraints, power repartition between blocks become fundamental. The unique block allowed to consume more power was the LNA in order to decrease the total SNR of the entire receiver as explained in Section II.B.2.

As presented in Figure 17, three architectures are investigated for the AM demodulation:

- a power detection using a mixer with the RF and LO inputs connected together,

- a coherent demodulation composed of a mixer and a local oscillator at the same frequency as the input signal,
- PN junction associated with a transformer.

The output signal is a PWM-like waveform and is low-pass filtered to recover the initial signal amplitude. Linearity is not significant as the PWM signal maximum frequency (around 2MHz) is substantially lower than the carrier frequency (2.45GHz).

2. LNA optimization

Common formulas for Noise Factor (F) and Noise Figure (NF) calculus, under matched conditions and with source at 290 K, are reminded in eq. 18 [60]

$$F = \frac{SNR_{input}}{SNR_{output}} \quad \text{EQ. } 18$$

where SNR is the Signal over Noise Ratio. For Noise Temperature T_{in} which are different from T_0, the achievable Noise Factor (F_a) is defined (eq. 19)

$$F_a = \frac{SNR_{input}}{SNR_{output}} \quad \text{EQ. } 19$$

The noise figure expression from the noise factor is reminded in eq. 20

$$NF = 10 * \log(F) \quad \text{EQ. } 20$$

Remembering that the noise power introduced by the propagation channel alone is -121dBm and that the estimated noise power concatenating the RF oscillator block with the propagation channel rises to -95dBm, the characteristics of the receiver in terms of noise is of primary importance.
Minimum achievable Noise Factor of the receiver is obtained considering the lowest output SNR needed to recover the signal. We fixed the minimum output SNR to 3 dB to allow PWM signal demodulation. Consequently using eq. 21, we can define the maximum acceptable Noise Factor (F_m) of the receiver, that we included into the receiver specifications.

$$10 * \log(F_m) = -87dBm - (-95dBm) - 3dB = 5\ dB \quad \text{EQ. } 21$$

Every value greater than this would result in inability to extract signal from noise at the receiver output.

As a direct consequence of the Friss equation [46] (reminded in eq. 22) the Noise Factor of the entire receiver is greatly dependent on the LNA noise factor and gain. Consequently we decided to optimize the LNA design in terms of power consumption and NF.

$$F_{total} = F_{LNA} + \frac{F_{demod} - 1}{G_{LNA}} + \frac{F_{filter} - 1}{G_{LNA}G_{demod}} \quad \text{EQ. 22}$$

where F_{LNA}, F_{demod} and F_{filter} are the noise factor of the LNA, the noise factor of the blocks composing each demodulating topology and the noise factor of the lowpass filter respectively. G_{LNA} and G_{demod} are the power gains with load of the LNA and the blocks composing each demodulating topology respectively.

As the LNA block was compulsory in both the solutions and significantly impact the overall architecture NF, its optimization using mathematical computation was first performed before its implementation in Cadence® and subsequent refinement.

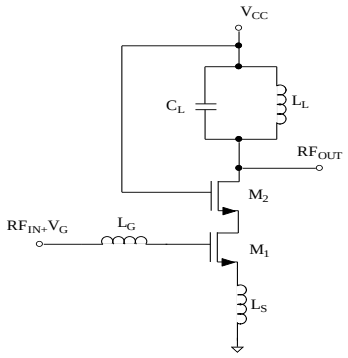

FIGURE 18: CIRCUIT OF THE LOW NOISE CASCODE AMPLIFIER

Figure 18shows the schematic of the implemented LNA. The cascode stage (M_2) is used to improve input-output isolation, reduce the Miller effect and, consequently, increase the bandwidth. The resonant circuit formed by L_L and C_L permits a high gain with a low voltage supply at the frequency of interest. With L_G and L_S a narrow band input impedance matching is obtained. The input transistor (M_1) is used in inductively degenerated common-source configuration. The width of the transistor and the other parameters of the circuit were mathematically computed using a similar development than the method presented by Thomas H. Lee [61] minimizing the NF while optimizing power consumption.

For each architecture type and for the LNA, we evaluated the receiver performances using a 0.13µm RF CMOS technology. Table 2shows the values obtained, from calculations, after some minor modifications according to the target CMOS 130 nm process.

TABLE 2: COMPONENT VALUES OF THE LNA OBTAINED BY MATHEMATICAL COMPUTATION

	Implemented values
Center Frequency	**2.475 GHz**
Voltage supply	**1.2 V**
Current Consumption	**10 mA**
L_L	**1.3 nH**
C_L	**3.18 pF**
$L_{M1,M2}$	**0.15 um**
$W_{M1,2}$	**165 um**
NF	**1. 4**
L_S	**0.14 nH**
L_G	**14.3 nH**

The results of simulations are summarized in Table 2. In practice equations used for this optimization were derived from first order modeling (SPICE level 1) and provided general characterization of the LNA further refined by Cadence® simulations (especially modifying the bias of M1), explaining the improvements in Table3.

TABLE3: PARAMETERS OBTAINED BY MATHEMATICAL COMPUTATION AND WITH CADENCE SIMULATION

	Mathematical computation	Cadence evaluation
RF Frequency	2.4GHz	**2.45GHz**
S21	>17dB	**24.7dB**
S11	-10dB	**-7.11dB**
S22	-10.1dB	**-1.5dB**

NF	<1.4 dB	**0.75dB**
Power Consumption	13.2 mW	**11.71mW**

(1) LNA Figure Of Merit comparison

As LNAs may use different technologies and respond to diverse specifications, their performance characterization is complex. In that intent, the Figure Of Merit (FOM) was developed to compare the different LNA designs and can also serve as a benchmark for future progress (eq. 1)[62]

$$FOM = \frac{S_{21} * IPP3 * frequency}{(F-1)P_{supply}} \quad \text{EQ. 23}$$

where S_{21} is the linear LNA gain, IIP3 is the 3rd order Input Inter modulation Product and has to be expressed in mW, frequency is the central working frequency of the LNA also expressed in GHz, F is the noise factor and P_{supply} is the power consumption of the LNA reported in mW. The variation of this formula including the LNA bandwidth is expressed in eq. 24[63]

$$FOM = \frac{S_{21} * BW * frequency}{(F-1)P_{supply}} \quad \text{EQ. 24}$$

where BW is the LNA bandwidth and must also be expressed in GHz. As the LNA bandwidth was not of importance in our application we excluded all literature relative to wide bandwidth LNA such as Ultra Wide Band (UWB) customized LNA. The FOM of the LNA developed is 4.5 which is in the range of current LNA state of the art FOM extending from 1 to 10 [63-66].

3. Receiver architectures implemented

The three architectures presented in Figure 17 were implemented in SPICE and they were compared in terms of power requirements and noise addition. The LNA and the filter were common to all the solutions. The bias circuitry is not shown in the Figures.

a) Solution 1: LNA and Power Detector

The input signal is the one received by the antenna (2.4GHz carrier modulated in amplitude by a PWM signal) and the LNA output is connected to the Local Oscillator input (LO +) as well as on the

RF input of the mixer. The power detector is therefore created using a mixer with its inputs connected to the same source. We designed a single balanced mixer because of its low power consumption. However as the DC offset is injected directly in the RF source, it degrades the mixer linearity [67], which is not of importance in our application.

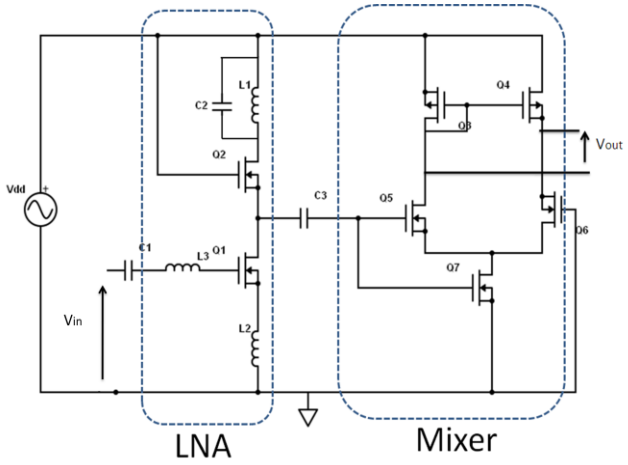

FIGURE 19: RECEIVER ARCHITECTURE SOLUTION 1 WITH A LNA AND A POWER DETECTOR

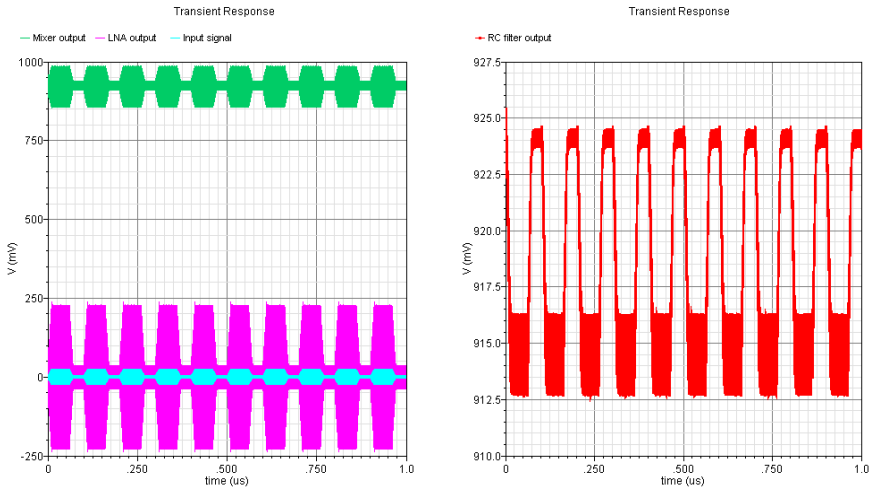

FIGURE 20: TRANSIENT SIMULATIONS INCLUDING THE INPUT SIGNAL, THE LNA OUTPUT, THE MIXER OUTPUT (LEFT) AND THE RC FILTER OUTPUT (RIGHT)

The designed mixer has a NF of 20dB, and its output is directly connected to the RC filter. The simplified schematic of the solution 1 is presented Figure 19 (with bias circuit removed for clarity reasons) and the associated transient simulations are exposed in Figure 20.

For the test case, the PWM signal was created with a 1 kHz sine wave which was sampled at 1MHz. The RF input signal is represented in light blue in Figure 20, its corresponding magnitude is low enough to make the LNA operate within the linear region. Removing the DC voltage, the output signal is represented in pink, where one can see that the ratio between the maximal and minimal magnitude is around 5, which is high enough for a further OOK demodulation. The effects of rising and falling times are also visible on the curve. As a result, after filtering, we obtained a signal that corresponds to the emitted signal, where the distortions and the low output magnitude are mainly due to the low power consumption of the Mixer (100µA).

b) Solution 2: LNA, Mixer and VCO

As the ring oscillator in the transmitter chain was not satisfying in term of jitter performances as described in Section II. H, the receiver oscillator chosen was a RLC oscillator instead.

Although most likely not ensuring a better signal transmission (in compare to reusing the same oscillator since the frequency drift was already introduced), this oscillator topology change permitted to proximately evaluate performances of a RLC oscillator for this application (in term of jitter, power consumption, temperature drift, power supply resistance, …).

The oscillator used is an L-C tank oscillator with a central frequency of 2.45GHz and frequency control (V_{tune}) to compensate the frequency shift due to temperature variations within the human body (presented in Figure 21). The width of the NMOS of the differential pair is 210µm and the length is 130nm, which drives a current of 10mA. The NF of the cross coupled pair was obtained with SPICE simulations and was found equal to 7dB. Then, using PSS analysis, we estimated the phase noise which was around -120dBc/Hz at 1MHz from the carrier (PWM maximal frequency) (a more accurate description of our implemented ring oscillator phase noise can be found in Section II.G.5).

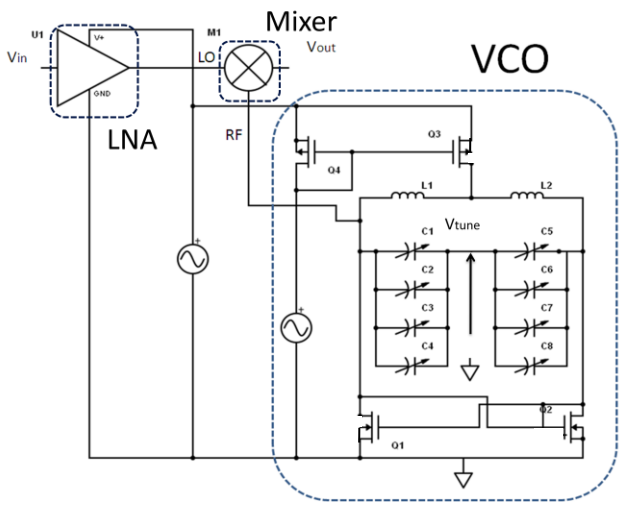

FIGURE 21: RECEIVER WITH MIXER AND VCO

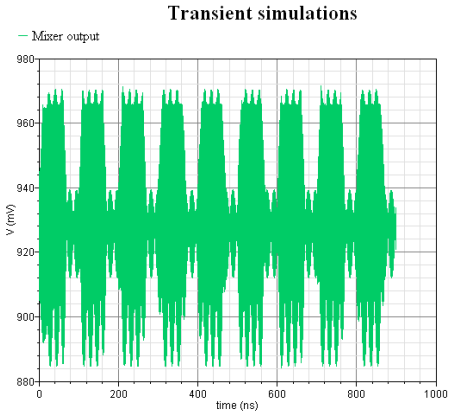

FIGURE 22: SECOND ARCHITECTURE MIXER OUTPUT TRANSIENT SIMULATION RESULTS

Transient simulation results are presented in Figure 22, where one can see that the output voltage magnitude of the mixer is more linear than in the previous architecture, at the cost of higher output oscillations due to the frequency shift between LO and RF. Indeed this shift is inevitable as low power constraints did not allow carrier recovery. Nevertheless this distortion may be removed by subsequent signal processing.

c) Solution 3: LNA, transformers and PN junction

The last solution implemented is based on transformers followed by a PN junction in order to cut the negative part of the RF signal. The use of magnetic components (inductors, transformers,…) is the main limitation to increase chip size and capacitive and magnetic coupling with substrate [68]. To reduce chip size, we used two consecutive transformers to obtain the desired mutual inductance, allowing the voltage to become superior to the built-in potential of the Gate-Drain junction (of a NMOS transistor used as diode). However the current diminution after the transformers associated with the low voltage gain of the NMOS transistor used as diode, are responsible for the very high noise factor of this entire solution (cf Figure 23). In fact the noise factor of only the transformers and the NMOS was around 2.5 but the power gain of this block was very low ($1.7*10^{-3}$).

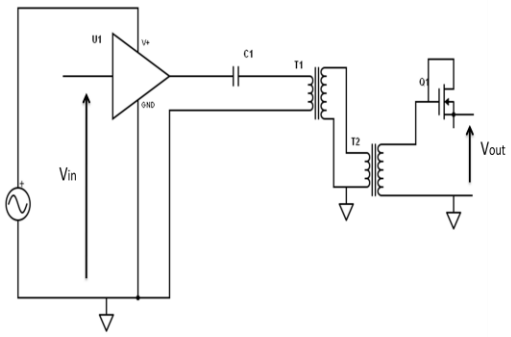

FIGURE 23: SOLUTION 3 COMPOSED OF LNA, TRANSFORMERS AND A NMOS USED AS DIODE

4. Architecture comparison

The main requirements of the receiver were its low power consumption and a much reduced NF. Maximizing SNR at the receiver output (before DSP computation) is hence very relevant and consists on minimizing the total noise factor of the receiver, as explained in Section VI.B.2.

TABLE4: NOISE FACTOR (F), NOISE FIGURE (NF) AND POWER CONSUMPTION COMPARISON FOR THE DIVERSE ARCHITECTURES. THE VOLTAGE GAIN, CURRENT GAIN AND POWER GAIN WERE COMPUTED WITHOUT THE FILTER BLOCK

	Power Detector	Mixer and VCO	Transformers and PN junction
Power consomption (mW)	11.91	21.4	1.9
Noise Factor (F)	2.57	2.61	101.6
Noise Figure (NF) (dB)	4.01	4.16	20.01
Voltage Gain (dB)	6.8	-0.5	-6.2
Current Gain (dB)	-38.4	-21.5	-34.4
Power Gain (dB)	-31	-22	-40.6

Total noise factor computation is expressed by the Friss formula as previously stated in eq. 22

The noise factors comparison for each solution is shown in Table4, as well as their respective power consumption estimation.

Based on these results, solution 3 offers very reduced power consumption. However this solution can be eliminated suffering of the very low power gain of the transformers and the diode ($G_{solution3}$), increasing the entire noise factor (F_{total3}) and might render the signal extraction from the noise not possible. Furthermore the layout of this solution may be complex to conceive due to severe chip surface constraints.

The solution with VCO is consuming twice as much power as the solution with the power detector. This results in a total extra energy of about 100mA*h per day (assuming that the device is activated during 8 hours per day).As discussed in Section II.B.3. the increase in power consumption of the RF frontend represents between 20% to 40% of the power consumed by the electrodes array depending on the selected topology.

Besides, as stated in Section II.G.5, the effect of the VCO phase noise is not significant compared to the frequency shift associated with the absence of carrier recovery in the receiver. This frequency shift may significantly corrupt the signal rectification as the signal translation into lower frequencies is followed by the RC filter.

In consequence, it is author belief that the first architecture should be preferred for this application. Optimization algorithms such as Non dominated Sorting Genetic Algorithm (NSGA-II) presented in [69] are available and could permit optimization of the overall architecture to maximize parameters of interest (still under work).

For this work we made a collaboration with the University of Mons (Belgium), the mathematical optimization was mainly performed by the microelectronic team of the Mons University. The optimization of the overall LNA and power detector architecture is ongoing by Mons University microelectronic team, using a nonlinear multi-objective optimization, based on the Genetic Algorithm NSGA II. This overall optimization may be necessary if the measured noise power inside the transmission channel would be greater that the estimated one, yet very close to the signal power received by the antenna.

5. RF front end state of the art

The overall transceiver power consumption is nowadays limited to a range between few mW and 50mW for top designs depending on the modules involved and their specific requirements [70-72].

The RF frontend part only may consume only 100µWin top designs whereas current power consumption performances from literature are approaching 5mW [73-79]. Our design is consuming more energy to lower the NF as indicated in the previous Section. Modern RF frontend receivers with a reduced NF (around 4 dB such as the one we obtained in simulations) are consuming a little more power (between 7-30mW but are associated with more complex architectures, rendering the comparison uneasy) [80, 81].

C. Receiver architecture behavioral modeling

The aim of the behavioral modeling of the receiver (behavioral modeling of the LNA and mixer solution) was to model the overall electrical system, in order to find critical blocks and technological advantages and limits of the overall architecture including electrodes stimulation. As discussed in Section I.C, the accuracy of the PWM was restricted to 8 bits due to perturbations impacting the duty cycle of the transmitter. This duty cycle may further be diminished if others disturbances were taken into account in the receiver part. The optimization of the critical blocks affecting the PWM accuracy may be performed or an architecture part modification (such as changing the type of

modulations) may also be anticipated. Modeling all the electrical system ensures extended testing capacities. These results defined blocks optimization or partial architecture redesign depending on the impact of the parameters tested on the overall circuit performances. Although architecture selection is generally made sooner than electrical design, unaccounted design issues may request architecture reworking (bottom up methodology). Furthermore the RF transmission at 2.45GHz may be particularly inefficient due to high absorption losses and can provoke damages to the brain, suggesting an possible entire architecture restudy with complete abandon of the transmission circuitry presented in [57]

1. Filter design and implementation

The only analog filter required in the receiver is the low pass filter for 2.45GHz signal rectification. The other filters have only modeling purposes and the physical filter implementation recommendations do not apply to them.

As the behavioral modeling of the entire chain was performed in Matlab® environment which does not efficiently integrate analog simulation, transformation of analog filters into equivalent digital ones was required.

The development of the methodology for complete filter design is reviewed extensively in [82] and in [83]for instance. The discussion of complete filter design is beyond the scope of this document and may be irrelevant for research purposes. The very succinct review of the analog and digital filter design methodology is proposed in this section to define the rectification filter and to understand precisely the issues associated with simulation frequency change, as it may be the case in block reuse with a different simulation tool. Design automation tools simulator automatically set the simulation frequency to several times the highest frequency found (this frequency hence corresponds to the sampling frequency). Because digital filters are highly dependent on simulation frequency value (the normalized cutoff frequency is equal to the real cutoff frequency divided by the sampling frequency), a simulation frequency change requires to modify the entire digital filters coefficient (redesign of the filters) to maintain the same frequency response of those digital filters. Hence a fixed simulation frequency equal to 10 times (for sufficient accuracy without lowering significantly the simulation time) the maximum receiver frequency (2.45 GHz), called f_s, was the solution retained. Digital filter with coefficient adjustment depending on the simulation frequency is another solution, not considered as it required increased development time.

The filters we designed were: one low pass filter and a band pass filter:

- The low pass filter was associated with signal rectification. Butterworth approximation function was selected ensuring reduced ripple in the passband [84]. In fact the SNR at the end of the LNA was already small as described in Section II.B, so for functional PMW demodulation, the ripple in the pass band had to be minimal.
- In order to model correctly the frequency response of the LNA (to model RC resonance inside the LNA), a band pass filter was added at the end of the LNA module. The characteristics of this filters were chosen from SPICE AC simulations performed on the LNA presented in Section II.B.2. This filter had only modeling purposes. In fact the LNA gain was not constant in its working frequency band, but displayed variations similar to ripple, hence to correctly model the LNA behavior, these variations were reproduced using Chebyshev filter type. For this modeling, purely digital filter such as Finite Impulse Response (FIR) filter may have been used as well but was discarded due to unrealistic transient response.

All the steps from the analog design of the low pass filter (the one associated with signal rectification), followed by the transformation of its transfer function in digital domain for computer based simulations are reviewed in the following part.

a) Analog Filter design

The ideal filter response is 1 in the passband and 0 in the stopband. The abrupt transition between the passband and the stopband cannot be reached physically [82]. Hence filter specifications graph and approximation functions are created. Filter specifications graph set the frequency response ranges where the filter approximation function must fit [82]. Filter specifications depend on the application and require frequency normalization and magnitude quantification in the standard procedure of analog filter design[82]. In Figure 24, filter specifications for low pass filter, associated with RF signal rectification, are established.

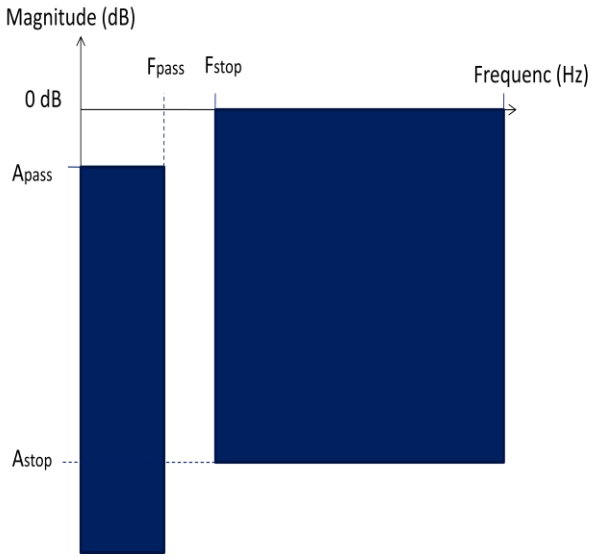

FIGURE 24: NORMALIZED FILTER SPECIFICATION GRAPH FOR LOW PASS FILTER DESIGN[82]. ALL THE CONSTANT VALUES FOR PRACTICAL FILTER CREATION CAN BE FOUND IN TABLE 5. THE REFERENCE FREQUENCY FOR NORMALIZATION WAS THE DESIRED CUTOFF FREQUENCY AND THE REFERENCE GAIN FOR NORMALIZATION WAS THE MAXIMUM GAIN IN THE FILTER PASS BAND.

The signal transmitted is RF modulated around 2.45GHz, and the baseband maximum frequency (which corresponds to the frequency of the LSB of the PWM) is$20000 * 2^{(8)} = 5.12\text{MHz}$ (further used in filter specifications). The ripple in the passband must be kept minimal because of the low SNR available and was found with SPICE simulations to be equal to 1dB. The important frequency interval between F_{pass} and F_{stop} permitted to decrease the number of stages available.

The filter design practical methodology can be found in [85], [86], or may be straightforward using analog filter approximation design and synthesis tools like FIESTAII®[87], dedicated Matlab® functions, Advanced Design System® (ADS®) filter design tool, etc.

Besides all the different filter types (high pass filter, passband filter, …) can be converted into a low pass filter using the transposition method (for approximation function calculus) and then back to their original forms[83].

TABLE 5: FILTER DESIGN PARAMETERS. FPASS, FSTOP AND $\mathcal{E}$ (=5 DB) FOR THE CHEBYSHEV FILTER WERE DEFINED USING SPICE SIMULATIONS. THE FILTERS PARAMETERS WERE OBTAINED USING ADS® DESIGN TOOL

	LOW PASS BUTTERWORTH FILTER	BAND PASS CHEBYSHEV FILTER (ONLY FOR MODELING PURPOSES)
F_{pass}	10e6	[2.018e9 ; 2.580e9]

F_{stop}	200e6	[1e9 ; 3.7e9]
A_{pass} (dB)	1	3
A_{stop} (dB)	20	20
Number of stages	2	2

The low pass filter physical architecture (filter topology) selected aimed to lower the power consumption. Consequently, Ladder topology was retained as it is only composed of passive components. The L section was preferred over the T section to minimize the inductance value for filter integration in the chip, as the inductance space occupation is related to its value (the implementation was directly performed by ADS software, as shown in Figure 25). However as L remains elevated (around 400nH), the filter may rather be outside of the chip.

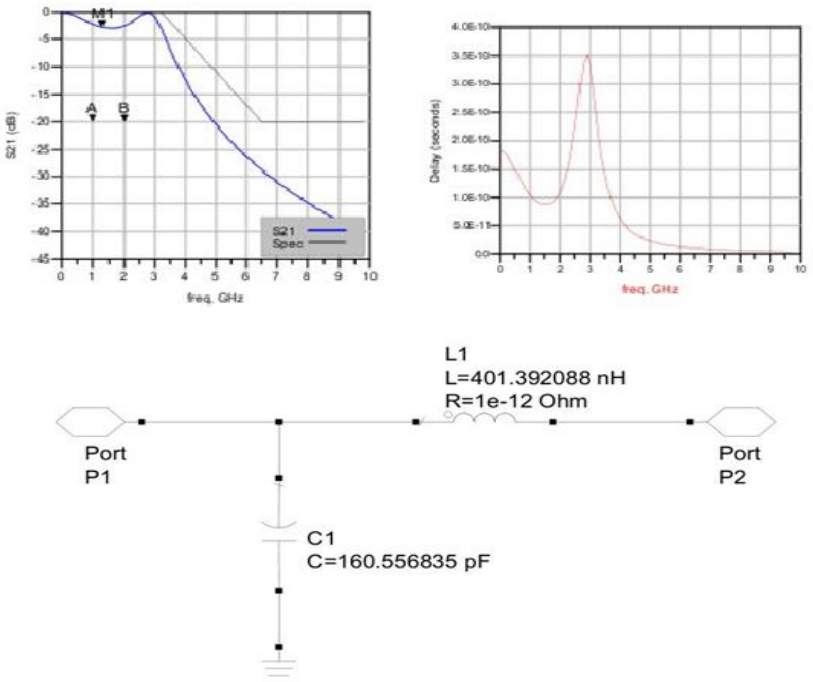

FIGURE 25: ANALOG FILTER DESIGN USING ADS® . A) MAGNITUDE RESPONSE. B) GROUP DELAY RESPONSE. C) LADDER IMPLEMENTATION DIRECTLY PERFORMED WITH ADS®

2. Digital filter design

To include these filters in the entire chain Matlab/Simulink®modeling, the transformation of analog filters into digital ones was performed. The transfer function of a discrete system is the z-transform of its impulse response and can fully describe a filter behavior[82]. Other ways to characterize a digital filter is by its impulse response or by the difference equation; the system equations in continuous time become a difference equation that rely the input x(n) and the output of a filter y(n), cf eq. 25. It should be noted that the frequency response of a digital filter only describes its steady state behavior [88].

$$y(n) = \sum_{i=0}^{M} b_i \, x(n-i) - \sum_{i=1}^{M} a_j \, y(n-j) \qquad \text{EQ. } 25$$

where n is the current sample, x and y are the filter input and output respectively and a_i and b_i are scalar coefficients.

Different analog to digital switching techniques exist such as impulse invariant, step invariant, matched z-transform methods and are evaluated in [82]. Bilinear transform was the one selected as it is the most commonly used in digital filter design. This transformation preserves filter stability and is bijective like every Mobius transformations [89]. The main drawback of the bilinear transform is the frequency distortion also called frequency warping. For low frequencies, the frequency mapping is linear but this is not the case for high frequencies [82]. The creation of a digital filter from an analog one should be done considering the frequency warping phenomena in order to obtain proportional cutoff frequencies. The methodology that indicates all the steps to pass from an analog filter to the equivalent digital filter using the bilinear transform can be found in [82],[90].

Using the bilinear transform, the conditions of stability change. For a digital filter to be stable, all its roots have to be inside the unit circle. However, several authors have indicated that this condition was too weak to ensure digital filter stability and proposed that if in the difference equation (cf eq. 35) the value of b_i coefficients is greatly lower than the value of a_i coefficients, the round off noise may be important and could make the filter unstable [91, 92]. Another hypothesis to ensure filter stability may be that in the difference equation the sum of all the a_i should be lower than 1 [93].

The impulse response of the low pass digital filter (using Butterworth approximation function) and then its bilinear transformation is presented in Figure 26.

As the difference equation is less resources consuming than the convolution method and results in an almost similar interval length than the input interval length, the difference equation implementation was preferred in order to model the digital filter block and to find the filter output. This digital filter

form (difference equation) fits particularly to our behavioral models as the simulations we performed were entirely temporal.

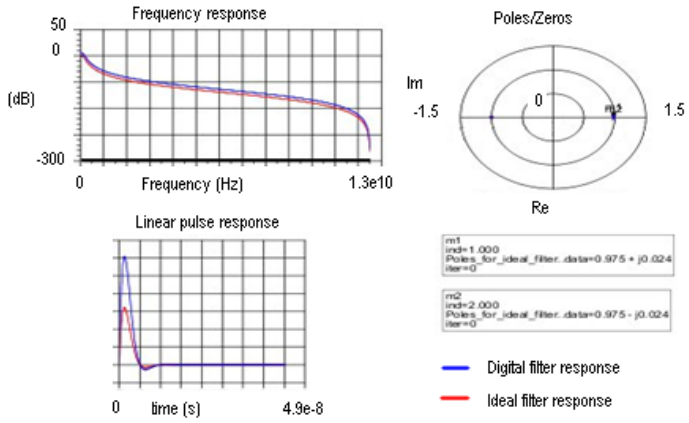

FIGURE 26: A) FREQUENCY RESPONSE OF THE DIGITAL FILTER. B) IMPULSE RESPONSE OF THE DIGITAL FILTER. C) ZEROS AND POLES OF THE DIGITAL FILTER

To conserve similar digital filter specifications and ensure filter stability, F_{pass} and F_{stop} were modified (for digital filter implementation only), as the simulation frequency was significantly higher than the cutoff frequency, resulting in poor ADS® filter design convergence. For instance, in the low pass filter used to rectify the received signal, F_{pass} was changed to 100MHz and F_{stop} was changed to 1GHz. Those frequencies still permit signal demodulation as no jitter was added to the oscillator model.

D. Critical parameters

Once the transient modeling for the overall RF chain completed and because each model contains inherent parameters, the study of these parameters variation on the output signal integrity was performed. The variation of these parameters between three different values (minimum, typical and maximal) was accomplished and the amplitude distortion between the signal sent and the one received was computed for each single variation. It should be noted that when a parameter value was modified, the other parameters remained constant discarding any correlation study between these. Hence no statistical correlation function can be extracted from the results. This choice was dictated by the high number of parameters evaluated (around 15). To initially evaluate the critical

parameters impacting the signal integrity, we compared the signal amplitude coming from the microphone with the signal received and PWM demodulated. This demodulation was first accomplished using a threshold detector, hence the output signal may not be reconstructed if the amplitude preceding the threshold detector was too low (explaining why the amplitude perturbation can reach 100% in some cases). An alternative solution (not tested in this modeling analysis) can be the use of a second low pass filter for PWM signal demodulation.

As presented in Figure 27, the parameters impacting the most the signal integrity are the preamplifier gain and the comparator offset which should be kept minimal. Then the LNA output signal, if too low, could affect the signal integrity as the output signal may be too weak for PMW demodulation using a threshold detector. Finally, a significant reduction of antenna gain or an inconsistency in propagation channel attenuation estimation may impair very profoundly the signal received.

If the typical value of each parameter was retained, there is around 12% of amplitude distortion between the signal coming from the microphone and the one received at the end of the transceiver. To decrease the amplitude distortion between these two signals, increasing PA gain, increasing antenna efficiency or decreasing the comparator offset may be investigated. In consequence, based on these results, antenna efficiency improvement and comparator offset lowering should be performed first.

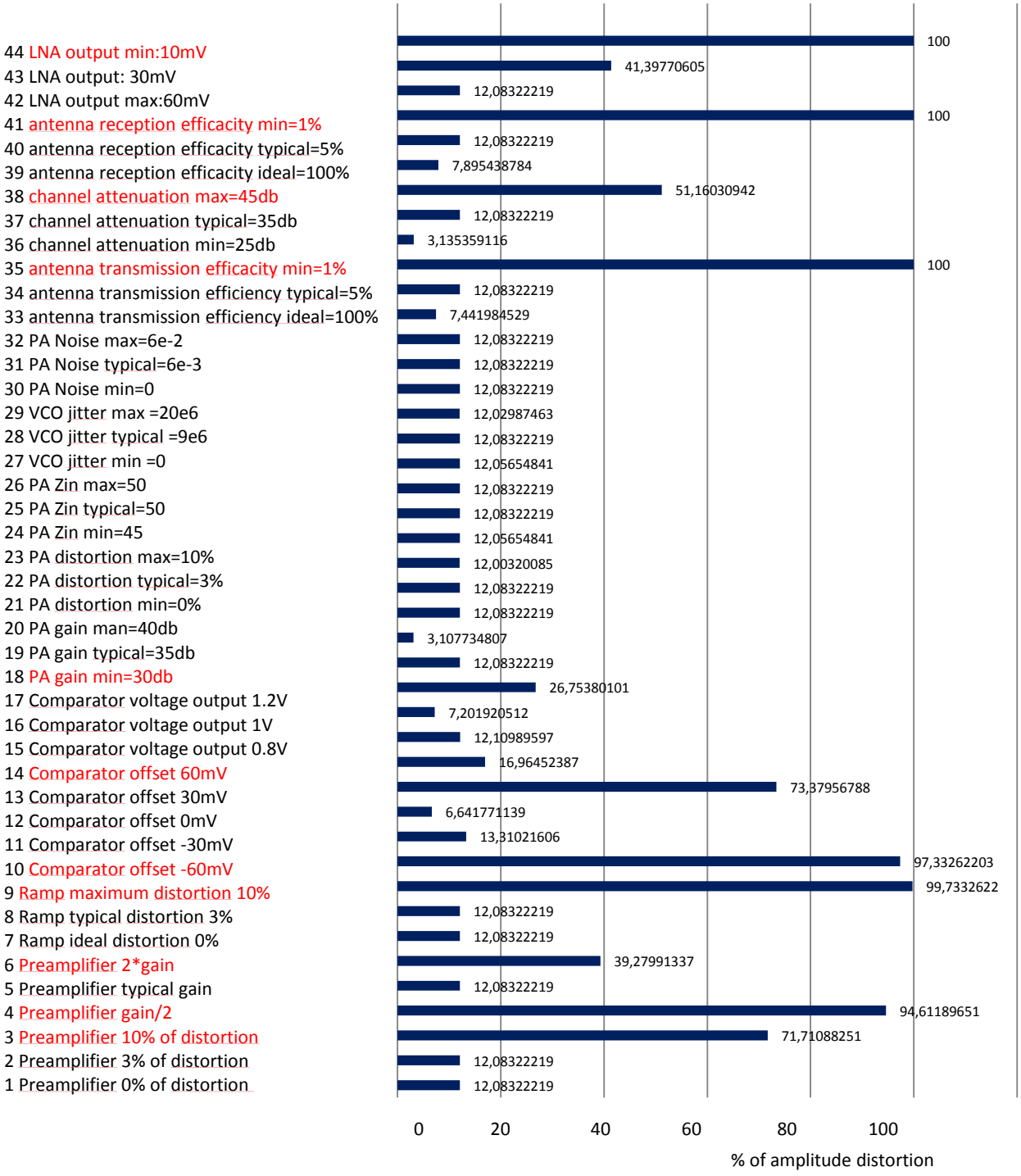

FIGURE 27: CRITICAL PARAMETERS STUDY

E. Phase noise modeling

1. Introduction to phase noise

The transmitter modulation choice is a time modulation (PWM), before sending the signal to RF frequencies. In consequence, the phase noise introduction in the oscillator associated with the PWM encoding may result in output signal distortions. Furthermore a second oscillator is used for the OOK modulation and phase noise is also of capital importance to ensure signal inclusion in the ISM frequency band retained. Phase noise study and restriction is hence essential for proper transceiver performances.

Circuit and device noises generally perturb oscillator's output as they introduce amplitude and phase noises. Often oscillators contain amplitude limitation mechanisms which limit amplitude noise. As a result phase noise is in general more significant and degrades oscillator performances. Linking phase noise with oscillator's parameters was performed by Leeson [94] who connected the oscillator power spectrum side band with circuit parameters that can be minimized by proper design. In[95], the mathematical analysis of the Leeson's formula has been performed and has conducted to a more general case, not only with a RLC filter in the feedback loop. However later measurements have shown limitations of the Leeson's theory [96]. The Linear Time Invariant (LTI) model of the oscillator system proposed by Leeson was hence replaced by a Linear Time Variant model (LTV) proposed by Hajimiri and Lee [97]. When a noise impulse current is injected to an oscillator node, it results into permanent phase error. Furthermore the phase noise contribution depends on the time of noise injection as explained in [97], justifying the need of a time variant model to link current noise with phase noise in oscillators. The LTV model proposed in [97] involves the computation of the Impulse Transfer Function (ISF) which is central for phase noise characterization. However both models suppose that the noises disturbing the oscillator are mainly white noise and pink noise (also called 1/f noise).

Numerous electronic automation devices simulators use specific input blocks and simulation types to simulate phase noise which are often computational resources greedy.

We wanted to create a homogenous system which permits to account for phase noise perturbations and to further extend this system to phase noise computation without the use of Spice simulation results using an Impulse Sensitivity Function (ISF) database for diverse oscillator topologies. This system was based on the filtering of the input noises (white noise and Flicker noise).

Only for LTI systems the Power Spectral Density (PSD) expression is simplified as described in the Annex B.2, thus worsening the LTV model of Hajimiri and Lee [97] into a LTI model was performed before comparing the obtained phase noise with SPICE simulations or direct measurements (only for the ring oscillator). Besides we developed a filtering function allowing the estimation of phase noise using input noises relative to the design technology selected.

Mathematical formalism associated with stochastic processes and mathematical systems analysis is inserted in Annex B.1 and Annex B.2. Furthermore the mathematical description of white noise and Flicker noise (or 1/f noise) and their physical interpretation is presented in Annex C

We also created a new function to express timing jitter from phase noise. The jitter of the oscillator used for PWM signal creation was statistically evaluated and resulted in the restriction of the PWM signal accuracy.

2. Additive process of the white noise and the 1/f noise

As defined in Annex B.1 the autocorrelation functions permits to characterize noises and led to the computation of their PSD. However the autocorrelation function is non linear and the addition of two noises will not result in addition of their autocorrelation and hence will not result in the direct addition of their PSD as developed in eq. 26.

Suppose X(t) and Y(t) two random processes (representing for instance white noise and 1/f noise):

$$E[\big(X(t1)+Y(t1)\big)\big(X(t2)+Y(t2)\big)] = E[X(t1)X(t2)] + E[X(t1)Y(t2)] + E[Y(t1)X(t2)] + E[Y(t2)Y(t1)] \quad \text{EQ. 26}$$

eq. 26 further simplifies if both processes are stationary. However, the simplification cannot fit here as 1/f noise is non-stationary [98]. The evaluation of the cross correlation functions is needed before computing the PSD of the additive process. The cross correlation function between white noise and 1/f noise is available in [99] and it is called the colored cross correlation function. In [99] authors assumed that both cross correlation functions are equal (eq. 27):

$$E[X(t1)Y(t2)] = E[Y(t1)X(t2)] = \frac{\lambda\sqrt{\alpha D}}{\tau 2}\exp\left(\frac{-|\,t1-t2\,|}{\tau 2}\right) \xrightarrow{\tau 2\to 0} 2\,\lambda\sqrt{\alpha D}\,\delta\,(\,t1-t2\,) \quad \text{EQ. 27}$$

where λ is a parameter that measures the strength of the correlation between X(t) and Y(t) and τ_2 is the correlation time between X(t) and Y(t). Correlation time is defined as the average time between molecular collisions for molecules in some state of motion and is the sum of three different times: the rotational correlation time, the residence time and the electron spine lattice relaxation time[99]. The time between two collisions for a molecule is very small and naturally tends to 0, explaining the limit. The result of the colored cross correlation is hence a delta dirac function multiplied by a coefficient proportional to the strength of the correlation between the X(t) process and the Y(t) process. The colored cross correlation is hence similar to the white noise autocorrelation function presented in Annex B.3. The autocorrelation function resulting from the addition of a white noise and a 1/f noise is thus the same as the autocorrelation of a 1/f noise added to the autocorrelation function of another white noise with different variance. To obtain the variance of the white noise X(t) from the PSD of the sum TF(E[(X(t1)+Y(t1))(X(t2)+ Y(t2))]), estimation of the correlation parameter λ is therefore of importance.

F. Assumptions made for model creation

The model created and presented in Section II.G was based on the following assumptions:

- We supposed that the cross correlation between white noise and Flicker noise is null as we supposed that this function was negligible compared to the autocorrelation of white noise. However this is mathematically incorrect as indicated above in this Section. This assumption aims to simplify the model and can account for the model divergence with the measurements.

By assuming that the colored cross correlation between the two input noises are null, the autocorrelation function of the sum of the two noises is supposed to be equal to the sum of the autocorrelation of the two noise processes, as indicated in eq. 28:

$$E\big[(w_1(t) + w_2(t))(w_1(t+\tau) + w_2(t+\tau))\big] = E[w_1(t)w_1(t+\tau)] + E[w_1(t)w_2(t+\tau)] + E[w_2(t)w_1(t+\tau)] + E[w_2(t)w_2(t+\tau)] \quad \text{EQ. 28}$$

$$\rightarrow E\big[(w_1(t) + w_2(t))(w_1(t+\tau) + w_2(t+\tau))\big] \approx E[w_1(t)w_1(t+\tau)] + E[w_2(t)w_2(t+\tau)]$$

where w_1 is the Gaussian white noise process and w_2 is the 1/f noise process and the operator E is the mathematical expectation.

- We further supposed that the sum of the white noise Gaussian process and the 1/f noise process is stationary. This assumption is controversial as various authors have advanced each hypothesis [98, 100].
- It was shown in [97], that the transfer function relating noise currents to phase distortion is time dependent. In fact different noise current injections in the same node but at successive starting times result in different phase perturbations. However in this paper we considered that the phase alterations over a period was constant, meaning that we supposed the transfer function as time invariant.

All these misleading assumptions were built to simplify the computation (thus greatly decreasing the simulation time) of the phase noise PSD. If the input process is assumed stationary and the transfer function is presumed time invariant, the phase PSD computation is simply expressed as (eq. 29)[101]:

$$S_{\varphi\varphi}(f) = |H(f)|^2 S_{XX}(f) \qquad \text{EQ. } 29$$

where S_{xx}, $S_{\phi\phi}$ are the PSD of the input process and phase noise process respectively and H is the Fourier Transform (FT) of the transfer function.

Tests have shown (cf Section II.G.5) that the errors introduced by these assumptions are narrow when compared to physical measurements, despite the fact that they are physically untrue.

Besides we only account for the phase noise around the first harmonic of the oscillator signal.

G. Creation of a new LTI model using Hajimiri and Lee theory

1. Leeson model

The Leeson formula permits to study the circuit parameters influence on the output phase noise in order to minimize it. It is presented in eq. 30 and gives the sideband power spectral density of the phase noise leading to identification of the most significant causes of phase noise in oscillators [94].

$$S_{\varphi\varphi}(f_m) = \frac{1}{2}\left[1 + \frac{1}{(f_m)^2}\left(\frac{f_0}{2Q_L}\right)^2\right]\frac{FkT}{P_{AVS}}\left(1 + \frac{f_{\frac{1}{f}}}{(f_m)}\right) \qquad \text{EQ. } 30$$

where Q_L is the quality factor with load, f_m the offset frequency, f_0 the oscillator central frequency, T the temperature, P_{AVS} is the average power through the resonator, F the noise factor of the active device and k the Boltzman constant.

The system transfer function permitting to obtain the output phase noise from the input noises (the 1/f noise and the white noise) is LTI.

In eq. 30 it can be seen that the power side band spectrum of the oscillator ($S_{\phi\phi}$) can be split into a transfer function (H_L) multiplied by the input noise PSD (S_{xx}).

Identifying H_L and S_{xx}, related to the Leeson model, is performed in eq. 31

$$H_L(f_m) = \frac{1}{2}\left[j + \frac{1}{(f_m)^2}\left(\frac{f_0}{2Q_L}\right) \right] \qquad \text{EQ. 31}$$

$$S_{xx}(f_m) = \frac{FkT}{P_{AVS}}\left(1 + \frac{f_{\frac{1}{f}}}{(f_m)} \right)$$

This identification is not new and can be found for instance in [97, 102, 103]

In this model, the intersection point of the 1/f noise and the white noise (called $f_{1/f}$) is the same as the intersection point of the output phase noise between the $1/f^3$ region and the $1/f^2$ region called ($f_{1/f3}$). However it is not always the case as noted by Hajimiri and Lee and furthermore the noise factor is obtained by measurements and not by theoretical expression which decreases the estimation power of this model. In addition the evaluation before simulation of Q_L may be difficult for other oscillator topologies than LC.

The Leeson model of phase noise is further extended in [95, 104] and both models describe the oscillator for noise analysis as an amplifier followed by a resonator on the feedback loop. In document [95], the mathematical analysis of the Leeson formula has been performed and has conducted to a more general case.

2. Hajimiri and Lee model of phase noise

Hajimiri and Lee [97] have demonstrated that the total single side band phase noise power spectral density due to white noise is:

$$S_{\varphi\varphi}\{f_m\} = \frac{\frac{{i_N}^2}{\Delta f}{\Gamma_{rms}}^2}{4{q_{max}}^2(f_m)^2} \qquad \text{EQ. 32}$$

where q_{max} is the maximum charge displacement across the capacitor, $i_N^2 / \Delta f$ the white noise PSD integrated over 1Hz bandwidth, Γ_{rms} the Root Mean Square (RMS) value of the Impulse Sensitivity Function (ISF) and f_m the offset frequency. Using a similar development, the total power sideband phase noise power due to 1/f noise is:

$$S_{\varphi\varphi}\{f_m\} = \frac{\frac{{i_N}^2}{\Delta f} 2\pi f_{1/f} {c_0}^2}{8qmax^2 (f_m)^3} \quad \text{EQ. 33}$$

where c_0 is given by the decomposition of the ISF into a Fourier serie as the ISF is a periodic function [97]:

$$\Gamma(f_O t) = \frac{c_0}{2} + \sum_{n=1}^{\infty} c_n \cos(n2\pi f_0 t + \theta_n) \quad \text{EQ. 34}$$

Where θ_n is the phase of the *n*th harmonic.

In particular the relation between the $f_{1/f3}$ (which is the frequency where the $1/f^3$ output noise becomes smaller of the $1/f^2$ output noise) and $f_{1/f}$ is given by eq. 35 [97]:

$$f_{1/f3} = f_{1/f} \frac{{c_0}^2}{2{\Gamma_{rms}}^2} \quad \text{EQ. 35}$$

It is worthwhile to note that $f_{1/f}$ and $f_{1/f3}$ frequencies are not equal in contradiction with the Leeson model.

3. Time invariant Hajimiri and Lee model

In a similar way that was made for the Leeson model, we wanted to identify input noises and a common filter function, allowing easier algorithmic implementation and hence faster simulation.

Supposing that the Hajimiri and Lee model is time invariant and that the colored cross correlation of the input noises are null, permit to combine eq. 32 and eq. 33. The phase noise PSD can hence be expressed as a system transfer function multiplied by the PSD of the input processes. The side band power spectral density of this new system is called S_{tt} and gives similar expression than the LTV model of the final PSD, although the mathematical assumptions to obtain it are incorrect.

$$S_{tt}\{f_m\} = \frac{1}{qmax^2 4}\left(\frac{{\Gamma_{rms}}^2}{(f_m)^2}\right)\left(\frac{{i_N}^2}{\Delta f} + \frac{\frac{{i_N}^2}{\Delta f} 2\pi f_{\frac{1}{f}} {c_0}^2}{2\,{\Gamma_{rms}}^2 f_m}\right) \quad \text{EQ. 36}$$

The identification of a filter function and the PSD of the input noises (white and Flicker noise) is shown in eq. 37

$$H_{tt}(f_m) = \frac{1}{qmax \;\; 2}\left(\frac{\Gamma_{rms}}{f_m}\right) \qquad \text{EQ. 37}$$

$$S_{xx}(f_m) = \left(\frac{{i_N}^2}{\Delta f} + \frac{\frac{{i_N}^2}{\Delta f} 2\pi f_{\frac{1}{f}} {c_0}^2}{2\,{\Gamma_{rms}}^2 f_m}\right)$$

However when we implemented this equation, the results were distant of approximatively 15dB to 25dB from Spice simulations results realized on two different oscillator topologies and presented in Section II.G.5.b).

The inclusion of cyclostationary noises coming from modulated noise sources (such as white noise originating from periodic bias current) or modulated signal paths (such as periodic operating point) [105] modified the ISF function as emphasized in the eq. 38 [97]. To the authors comprehension, when cyclostationary noises exceed the other noise sources, it results in ISF new definition [97]:

$$\Gamma_{eff}(t) = \;\; \Gamma(t) * \alpha(t) \;\; with \alpha(x) = \frac{i_{n(t)}}{i_{n0}(t)} \qquad \text{EQ. 38}$$

where Γ is the ISF function (which mathematical expression is function of the oscillator output signal and is presented in [97]), i_n is the cyclostationary process and i_{n0} is the white noise process. α is a periodic dimensionless value with a peak value of unity [97]

Consequently we modified eq. 37 by replacing Γ by Γ_{eff} , giving other values of c_n.

As precised in [97], the cyclostationarity noises are increased in LC oscillators in compare to ring oscillators.

4. System creation

The implementation of the eq. 37 was made using Matlab®. The computation of the PSD was performed with the periodogram estimator or by taking the Fourier transform of the autocorrelation function (as input noises are white noises). Both techniques gave very similar results. The system used to simulate phase noise is presented in Figure 28.

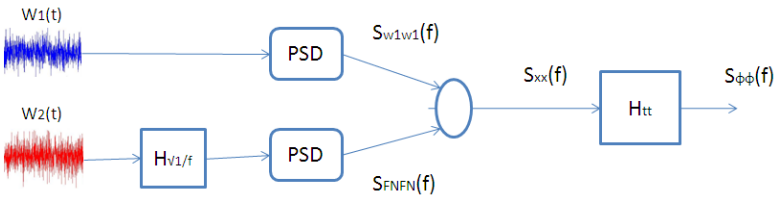

FIGURE 28: BLOCK DIAGRAM CREATED TO COMPUTE PHASE NOISE

where $H_{V1/f}$ is the filter converting white noise into Flicker noise and was created mathematically. It should be notified that using the assumptions made in Section II.F, Flicker noise PSD may also be obtained by computing first the PSD of white noise and then multiplying the PSD by a simple 1/f factor, further increasing the simulation time. As cross correlation were supposed null, both inputs PSD were added to obtain the input noise PSD (S_{xx}), and further filtering using H_{tt}, permitted to obtain the phase noise PSD ($S_{\phi\phi}$).

5. Results

a) Oscillator topologies for tests

The first oscillator, designed with Cadence®, is an RLC VCO with a central frequency of 2.45GHz, presented Figure 29. The width of the NMOS of the differential pair is 210µm and their length is 130nm.

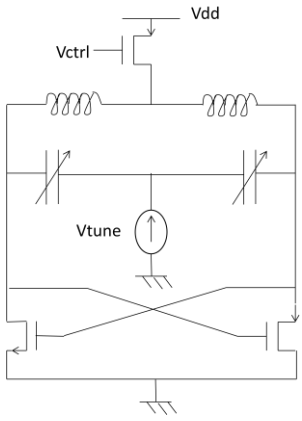

FIGURE 29: VCO RLC OSCILLATOR SIMULATED IN CADENCE WITH A CENTRAL FREQUENCY OF 2.45GHZ

The second oscillator used is a 3 stages ring oscillator with a central frequency of 2.67GHz (but can be modified to 2.45GHz using variable capacitors or biasing currents) based on CMOS inverters. This oscillator was realized and measures were extracted from its tests. The simplified electric schematic of this oscillator is presented Figure 30.

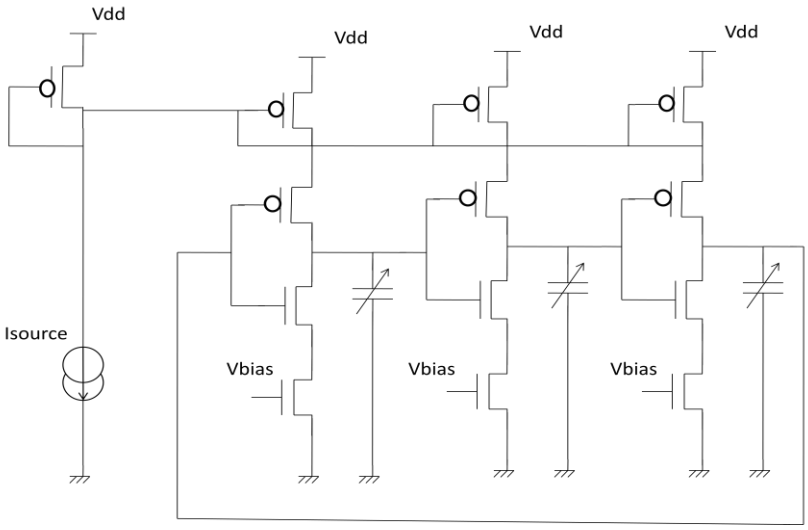

FIGURE 30: VCO RING OSCILLATOR IN TECHNOLOGY CMOS 130NM

b) Simulations and measurements

For both oscillators topologies, the result extracted from SPICE simulations are compared first to the Leeson model to ensure that the filter time invariance gives close result and then with the time invariant Hajimiri and Lee model that we created (H_{tt}). Only for the ring oscillators the tests were available allowing the best reference for models comparison.

(1) RLC oscillators simulations

The noise factor was obtained with SPICE simulations and was found equal to 4.47. P_{avs} was estimated at 4.8mW. To estimate the Q_l, S-parameters analysis was run with an intrinsic resistance in parallel of the inductance of 20Ωhms and a load resistance of 50Ωhms. Q_l was found to be around

1.7. The value of $f_{1/f}$ for the two NMOS was determined with a noise analysis and found around 300MHz.

The comparison between the SPICE simulation of the VCO phase noise and the results obtained from Matlab® implementation of the Leeson model is presented in Figure 31.

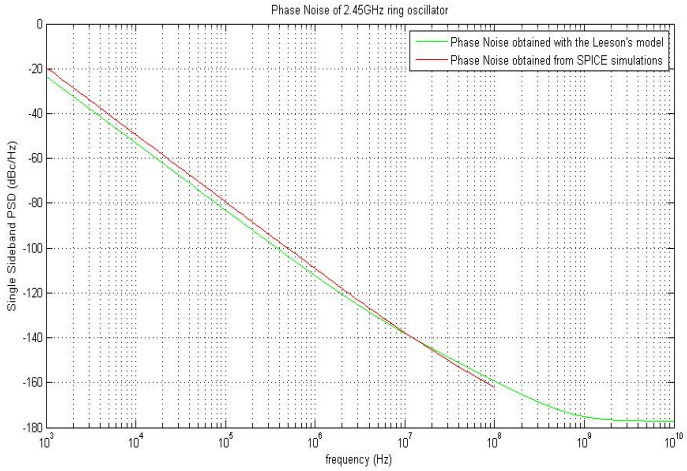

FIGURE 31: COMPARISON BETWEEN THE PHASE NOISE POWER SPECTRUM OBTAINED BY SPICE SIMULATIONS AND THE PHASE NOISE POWER SPECTRUM OBTAINED WITH THE LEESON'S MODEL

Satisfying compliance is obtained between the two simulations with a maximum error less than 4dB (cf. Figure 31). When $f > f_{1/f}$ the Lesson's model shows a smaller slope than the phase noise power spectrum simulated with SPICE most probably due to error in the $f_{1/f}$ computation ($f_{1/f}$ may be greater than the one estimated). Furthermore the Leeson model was modified with the addition of a thermal noise in order to keep it in realistic values for large offset frequencies (Δf> 1GHz).

The Hajimiri and Lee model considered here is the time invariant one (H_{tt}). The corresponding simulation results are presented in Figure 32.

The most challenging value to obtain to implement the Hajimiri model was the precise ISF function. As stated in Section II.G.2, the effective ISF was computed to include cyclostationary noises which impact greatly a RLC oscillator. We use the following expression for the ISF [97]:

$$\Gamma(x) = \frac{f'}{f'^2 + f''^2} \qquad \text{EQ. } 39$$

where f is the oscillator output. The determination of the α function (eq. 38) is based on the shape of the cyclostationary noise current which has a similar shape to the drain current of the NMOS transistor.

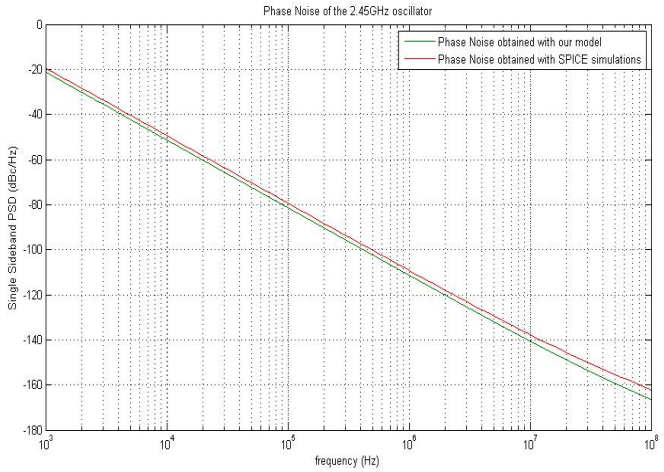

FIGURE 32: COMPARISON BETWEEN THE PHASE NOISE PSD OBTAINED BY SPICE SIMULATIONS AND THE IMPLEMENTATION OF THE TIME INVARIANT HAJIMIRI AND LEE MODEL.

The number of points from SPICE simulations is sometimes insufficient as the fundamental tone is at 2.45GHz. In consequence to compute the first and second derivatives of the oscillator output, low pass filters were used and may explain small uncertainties in parameters computation.

By performing the same development than in [97], c_o was found equal to -0.36 and Γ_{rms} equal to 0.073.

Good compliance is obtained also between the SPICE simulations and the time invariant Hajimiri and Lee model created. A maximum error of 5 dB is present between the different simulation results. Supposing time invariant the Hajimiri and Lee model is hence conceivable in the particular case of a RLC VCO. Furthermore the error is stronger when $f > f_{1/f3}$ most probably due to inaccurate Γ or poor $f_{1/f}$ estimation.

(2) Ring oscillator simulations and measurements

In the series of measurements performed on our CMOS prototype with the phase noise analyzer Agilent® 5500, there is a flat curve for frequencies lower than 200 kHz (cf. Figure 33). The most likely explanation is that noise present on the DC supply voltage also called “power pushing” modifies the central oscillation frequency of the ring oscillator. The PLL inside the measurement device was not able to lock the ring oscillator central frequency with accuracy and the measures were erroneous for offset frequencies lower than 200 kHz.

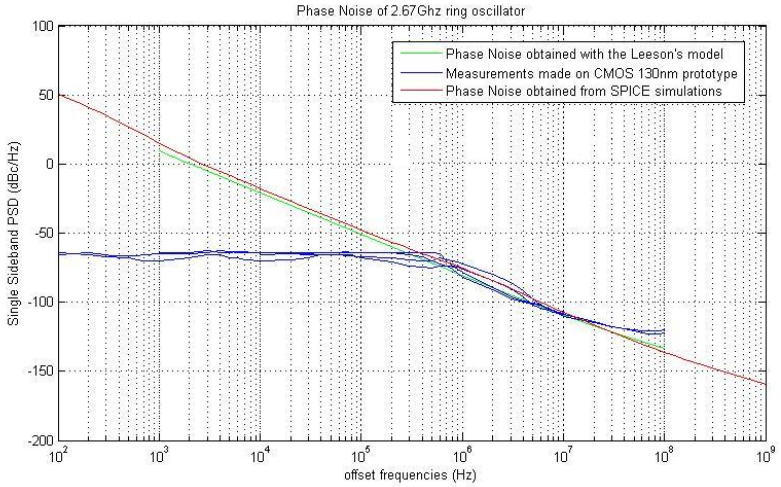

FIGURE 33: COMPARISON BETWEEN THE PHASE NOISE PSD OBTAINED BY SPICE SIMULATIONS, THE PHASE NOISE PSD OBTAINED WITH THE LEESON'S MODEL AND THE MEASUREMENTS MADE ON A CMOS PROTOTYPE FOR THE RING OSCILLATOR

Figure 34 presents the variation in the central oscillation frequency of the ring oscillator for a modification of the supply voltage between 1.19 and 1.21 V. As expected the central frequency changed between 2.71GHz and 2.48GHz. Therefore to obtain a central frequency variation lower than 200 KHz, the noise in the voltage supply in our design should be far less than 0.01V, which is difficulty achievable.

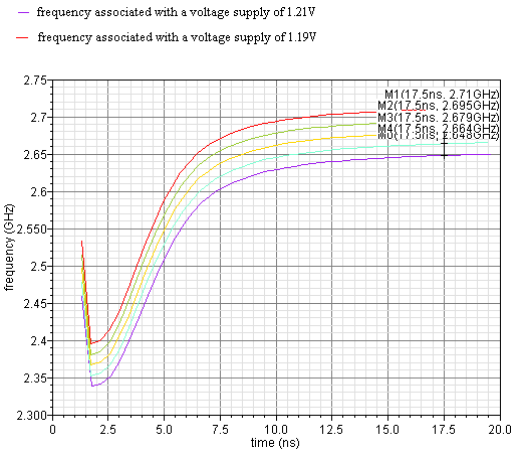

FIGURE 34:FREQUENCY VARIATION OF THE CENTRAL FREQUENCY OF THE RING OSCILLATOR DEPENDING ON VOLTAGE SUPPLY MODIFICATIONS

As the Leeson formula was first developed to compute phase noise in RLC oscillator [94], the Leeson formula implementation for other oscillator topologies may be tricky. In the document [106], the computation of the implicated parameters of the Leeson formula, but this time related to a ring oscillator, is performed. For convenience two of these formulas are repeated here:

$$Pavs = n * N_b * Vdd * qmax * fo \qquad \text{EQ. } 40$$

And

$$Ql = \frac{N_b}{2}\sin\left(\frac{N_b}{2}\right) * \sqrt{\frac{3\pi Vmax}{8Vdd}}$$

$$qmax = C_{eq} * \max(V_{out})$$

where n is a technology factor around 0.7 and N_b is the number of stages of the ring oscillator. C_{eq} is the equivalent capacity of the node where the input current is injected. C_{eq} was determined replacing all the MOS by a SPICE 2 RF equivalent schematic and was found equal to 25fF.

Figure 33reveals very close results between the SPICE simulations and the Leeson model (less than 3db of error) but is farer from the measurements, especially for very high offset frequencies (>1GHz). The measurements however were not performed on the ring oscillator directly but a PA was connected after the ring oscillator and the output pin used for the measurements was the output of the PA. The noise of the PA may increase the noise floor of the ring oscillator and that could explain the flattening of the phase noise curve for very high offset frequencies.

As explained in detail in the Hajimiri document related to phase noise computation for ring oscillators[107], the effective ISF function is very closed to the ISF function meaning fewer perturbations from cyclostationary sources. After computing the ISF from eq. 39, c_o was found equal to 0.0567 and Γ_{rms} equal to 0.1334 meaning a closer $f_{1/f3}$ from $f_{1/f}$ for the ring oscillator than the RLC oscillator.

In Figure 35, it can be noted than the absolute margin between the time invariant Hajimiri model (H_{tt}) and the SPICE simulation may reach 10db only for very high offset frequencies maybe due to poor $f_{1/f3}$ estimation. In fact for smaller frequencies the difference is around 3dB, and because of a too low $f_{1/f3}$ estimation in our model, the slope is only of -20db/decades for frequencies greater than 10MHz in our model which is not the case for SPICE simulations (still a -30db/decades slope). However, our model is closer to the measurements than the SPICE simulations are. For this special case of ring oscillator topology, we can conclude that the time invariant Hajimiri model (H_{tt}) can be applied to determine phase noise with sufficient accuracy.

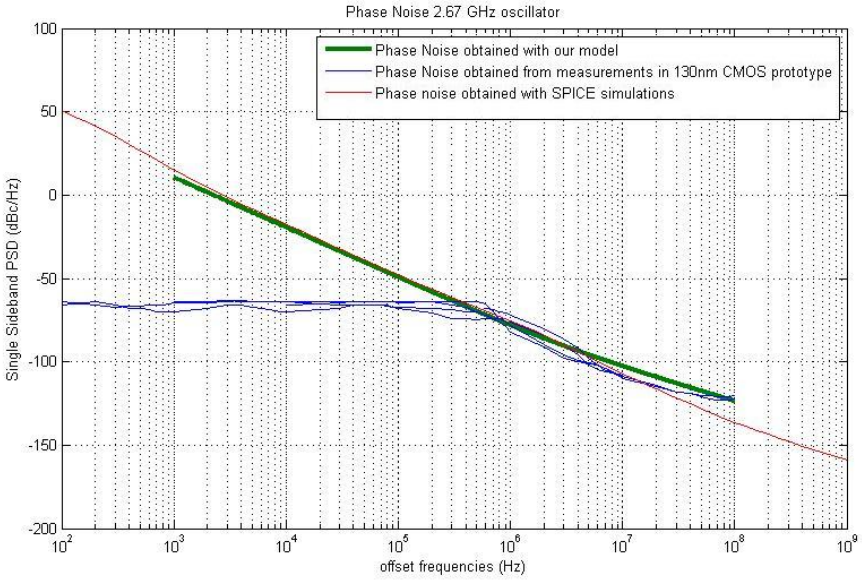

FIGURE 35: COMPARISON BETWEEN THE PHASE NOISE PSD OBTAINED BY SPICE SIMULATIONS, THE PHASE NOISE PSD OBTAINED WITH THE TIME INVARIANT HAJIMIRI MODEL AND THE MEASUREMENTS MADE ON A CMOS PROTOTYPE FOR THE RING OSCILLATOR

As this electronic design for the RLC and the ring oscillator topologies are very common, the results obtained in this document may be extended to not only single designs but also to these two topologies.

(3) Simulation time:

Using the Leeson model implementation or the time invariant model we created from Hajimiri and Lee theory permits to fasten simulation by approximately 10^3 times, in the same computer. In fact the simulation took only few seconds, whereas for SPICE simulations (BSIM 3), it lasted several hours for the ring oscillator phase noise simulation. For RLC oscillator, the time gain is less significant as SPICE simulations are faster due to the decrease number of transistors.

(4) Phase noise estimation using Time Invariant Hajimiri and Lee Model

As we obtained good compliance between our model simulation and the SPICE ones for the two oscillator topologies, we wanted to create a phase noise estimation system, in order to obtain phase noise perturbations before the design of the oscillator. However this system has the following limitations:

- The phase noise can be estimated only for offset frequencies close to the oscillator carrier which corresponds to the $1/f^3$ and $1/f^2$ regions. These offset frequencies are most of the time the ones of interest in phase noise study.
- The phase noise estimation is restricted to oscillators with low cyclostationary noises. Meaning that Γ_{eff} is close to Γ. It is the case in ring oscillators as described in Section II.G.2

Leeson model of phase noise does not permit easy estimation of phase noise before oscillator simulation mainly due to difficulty in estimating the noise factor F (cf Section II.G.1).

However in the model we created, the computation of H_{tt} can be obtained before the oscillator design, first by computing the ISF function which is approximated by eq. 39 [97], and is only dependent on the oscillator output signal. By extracting oscillator (with different type of topologies) output functions from literature, a database of ISF functions can be created. However, as described above, it is only valid for topologies where cyclostationary noises are not significant such as ring oscillators, etc. Once the ISF function is obtained, all the c_n coefficients are known from eq. 34 [97].

The other variable to estimate is q_{max} which is equal to C_{eq} multiplied by V_{max}. Recalling that C_{eq} is the equivalent capacity of the node where the input current is injected, it can be theoretically computed using the analog model of the oscillator. In the same way using the theoretical analog model of the oscillator, V_{max} can be estimated without requiring precise Spice simulations.

Although incomplete, the presented work could be fulfilled to theoretically evaluate oscillator output waveforms (hence corresponding ISF), C_{eq} and V_{max} for phase noise estimation without benefits of Spice simulations. This would most likely allow very significant architecture selection and design time savings.

H. Timing jitter estimation

1. Timing jitter introduction

The transitions spacing over time in any given oscillator are not constant but fluctuate, which commonly define timing jitter. Although several jitter definitions exist such as period jitter, long term jitter and cycle to cycle jitter [108, 109], all these quantities can be defined from the jitter accumulation description. Besides only random jitter is studied in this document, discarding any deterministic jitter effect. Naming ΔT the measurement time interval period, and ε_i the random variable with gaussian distribution, zero mean and variance $\sigma_{\varepsilon i}^2$, it can be proved [110] that the accumulation jitter over time is a gaussian random process with zero mean and variance σ_{jitter} such as defined by EQ. 41 [110]:

$$Jitter(t) = \sum_{n=1}^{floor(\frac{\Delta T}{T_0})} \varepsilon_n \qquad \text{EQ. 41}$$

where T_0 is the oscillator period and ε_n are the random gaussian variables representing the timing error introduced at each period transitions. floor function permits to find the truncated value, giving an integer value. Furthermore the variance of the cumulative jitter process is defined as [110], with N being the number of period (or similarly the number of transitions) in the time measured interval ΔT [110]:

$$\sigma_{jitter}^2 = \begin{cases} \sigma_{\varepsilon 1}^2 + \sigma_{\varepsilon 2}^2 + \cdots + \sigma_{\varepsilon N}^2 = N\varepsilon^2 & if\ \sigma_{\varepsilon i}^2\ are\ uncorrelated\ and\ discribed\ by\ similar\ fluctuations\ \varepsilon \\ N^2\varepsilon^2 & if\ \sigma_{\varepsilon i}^2\ are\ totally\ correlated\ and\ discribed\ by\ similar\ fluctuations\ \varepsilon \\ N^\alpha \varepsilon^2 \ \ with\ 1 \le \alpha \le 2 & in\ the\ general\ case\ (assuming\ that\ each\ oscillator\ period\ can\ be\ discribed\ by\ similar\ fluctuations\ \varepsilon) \end{cases} \qquad \text{EQ. 42}$$

The statistics of the timing jitter depends on the correlation of the jitter at the end of each period and more physically on the correlation of the noise sources creating it [111]. If each transition period is affected by uncorrelated noise sources, the total variance of the jitter is equal to the sum of the variances of the timing fluctuations introduced at each stages. As the number of transitions N is proportional to the time measured ΔT, in this particular case, the variance of the jitter is proportional to the time measured ΔT [111].

$$\sigma_{jitter}^2 = k_1 \Delta T \qquad \text{EQ. 43}$$

When noise sources are totally correlated such as supply or substrate noise, the standard deviations rather than the variance add [111], justifying EQ. 44.

$$\sigma_{jitter}^2 = k_2 \Delta T^2 \qquad \text{EQ. 44}$$

In the general case however both correlated and uncorrelated noise sources exist in a circuit resulting in correlated and uncorrelated timing perturbations at transitions, as described in EQ. 45:

$$\sigma_{jitter}^2 \sim \Delta T^{\alpha} \quad with\, 1 \leq \alpha \leq 2 \qquad \text{EQ. 45}$$

In a log-log plot of the jitter standard deviation over the measured time delay ΔT, the uncorrelated jitter is more important for smaller ΔT, whereas correlated jitter is more significant for longer measurement time, due to their respective mathematical properties

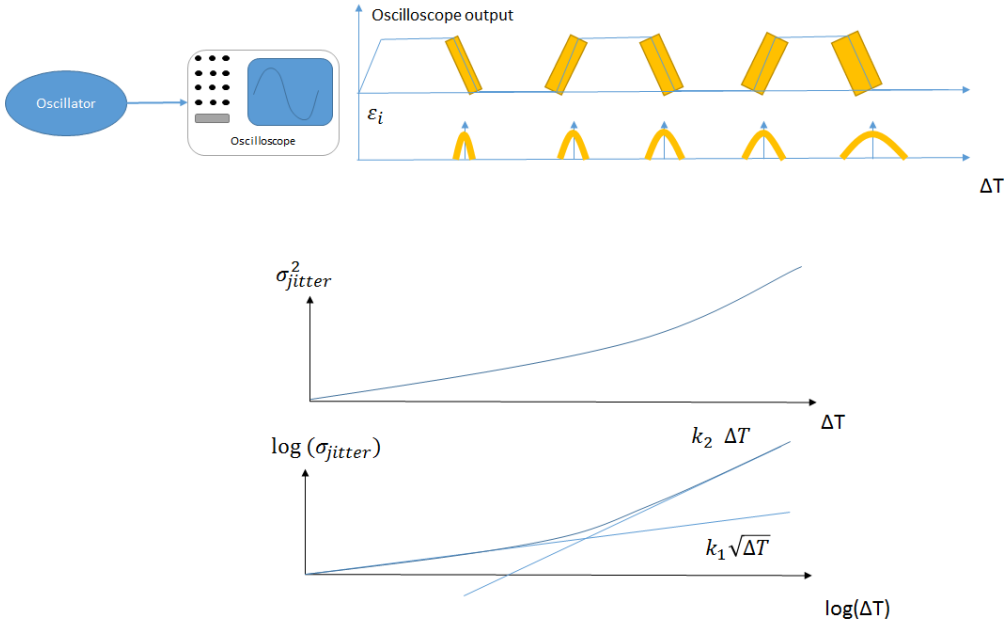

FIGURE 36 : JITTER MEASUREMENT IN A TIME INTERVAL (THIS FIGURE IS REDRAWN FROM [111])

2. Relation between jitter and phase noise

a) Jitter Accumulation process

The output of an oscillator perturbed by phase noise $\varphi(t)$ can be described by EQ. 46:

$$V_{out}(t) = A(t)\cos\big(2\pi f_0 t + \varphi(t)\big) \qquad \text{EQ. 46}$$

Phase noise $\varphi(t)$ can be further related to the frequency variations around f_0 called Δf as presented in EQ. 47[112]:

$$\forall\, t \in [0;T], \quad \varphi(t) = 2\pi \int_0^t \Delta f(t)dt \qquad \text{EQ. 47}$$

The Jitter Accumulation process (JAP) is defined by $JAP(t,\Delta T) = \varphi(t+\Delta T) - \varphi(t)$ which represents the phase perturbation associated with the time measured ΔT (the phase is accumulated due to jitter in the ΔT interval). The JAP is improperly named as it is a phase difference rather than a jitter. JAP is proportional to the measurement of the jitter in the [t; t + ΔT] interval, starting at any random time t. For a better comprehension, the JAP will be called $\Delta\varphi(\Delta T)$. JAP and the jitter can be related using EQ. 48, as it is the jitter which results in phase perturbation [113]:

$$JAP(t,\Delta T) = \varphi(t+\Delta T) - \varphi(t) = \omega_0\,(Jitter(t+\Delta T) - Jitter(t)) \qquad \text{EQ. 48}$$

From EQ. 48, the variances relation between phase perturbations and the jitter:

$$\sigma^2_{JAP(t,\Delta T)} = \sigma^2_{\Delta\varphi(\Delta T)} = \omega_0^2\sigma^2_{Jitter(\Delta T)} \qquad \text{EQ. 49}$$

It should be noted that in the particular case that t=0 and supposing that the initial jitter is null $(Jitter(0) = 0)$ as well as the initial signal phase noise ($\varphi(0)$ = 0), EQ. 48 reduces to:

$$JAP(\Delta T) = \varphi(\Delta T) = \omega_0\,(Jitter(\Delta T)) \qquad \text{EQ. 50}$$

Hence the relation between variance is further simplified as expressed in EQ. 51:

$$\sigma^2_{JAP(\Delta T)} = \sigma^2_{\varphi(\Delta T)} = \omega_0^2\sigma^2_{Jitter(\Delta T)} \qquad \text{EQ. 51}$$

Remembering that the phase noise variance is equal to the integral of the phase noise PSD as shown in Annex B.1, the timing jitter variance and its statistical properties are easily deduced from the phase noise PSD. This relation can be found in various documents [111, 112, 114], and is a good approximation of the timing jitter process statistical properties. However as the timing jitter value is critical for the application (restricting the PWM accuracy), a more precise conversion from phase noise to timing jitter is required.

b) Phase noise Power Spectral Density to timing jitter conversion

Several authors have proposed formulas to convert phase noise PSD into timing jitter with small discrepancies between them [115, 116]. Three of these formula will be developed as they can be simply implemented and they do not required strong mathematical background.

(1) Defining the JAP process with a LTI system

This discussion is further detailed in [113]. It can be shown in [113] that the JAP is a gaussian random process with zero mean and this process can be expressed as a convolution of a gaussian white noise with the impulse response of a Linear Time Variant (LTI) system called h(t) and developed in EQ. 52[113]:

$$h(t, \Delta T) = \delta(t + \Delta T) - \delta(t) \qquad \text{EQ. 52}$$

where δ(t) is the delta dirac function.

Using the Wiener Khintchine theorem presented in Annex B.1, an remembering that the gaussian white noise is a stationary process entering into a LTI system, the autocovariance of the JAP, named $R_{JJ}(\tau)$ is defined in EQ. 53[113]:

$$R_{JJ}(\tau) = \int_{-\infty}^{\infty} S_{\varphi}(f)|H(j2\pi f)|^2 \, e^{j2\pi f\tau} df \qquad \text{EQ. 53}$$

$$\rightarrow R_{JJ}(\tau) = 8\int_{0}^{\infty} S_{\varphi}(f) sin(\pi f \Delta T)^2 \cos(j2\pi f\tau) df$$

where $S_{\varphi}(f)$ is the PSD of the phase noise. The PSD of the phase noise has a $1/f^3$ behavior followed by a $1/f^2$ behavior as described in Section II. G. The PSD of $S_{\varphi 2}(f)$ which represents the $1/f^2$ phase noise contribution has shown in EQ. 54[113]:

$$S_{\varphi 2}(f) = \frac{K_2}{f^2 + \gamma_2^2} \qquad \text{EQ. 54}$$

where K_2 is the $1/f^2$ figure of merit and γ_2 the cutoff frequency [113]. In this case the autocorrelation of the JAP is defined by EQ. 55:

$$R_{J2J2}(\tau) \approx \begin{cases} 4K_2\pi^2\Delta T & if\ \tau = 0 \\ 0 & otherwise \end{cases} \qquad \text{EQ. 55}$$

For the $1/f^3$ noise portion, the PSD is expressed as:

$$S_{\varphi 3}(f) = \frac{K_3}{|f|^3 + \gamma_3^3} \quad \text{EQ. 56}$$

where similarly K_3 is the $1/f^3$ figure of merit and γ_3 the cutoff frequency [113]. The autocorrelation of the JAP for this noise portion is much more complex and only the value for $\tau = 0$ is of interest as the JAP variance is investigated, this value is developed in EQ. 57[113]:

$$R_{J3J3}(0) = -8K_3\pi^2\Delta T^2(\Lambda + \log(2\pi\gamma_3\Delta T)) \quad \text{EQ. 57}$$

where $\Lambda = \Gamma - 3/2$ where Γ is the Euler-Mascheroni constant and is equal to 0.5772 [113]. However as the variance cannot be negative, this relation is valid for $\Delta T < \frac{10^{0.5772}}{2\pi\gamma_3}$. Extracting the tangent of the $R_{J3J3}(0)$ formula permits to obtain the timing jitter for longer observation time.

Assuming that φ_2 and φ_3 are mutually independent the total autocorrelation of the JAP can be expressed as [113]:

$$R_{JJ}(\tau) = R_{J2J2}(\tau) + R_{J3J3}(\tau) \quad \text{EQ. 58}$$

The calculated variance of the JAP is hence proportional to the time measured ΔT or to its square value depending on the type of noise considered, justifying the results found in Section I.H.1.

(2) Standard deviation of the timing uncertainty computation from phase noise

The following discussion is greatly inspired by [111]. The variance of the timing jitter process can also be expressed by EQ. 59[111]:

$$\sigma^2_{\Delta\varphi(\Delta T)} = E[(\varphi(t + \Delta T) - \varphi(t))^2] \quad \text{EQ. 59}$$

$$\rightarrow \quad \sigma^2_{jitter(\Delta T)} = \frac{1}{\omega_0^2}E[(\varphi(t + \Delta T) - \varphi(t))^2]$$

$$\rightarrow \sigma^2_{jitter(\Delta T)} = \frac{1}{\omega_0^2}E\left[\left(\varphi(t)\right)^2\right] + \frac{1}{\omega_0^2}E\left[\left(\varphi(t + \Delta T)\right)^2\right] - \frac{2}{\omega_0^2}E[\varphi(t)\varphi(t + \Delta T)]$$

The autocorrelation function of $\varphi(t)$ is defined as:

$$R_{\varphi\varphi}(\tau) = E[\varphi(t)\varphi(t + \Delta T)] \quad \text{EQ. 60}$$

Using the above equation, the variance of the timing jitter process can be rewritten as [111]:

$$\sigma^2_{jitter(\Delta T)} = \frac{2}{\omega_0^2}\left[R_{\varphi\varphi}(0) - R_{\varphi\varphi}(\Delta T)\right] \quad \text{EQ. 61}$$

As detailed in [111], the relation between clock jitter and phase noise is expressed by EQ. 62:

$$\sigma^2_{jitter(\Delta T)} = \frac{8}{\omega_0^2}\int_0^{\infty} S_\varphi(f) sin(\pi f \tau)^2 \, df \qquad \text{EQ. 62}$$

Such mathematical description permits to obtain the variance of the jitter as developed in [111]. This result is almost similar to the result obtained with the JAP estimation using a LTI system as the mathematical development are very close.

In the particular case of a single white noise source, an expression of the phase noise variance can be computed as presented in [111], which is reminded in EQ. 63 (assuming that the observation time is much longer than the oscillator period or multiple of this period):

$$\sigma^2_{\Delta\varphi WN} = \frac{\Gamma_{rms}{}^2 \frac{{i_N}^2}{\Delta f}}{2\, qmax^2}\, \Delta T \qquad \text{EQ. 63}$$

where the various elements were defined extensively in Section II.G.3. This expression was computed with the help of EQ. 62 and eq. 32 and supposing that the input current was a white noise source. Changing the expression of the input current into a 1/f noise source and following the same methodology permits to obtain the value of $\sigma^2_{\Delta\varphi 1/f}$ for a single 1/f noise source [111], which is equal to:

$$\sigma^2_{\Delta\varphi 1/f} = \left(\frac{{i_N}^2}{\Delta f} * \omega_{\frac{1}{f}nmos} + \frac{{i_N}^2}{\Delta f} * \omega_{\frac{1}{f}pmos}\right) * \frac{c_0^2}{16\,\pi\, qmax^2}\Delta T^2 \qquad \text{EQ. 64}$$

where $\omega_{\frac{1}{f}nmos}$ and $\omega_{\frac{1}{f}pmos}$ are cutoff pulsations where 1/f noise is less important than white noise in nmos and pmos respectively. These parameters are dependent on the components utilized for the oscillator design and can be extracted running a noise analysis in Cadence®. They were found equal to 1.25e8 rad.s^{-1} and to 6.27e7rad.s^{-1} respectively. According to [117], these values can also be found theoretically.

(3) Timing jitter computation using the frequency noise

Remembering EQ. 47, which relates phase noise (φ) to frequency offset (Δf):

$$\forall\, t\ \in [0;T], \quad \varphi(t) = 2\pi \int_0^t \Delta f(t)dt \qquad \text{EQ. 65}$$

Assuming that the frequency offset is a random gaussian process [112], the variance of the phase deviation (σ_φ) can be computed from the autocorrelation of the frequency offset $R_{\Delta f \Delta f}$ as indicated in EQ. 66 [112]:

$$\sigma_\varphi^2(t) = 2.2\pi^2 \int_0^t R_{\Delta f \Delta f}(\tau)(t - \tau)d\tau \qquad \text{EQ. 66}$$

Considering the baseband signal as expressed in eq. 67, its relative spectrum is developed (the Wiener Khintchine theorem applies since the phase noise is supposed stationary in this demonstration), and its contribution to the spectrum output is expressed in EQ. 67 [112]:

$$V_{BB}(t) = \cos\big(\varphi(t)\big) \qquad \text{EQ. 67}$$

$$\rightarrow\ R_{vBBvBB}(t) = e^{\frac{-\sigma_\varphi^2(t)}{2}}$$

$$S_{vBB}(f) = 2\int_0^\infty e^{\frac{-\sigma_\varphi^2(t)}{2}} e^{j2\pi ft}\, dt$$

$$S_{Vout}(f) = \frac{1}{2}\left(S_{vBB}(f - f_0) + S_{vBB}(f + f_0)\right)$$

where f_0 is the oscillator central frequency and $\sigma_\varphi^2(t)$ the phase noise variance defined in EQ. 66

The phase perturbations due to white noise frequency modulation can be defined in term of jitter or phase noise PSD. The PSD of a white noise is expressed by EQ. 68, and as it is a stationary process, its relative autocorrelation function can be easily extracted (EQ. 68) [112]:

$$S_{Wn}(f) = Constante = C_1 \qquad \text{EQ. 68}$$

$$R_{WNWN}(t) = C_1\delta(t)$$

Using EQ. 66, as white noise is usually modeled with a gaussian distribution, the rms phase jitter can be computed [112]:

$$\sigma_{\varphi WN}(t) = \sqrt{2\, D_\varphi\ t} \qquad \text{EQ. 69}$$

with D_φ called the phase diffusion constant and is equal to [112]:

$$D_\varphi = 2\,\pi^2 C_1 \qquad \text{EQ. 70}$$

The baseband PSD is obtained inserting EQ. 69, into EQ. 67 [112], giving the Lorentzian describing the PSD of the phase noise perturbations as already discussed by various authors [118]:

$$S_{vBB}(f) = 2\int_0^\infty e^{\frac{-\sigma_{\varphi WN}^2(t)}{2}} e^{j2\pi ft}\, dt = \frac{2\, D_\varphi}{{D_\varphi}^2 + (2\pi f)^2} \qquad \text{EQ. 71}$$

When the frequency offset is caused by 1/f noise, the PSD of the offset is directly obtained using a constant called K, determining the strength of the modulation as developed in details in [112]. However it is important to note that the observation time ΔT is limited and any spectral components with frequency lower than the reciprocal frequency of the observation time cannot be distinguished from the DC components of the signal [112]. Hence the observed offset frequency noise PSD can be defined as [112]:

$$S_{\Delta f}\big|_{\Delta T} = \begin{cases} \frac{K}{|f|} & if \quad |f| > \frac{1}{\Delta T} \\ 0 & if \quad |f| < \frac{1}{\Delta T} \end{cases} \qquad \text{EQ. 72}$$

It should be noted than the random process associated with the $S_{\Delta f}\big|_{\Delta T}$ PSD also referred as band limited 1/f noise is a WSS process and hence its autocorrelation can be simply extracted as detailed accurately in [112]. The band-limited 1/f noise is of great value in converting phase noise into jitter, making the conversion easier as illustrated in Annex B.1.

Complete discussion from autocorrelation extraction of band-limited 1/f noise to phase noise variance and ending with phase noise PSD can be found in [112]. Only main results are reported in this Section, such as phase noise variance (EQ. 73) and phase noise PSD associated with band limited 1/f noise (EQ. 74):

$$\sigma_{\varphi 1/f}(t) \approx 2\pi\sqrt{K}\sqrt{1.85 + 2\ln(\frac{\Delta T}{2\pi t})}\, t \qquad \text{EQ. 73}$$

and

$$S_{VBB}(f) = \frac{S_{\Delta f}\big|_{\Delta T}}{f^2} = \frac{K}{|f^3|} \qquad \text{EQ. 74}$$

These results are close to the ones obtained using the JAP process with a LTI system description.

For large offset frequencies the phase noise PSD follows the white noise frequency modulation spectrum, for offset frequencies closer to 0, the phase noise PSD follows the power law defined with the band-limited 1/f noise frequency modulation. In similar ways, for small delay times, the jitter is mainly influenced by white noise frequency modulation and for longer delay times the opposite is true [112].

c) Concluding remarks on timing jitter estimation

The above presented methods, reviewed from existing literature are particularly straightforward to convert phase noise into timing jitter. This conversion helps to understand the phase noise effects in the transceiver transient model. It can be notified that for all the methodologies presented, timing jitter is assumed to be a gaussian process which variance is function of the observation time as indicated in EQ. 75:

$$\sigma_{\Delta T}^2 = c\,\Delta T + k\,\Delta T^2 \qquad \text{EQ. 75}$$

where c depends on the properties of the $\frac{1}{f^2}$ phase perturbations (maybe caused by a frequency modulation with white noise sources) and k is related to the properties of the $\frac{1}{f^3}$ phase perturbations (perhaps attributed to a frequency modulation with 1/f noise sources).

3. Timing jitter estimation for PWM accuracy deduction

The transmitter involves two oscillators, one directly associated with the PWM modulation (it resets the ramp signal) and the other one associated with the OOK modulation as discussed in Section I.B. Obviously the oscillator impacting the most the PWM signal is the one associated with the ramp resets although the 2.45GHz oscillator may also diminish the PWM precision. Two different methodologies will be utilized for the timing jitter computation of each oscillator to better illustrate the previous discussion. The timing jitter of each oscillators does not affect similarly the PWM accuracy and in each case the number of bits (N_{PWM}) reached by the PWM will be extracted and solutions will be introduced to increase it. Besides it should be reminded that the PWM accuracy is already limited to 8 bits from the Section I.C.6 development.

a) N_{PWM} restrictions associated with the first oscillator

This oscillator timing jitter estimation was performed defining a JAP process entering into a LTI system. The discussed oscillator has a central frequency of $20000 * (2^{N_{PWM}})$, and choosing N_{PWM} equal to 8 bits as starting value gives f_{osc1} = 5.12 MHz and a period around 19.5µs. Using the phase noise spectrum extracted with Cadence, the parameters $K_2, \gamma_2, K_3, \gamma_3$were extracted and depicted in *TABLE 1*.

TABLE 1: PARAMETERS USED FOR THE FIRST OSCILLATOR TIMING JITTER ESTIMATION

Parameters	Values
K_2	1110.12
γ_2 (Hz)	5.47e7
K_3	9.99e11
γ_3 (Hz)	9.6e5
c_1 (s)	9.55e-1
k_1	9.3e-4

The timing jitter associated with this oscillator can hence be expressed as:

$$\sigma_{\Delta T}^2 = \frac{1}{2\,\pi\, f_{osc1}^2}\,(\,c_1\,\Delta T + \,k_1 \Delta T^2\,) \qquad \text{EQ. 76}$$

$$\rightarrow \;\; \sigma_{\Delta T}^2 = \frac{1}{2\,\pi\,(20000 * (2^{\mathrm{N_{PWM}}}))^2}\,(\,c_1\,\Delta T + \,k_1 \Delta T^2\,)$$

where c_1 and k_1 are defined in *TABLE 1*. As indicated in EQ. 76, the timing jitter variance increases with the observation time and decreases when increasing the precision of the PWM. However this deduction is in this case (time modulation) erroneous as greater is the PWM number of bits (giving the PWM accuracy), lower is the time interval of the Least Significant Bit (LSB) which is equal to $\frac{1}{20000*(2^{\mathrm{N_{PWM}}})}$ and hence greater is the impact of the oscillator jitter. FIGURE 37 helps in understanding this concept as the oscillator is used to reset the ramp every 1/20e3 period. Greater is the jitter and greater are the ramp timing distortions, finally resulting in superposition of the PWM points. Besides if the observation time increases, the oscillator jitter variance increases resulting in comparable PWM signal disturbances. For a more graphical representation of the errors, every single combination of the PWM signal is associated with a particular place on the unity circle with equidistant space between points. The maximum number of bits that can be reached by the PWM signal depends greatly on the timing variance of the first oscillator which is function of the observation time. For observation times around 0.1ms, the maximum accuracy of the PWM is 4 bits.

Introduction of a Phase Lock Loop (PLL) [119] or lowering the phase noise of this oscillator by improved electronic design, is compulsory as the device should function for several hours.

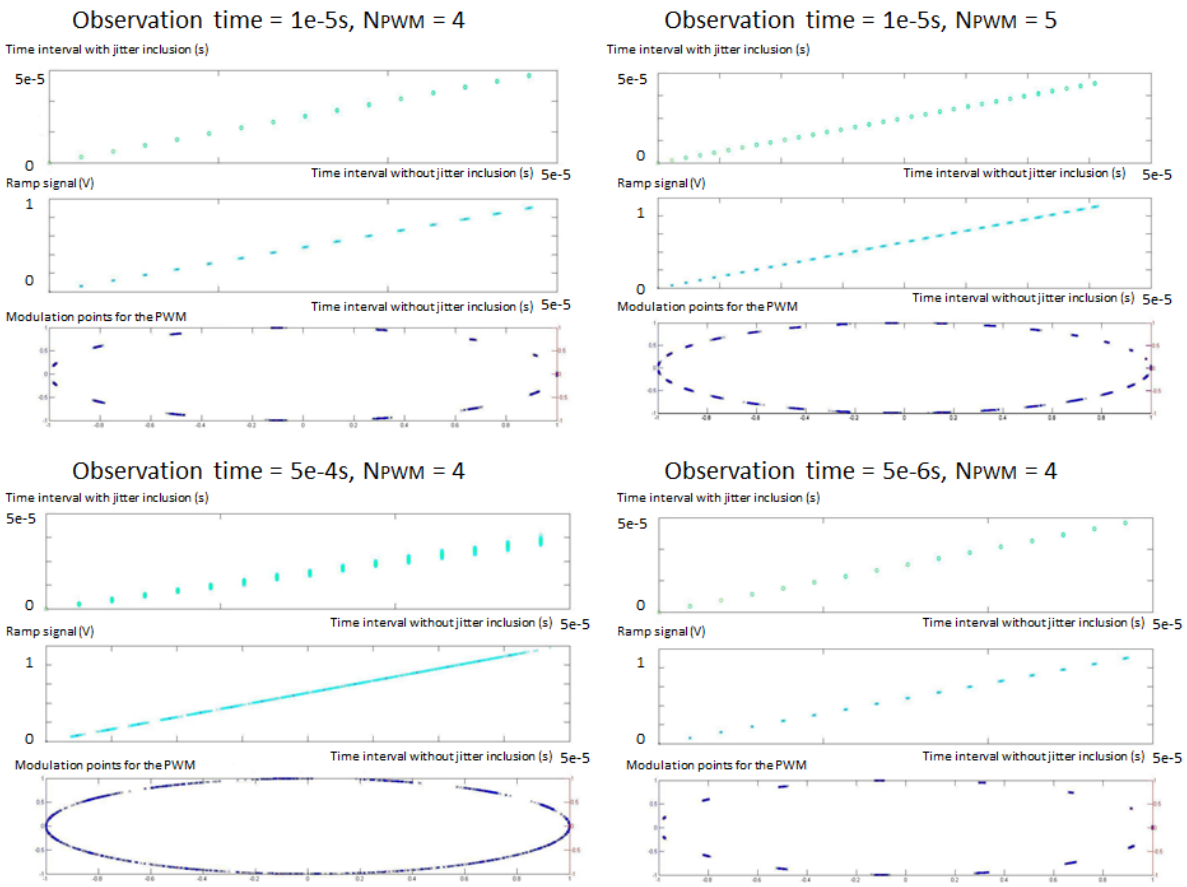

FIGURE 37: PWM ACCURACY IS ASSOCIATED WITH THE TIMING JITTER OF THE FIRST OSCILLATOR WHICH STATISTICAL PROPERTIES ARE ASSOCIATED WITH THE NUMBER OF BITS CHOOSEN AND WITH THE OBSERVATION TIME DURATION

b) PWM restrictions associated with the 2.45GHz oscillator

The 2.45GHz oscillator is associated with the OOK modulation and is not directly connected to the PWM signal creation. In consequence the impact of its jitter on the PWM signal characteristics will be studied in a more conventional manner. The theory used to compute the standard deviation of the timing uncertainty from phase noise is the one developed by Hajimiri and Limotyrakis and has been reviewed in Section II.H.2.b)(2), since several involved parameters have been already computed in Section II.G.

Following the methodology of Section II.H.2.b)(2), the ISF computation from phase noise spectrum and the white noise PSD estimation leads to the timing jitter:

$$\sigma_{\Delta T}^2 = \frac{1}{2\,\pi\,f_{osc2}^2}\,(\,c_2\,\Delta T + \,k_2 \Delta T^2\,) \qquad \text{EQ. 77}$$

where c_2 was equal to 1.13e10s, k_2 was equal to 4.19e3 and f_{osc2} to 2.45GHz.

As already discussed in Section II.H.1, timing jitter is considered as a gaussian process with zero mean and variance $\sigma_{\Delta T}^2$. Furthermore the empirical 3-sigma rule applied in gaussian process states that for a zero mean gaussian process the probability that the process is in the -3 * standard deviations to 3 * standard deviations interval is 99.7%. In consequence the maximum value of ΔT (ΔT_{max}) can be extracted from eq. 78, in order to obtain a standard deviation equal to half of the LSB signal period divided by 3.

$$\sqrt{\sigma_{\Delta T}^2} = \sqrt{\frac{1}{2\,\pi\, f_{osc}^2}\,(\,c_2 \Delta T_{max} + k_2 \Delta T_{max}^2)} = \frac{1}{2 * 3 * 20000 * (2^{N_{PWM}})} \qquad \text{EQ. 78}$$

ΔT_{max} was found approximately equal to 2.25e-5s.This value is inferior to the PWM total period which is $\frac{1}{20000}$ s, and because it is an OOK modulation (the oscillator is on the OFF state when the PWM signal is null, according to the electrical architecture defined in Section I.B), the influence of this high frequency oscillator on the PWM signal is negligible.

I. Closure remarks

To ensure reduced power consumption and low noise introduction, the receiver frontend architecture made of a LNA, a mixer and a low pass filter was retained. We created behavioral models of the blocks composing this RF frontend architecture and concatenated them with the behavioral models of the transmitter and the propagation channel in the Matlab/Simulink® environment. Among the numerous parameters that we varied in order to determine critical blocks, the ones impacting the most the signal integrity were the preamplifier gain, the comparator offset and the LNA gain. Furthermore, a significant reduction of the antenna gain or an inconsistency in propagation channel attenuation estimation may corrupt very deeply the transceiver output.

Phase noise was studied independently as related signal corruption cannot be removed by other blocks tuning. Phase noise study is statistical and its conversion to timing jitter was required for its inclusion in the transient models created. We further simplified this study and applied it to two different oscillators topologies (ring- and LC tank-oscillators).Based on the oscillator timing jitter inclusion in the PWM process, we found that timing jitter had a huge impact on the PWM signal accuracy leading to a maximal PWM resolution of4bits for an observation time of 0.5ms instead of the initial 8 bits at 20kHz in the noiseless case presented in Chapter 1. Hence the inclusion of PLL

architecture is required for the low frequency oscillator to diminish such jitter perturbations on the PWM signal and also possibly for 2.45 GHz oscillator to respect ISM frequency band specifications.

J. Work published

- Comparison of receiver architecture in terms of power consumption and Noise Figure for cochlear implants application, U. Cerasani, W. Tatinian, P. Ndungidi, F. Dualibe, C. Valderrama, ICONS, February 2014, Nice (FRANCE)
- Implementation of phase noise theories for transient simulations, U. Cerasani, W. Tatinian, Forum SAME, October 2012, Sophia Antipolis (FRANCE)

K. Work submitted

- Rapid phase noise simulation for diverses oscillator topologies, based on simplification of Hajimiri and Lee phase noise description,U. Cerasani, W. Tatinian, Y. Vaiarello, IEEE Electronics Letters, 2014

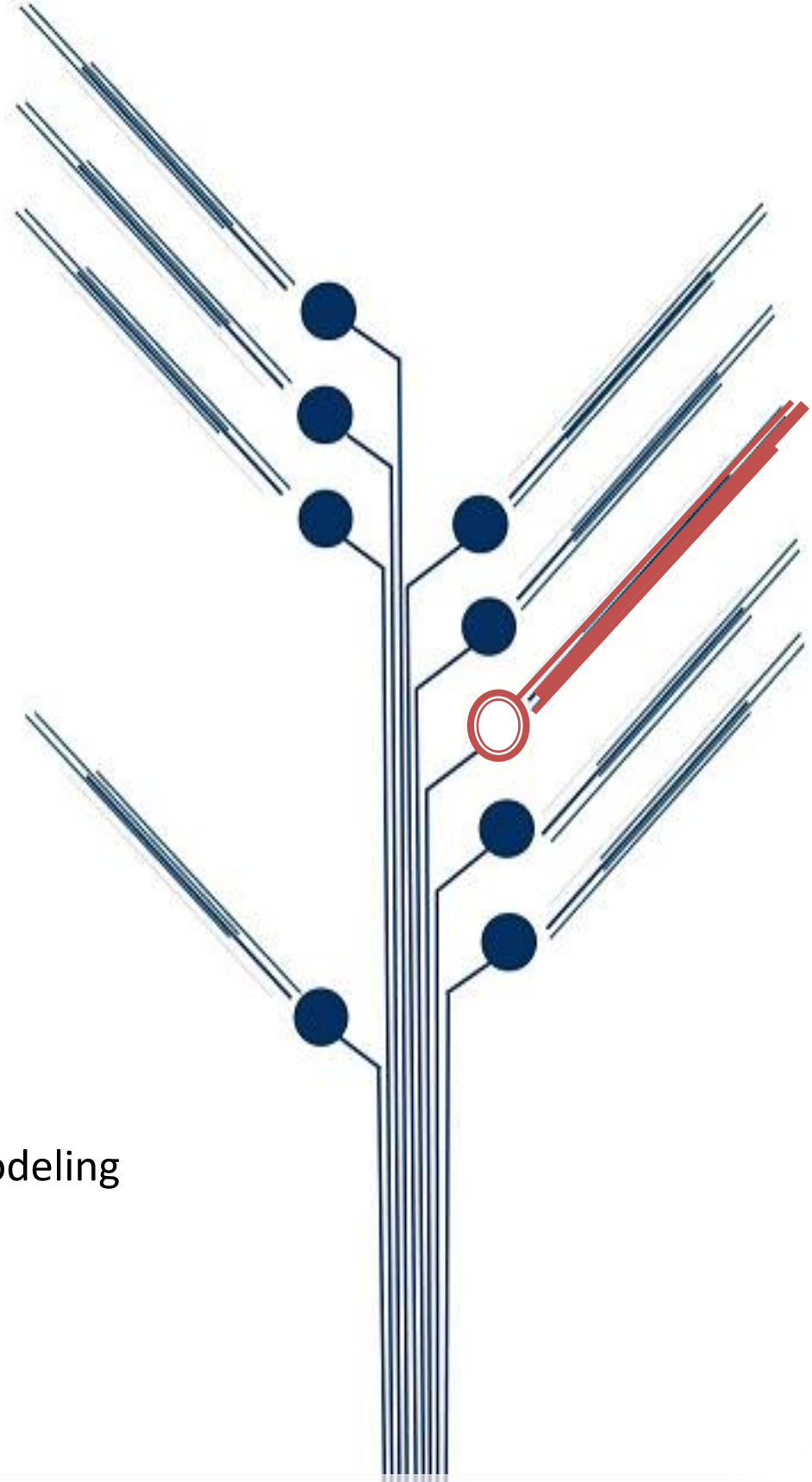

Chapter III:

Healthy cochlea modeling

A. Opening notifications

This chapter aims to provide theoretical basis of the hearing process from sound wave reception in the external ear to nerve fibers stimulation inside the cochlea. The models we developed are mainly mathematical, mechanical and electrical in order to embrace the overall system. We gathered current literature physical description of various parts of hearing process and proposed an overall heterogeneous description of this process. To render this model compatible with the ones developed in the previous chapters, we favored mathematical and electrical like description (e.g. organ of Corti electro-mechanical equivalent model we adapted from anatomical description).

As some hearing mechanisms are still under study and not fully understood yet, many theories compete to describe the various parts of the hearing process. The author's choice for model implementation was based on the most quoted theories.

This modeling work is necessary to understand advantages and limitations of cochlear implants and provide new considerations for possible device improvements.

B. Introduction to hearing process

The ear is a receptive organ: it translates physical pressure changes into a perceptual experience [120]. The ear contains three functional parts: the outer ear which captures sound waves, the middle ear which avoids energy loss in the sound wave conversion into a wave propagating inside a liquid (the perilymph) and the inner ear which transforms the wave into an electrical signal allowing brain interpretation. Other functions associated with the different parts of the ear are further described in [121, 122]and are not presented in this document.

Hearing perception and sound recognition are performed by the brain which interprets the electrical signals sent by the Hair Cells (HC), once a sound wave excites the tympani (further details are provided in Section III.D). Superior olive, Inferior coliculus, medial geniculate nucleus, auditory cortex may play a role in sound perception, localization and interpretation (as shown in Figure 38) although little is known about their role [120, 123]. More details are available in [124]about sensory pathways in the central nervous system.

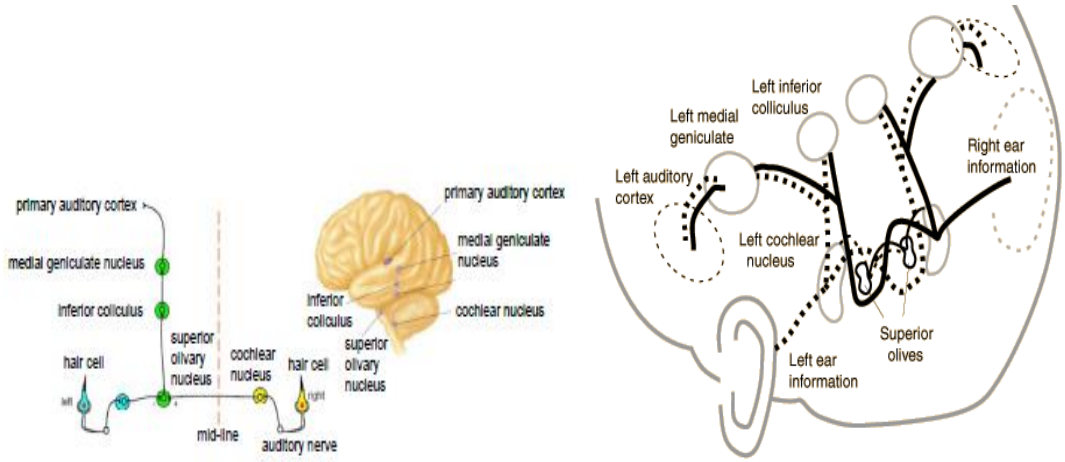

FIGURE 38: BRAIN INVOLVED CENTERS FOR HEARING PROCESSING (ATTRIBUTED TO[120, 123])

The hearing process is hence very complex, involving many organs and is nowadays partly understood. The physiological description of the three parts of the ear is reminded in Figure 39 and Figure 40.

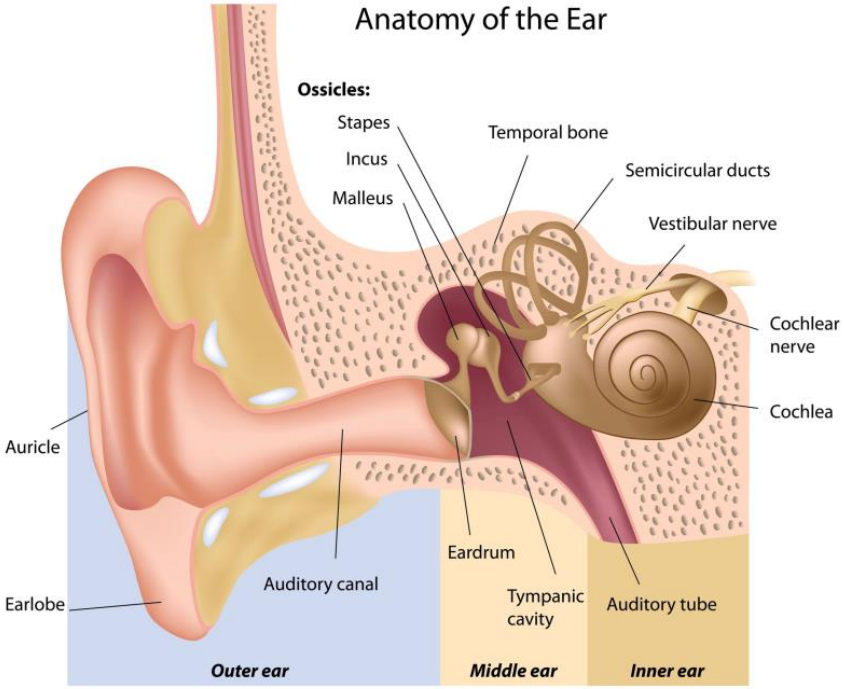

FIGURE 39: EAR DESCRIPTION (EXTRACTED FROM [125])

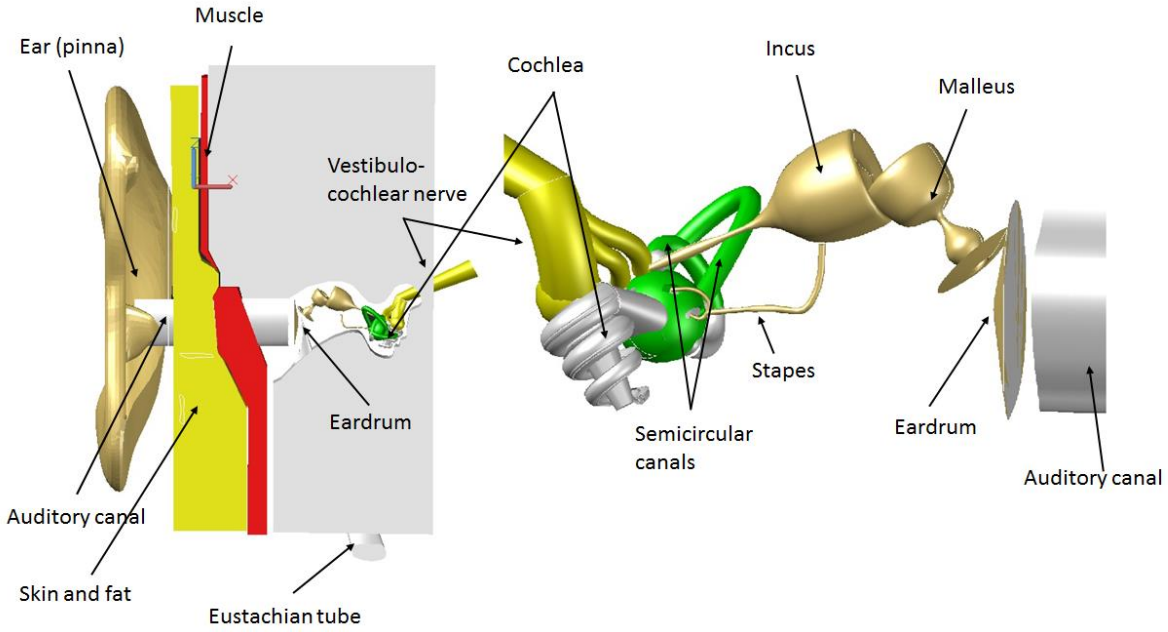

FIGURE 40: EAR STRUCTURE MODELED WITH AUTOCAD®

C. Middle air impedance matching

The external ear is not discussed or modeled in this document. We discarded the study of the pinna contribution to sound localization as well as the frequency filtering and resonance associated with the ear canal.

When an acoustic wave traveling inside the outer ear canal strikes the eardrum, the ossicles located inside the middle ear then amplify the sound intensity. This is achieved by producing a lever effect. The last ossicle (stirrup) hits the oval window of the cochlea. The fluid (perilymph) inside the scala vestibuli of the cochlea provides support for mechanical waves propagation. The amplification provided by the ossicles aims to correct the loss of energy associated with the impedance change at the air to liquid interface [126] (Figure 39).

Figure 41 [127] shows the physical schematic associated with the middle ear. When the sound wave hits the eardrum, there is an amplification of 26 dB explained by the difference in area of the eardrum which is 15 times the one of the oval window, as explained by eq. 79 [127]

$$\frac{P_2}{P_1} = \frac{A_2}{A_1} * \frac{L_2}{L_1} \approx 26db \qquad \text{EQ. 79}$$

where P_1 is the power associated with the sound wave and P_2 the power of the mechanical wave transmitted by the stirrup. A_1 is the area of the eardum and A_2 is the area of the oval window. L_1 and L_2 represent the distances indicated in Figure 41.

However because of the impedance mismatch in the oval window interface (the mechanical wave is converted into a wave propagating inside a liquid, as the scala vestibuli of the cochlea is filled with a lymphatic type solution), the transmitted power from the mechanical wave into the liquid wave is reduced by 29db as expressed by the power transmission coefficient [127]

$$\tau = \frac{4 * Z_{air} * Z_{fluid}}{(Z_{air} + Z_{fluid})^2} \approx -29db \qquad \text{EQ. 80}$$

where Z_{air} is the impedance of the air and the Z_{fluid} is the impedance of the liquid inside the scala vestibuli. As demonstrated by various authors [128, 129], the main function of the ossicles in the middle ear is to reduce the power loss due to the impedance mismatch.

For the following parts, we considered that the wave power at the oval window interface is equal to the power of the air wave.

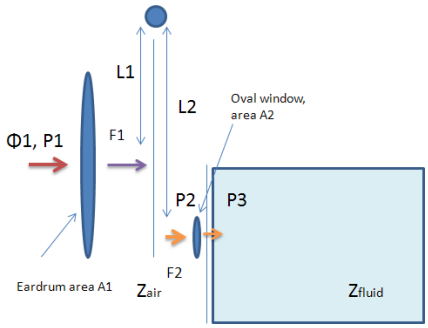

FIGURE 41: MIDDLE EAR SCHEMATIC, Φ1 IS THE SOUND WAVE HITTING THE EARDRUM AND P1, P2, P3 ARE THE ASSOCIATED POWER (EXTRACTED FROM [127])

D. Wave propagation theories inside the cochlea

The theory of hearing attempts to explain the physical transformation of the sound wave leading to nerve fiber stimulation. Four major hearing theories will be described in this document and further precisions are available in [130]. The hearing theories may be divided into place coding theories and temporal coding theories

- Place coding theories:
    - Resonant theory: Helmholtz proposed that the cochlea was composed of segments with diverse degree of tension based on their position inside the cochlea. The

segments were responsive only to certain frequencies and the cochlea was acting as an harp where only one string was vibrating depending on the sound wave frequency.

- The above theory was demonstrated inexact by Von Bekesy who proposed the traveling wave theory. In fact the Basilar Membrane(BM) is not under radial tension, the energy of the wave traveling inside the perilymph is taken up by the BM resulting in its vibration [131].

- Temporal coding theories:
  - The telephone theory assumes that the BM entirely and singularly vibrates when stimulated by a sound and further decoding is performed in the brain. However as nerve fibers can fire only once per millisecond, it would not be possible to perceive sounds with a frequency above 1000Hz. Another problem with this theory is that a damaged cochlea may respond to certain frequencies [132].
  - The volley theory: This model was based on the telephone theory and aimed to explain the frequency perception above 1000Hz. In this theory, the nerve fibers of the BM respond to a BM variation with different time delays and when these delays are combined, a greater frequency of sound can be sent to the brain.

The BM motions in response to acoustic signals in the resonance theory and telephone theory were all shown conceivable (depending on the BM elasticity and on the part of the cochlea) and incorporated into a same physical model (traveling wave theory) by Von Bekesy [133].

E. Traveling wave theory model implementation

The cochlea is the central structure of the inner ear. It works by converting a wave propagating inside the perilymph into nerves stimulation using the complex organ of Corti structure. Inside the cochlea, the Hair Cells (HC) are stimulated by the basilar membrane vibrations and release chemical messengers which excite nerve cells (more details are available in Section III.G).

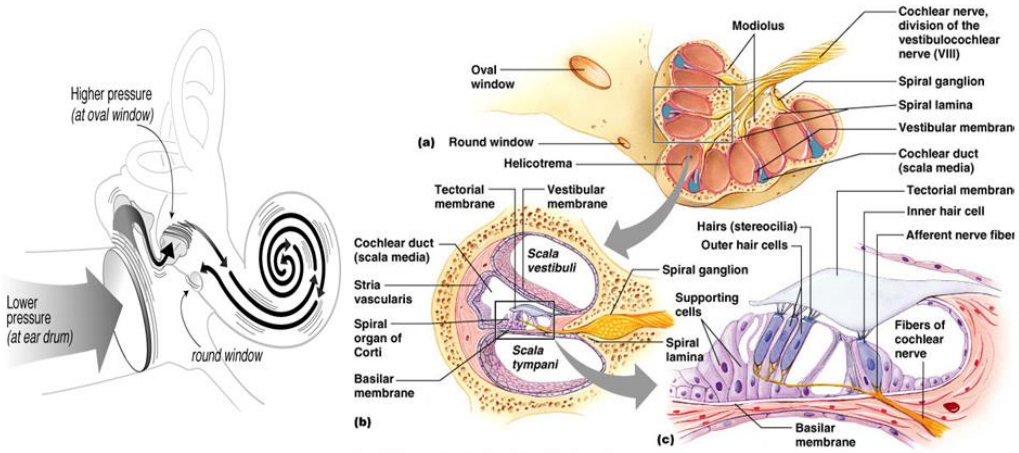

FIGURE 42: BASIC PROPAGATION OF THE MECHANICAL WAVE INSIDE THE MIDDLE EAR (LEFT). ANATOMY OF THE COCHLEA (RIGHT). THE FIGURES ARE ATTRIBUTED TO [134]

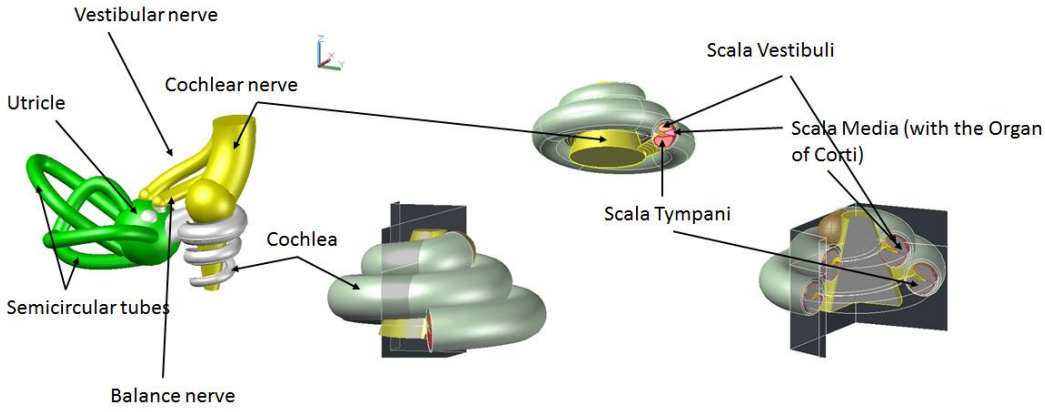

FIGURE 43: COCHLEA STRUCTURE MODELED WITH AUTOCAD®

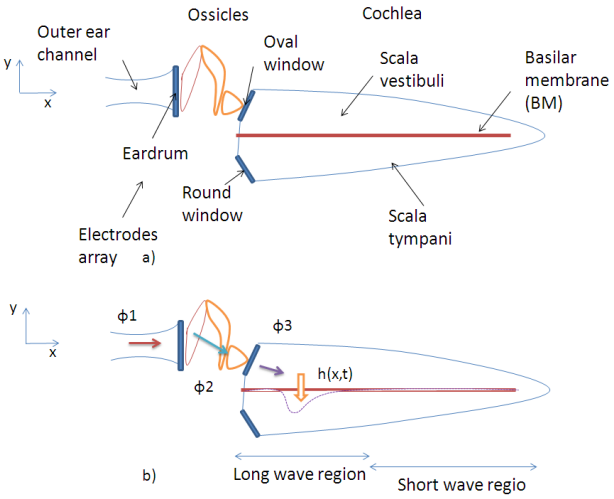

FIGURE 44.A) EAR SCHEMATIC WITH INCLUSION OF THE ELECTRODES ARRAY INSIDE THE COCHLEA. B) EAR SCHEMATIC AND THE WAVE PROPAGATION LEADING TO A BASILAR MEMBRANE HEIGHT CHANGE (H(X,T))

According to biophysical theories [135, 136] when a mechanical wave propagates inside the cochlea, the BM distorts to absorb the wave energy. In consequence the height (denoted as h(x,t) in the following parts) of the BM excitement mainly depends on the sound intensity as well as the position along the $\overrightarrow{\mathrm{Ox}}$ axis (that we called x which is the distance from base of the cochlea). In fact the cochlea has different mechanical properties (different stiffness and mass) changing with the distance from the base and hence the mechanical wave makes vibrating only a precise area of the cochlea depending on the wave frequency. The width (denoted as W(x)) of the BM excitement around the resonance greatly depends on the distance from the cochlea base (called x). As the number of excited HC depends on W(x) the number of auditory fibers excited is hence associated with the width of BM vibration (more information are provided in Section III.C) .

The cited wave propagation theory is quickly reviewed in this section for a better understanding of the biophysics of hearing and for determining the characteristics of the BM resonance in terms of amplitude and width. This theory and the computations are extracted from [137]and[127], the main results are recalled here for the reader's convenience.

Suppose a sound wave ϕ_1 with the mathematical description given by eq. 81

$$\varphi_1 = A_1 exp^{i(k1*x-\omega*t)} \qquad \text{EQ. } 81$$

where A_1 is the sound amplitude, k_1 is the wave number and ω is the pulsation. The wave is supposed propagating in the x direction.

This sound wave then results in a wave propagating inside the scala vestibuli (called ϕ_3) and its general form is extracted from [137]:

$$\varphi 3 = \frac{A_3}{2} * [exp^{(i(k*conj(z)-\omega*t))} + exp^{(i(k*z-\omega*t))} + exp^{(-i(conj(k)*z-\omega*t))} + exp^{(-i(conj(k)*conj(z)-\omega*t))}] \qquad \text{EQ. } 82$$

where A_3 is the amplitude of the liquid wave, k is the wave number and z the complex variable: z = x +iy. The *conj* operator represents the conjugate function. ϕ_3 is not collinear with x but propagates inside the 2 directions. The eq. 82is simplified in [137] into two equations: one for the long wave region (where the wavelength is long compared to the duct height, which is the region near the base of the cochlea) and one for the short wave region (where the wavelength is similar to the duct height). It is indicated in [137] that only in the short wave region, the propagation loss becomes significant. However as we considered that the losses are still important in the long wave region, we chose to only apply the short wave region equation for the entire cochlea (eq. 83):

$$\varphi_3 = A_3 * exp^{(k_r y - k_i x)} * \cos(k_r x + k_i y - \omega t) \quad \text{EQ. 83}$$

where $k = k_r + ik_i$ is the wavenumber. Applying the Newton formula inside the cochlea and discarding the basilar membrane mass and the cochlea tension gives the value of $k_r$and k_i which depends on the distance x (the complete description is performed in[137]).

Mathematical equations developed in[137] lead to the following relation between membrane height displacement (called h(x,t)) and auditory wave:

$$\frac{\partial h(x,t)}{\partial t} = -\frac{\partial \varphi_3(x,y,t)}{\partial y} \quad \text{EQ. 84}$$

Solving this equation permits to obtain the BMheight displacement (h(x,t)). We use the software *Maple®* to implement the BM height displacement for a sound wave with a frequency of 600Hz (Figure 45):

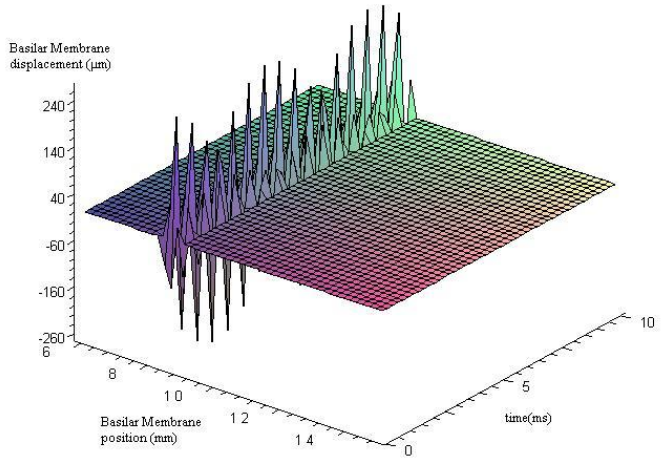

FIGURE 45: BASILAR MEMBRANE DISPLACEMENT (NM) WITH RESPECT OF THE DISTANCE FROM THE COCHLEA BASE (X IN µM) AND TIME (MS) FOR A 600HZ INPUT ACOUSTIC WAVE

One can observe that the BM displacement is a function of the distance from the cochlea base and the amplitude of the auditory wave.

The width of the BM displacement greatly depends on the position x as shown inFigure 46. The detection of a BM displacement permits to obtain the width of this excitement:

$$W(t) = \int_{X_W} h(x,t)dx \quad \text{EQ. 85}$$

$$with\ X_W = \{x \mid abs(h(x,t) \geq threshold\}$$

The BM movement compresses the organ of Corti resulting in a membrane potential variation in the corresponding auditory fiber. If this potential variation is greater than a threshold voltage around 30mV[138], the nerve fiber is excited. We implemented the mechanical model of the organ of Corti found in [139]and more details are provided in Section III.G as well as the threshold value definition.

Extraction of the width W for acoustic waves of different frequencies varying from 60Hz to 20kHz (hence resulting in different place of excitation of the BM) is shown in Figure 46.

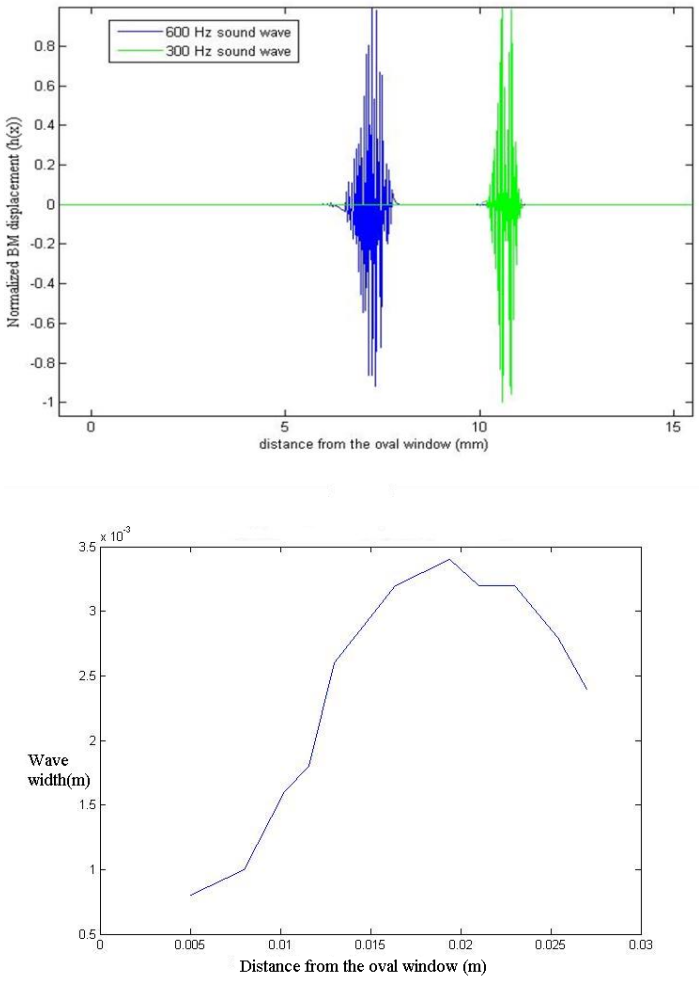

FIGURE 46.A: COMPARISON OF A BASILAR MEMBRANE EXCITATION BY A 600HZ SOUND WAVE AND BY A 300HZ SOUND WAVE WHICH MAKE THE BM TO RESONATE AT DIFFERENT PLACES(X) WITH DIFFERENT BASILAR MEMBRAN EEXCITATION WIDTH (W). B: REPETITION SIMILAR EXPERIMENT USING THE SAME MATHEMATICAL MODEL FOR DIVERSE FREQUENCIES GIVES THE FUNCTION W(X)

The relation between the distance from the oval windows where the BM displacement is maximal and the frequency of the acoustic wave is given by repetition of the experiment for sound input wave frequencies covering all the human frequency hearing range. This experiment was

carried out and is not shown in this document as it gives close results with the Greenwood function. Because the Greenwood function [140] verified by physical experiments [141], it was used thereafter in the document to express the distance x where h(x) is maximal in function of the soundwave frequency, rather than using the obtained function.

F. Biophysical limits of human hearing

The wave traveling inside the cochlea has a speed of about 12 m/s at the basal (high frequency) end and slows to about 2 m/s at the apical (low frequency) end [37]. The human cochlea measures around 35mm. To reach the apical end, the wave inside the cochlea makes 17.5ms as expressed by eq. 86

$$t_{SC} = \frac{Cochlea\ position}{Velocity\ of\ the\ wave\ at\ this\ position} \qquad \text{EQ. } 86$$

where t_{SC} is the time needed for BM stimulation depending on the wave velocity traveling inside the cochlea.

After 17.5 ms, the apical end of the BM (for low frequency) vibrates if properly stimulated. This BM vibration phenomenon resulting of wave excitation has a frequency of 57.14Hz. This frequency value is very close to the human hearing lowest frequency capability. Similarly if we suppose that the Hair Cells (HC) distribution starts very close to the basal end of the cochlea (for instance 0.5mm)[142], the time needed for the BM to oscillate at the basal end is around 0.03ms which corresponds to a frequency of 30kHz (close to the human maximum hearing frequency capability). This new correlation between BM variations and the wave velocity inside the cochlea may explain the human hearing interval frequency. It may further indicate that the frequency sensitivity of the cochlea is mostly dependent on cochlea physical properties (such as stiffness or width for example) variations along its distance and that the BM vibration time is close to Action Potential (AP) time interval. This could also indicate why different mammal species can hear at lower frequency (because of a propagating wave with reduced velocity or because of an increase length of their cochlea for instance) and bring new insights on why some mammals species can hear ultrasounds (higher velocity wave propagation inside their cochlea, maybe because of different BM physical characteristics or different perilymph composition for instance).

Furthermore in very loud environment the Inter Spike Delay (ISD), which is the time delay between two consecutive APs, lowers (it could reach 5ms) and this result in incapacity to properly process low frequency sounds (as the time needed for the BM excitement is around 17ms).

G. Modeling the organ of Corti structure

According to biophysical theories [143, 144]when a mechanical wave propagates inside the cochlea, the BM distorts to absorb the wave energy, resulting in a height variation of the BM which compresses the organ of Corti. As shown in Figure 48, the organ of Corti is composed of Hair Cells (HC) (Outer Hair Cells (OHC) and Inner Hair Cells (IHC)), which have stereocilia at their end. When BM vibrates, stereocilia position changes allowing potassium channels to open [138, 145]. Opening of the potassium channels creates the depolarization of the HC allowing complex mechanisms to take place (reviewed in [132, 146, 147]), and finally, resulting in neurotransmitter released in the synapse. Once released, these neurotransmitters travel to the post synaptic cell (the nerve fiber) and creates the depolarization of the nerve fiber. This depolarization, if sufficiently important, generates an Action Potential (AP) running through the nerve cell membrane [148, 149] (cf. Figure 48).

Various mechanical models have been presented for the organ of Corti structure [45], [150], [151], [152], [153] as well as for the stereocilia displacement [154-157]

Besides physiological studies aiming to explain the HC membrane potential variations with the stereocilia displacement, following the BM motion are available with a general agreement about the mechanisms involved. Studies found in [152, 158, 159] are based on OHC experiments and relate OHC membrane potential variations in function of the stereocilia angle.

The synapse is still an extended area of research, aiming to understand the phenomenal brain complexity. Numerous postsynaptic receptors, neurotransmitters, reuptake mechanisms as well as more complex effects such as Long Term Potentiation (LTP), are still under study and several new molecules are produced each year by the pharmaceutical industry targeting these proteins. Synapses are separating hair cells with afferent nerve cells. The anatomical description of afferent nerve cells and their HC connections can be found in [142, 160]. To the author's knowledge, no

study are indicating the precise HC depolarization value needed or the number of HCs required to stimulate an afferent nerve cell response (an action potential generation).

This Section may partially fill the modeling gap between the presented models, connecting the BM displacement with the afferent nerve cells stimulation and developing each step of the theoretical solutions. The models were mainly mathematical and the softwares used were Matlab®, Maple® and a SPICE simulator.

1. Organ of Corti mechanical model

The organ of Corti is a structure found only in mammals which responds to fluid vibrations of the cochlea [39]. Organ of Corti is mainly composed by the BM, Deiters cells which support Outer Hair Cells (OHC) and Inner Hair Cells (IHC). The two hair cells type have hair like structure at their top, called stereocilia. Above them the Tectorial Membrane (TM) extents parallel to the BM [41, 43].

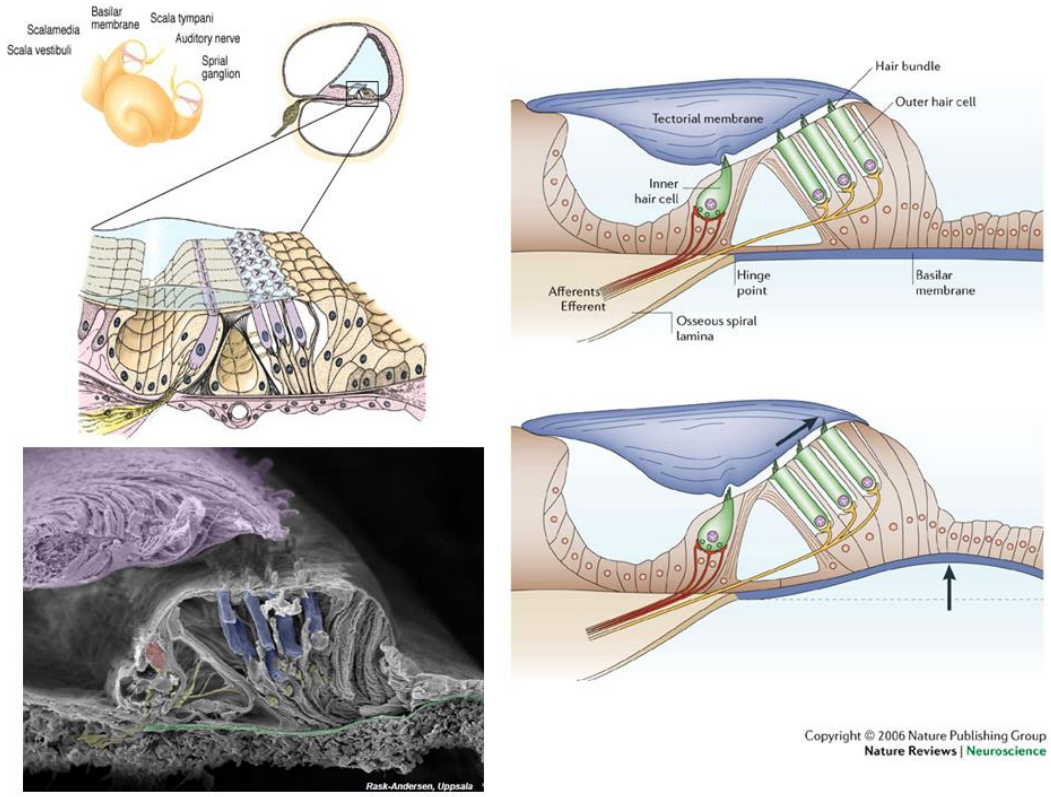

FIGURE 47: INNER EAR STRUCTURE (LEFT) AND ORGAN OF CORTI DISPLACEMENT DUE TO BASILAR MEMBRANE VIBRATION. THE FIGURES ARE ATTRIBUTED TO [134], [15] AND [161]

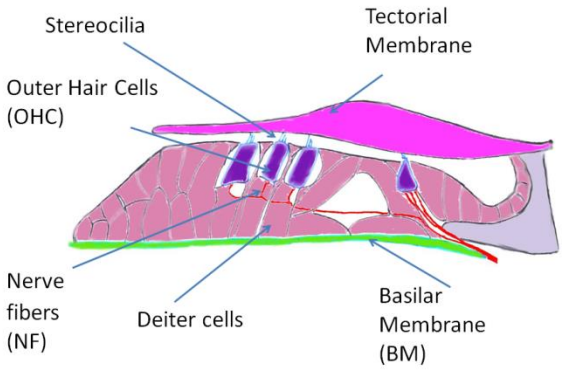

FIGURE 48: ORGAN OF CORTI

Diverse mechanical models of the organ of Corti are available in the literature [45], [150], [151], [152], [153]. However the precise mechanical and mathematical description has yet to be fully defined. As experiments [162] in radial shearing motion are limited (they aim to link the BM movement with the TM longitudinal and radial angle), we hence supposed that the TM was fixed. Furthermore the TM variations also depend on the Reissner's membrane variations and hence BM displacement cannot fully define the TM radial and longitudinal displacement. To the author's knowledge, this phenomenon is nowadays poorly described in literature.

The mechanical equivalent of the organ of Corti we proposed is shown in Figure 49:

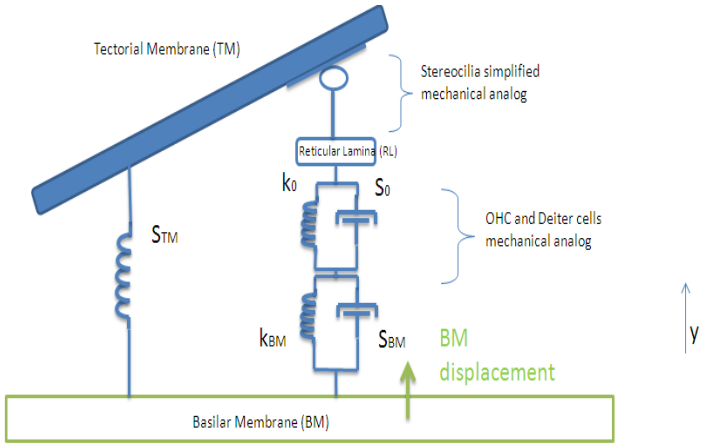

FIGURE 49: MECHANICAL ANALOG OF THE ORGAN OF CORTI (ONE DIMENSIONAL ANALOG)

This mechanical equivalent is simplified as it only takes into account the vertical movement (along the y direction in Figure 49). It is hence a 1 dimension mechanical model, where k_0 represents

the spring coefficients of the OHC and Deiters cells, k_{BM} the spring coefficient of the BM, RL is the reticular lamina, S_{TM} is the TM damping coefficient, S_0 is the OHC and Deiters cells damping coefficient and S_{BM} is the BM damping coefficient. The boxes represent masses. The values of k_0, k_{BM}, S_0 and S_{BM} are extracted from [163] as well as the mass values of the BM and RL. The damping coefficients were extracted from [164] and all these values are recalled in Table 6 for reader's convenience.

TABLE 6: MECHANICAL MODEL COEFFICIENTS EXTRACTED FROM [165] AND FROM [164]. IT SHOULD BE SPECIFIED THAT THE VARIATIONS OF THE COEFFICIENT WITH THE COCHLEA POSITION ARE OFTEN NONLINEAR.

Values obtained per 10µm radial section	Base	Apex
Basilar Membrane mass (g)	2.76e-9	14.2e-9
Basilar Membrane static compliance (k_{BM}) (N/m)	10e-10	10e-14
Basilar Membrane friction coefficient (S_{BM}) (N.s/m^{-1})	150e-9	150e-9
Reticular Lamina mass (g)	0.74e-9	36.1e-9
Reticular Lamina static compliance (N/m)	4.18	0.147

As explained above, we supposed S_{TM} very low and because the force applied to the stereocilia cannot move the TM (mass of TM >> mass of the stereocilia), we neglected S_{TM} and we supposed that TM was not moving. Hence the mechanical analog of the organ of Corti (presented in Figure 49) became the one presented in Figure 50:

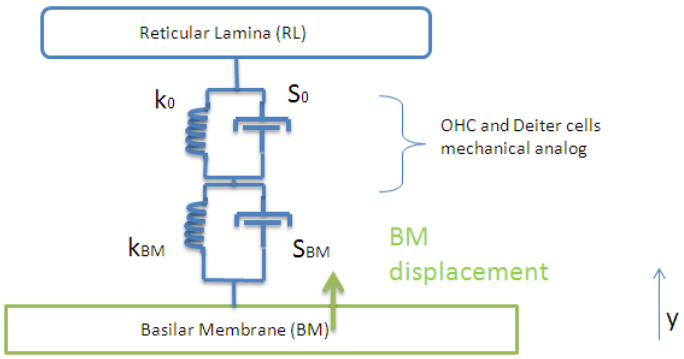

FIGURE 50: SIMPLIFIED MECHANICAL ANALOG OF THE ORGAN OF CORTI

This mechanical model is very similar to the one that can be found in [153]. Using the mechanical electrical analogy in [166], we modeled the force applied to the RL mass as the current going through the capacitor in Figure 51.

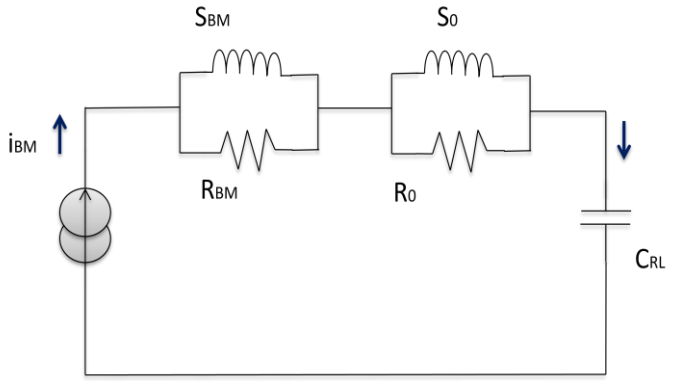

FIGURE 51: ELECTRICAL ANALOG OF THE SIMPLIFIED MECHANICAL MODEL REPRESENTING THE ORGAN OF CORTI TO ALLOW EXTENDED SIMULATIONS WITH ELECTRONIC ADVANCED DESIGN (EAD) TOOLS

In the analogy used, currents represent forces, inductors are equivalent to compliance ($^1/_k$), resistances are equivalent to lubricity ($^1/_S$) and masses are equivalent to capacitors.

As $i_{BM} = i_c$ that means that the force applied perpendicular to the BM is equal to the one applied perpendicular to the RL.

Furthermore the ratio between the BM mass (m_{BM}) and the RL mass (m_{RL}) varies between $\frac{1}{3}$ at the base and around 2 at the apex [165]. Hence the ratio between the BM acceleration ($\frac{\partial^2 y_{BM}}{\partial t^2}$) and the RL acceleration makes similar variation ($\frac{\partial^2 y_{RL}}{\partial t^2}$) as expressed in eq. 87

$$m_{BM}\frac{\partial^2 y_{BM}}{\partial t^2} = m_{RL}\frac{\partial^2 y_{RL}}{\partial t^2} \qquad \text{EQ. } 87$$

$$As\ \frac{m_{BM}}{m_{RL}} \in \left[\frac{1}{3}, 2\right] \Rightarrow \frac{\frac{\partial^2 y_{RL}}{\partial t^2}}{\frac{\partial^2 y_{BM}}{\partial t^2}} \in \left[\frac{1}{3}, 2\right]$$

From various experiments [167, 168], it has been shown that the amplitude of the RL displacement was close to the amplitude of the BM displacement, which validates our mechanical model. Inaccuracies may come from the TM supposed fixed as well as oversimplification in supposing that the mechanical equivalent of the organ of Corti was moving in a single direction only.

2. Stereocilia displacement

The BM displacement creates a vertical movement of the IHC and OHC and hence of the stereocilia. As stereocilia is an hair cell tissue, it contracts and slides over the TM. OHC stereocilia are anchored in the TM [169] while IHC stereocilia are not attached to the TM in their resting position and the contact between these two structures is only happening during important BM excitement [170] (suggesting that hearing precision may be more related to OHC than to IHC).

We decided to model the stereocilia motion of OHC as being only a sliding motion associated with no vertical compression, as we thought that the angle between the TM and the stereocilia (called α_{TM} in Figure 52), avoided any strong compression.

As presented in Figure 52, we modeled the stereocilia TM connection in a wagon rail motion type with no compression of the stereocilia.

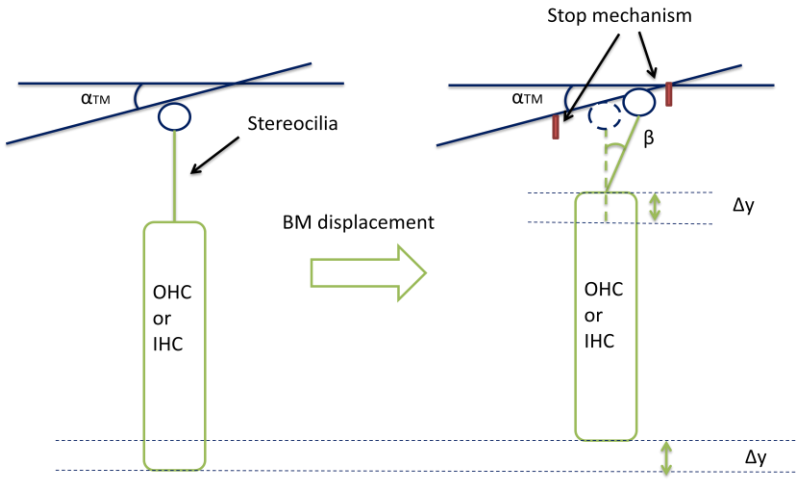

FIGURE 52: MECHANICAL MODEL OF THE STEREOCILIA MOTION

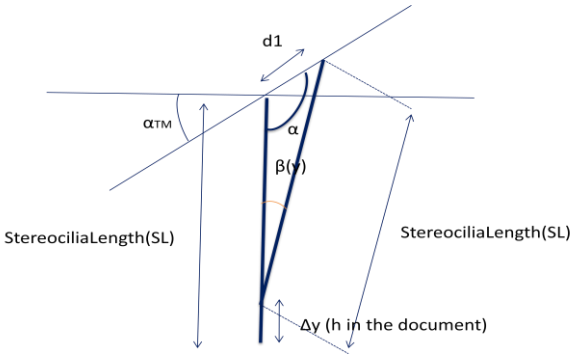

FIGURE 53: MATHEMATICAL DESCRIPTION OF THE STEREOCILIA MOVEMENT

Δy is the displacement of the BM (or similarly of the RL) and β is the deflection angle which is the angle between the resting position of the stereocilia and the stereocilia position when the BM (or similarly the RL) is moved.

Using the model presented in Figure 53 and the Al-Kashi formulas [171] we developed the following system (eq. 88):

$$\begin{cases} SL^2 = (SL - \Delta y)^2 + d_1^2 - 2 * (SL - \Delta y) * d_1 \cos(\frac{\pi}{2} + \alpha) \\ d_1^2 = SL^2 + (SL - \Delta y)^2 - 2 * SL * (SL - \Delta y) * \cos(\beta) \\ d_1 = 2 * SL * \sin(\frac{\pi - \beta}{2}) \end{cases} \quad \text{EQ. 88}$$

where SLis the length of the stereocilia which is between 1µm (at the base) and 5µm (at the apex) of the cochlea [172]. Typically the RL displacement (Δy) around 500nm induces a deflection angle of approximatively 2 degree [173], so the stereocilia length is far greater than the RL displacement for normal amplitude sound stimulation, suggesting that in this case, the variations in the deflection angle are small enough and that they can be approximated by a linear function.

The OHC potential is linearly related to the deflection angle in a |5°| interval [152, 158, 159] and saturation phenomenon appear at a deflection angle lower than -10° or greater than +10°. The model we developed must hence contain a stop mechanism associated with the deflection angles lower than -10° or greater than +10° to be accurate.

The mechanical model presented in this document considers OHC as it is more described in literature, however very similar mechanisms define IHC movement.

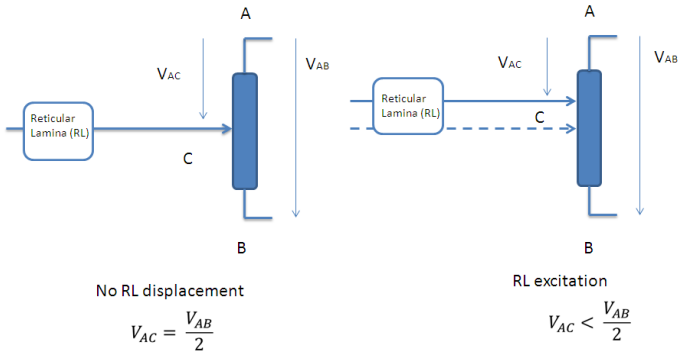

FIGURE 54: PIEZOELECTRIC MODEL OF THE STEREOCILIA

As previously stated by authors [174, 175], the organ of Corti acts as a piezoelectric material: when a mechanical strength is applied to the BM, the membrane potential of the hair cells (OHC or IHC) change. To represent the piezoelectric behavior of the organ of Corti we used a potentiometer linked to the stereocilia deflection angle or more simply to the RL height displacement as explained in Figure 54.

The entire electric and mechanic model of the organ of Corti which adds all the models presented in this Section, is shown in Figure 55.

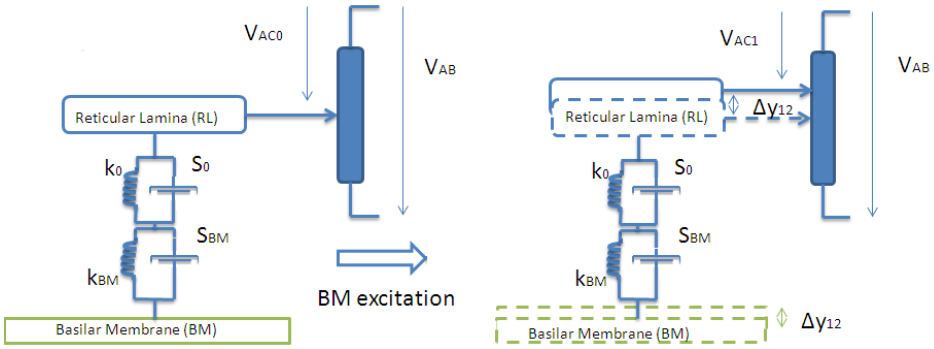

FIGURE 55: ENTIRE MECHANICO-ELECTRIC ANALOG DEVELOPED FOR THE ORGAN OF CORTI STUDY

3. Nerve cells excitation due to hair cells movement

At the tip of the IHC and OHC there are hair bundles also called stereocilia [176]. Stereocilia are surrounded by a fluid (the endolymph) which is rich in K^+ ions. There are filamentous connections (called tip links) between each cilia [177-179]. When the stereocilia performs a rotational motion, the tip links are stretched and the ionic channels (K_v7.4 and TRP4) open and admit K^+ ions and C_a^{2+}ions respectively [152] to enter inside the Hair Cells (IHC or OHC). The mechanism described below concerns the IHC, more complex processes occur in OHC as OHC express more motor proteins such as prestin [180], etc. The current concept is that the tip links are connected to the channel gates, allowing the mechanical gate of the channels to be opened when the tip links elongate and conversely to close them when the tip links shorten [178, 181] (Figure 56).

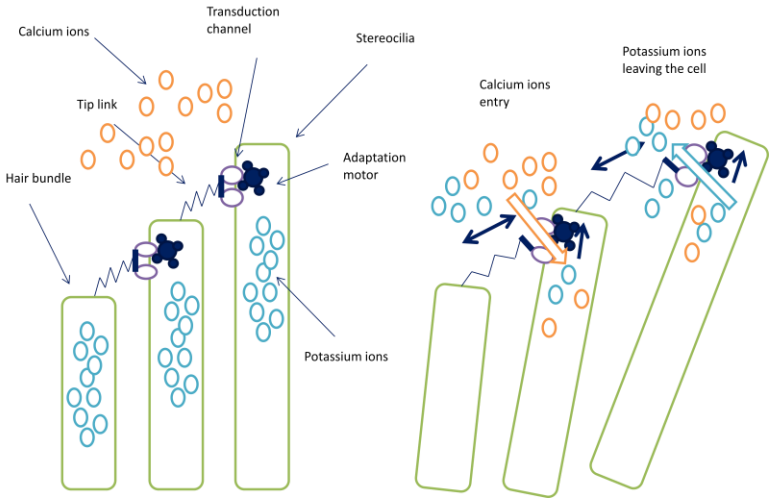

FIGURE 56: WHEN BM IS EXCITED, TIP LINKS MOVE AND ALLOW IONIC CHANNELS TO OPEN WHICH IS THE STARTING POINT OF THE HAIR CELL MEMBRANE DEPOLARIZATION (REDRAWN FROM [178])

Because more positive ions are entering inside the cell than the ones that are leaving the cell, the membrane depolarizes (however the equilibrium potential of K^+ is not -97mV because in this precise case, the concentration of K^+ ions in the perilymph is greater than usual). Depolarization of the IHC results in the activation of Voltage Gated Ions Channels ($Ca_v1.3$) located along the lateral cell membrane. KCNQ4 channels allows K+ to leave the cell, whereas calcium channels increase the cellular concentration of C_a^{2+}[182]. The influx of C_a^{2+} activates the neurotransmitter (glutamate) release at the base of IHC, close to the nerve fibers (in the synapse). The amount of glutamate release is proportional to the voltage membrane depolarization strength [183]. This mechanism is controversial as some authors suggest that the Ca^{2+} concentration increase in the cell cytoplasm is due to Inositol trisphosphate (IP3) activation pathways due to ATP binding during IHC mechanical rotation [184]. As previously stated the voltage membrane depolarization depends on the rotational angle made by the stereocilia once excited (the precise description of the Organ of Corti and model is described in Section III.G.2). Glutamate binds to receptors located in the afferent nerve fiber terminal, resulting in action potential generation in the afferent nerve cells (if the stimulus is strong enough) [183].

Experiments show that there is a linear relation between the firing rate (number of spikes per second, also called spikes frequency) and the sound wave amplitude in dB [185-188]. As a relation between the OHC membrane voltage (V_{OHC}) and the sound wave amplitude can also be extracted, we can suppose that the spikes firing rate depends on OHC membrane voltage and that similar deductions can be made for IHC.

Remembering that IHC are not directly producing AP which is made by the afferent nerve fiber due to V_{IHC} change, we are proposing a possible mechanism that links V_{IHC} and AP generation.

4. Theoretical results using the model developed

The electro-mechanical modeling presented in the previous Section aims to connect the BM height variation, following a sound wave detection with the OHC voltage variation. Two sound waves of 50dB of amplitude and a frequency of 300Hz and 600Hz were used for theoretical model testing. The BM height displacement for 50dB sound waves with a frequency of 300Hz and 600Hz (described in Section III.E) is redrawn in Figure 57:

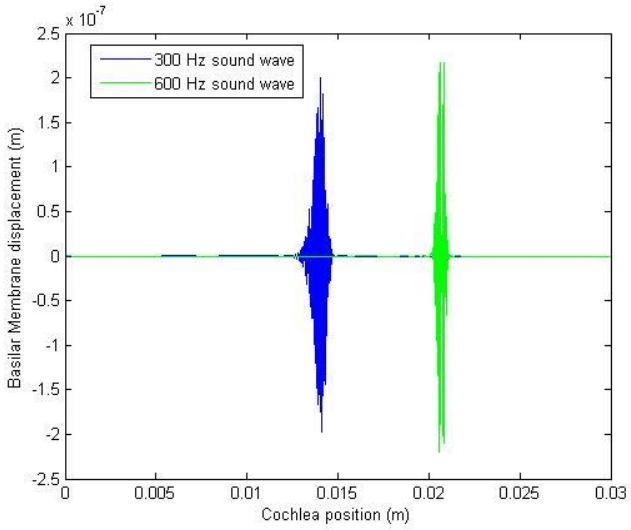

FIGURE 57: BASILAR MEMBRANE DISPLACEMENT ASSOCIATED WITH 50DB 300HZ AND 600HZ SOUND WAVE

The use of the equations presented in eq. 84, gave the stereocilia displacement associated with these BM height variations (Figure 58).

Using the mathematical relation found in [152, 158, 159](obtained from experimental data performed on OHC), we transformed the stereocilia motion into OHC potential. It should be noticed that as this mathematical relation was defined only in a certain range, we performed a polynomial extraction to obtain values outside the given interval. Furthermore we suppose in this document that IHC dynamics are similar to OHC dynamics. This assumption may be inaccurate but was necessary, as to the authors' knowledge, no such data were extracted from IHC displacement.

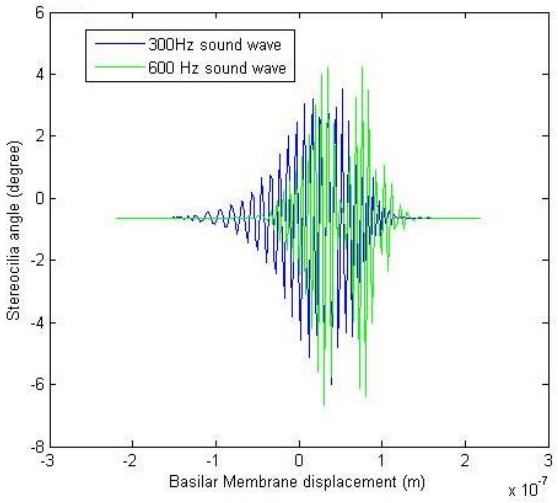

FIGURE 58: STEREOCILIA ANGLE ASSOCIATED WITH 50DB SOUND WAVES OF 300HZ AND 600HZ

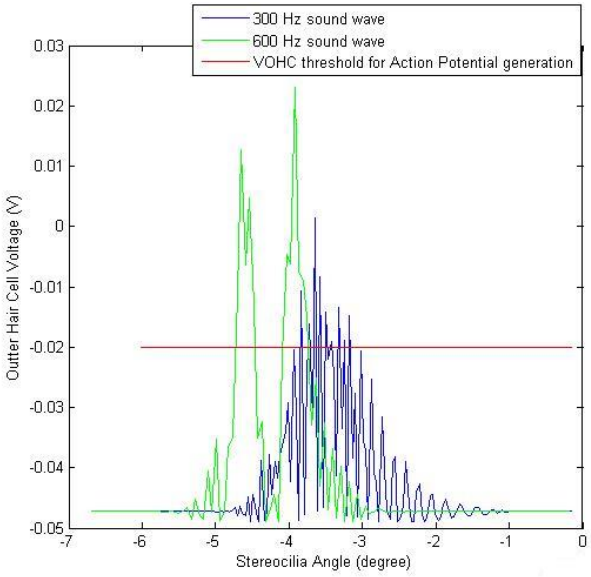

FIGURE 59: OUTER HAIR CELL MEMBRANE POTENTIAL VARIATION PRODUCED BY 300HZ AND 600HZ 50DB SOUND WAVES. THE RED LINE IS THE OUTER HAIR CELL MEMBRANE VARIATION REQUIRED TO PRODUCE AN ACTION POTENTIAL

5. Synapse modeling

Consequently to IHC release of glutamate in the synaptic cleft, glutamate receptors in postsynaptic afferent nerve, also called type I Spiral Ganglions Cells (SGC), provoke nerve cell excitation (voltage membrane change) and may produce an AP. The mechanisms by which IHC are stimulated (mechanical stimulation of the tip links which open the ionic channels) and release the

neurotransmitters to excite afferent nerve cells are very different from afferent nerve cell signal production (glutamate-mediated postsynaptic excitation of neural cells), and propagation. Dendritic input potentials variation also known as dendritic Excitatory Post Synaptic Potentials (EPSP) produce an afferent nerve cell soma depolarization that may result in an AP creation on those cells.

Glutamate receptors in postsynaptic afferent nerve cells (ionotropic receptors (AMPA, NMDA,…) and metabotropic receptors (allowing nerve cell response modulation as developed in [183]) stimulate ions entry inside the cell, producing a depolarizing current (excitatory post synaptic current) [189, 190]. If enough glutamate receptors are activated, this may trigger an AP generation in the postsynaptic neuron.

a)

b)

c)

d)

FIGURE 60: DYNAMICS OF THE SYNAPTIC TRANSMISSION, FROM NEUROTRANSMITTER LIBERATION IN THE PRESYNAPTIC CELL (IHC), SYNAPSE DIFFUSION, RECEPTOR ANCHORAGE AND TO IONS PENETRATION IN THE POST SYNAPTIC CELL[191-193]

a) Ribbon synapse

Neuronal ribbon synapses constitute a special subclass of chemical synapses, characterized by multivesicular release mechanisms as well as unusual calcium channel positioning allowing increased exocytosis cycle resulting in extremely fast, precise and sustained release of glutamate in the synaptic cleft in response to presynaptic cell membrane potential change. This augmented and continuous glutamate release allows very efficient neurotransmission which is of great importance for perception of complex senses such as vision or hearing (sound amplitude perceived can cover six order of magnitude [194]). The synaptic ribbon is a structure positioned several nanometers away from the pre-synaptic membrane and tethers 100 or more synaptic vesicles. Each pre-synaptic cell may possess from 10 to 100 ribbons anchored at the membrane [195-197]. In experiments

quantifying the sizes of presynaptic ribbons and postsynaptic AMPA receptor patches in more than 1200 synapses in mouse cochleas performed in [198, 199], it was established that each nerve cell contacts only one hair cell ribbon synapse, justifying the numerous type 1 Spiral Ganglion Cells (SGC) connecting each single IHC. Ribbon synapses unchangingly use glutamate as the primary transmitter [200].

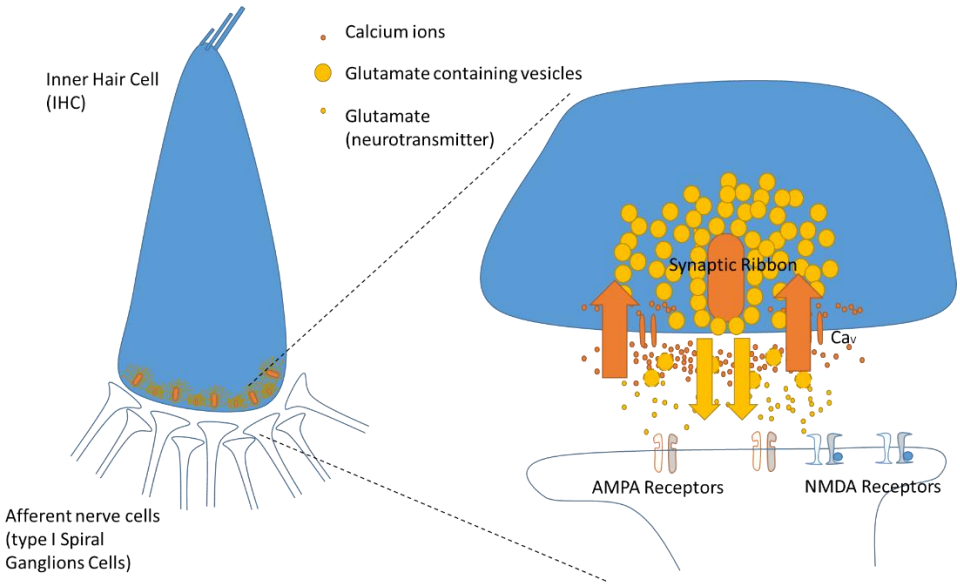

FIGURE 61: HAIR CELL RIBBON SYNAPSE MODELING. FOLLOWING INNER HAIR CELL (IHC) DEPOLARIZATION, CALCIUM IONS ENTER INSIDE THE IHC ALLOWING GLUTAMATE VESICLES TO BE RELEASED IN THE SYNAPTIC CLEFT. THE PRECISE MECHANISMS OF VESICLES EXOCYTOSIS AT A RIBBON SYNAPSE ARE COMPLEX AND STILL PARTIALLY UNDERSTOOD [201, 202]

b) Presynaptic model

The ionic channels open when the presynaptic membrane potential ($V_{presynaptic}$) is greater than the opening threshold voltage for Voltage Gated Ca^{2+} Channels (Ca_v), allowing Ca^{2+} ions entry inside the presynaptic cell which permits the release of the glutamate neurotransmitter in the synapse. In this case, the presynaptic cell corresponds to an activated IHC but this mathematical model can be extended with simplicity to other types of presynaptic cells. The ionic channels dynamics are described by the following equation (eq. 89) [191-193]:

$$I_{ion} = \overline{g_{channel}} * \left(V_{presynaptic} - V_{channel}\right) * \rho_{channel} * m_{channel}^{n} \qquad \text{EQ. 89}$$

where $\overline{g_{channel}}$ is the conductivity of the ionic channel, $V_{channel}$ is the channel voltage activation threshold, $\rho_{channel}$ the presynaptic cell channel density (often neglected by various authors), $m_{channel}$

the probability that the channel is in its opened state and n the number of gates composing the channel. In the following development we assumed that n=1 and we suppose that $\rho_{channel}$ was already included in channel conductivity. This simplification is often retained by various authors as it does not alter the comprehension of ions dynamics in the synapse.

The probability that the channel is in its opened state ($m_{channel}$) is described by functions $\alpha(V_{presynaptic})$ and $\beta(V_{presynaptic})$ (Figure 62) [203, 204].

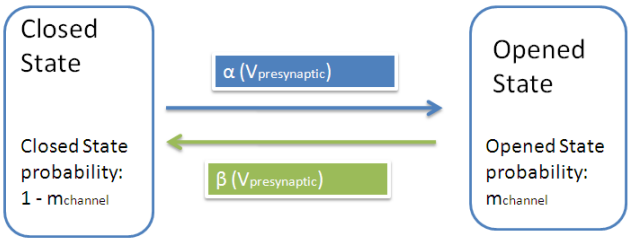

FIGURE 62: KINETIC MODEL OF PRESYNAPTIC CELL GLUTAMATE RECEPTORS

where $\alpha(V_{presynaptic})$ represents the opening rate of the channel and $\beta(V_{presynaptic})$ the closing rate of the channels. These functions are extracted from experiments and are easily available on literature [203, 204].

Applying the law mass principle permits to obtain the differential equation found in [193, 205], and reminded in eq. 90

$$\frac{d\, m_{channel}}{dt} = \alpha(V_{presynaptic}) * (1 - m_{channel}) - \beta(V_{presynaptic})(m_{channel}) \qquad \text{EQ. } 90$$

From this mathematical model, further parameters can be extracted such as the fraction of channels which are in the open state if the presynaptic membrane potential is hold at a constant potential. This parameter is obtained when t is very large (eq. 91) [206].

$$m_{channel,t\to\infty}(V_{presynaptic}) = \frac{\alpha(V_{presynaptic})}{(\alpha(V_{presynaptic}) + \beta(V_{presynaptic}))} \qquad \text{EQ. } 91$$

Furthermore the average time needed for the channel to change state is given by eq. 92 [206]:

$$\tau_m(V_{presynaptic}) = \frac{1}{(\alpha(V_{presynaptic}) + \beta(V_{presynaptic}))} \qquad \text{EQ. } 92$$

The dynamics of a receptor is more complex than the one presented by the differential eq. 90. Other models such as Markov chain [193] or other kinetic schemes as the ones presented in [207] are available to model more precise behavior. As the channel opening is probabilistic, stochastic

description of the channels dynamics are also available [208] but were discarded in this document to ease the computations.

In a presynaptic neuron (or IHC in our case), depolarization which is caused by stereocilia displacement or more generally due to AP arriving at the presynaptic neuron synapse for instance, will cause Ca^{2+} channels to open, leading to calcium ions entry and finally to vesicles fusion (containing the glutamate) with the presynaptic membrane. Vesicles fusion with the presynaptic membrane liberates glutamate into the synaptic cleft. The number of glutamate released is hence directly proportional to the fraction of channels maintained in the opened state for a presynaptic potential ($V_{presynaptic}$) as described in eq. 93:

$$T_{glutamate} = T_{max} * m_{channel} \quad \text{EQ. 93}$$

where $T_{glutamate}$ is the concentration of glutamate in the synaptic cleft and T_{max} is the maximum glutamate concentration (when all the channels are opened).

The mathematical model reused in this document, extracted from [206], gives the analytical solution of $m_{channel}$ (which is defined in eq. 94)

$$m_{channel}(V_{presynaptic}, t) = m_{channel,t\to\infty}(V_{presynaptic}) - \left(m_{channel,t\to\infty}(V_{presynaptic}) - m_{channel,t\to\infty}(0)\right) * exp^{\frac{-t}{\tau_m}V_{presynaptic}} \quad \text{EQ. 94}$$

Replacing this solution in eq. 89, permits to obtain the general conductance of the channel (recalled in eq. 95)

$$g_{channel} = \overline{g_{channel}} * \left(V_{presynaptic} - V_{channel}\right) * m_{channel,t\to\infty}(V_{presynaptic}) - \left(m_{channel,t\to\infty}(V_{presynaptic}) - m_{channel,t\to\infty}(0)\right) * exp^{\frac{-t}{\tau_m}V_{presynaptic}} \quad \text{EQ. 95}$$

Another mathematical model for the transmitter concentration in the synaptic cleft is to consider that the vesicles fusion with the presynaptic membrane happens very fast, hence the number of transmitters released is dependent on the number of channels maintained in an opened state at a fixed presynaptic potential (hence replacing $m_{channel}$ by $m_{channel,t\to\infty}$ in eq. 93). In this case $T_{glutamate}$ is simply given by eq. 96

$$T_{glutamate} = T_{max} * m_{channel,t\to\infty} = \frac{T_{max}\,\alpha(V_{presynaptic})}{(\alpha(V_{presynaptic}) + \beta(V_{presynaptic}))} \quad \text{EQ. 96}$$

This model of transmitter release is often preferred in literature [191, 193, 209].

Considering usual synaptic models results in Excitatory Post Synaptic Potentials (EPSP) (that are the potentials of the afferent nerve cells due to the IHC depolarization) around 5mV for AMPA Receptors (absolute values) [210-212] and 3mV for NMDA Receptors [212, 213], unable to generate an AP. Besides the non continuous stimulation of post synaptic cells in usual synapse is incompatible with the maintained hearing sensation of a continuous sound. IHC have ribbon structures close to the synapse allowing precise, continuous and fast glutamate release in the synaptic cleft as described in Section I.G.5.a).

Various mathematical models of ribbon synapses have been developed in literature [214], and their conclusions will be adapted in our model. We created a mathematical function estimating the quantity of glutamate released in the synaptic cleft depending on $V_{presynaptic}$ and on time. We estimated as a first approximation than this function could be split into two independent functions, one related only to the presynaptic membrane potential and the other only to time as described by eq. 97:

$$T_{glutamateribbon} = T_{glutamateribbon1}(V_{presynaptic}) * T_{glutamateribbon2}(t) \qquad \text{EQ. 97}$$

The concentration of Ca^{2+} entering inside the IHC following IHC depolarization has been quantified experimentally [214] and the glutamate quantity released in the synapse is directly proportional to the Ca^{2+} concentration inside the IHC (until vesicles exocytosis saturation when more than 1mMol of Calcium is entering inside the IHC)[214] [199]. Besides Calcium Voltage Channels are time dependent and we supposed frequency of glutamate released into the ribbon synapse identical to the frequency of glutamate clearance. Consequently we used the Calcium concentration inside the IHC in function of the presynaptic voltage potential to determine the quantity of glutamate released into the ribbon synapse in function of this potential and we used the time dynamics of the Calcium Voltage Channels to estimate the temporal fluctuation of the glutamate into the ribbon synapse. This second relation does not include exocytosis or endocytosis mechanisms and discards reuptake mechanisms lowering its physical interest, however it models roughly the glutamate quantity into the ribbon synapse, provided non saturation of the vesicles released due to very important IHC intracellular Calcium.

Furthermore the maximum quantity of glutamate released in the ribbon synapse was defined in [214] and is close to the maximum quantity of glutamate released by an entire normal synapse. We modeled the glutamate quantity released in the ribbon synapse applying eq. 98:

$T_{glutamateribbon}$ EQ. 98

$$= \left(T_{maxribbon} \left(\frac{1}{1 + e^{\frac{-\left(V_{presynaptic} - V_{p1}\right)}{\tau_1}}} + \frac{1}{1 + e^{\frac{\left(V_{presynaptic} - V_{p2}\right)}{\tau_2}}} \right) + T_{min} \right) * \left(\frac{t - t_0}{\tau} * e^{1 - \frac{t - t_0}{\tau}} \right)$$

where V_{p1} is the glutamate activation threshold potential and was set to -10mV, V_{p2} is the glutamate deactivation voltage and was found around 50mV. τ_1 and τ_2 are respectively the raising constant and the falling constant both set to $0.01V^{-1}$. T_{min} is the minimum glutamate released fixed to 1µMol since the ribbon synapse constantly release glutamate. t_0 is the time when the intracellular Calcium is maximal and is fixed at 7ms. τ represents the decay time constant and was found equal to 0.01s to obtain the same dynamics as in various experiments.

Figure 63 exhibits the quantity of glutamate released in the ribbon synapse in function of the IHC (presynaptic cell) potential and the time, following our model implementation in Maple®. The function shape of the glutamate released in the synaptic cleft can be related to experimental results presented in [215], although precise comparison is difficult since adequate testing was not performed.

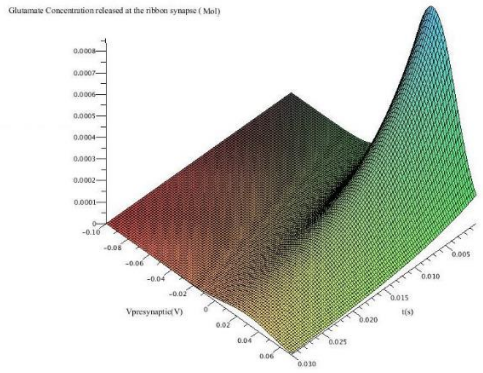

FIGURE 63: GLUTAMATE RELEASED IN THE SYNAPTIC CLEFT AT A RIBBON SYNAPSE (MODELED WITH MAPLE®)

c) Synaptic cleft model

There are more than 10^{14} neurons in the human body and each of these may contain up to 10^5 or even more synapses. The synapses may be electrical (gap junctions) or chemical with

neurotransmitters used as signaling molecules [216]. Additionally the same neurotransmitter may bind with different affinity to different postsynaptic neurons receptors and may result in various neuronal responses.

The mathematical model proposed here is very basic discarding complex mechanisms such as neurotransmitter reuptake.

We considered in this model that the neurotransmitters sent into the synaptic cleft by the presynaptic neurons travel to the postsynaptic membrane where they bind to postsynaptic membrane receptors, as described by eq. 99[217]:

$$I_{synapse} = \sum_j w_j * \sum_j g_{channel}(t - t_j^{(f)}) * (V_{presynaptic} - V_{channel}) \qquad \text{EQ. } 99$$

where j is the number of neurons releasing neurotransmitter into the synapse (we supposed for simplification purposes that j=1), w_j is the synapse efficiency (supposed equal to 1) and t_j is the time needed for the presynaptic neuron to fire (as described in Section I.C, mean inter spike delay is around 15ms for auditory nerve fibers).

d) Postsynaptic receptors mathematical modeling

The aim of the mathematical synapse modeling in this work is to express the postsynaptic (type II SGC) membrane potential variations ($\Delta V_{postsynaptic}$) as a function of the presynaptic membrane potential ($V_{presynaptic}$), and modeling choices were made for that intent.

When the neurotransmitters arrive in the postsynaptic membrane receptors (generally on activator sites of gated channels), it will allow ionic channel opening resulting in ions diffusion (such as Na^+, K^+). These ions are entering or leaving the postsynaptic cells depending on their resting concentration in the various compartments. This ionic diffusion will modify the postsynaptic cell membrane potential ($V_{postsynaptic}$). This potential is defined by a set of equations, attributed to Hodgkin and Huxley [149, 209, 218-220], mathematically describing the action potential generation.

The postsynaptic membrane current associated with neurotransmitter glutamate arrival is expressed by the following equation (eq. 100) [209, 221]:

$$I_{postsynaptic} = \overline{g_{channel}} * m_{channel}^n * \rho_{channel} * (\Delta V_{postsynaptic} - V_{channel}) \qquad \text{EQ. } 100$$

This equation is very similar to the presynaptic membrane conductivity equation and the same assumptions about n and $\rho_{channel}$ were considered.

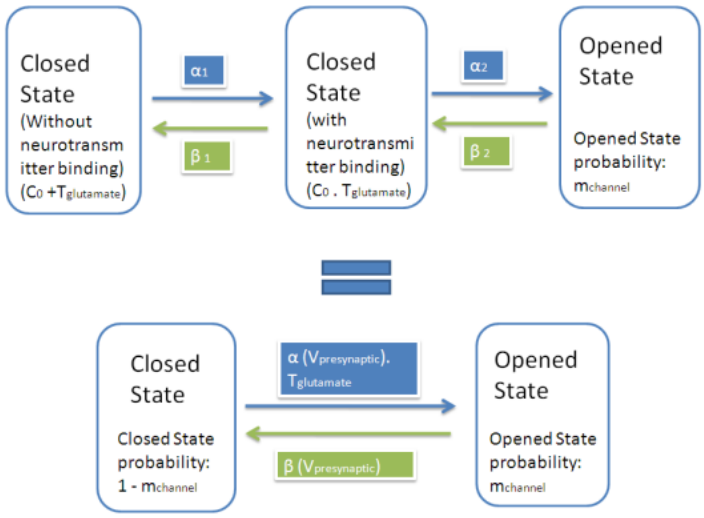

FIGURE 64: KINETIC MODEL OF THE POSTSYNAPTIC RECEPTORS

Similarly to the presynaptic conductivity, the following equation (eq. 101) is used to describe the channel opening probability. However this time the rate opening function is weighted by the partial transmitter concentration inside the synapse, as the channels only open if neurotransmitters are binding to it [191] as described by Figure 64.

$$\frac{d\,m_{channel}}{dt} = \alpha(V_{presynaptic}) * T_{glutamate} * (1 - m_{channel}) - \beta(V_{presynaptic})(m_{channel}) \qquad \text{EQ. } 101$$

The meaning of the different parameters were defined in Section III.G.5.a)

The mathematical system describing the AP generation was introduced by Hodgkin and Huxley [206, 218] and is recalled in eq. 102, for reader's convenience. This system precisely models the physics of the AP, in particular the behavior of the voltage channels present in the nerve cell surface.

$$\begin{cases} -C_m \frac{dV_m}{dt} = \overline{g_{Na}} * m^3 * h^1 * (V_m - V_{Na}) + \overline{g_k} \\ * n^4 * (V_m - V_k) + g_l * (V_m - V_l) + I_{in}(t) \\ \frac{d\,n}{dt} = \alpha_n(V_m) * (1 - n) - \beta_n(V_m)(n) \\ \frac{d\,h}{dt} = \alpha_h(V_m) * (1 - h) - \beta_h(V_m)(h) \\ \frac{d\,m}{dt} = \alpha_m(V_m) * (1 - m) - \beta_m(V_m)(m) \end{cases} \quad \text{EQ. } 102$$

where $\overline{g_{Na}}$ is the conductance of the Voltage gated Sodium channels (Na_v), V_{Na} is the potential of Na^+ inversion. $\overline{g_k}$ is the conductance of the Voltage gated Potassium channels (Nk_v), V_k is the K^+ ions potential inversion. g_l is the conductance of the channels associated with the leakage current and V_l is the reversing potential of these channels. I_{in} is the input current injected in the nerve cell, for instance during neurotransmitters release in the synapse. As the Na_v channels have a set of 3 identical, rapidly-responding, activation gates (the m-gates), and a single, slower-responding, inactivation gate (the h-gate)[222], this explains the power value of the probabilistic functions associated with the channel gate opening m and h. The voltage gated potassium channels contain a single class of gate consisting of 4 individual activation gates (the n-gates), which respond more slowly than the activation gates of the Na_v channels [222]

The factors α_i and β_i are called the transition rate constants, where α_i represents the number of times per second that a gate which is in the closed state opens, while β_i represents the number of times per second that a gate which is in the opened state closes [222].These functions are easily found on literature [206, 223, 224].

C_m is the postsynaptic membrane capacitance and was supposed constant to simplify the computations. This postsynaptic membrane capacitance value has a major impact on the time response of $V_{postsynaptic}$ and was computed from nerve fibers capacitance (1µF/cm^2) [225, 226] multiplied by the surface covered by a ribbon synapse (diameter of a ribbon synapse active zone around 0.1µm) [199].

We hence obtained a system with 6 equations and with 7 unknown variables, which are sufficient to express $V_{postsynaptic} = f(V_{presynaptic})$, as emphasized in eq. 103[191, 205, 206]:

$$
\begin{cases}
-C_m \dfrac{dV_{postsynaptic}}{dt} = \overline{g_{Na}} * m^3 * h^1 * \left(V_{postsynaptic} - V_{Na}\right) + \overline{g_k} \\
\quad * n^4 * \left(V_{postsynaptic} - V_k\right) + g_l * \left(V_{postsynaptic} - V_l\right) \\
\quad + \overline{g_{channels}} * m_{channels}\left(V_{postsynaptic} - V_{channel}\right) \\
\dfrac{d\,n}{dt} = \alpha_n\left(V_{postsynaptic}\right) * (1 - n) - \beta_n\left(V_{postsynaptic}\right)(n) \\
\dfrac{d\,h}{dt} = \alpha_h\left(V_{postsynaptic}\right) * (1 - h) - \beta_h\left(V_{postsynaptic}\right)(h) \\
\dfrac{d\,m}{dt} = \alpha_m\left(V_{postsynaptic}\right) * (1 - m) - \beta_m\left(V_{postsynaptic}\right)(m) \\
\dfrac{d\,m_{channel}}{dt} = \alpha_{channel}\left(V_{postsynaptic}\right) * T_{glutamateribbon} * \\
\quad (1 - m_{channel}) - \beta_{channel}\left(V_{postsynaptic}\right)(m_{channel}) \\
T_{glutamateribbon} = \left(T_{maxribbon} \left(\dfrac{1}{1 + e^{\frac{-\left(V_{presynaptic} - V_{p1}\right)}{\tau_1}}} + \dfrac{1}{1 + e^{\frac{\left(V_{presynaptic} - V_{p2}\right)}{\tau_2}}} \right) + T_{min} \right) \\
\quad * \left(\dfrac{t - t_0}{\tau} * e^{1 - \frac{t - t_0}{\tau}} \right)
\end{cases}
\qquad \text{EQ. } 103
$$

The last two equations were developed in Section III.G.5.a). It should be noted that the channel parameters are the parameters of the channels in the postsynaptic membrane, whereas only the $T_{glutamateribbon}$ function concerns the presynaptic membrane channels.

The system presented in eq. 103 can be solved numerically, and the various parameters values may be found in [206, 223, 224], although there is sometimes controversies between documents about these values.

When $V_{postsynaptic}$ is greater than $V_{1/2Na}$ (which is the potential that the postsynaptic membrane has to reach to activate half of the Na_v channels and is around -20mV), an AP is generated [227]. An AP has always the same physical characteristics hence the same mathematical description with a peak of 30mV reached in approximately 0.2ms (average value for AP propagating in nerve fibers). Consequently, it is sufficient to only compute the increase in the postsynaptic membrane potential associated with the transmitter released, as described in eq. 104

$$
\Delta I_{postsynaptic} = \overline{g_{channels}} * m_{channels}\left(\Delta V_{postsynaptic} - V_{channel}\right) \qquad \text{EQ. } 104
$$

This permits to reduce the system presented in eq. 103, into the following one (eq. 105)

$$\begin{cases} -C_m \dfrac{d\Delta V_{postsynaptic}}{dt} = \overline{g_{channels}} * m_{channels} \\ \left(\Delta V_{postsynaptic} - V_{channel}\right) \\ \dfrac{d\, m_{channel}}{dt} = \alpha_{channel}\left(\Delta V_{postsynaptic}\right) * T_{glutamateribbon} * \\ (1 - m_{channel}) - \beta_{channel}\left(\Delta V_{postsynaptic}\right)(m_{channel}) \\ T_{glutamateribbon} = \left(T_{maxribbon} \left(\dfrac{1}{1 + e^{\frac{-\left(V_{presynaptic} - V_{p1}\right)}{\tau_1}}} + \dfrac{1}{1 + e^{\frac{\left(V_{presynaptic} - V_{p2}\right)}{\tau_2}}} \right) + T_{min} \right) \\ * \left(\dfrac{t - t_0}{\tau} * e^{1 - \frac{t - t_0}{\tau}} \right) \end{cases} \quad \text{EQ. 105}$$

We may further specify that the enzymatic inactivation of the neurotransmitters in the postsynaptic cells are related to the activation rate and inactivation rate constant as described in [205].

e) Postsynaptic membrane receptors

Various experiments have reported that AMPA receptors mediate fast synaptic transmission at the hair cell afferent synapse [195, 201].

Immunolabelling study have indicated that Kainate-type Glutamate receptors (KAR) are expressed in both IHC, OHC and Spiral Ganglion Cells (SGC) and may be possibly involved with OHC acoustic transmission [228].

NMDA receptors responses of SGC are particularly relevant for salicylate induced tinnitus study models, suggesting an implication of these receptors in sounds perception [195, 229]. NMDA receptors require activation of the postsynaptic cell in order to become open as a Magnesium ion is blocking the canal in their normal state. In consequence it is hence very likely that NMDA receptors work to modulate postsynaptic cell activation following AMPA receptors opening.

Using molecular biology and immunolabeling method, it was shown in [230], that glutamate also activates second messenger systems via G-protein-coupled metabotropic glutamate receptors (mGluRs) and their activation did not initiate postsynaptic nerve cell response but raised the excitatory postsynaptic cell response of Spiral Ganglions neurons.

Purinergic receptors are expressed in almost all the cells of the organ of Corti structure, they are involved in various complex pathways partially understood mainly as second messengers [231].

A number of substances have been proposed to function as neurotransmitter from efferent input (from the lateral part of the efferent olivocochlear system), stimulating the IHCs or OHCs such as acetylcholine, gamma-aminobutyric acid (GABA), dopamine, enkephalin and dynorphin [232].

We decided to only model AMPA and NMDA Receptors as they mainly contribute to the auditory nerve cell response and because they are the most characterized in electrophysiological literature.

(1) AMPA receptors

AMPA receptors are ionotropic transmembrane receptors for glutamate, that mediates fast synaptic transition as they open and close rapidly. Their name is derived from the artificial glutamate analog α-amino-3-hydroxy-5-methyl-4-isoxazolepropionic acid (AMPA) acting as an agonist [233] . Each AMPAR has four sites to which an agonist (such as glutamate) can bind which opens the pore. The channel opens when two sites are occupied [234] and increases ionic current as more binding sites are occupied [235]. Once open, the channel may undergo rapid desensitization, described by various mathematical temporal functions [204, 208]. The AMPA Receptors may be permeable to sodium, potassium and calcium (depending on the presence of the GluR2 subunit). Long Term Potentiation (LTP) involved in synaptic plasticity [216], implicated in memory study is not modeled in this document. In specialized auditory nuclei, AMPA receptor kinetics may be extremely rapid with rise and decay time constants in the millisecond range [236]. We implemented the above equations with the software Maple® and the results are presented in Figure 65 and in Figure 66.

AMPA receptors opening probability function (n_{AMPA}) model implementation indicates that the AMPA receptors opening starts when $V_{presynaptic}$ reaches -20mV and quickly decrease after 1ms, except if there is elevated presynaptic membrane depolarization.

The AMPA receptors conductance points out that for time greater than 5ms or for presynaptic membrane potential below -40mW, the current passing through the AMPA receptor is reduced in accordance with the n_{AMPA} results.

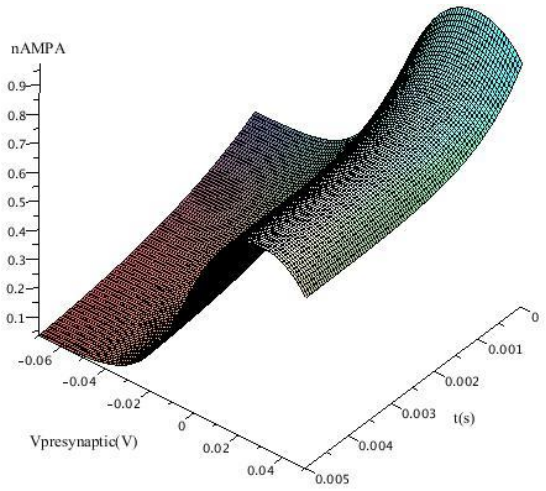

FIGURE 65: AMPA RECEPTOR OPENING PROBABILITY FUNCTION (N_{AMPA}) PLOTTING RELATED TO THE PRESYNAPTIC MEMBRANE POTENTIAL AND TO TIME

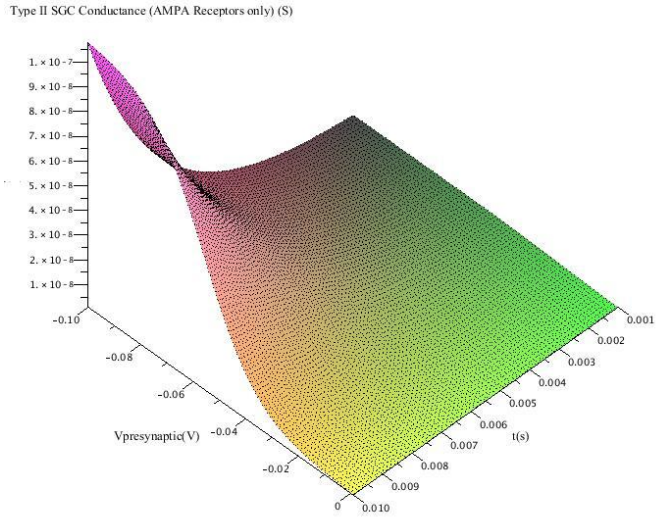

FIGURE 66: POSTSYNAPTIC CELL CONDUCTANCE FUNCTION ASSOCIATED WITH AMPA RECEPTORS ONLY, PLOTTING RELATED TO THE PRESYNAPTIC MEMBRANE POTENTIAL AND TO TIME

Although temporal functions, modeling the AMPA receptors temporal dynamics, are available in literature [204, 208], we preferred to implement the general mathematical model of a receptor in order to conserve the relation with the presynaptic membrane potential ($V_{presynaptic}$). In fact considering only the temporal function describing the AMPA receptor dynamics and using this function in both systems presented in eq. 103 and eq. 105, led to inability to correlate $V_{postsynaptic}$ with $V_{presynaptic}$ as $m_{channel}$ is only depend on t and not on $V_{presynaptic}$ in this case.

The system used to model $V_{postsynaptic}$ in function of $V_{presynaptic}$ for AMPA receptors only is presented in eq. 106

$$\begin{cases} -C_m \dfrac{d\Delta V_{postsynaptic}}{dt} = \overline{g_{AMPA}} * m_{AMPA} \\ \left(\Delta V_{postsynaptic} - V_{AMPA}\right) \\ \dfrac{d\, m_{AMPA}}{dt} = \alpha_{AMPA}\left(\Delta V_{postsynaptic}\right) * T_{glutamateribbon} * \\ (1 - m_{AMPA}) - \beta_{AMPA}\left(\Delta V_{postsynaptic}\right)(m_{AMPA}) \\ T_{glutamateribbon} = \left(T_{maxribbon} \left(\dfrac{1}{1 + e^{\frac{-(V_{presynaptic} - V_{p1})}{\tau_1}}} + \dfrac{1}{1 + e^{\frac{(V_{presynaptic} - V_{p2})}{\tau_2}}} \right) + T_{min} \right) \\ * \left(\dfrac{t - t_0}{\tau} * e^{1 - \frac{t - t_0}{\tau}} \right) \end{cases} \quad \text{EQ. 106}$$

The values for the different parameters related to the AMPA receptors can be found in various documents [191, 204, 205, 208]. However these values are not similar between the documents and we modified these in order to obtain the same temporal dynamics as the ones obtained in experiments. In documents [205, 216, 237, 238] the Excitatory PostSynaptic Potential (EPSP) are presented for various presynaptic stimuli for AMPA Receptors, giving the time response of the post synaptic cell to these particular stimuli. Although these stimuli are limited in number, they do provide a testing environment for our model and authorizes constant values identification. The parameters values obtained are presented in Table 7.

TABLE 7: AMPA RECEPTORS PARAMETERS USED IN THE MAPLE® SOFTWARE IMPLEMENTATION

Parameters	Values
V_{AMPA} (V)	0e-3
$\overline{g_{AMPA}}$ (S)	5e-10
α_{AMPA} (M/s)	5e5
β_{AMPA} (M/s)	400
τ_1 (V^{-1})	10e-3
τ_2 (V^{-1})	10e-3
t_0 (s)	7e-3
τ (s)	1e-2
T_{max} (M)	1e-3

The analytical resolution of the system presented in eq. 106, was performed using Maple® Software and is not proposed here as the mathematical solution contains numerous terms. It should

be notified that the constants of this solution were set in order to obtain values suitable with experiments. The general shape of the solutions obtained were as presented but the precise mathematical values of the solutions were set to fit physical experiments such as whole cell patch-clamp recordings from afferent dendrites with IHC contacts in excised postnatal rat resulting in Excitatory PostSynaptic Potentials (EPSP) of variable amplitude (1–35 mV) with time constant of rise times of about 1 ms and time constants of decay of about 5 ms at room temperature (presented in [239]). In [240, 241] current-clamp recordings were performed from IHCs and voltage-clamp recordings from afferent fibers in postnatal rats gave similar results.

n_{AMPA} and g_{AMPA} functions are plotted in Figure 65 and in Figure 66. The opening probability of the AMPA receptors is directly related to the presynaptic cell membrane potential in our model. Furthermore both figures emphasize that the AMPA receptors are only activated during few milliseconds before they start closing.

The mathematical description of the postsynaptic membrane potential ($\Delta V_{postsynaptic}$) in function of the time and the presynaptic membrane potential ($V_{presynaptic}$) restricted to AMPA receptors only is proposed in Figure 67 where the inactivation time is much more important than the AMPA receptor one, mainly because of the nerve cell membrane capacitance value.

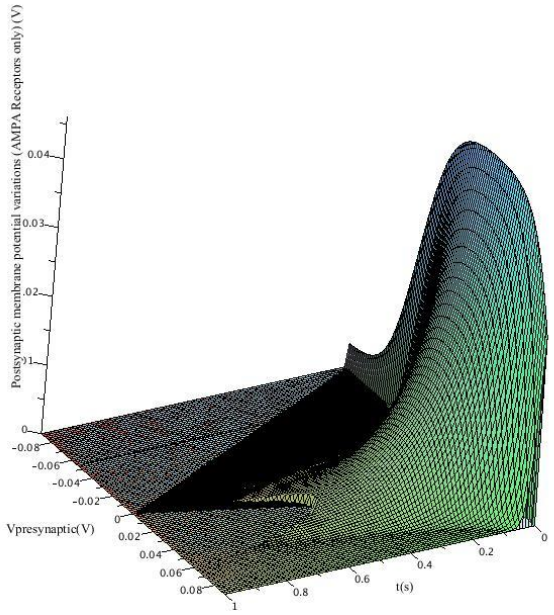

FIGURE 67: POSTSYNAPTIC MEMBRANE POTENTIAL VARIATIONS RELATED TO PRESYNAPTIC VOLTAGE AND TIME FOR AMPA RECEPTORS

(2) NMDA Receptors

The NMDA Receptors are another type of ionotropic glutamate receptors, N-methyl-D-aspartate (NMDA) is the name of a selective agonist that binds to NMDA receptors, giving the name to this receptor class. Activation of NMDA receptors results in the opening of an ion channel that is nonselective to cations [242]. The NMDA receptor channel is blocked by Mg2+ at resting membrane potential and to unblock it, the postsynaptic cell must be depolarized [243].Therefore two conditions are needed for NMDA Receptors opening: glutamate must be bound to the receptors, and the postsynaptic cell must be depolarized. When these two conditions are realized the NMDA receptors displace the Mg2+ ions blocking the channel, allowing diffusion processes to occur. This property of the NMDA receptor explains many aspects of Long-Term Potentiation (LTP) and synaptic plasticity, not studied in this document [243]

The fraction of channels that are not blocked by Mg2+ ions is given by the formula extracted from [204, 205, 244] and recalled in eq. 107.

$$B\left(V_{postsynaptic}\right) = \frac{1}{1 - \eta[Mg^{2+}] * exp^{-\upsilon V_{postsynaptic}}} \qquad \text{EQ. } 107$$

where the parameters η and υ can be found in [204, 205, 244]. $[Mg^{2+}]$ is the extracellular magnesium concentration and is around 1 milliMole in physiological conditions.

To the author's belief, NMDA receptors cannot be modeled efficiently with the deterministic differential equations used in eq. 101, as the time solution of this differential equation is composed of a simple exponential modeling the receptor closure. This supposes that the receptor opening is instantaneous. For NMDA receptors the opening time (defined by its raising time) is around 20ms which is comparable to its closing time (defined by its falling time which is between 25 and 125ms) [204]. The temporal behavior of the channel opening probability function is rather defined by two exponential functions, one defining the opening of the receptor and the other one its closure as described in [204, 205]. This temporal behavior can be obtained using more complex kinetics model leading to second order derivatives of m_{NMDA}. Besides if we consider only the temporal description of the NMDA channel opening probability (m_{NMDA}), the connection between m_{NMDA} and the presynaptic voltage ($V_{presynaptic}$) will be lost, hence we will not be able to correlate $\Delta V_{postsynaptic}$ and $V_{presynaptic}$. To still maintain the m_{NMDA}dependency on $V_{presynaptic}$, and facilitate solution convergence of the differential equations we discarded the NMDA receptors raising time response and use the simple first order differential system of synaptic receptors already discussed multiplied by the

magnesium block function (B). Whereas inaccurately describing the NMDA receptors time response, this NMDA receptor modeling may also be preferred by various authors [205] (cf Figure 68). We selected this NMDA model to decrease the simulation time as the postsynaptic membrane voltage variation was our major concern rather than the precise temporal dynamic of this receptor.

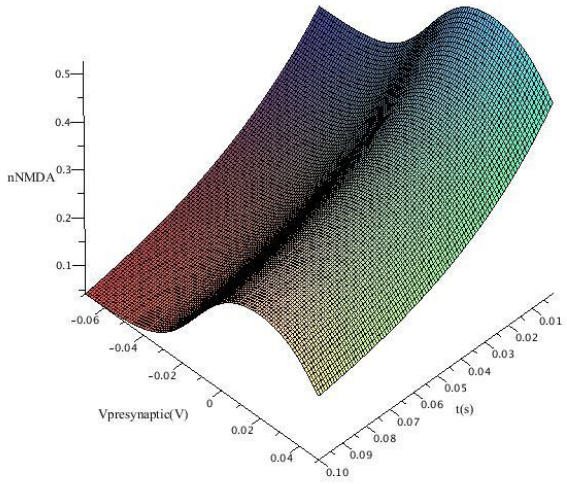

FIGURE 68: NMDA RECEPTOR OPENING PROBABILITY FUNCTION (N_{NMDA}) PLOTTING RELATED TO PRESYNAPTIC MEMBRANE POTENTIAL AND TIME (THE $B(V_{POSTSYNAPTIC})$ FUNCTION WAS NOT INCLUDED)

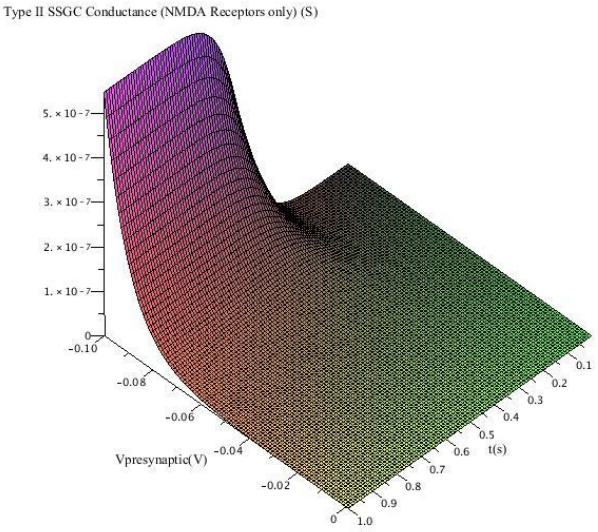

FIGURE 69: POSTSYNAPTIC CELL CONDUCTANCE ASSOCIATED WITH NMDA RECEPTORS ONLY

NMDA opening probability is presented in Figure 68 showing an elevated inactivation time (100ms) when compared to AMPA receptors. NMDA receptors conductance is exposed in Figure 69

and indicates that less presynaptic membrane depolarization compared to AMPA receptors is required for ionic current to pass through (10-20mV) and that there is a marked channel inactivation for times greater than 0.4s.

The system permitting to correlate $V_{postsynaptic}$ with the presynaptic membrane potential with only NMDA receptors insertion is described in eq. 108

$$\begin{cases} -C_m \frac{d\Delta V_{postsynaptic}}{dt} = \overline{g_{NMDA}} * B(\Delta V_{postsynaptic}) \\ m_{NMDA}(\Delta V_{postsynaptic} - V_{NMDA}) \\ \frac{d\, m_{NMDA}}{dt} = \alpha_{NMDA}(\Delta V_{postsynaptic}) * T_{glutamate} * \\ (1 - m_{NMDA}) - \beta_{NMDA}(\Delta V_{postsynaptic})(m_{NMDA}) \\ B(V_{postsynaptic}) = \frac{1}{1 - \eta[Mg^{2+}] * exp^{-\upsilon V_{postsynaptic}}} \\ T_{glutamateribbon} = \left(T_{maxribbon} \left(\frac{1}{1 + e^{\frac{-(V_{presynaptic} - V_{p1})}{\tau_1}}} + \frac{1}{1 + e^{\frac{(V_{presynaptic} - V_{p2})}{\tau_2}}} \right) + T_{min} \right) \\ * \left(\frac{t - t_0}{\tau} * e^{1 - \frac{t - t_0}{\tau}} \right) \end{cases} \quad \text{EQ. 108}$$

The values for the different parameters related to the NMDA receptors can be found in various documents [191, 204, 205, 208] but inconsistencies exist about these values. As for AMPA receptors associated dynamics, we selected parameter values in order to obtain experimental time and voltage dynamics similar to those in [205, 216, 237, 238] for the same presynaptic cells stimuli. These parameters values obtained are presented in Table 8.

TABLE 8: NMDA RECEPTORS PARAMETERS USED IN THE MAPLE® SOFTWARE IMPLEMENTATION

Parameters	Values
V_{NMADA} (V)	0e-3
$\overline{g_{NMDA}}$ (S)	23e-12
α_{NMDA} (M/s)	1.1e4
β_{NMDA} (M/s)	18
η (M)	0.33e-3
υ (V)	0.11e-3
$[Mg^{2+}]$ (M)	1e-3 – 2 e-3
τ_1 (V^{-1})	10e-3
τ_2 (V^{-1})	10e-3
t_0 (s)	7e-3
τ (s)	1e-2

T_{max} (M)	1e-3

We extracted the analytical solution of the system presented in eq. 108 using Maple® software. The numerical approximation of the solution was obtained and displayed close shape similarities with the postsynaptic cell depolarization associated with AMPA receptors only. Of particular importance was the maximum voltage peak of $\Delta V_{postsynaptic}$ around 35mV. The duration of this peak was by far greater than the duration associated with AMPA receptors as the resting state was restored after approximately 900ms.

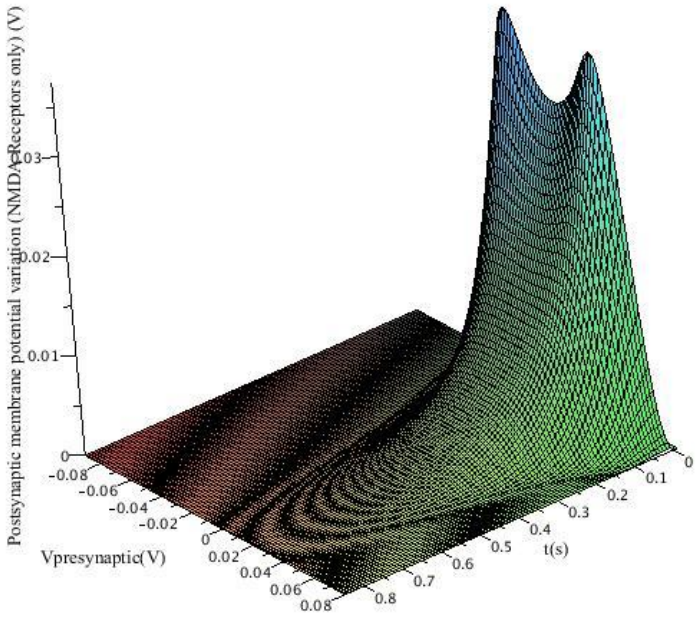

FIGURE 70: POSTSYNAPTIC MEMBRANE POTENTIAL VARIATIONS RELATED TO PRESYNAPTIC VOLTAGE AND TIME FOR NMDA RECEPTORS

The differential equations resolutions lead to constants parameters which were set in order to obtain a solution similar to experimental data extracted from voltage clamp techniques realized on NMDA receptors of various neuron types [205, 216]. IHC or afferent SGC EPSPs only attributed to NMDA Receptors could be obtained using NMDA Receptors antagonists (D(-)-2-amino-5-phosphopentanois acid and by the phosphatase inhibitor okadoic acid) and then comparing this solution with control EPSPs, as exemplified in pyramidal neurons [210, 245]. However EPSPs recording associated only with NMDA Receptors for afferent SGC cells are still lacking as far as the author knows.

f) Total Postsynaptic Membrane Potential

The total postsynaptic membrane potential variation ($\Delta V_{postsynaptic}$) also called Excitatory PostSynaptic Potential (EPSP) is given by the sum of the various depolarization associated with neurotransmitter release weighted by the partial density of these different types of receptors in the postsynaptic cell as described by eq. 109 (results using only AMPA receptors and NMDA receptors were considered in this equation which can easily be extended to other receptors provided the receptors dynamics and postsynaptic membrane density). The postsynaptic membrane potential ($V_{postsynaptic}$) or EPSP is simply the addition of the resting potential with $\Delta V_{postsynaptic}$, as long as no AP is produced (if $\Delta V_{postsynaptic}$ is lower than $V_{1/2Na}$ (half activation potential of Na_v chnnels), as expressed in eq. 109)

$$\Delta V_{postsynaptic}total = wr_{AMPAR} * \Delta V_{postsynamptic}{}_{AMPAR} + wr_{NMDAR} * \Delta V_{postsynaptic}{}_{NMDAR} \quad \text{EQ. } 109$$

where wr functions represent the partial density of one receptor type in the postsynaptic membrane.

$$EPSP = \begin{cases} V_{rest} + \Delta V_{postsynaptic}{}_{total} \\ if\ (\Delta V_{postsynaptic}total) < V_{1/2Na} \\ Action\ Potential\ waveform \\ if\ \Delta V_{postsynaptic}{}_{total} \geq V_{1/2Na} \end{cases} \quad \text{EQ. } 110$$

where $V_{1/2Na}$ is the half activation potential for Na_v 1.5 channels and is around -20.89mV [223]. Simulated EPSPs associated with AMPA receptors only are shown in Figure 71 and EPSPs associated with NMDA receptors only are shown in Figure 72. The modeled developed do not include the AMPA receptors contributions on the NMDA receptors associated EPSPs and inversely, occurring in real experiments. However our mathematical model can be easily extended to take into account these correlations.

Implementing the above equation leads to APs generation for postsynaptic membrane potential variations greater than $V_{1/2Na}$. As indicated the APs absolute magnitude is fixed to approximately 100mV.

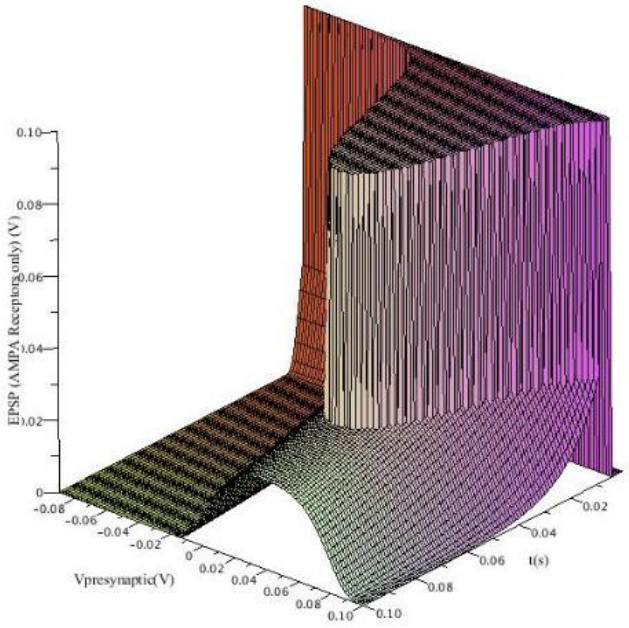

FIGURE 71: SIMULATED EXCITATORY POSTSYNAPTIC POTENTILAS (EPSP) (ABSOLUTE MAGNITUDE) ASSOCIATED WITH AMPA RECEPTORS ONLY

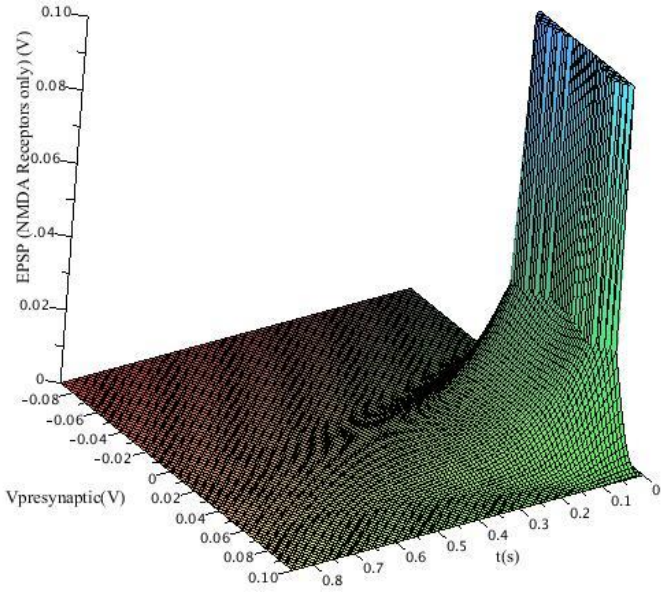

FIGURE 72: SIMULATED EXCITATORY POSTSYNAPTIC POTENTIALS (EPSP) (ABSOLUTE MAGNITUDE) ASSOCIATED WITH NMDA RECEPTORS ONLY

From the results extracted in this model, the excitation of a single ribbon synapse on IHC is able to generate an AP on type II SGC based on AMPA receptors or NMDA receptors responses alone. In fact the maximum variation in the postsynaptic membrane potential, once summed all the receptors

contribution is around 40mV, which is sufficient to stimulate an AP on these cells (the postsynaptic variation must be above $V_{1/2Na}$).

Several nerve fibers are generally connected to a single IHC [185, 246, 247], suggesting sufficient stimulus to generate several AP. Every type II SGC cells are most probably connected to a single ribbon synapse based on microscopic imaging studies [198].

Furthermore several hypotheses can be made to better explain the transmission efficiency at the Inner Hair Cell ribbon synapse. Although these following hypotheses are highly speculative and based on modeling conclusions, they aimed to explain the very accurate and powerful ribbon synapse transmission and experiments should be developed accordingly.

If we consider the mathematical model of synaptic transmission presented in this document and previously used by various authors [191, 208]as realistic, this may suggest that glutamate ionotropic receptors are sufficient to stimulate an AP and that other ionotropic receptors maybe associated with different neurotransmitters, might be present. For instance glutamate metabotropic receptors also exist in the postsynaptic cell possibly increasing its depolarization (more details in[147]). However the time response of metabotropic receptors is usually longer than ionotropic receptors ones and may not suit with sound wave velocity [248].

Other neurotransmitter signaling may be released by HC (acetylcholine, serotonin, …), suggesting complementary HC metabolism. These neurotransmitters could hence potentiate the glutamate response.

Another hypothesis may be that if the sound stimulus resulting in BM vibration is maintained for a certain time, this suggests increased neurotransmitter accumulation in the postsynaptic membrane receptors. Supposing that the total postsynaptic membrane potential is the addition of all the membrane potential variations in time and in space and that glutamate reuptake or internalization mechanisms could be saturated, this may imply that the repetition of the same stimulus (at the same frequency) in time, brings enhanced neurotransmitter in the synaptic cleft, that possibly increase the AP stimulating frequency (hence decreasing the Inter Spike Delay).

Ionotropic receptors with different voltage dynamics or in higher density might also result in a postsynaptic membrane potential greater than usual postsynaptic neuronal. Literature studies seem to suggest that the number of AMPA Receptors in HC ribbon synapses is similar to the number of AMPA Receptors in other brain neurons (there are between 10-200 AMPA receptors in cerebellum or pyramidal cells [249, 250] and around 100 AMPA receptors at ribbon synapses [251]).

Other type of voltage sodium gated channels with lowered half activation potential may be present in the post synaptic cells (spiral ganglions), hence having a decreased voltage threshold for AP generation.

Stochastic resonance associated with neuronal noise, in particular with synaptic noise could be enhanced in ribbon synapses, intensifying the postsynaptic cell depolarization allowing to quickly reach half activation potential of the Na_v 1.5 channels for AP generation [252].

All these speculations should be verified and physical experiments should be designed accordingly.

Such a complete heterogeneous model of the internal ear has never been developed previously as far as the author's knows, and aims to theoretically connect essential parts of the hearing process. Further, this model could be used to study organ of Corti components responses when physiological experiments are difficult to carry out. This precise model may bring a greater comprehension of physiologic mechanisms associated with inner ear damages. Besides it may be possible to precisely target the source of a few hearing disorder.

H. Closure remarks

The implementation and creation of heterogeneous models was presented in this chapter aiming to understand the hearing process for CI improvements. The models we created describe the organ of Corti mechanical response, the sterocilia displacement and the synapse transmission. In addition the middle ear description, the basilar membrane displacement and the hair cell potential variation were implemented from existing theories. All models were adapted to fit in the Matlab/Simulink heterogeneous modeling environment.

Two sound waves of 300 and 600 Hz respectively with 50dB of amplitude were used as test signals. The corresponding variations (physical, mechanical and electrical) from the eardrum to the hair cells membrane potential were reported to validate this modeling realization.

I. Work submitted

- Multi domain modeling of the cochlea: from Basilar Membrane stimulation to Spiral Ganglion cells depolarization, U. Cerasani, W. Tatinian, Neuroscience, Elsevier Journal, 2014

- Auditory nerve spike train mathematical modeling including various sources of neuronal noise, U. Cerasani, W. Tatinian, Computational Neuroscience, Elsevier Journal, 2014

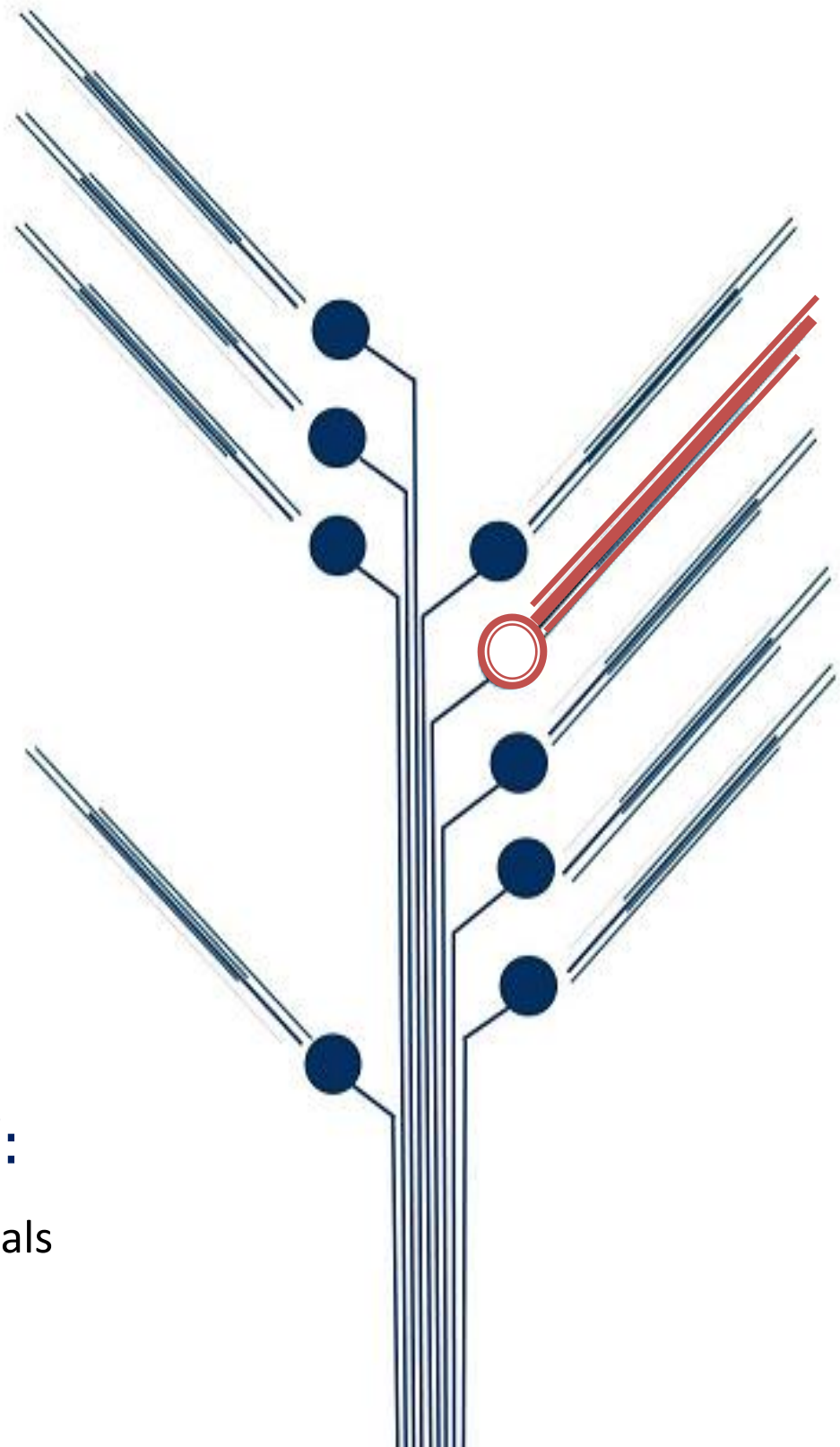

Chapter IV:

Nerve fibers signals

transmission and recording

A. Opening notifications

Measurements of nerve fibers excitation are nowadays directly performed by back telemetry. As an example evoked Compound Action Potential (eCAP) recording may be used to obtain information regarding the nerve fibers stimulated. In that intent eCAP modeling, resulting from sound wave reception and evaluated with the models developed in the previous chapter, would permit our overall created system comparison with experimental measurements. To precisely model an eCAP over time, spikes train dependence with sound wave intensity were investigated.

The statistical firing frequency of a neuron has been shown to depend mainly on sound wave amplitude and spike train can be efficiently described as a Poisson process. Most particularly we applied our model to different sound wave amplitudes and theoretically recreate their associated single nerve fiber spike train (statistical evaluation). After adding many nerve fibers with the same distribution we approximated the overall electrical response of auditory nerve.

Furthermore the propagation of an action potential along a nerve fiber is currently modeled using the cable theory adapted to neurons or with a mathematical system made of the Hodgkin-Huxley equations associated with the wave propagation equation. After reviewing the limits of such models, we proposed a new analog model ensuring same wavelength, velocity and frequency as a typical measured action potential.

In addition current electrophysiological recording techniques are then discussed in the last Section of this Chapter.

B. Action potential propagation model

Excitable cells as nerve fibers are able to transmit information in an electric manner. The variation of the nerve fiber membrane potential starts at a neuron place then propagates along all the nerve fiber as a transversal wave. This electric wave permits the information transmission.

At one end of the nerve cell, neurotransmitters are released inside a synapse, which results in the postsynaptic cell excitement. This stimulation is called Action Potential (AP) generation and is reviewed in [208, 221, 253].The AP consists in a variation of the membrane potential of the nerve fiber locally starting at the synapse generally. The propagation of the AP on the nerve fiber

membrane consists on an electric field propagation on the nerve cell surface. This propagation may be seen as a transverse electromagnetic wave.

Because it is caused by repeated ionic diffusion, the AP velocity is around 20m/s, which makes the electromagnetic theory incompatible to model the AP propagation.

The two most widespread theories developed to model the AP propagation in the nerve fiber are the cable model theory and the Wave theory using the Hodgkin Huxley equations of the AP generation and are reviewed in Section III.G.5.

The cable model theory describes the diffusion of electrons inside a conductive wire. This theory precisely defines the AP spatial propagation but fails to describe its temporal response. Furthermore the electron velocity in cables or other materials such as nerve fibers is several orders of magnitude higher than the AP practical velocity, making this model inappropriate.

The wave propagation theory using the Hodgkin Huxley equations is very precise and incorporates the physical mechanisms of the AP generation. As those equations are complex, this model is poorly used and often restricted to interpretative purposes.

In this Section, we propose an alternative electric model which incorporates the physical processes and respect the AP practical velocity, wavelength and frequency.

1. Physics of an action potential generation

The membrane resting potential (V_m) of a neuron is around -70mV [254, 255]. When an impulse current is injected in a nerve cell, if it is sufficiently important, it will produce nerve membrane depolarization, which will open the Voltage Gated Sodium Channels (Na_v). Once these channels are opened, sodium ions flow occurs, where the ions direction results from two main forces: the electronic force resulting from the different ionic concentration between the intracellular and extracellular space and their concentration gradient differences between the intracellular and extracellular space.

Following this membrane depolarization, Na^+ ions enter inside the neuron, which provokes V_m to rise significantly. Then, the Voltage Gated Potassium channels (Nk_v) open and K^+ ions start to leave the cell. As positive charges leave the cell, the neuron undergoes depolarization then overshoot (as the V_m potential becomes positive. More precisions in Figure 75). During this time Na_v channels start to close first, followed by the closure of Nk_v channels.

Ions channel inactivation is time and voltage dependent as explained in [220]. Finally Na^+/K^+ATPases restore progressively the resting state ions concentration, first at the stimulus site, then toward all the axon.

Once entered inside the neurons, Na^+ ions diffuse in area where they are less concentrated, causing the next neuron area to depolarize (the membrane potential in the next area makes the same variations than the stimulus site region). More detailed information can be obtained in [256], [257] and [258].

The AP generation in nerve fibers is still an extended area of research [259], [260]. Once a chemical (or even mechanical) stimulus creates a nerve fiber depolarization greater than the Na_v threshold, Na_v opens and there is a massive load of Na^+ inside the nerve cell which is the starting point of AP generation.

The probability of Na_v opening is partly driven by neuron voltage (if not in their inactive state) and the closure probability of Na_v is time and voltage dependent [220, 261].

Figure 73displays the mean activation time and mean inactivation time of Na_v which depend on the cell membrane voltage (redrawn from [220]).

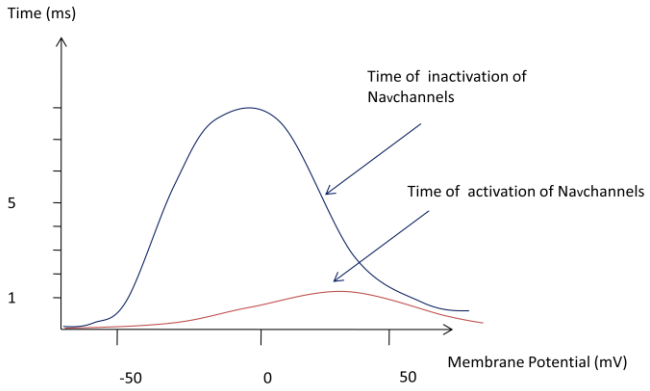

FIGURE 73: ACTIVATION AND INACTIVATION TIME OF THE NAV CHANNELS DEPENDING ON THE NERVE MEMBRANE POTENTIAL (ATTRIBUTED TO[220])

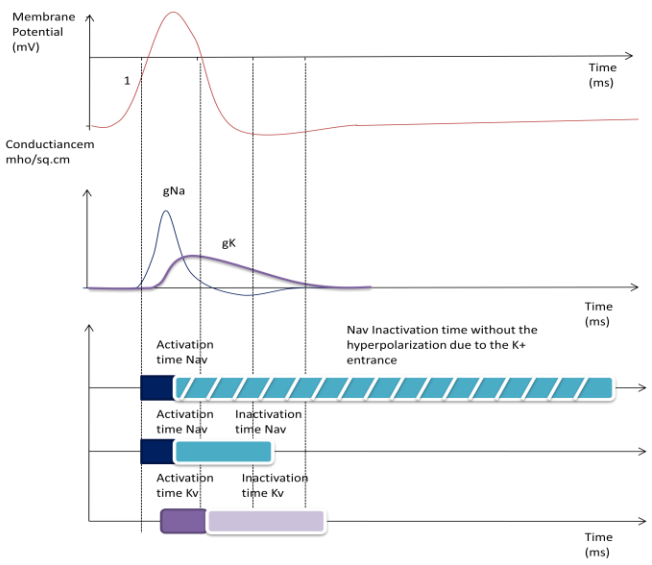

FIGURE 74: AP GENERATION, Na_V CHANNEL CONDUCTANCE AND K_V CHANNEL CONDUCTANCE EXTRACTED FROM [262]. THE CHRONOGRAPHS EXPLAIN WHY THE Na_V CLOSURE IS REACHED AFTER ONLY 2MS. THIS CLOSURE IS MADE POSSIBLE BECAUSE OF ENTRANCE OF POTASSIUM IONS HYPERPOLARIZING THE NERVE

Hence both the probability of activation, the probability of inactivation and the inactivation time are influenced by cell membrane voltage for Na_v channels.

Resulting from these data, when there is an increase in the afferent nerve cell membrane potential (following the IHC depolarization resulting in glutamate release in the synapse), the opening probability of Na_v channels increases (there are more Na_v channels in the opening state) but the Na_v channels time for inactivation also increases.

If the stimulus of the nerve cell was held constant (as done in patch clamp techniques), the mean inactivation time of the Na_v channels would be around 8ms (cf Figure 74) whereas in physical experiments the inactivation time is a little greater than the absolute refractory period (which is the period when Na_v channels are maintained in their inactivate state and no AP can be generated). This period is around 2ms [263]. This can be explained by the opening of the K_v channels just after the Na_v channels opening which allows potassium ions flow inside the nerve cell, hyperpolarizing its membrane. As a consequence, the inactivation time of the Na_v channels decreases greatly as the neuron membrane potential is close to 0mV (as indicated in Figure 74). This precise mechanism is reviewed in details in Figure 75.

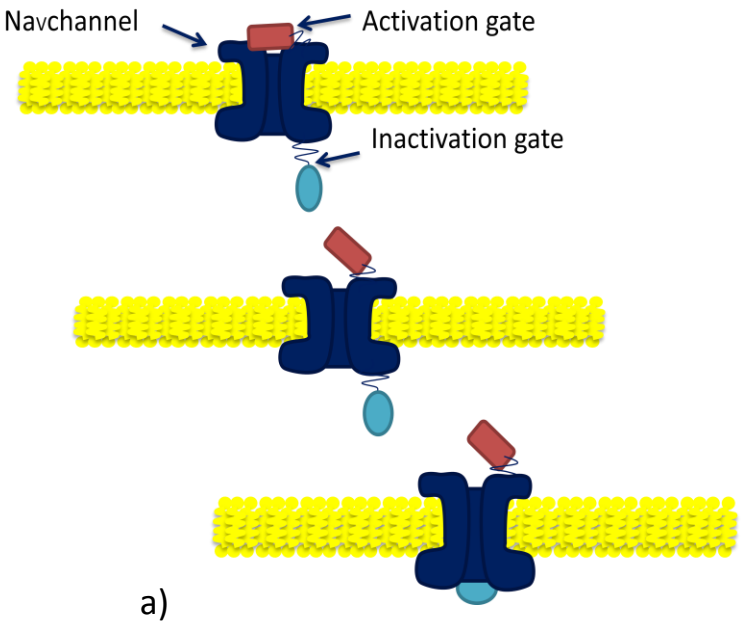

Resting State:
Inactivation Gateopened
Activation Gateclosed

Activated State:
Inactivation Gateopened
Activation Gateopened
=> Flow of Na+ ions inside the cell

Resting State:
Inactivation Gateclosed
Activation Gateopened

a)

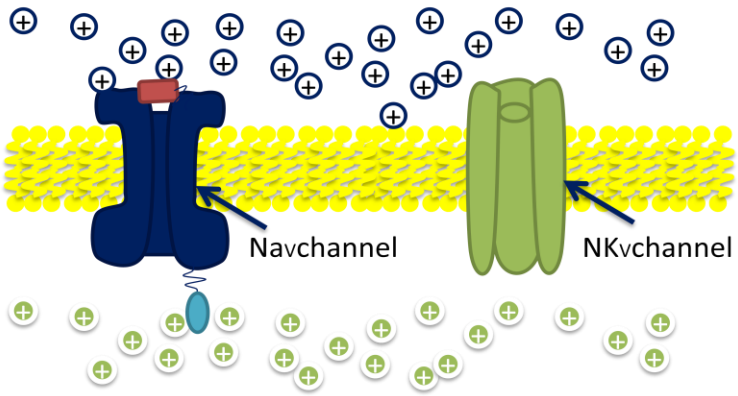

At t=0 (before stimulus)
Navchannel are in theirresting state and NKvchannels are closed

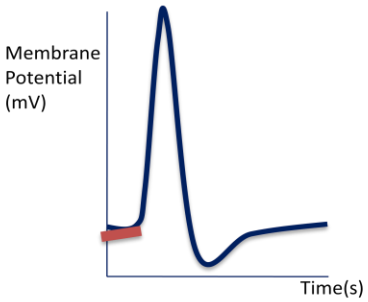

b)

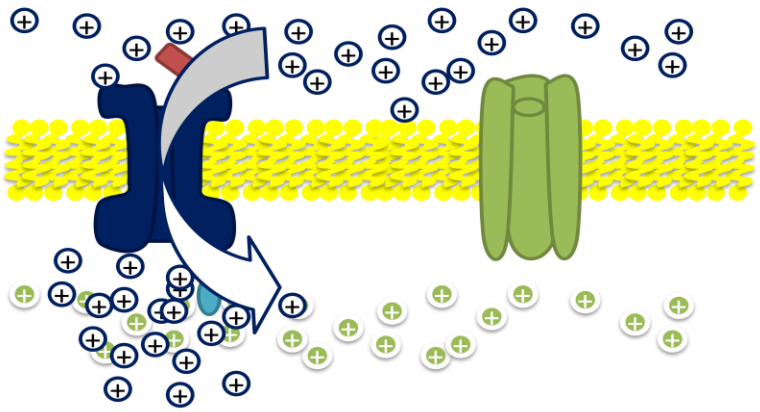

At t=1ms (Depolarization)
Navchannel are open due to various stimulus type (mechanical, electrical, chemical) and Na+ ions enter the cells.
NKvchannelsare closed

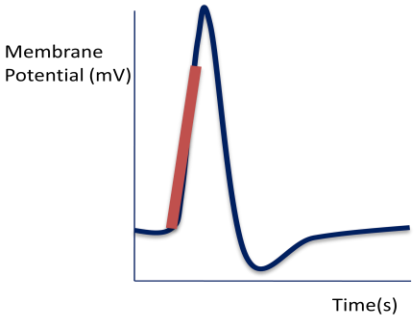

c)

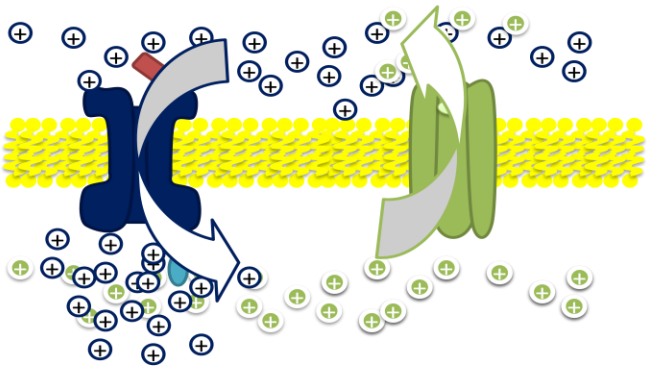

d)

At t=0.2ms (Repolarization)

Navchannel are still open but they are entering in theirresting state (time inactivation as well as potential inactivation). Na+ ions enteredinside the cell are diffusingintolessconcentrated area. NKvchannelsopen as membrane potentialreaches the NKvchannel voltage openingthreshold. As K+ ions are leaving the cell the membrane potentialstarts to decrease

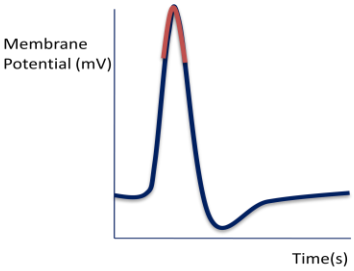

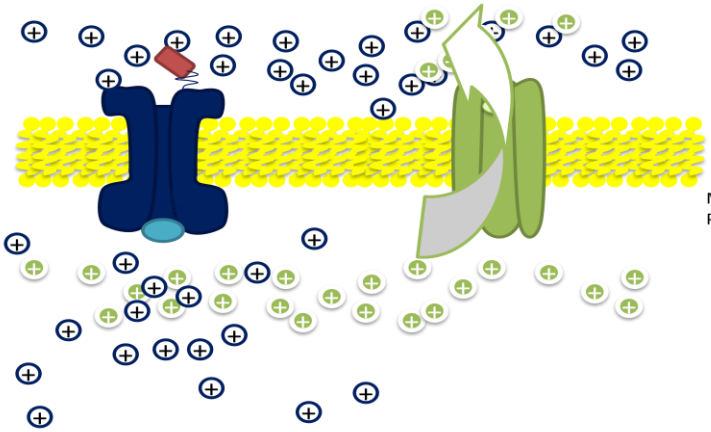

e)

At t=3ms (hyperpolarization)

Na+ channel are in theirresting state and K+ channels are beginning to close

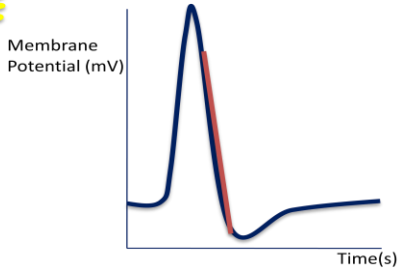

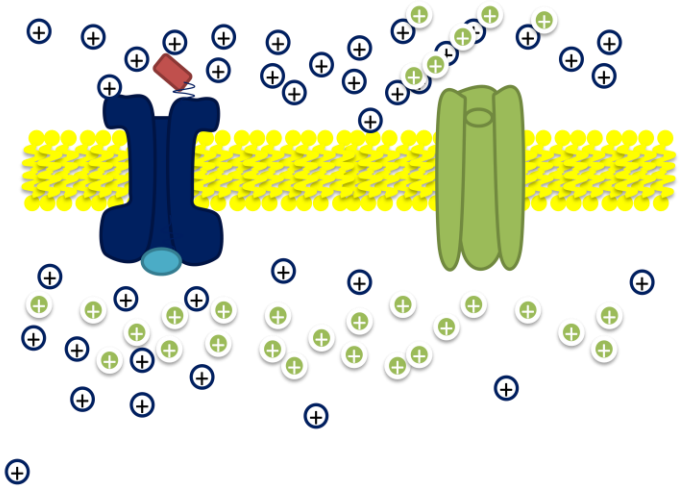

f)

At t=4ms(hyperpolarization)

Na+/K+ ATPases are restoringthe resting membrane potential by reestablishing the resting concentration of Na+ and K+ inside the cells

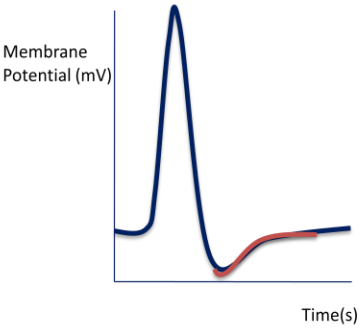

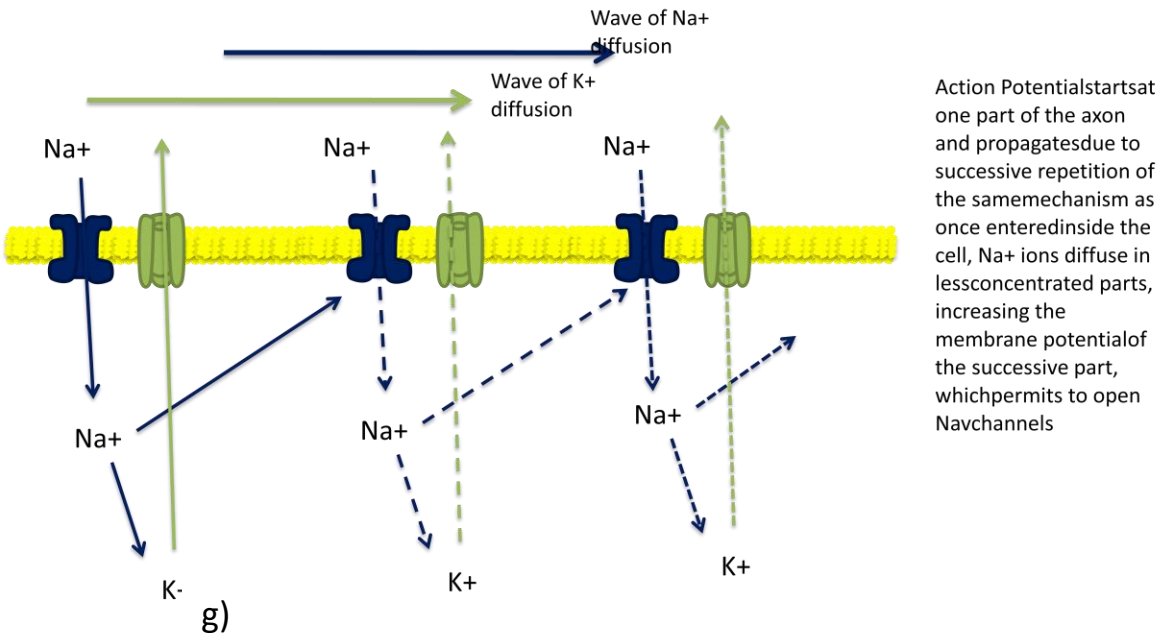

FIGURE 75: A) DIFFERENT STATES OF THE N_{Av} CHANNELS. B), C), D), E), F): AP RELATION TO NERVE IONIC DISTRIBUTION CHANGES. G) PROPAGATION OF THE AP FROM A NEURON REGION TO A CONSECUTIVE ONE. EXTRACTED FROM [263-266]

2. Action potential propagation along the nerve fiber

The massive Na^+ movement entering inside the nerve cell, followed by the K^+ ions leaving the cell are the main events creating an AP. Once entered inside the nerve cell, Na^+ ions start diffusing to area where there are less concentrated (diffusion mechanism). The Na^+ diffusion from one area of the neuron to the next area is at the origins of the AP propagation.

The ion drift from a neuron portion to other neuron portion can be modeled similarly as electron drift inside a conductive wire along the gradient of the electrical potential, explaining the physical relation between the ion drift and the cable theory.

a) Cable model theory

To model the propagation of an Action Potential (AP) among a nerve fiber, the cable model theory was adapted to neurons by K.S. Cole, A.L. Hoglgkin and Rushten [267, 268] and[269]. The linear cable equation model, which can be found in [269, 270] and reminded ineq. 111, models the

membrane potential variation of the nerve fibers depending on the distance from its initial stimulation position.

$$\frac{1}{r_i} * \frac{\partial^2 V_m(x,t)}{\partial x^2} = C_m * \frac{\partial V_m}{\partial t} + \frac{V_m}{r_m} \quad \text{EQ. } 111$$

where V_m is the nerve cell membrane potential, C_m the membrane capacitance, r_m is the longitudinal membrane resistance of the neuron and r_i the axial resistance. The values of the different parameters can be found in[269]. This equation describes a diffusion process.

The partial differential equation of the cable model theory has a unique solution if the initial conditions are well defined and is very similar to the heat diffusion equation through a thermal conductor [268].

The steady state solution ($\frac{\partial V_m}{\partial t} = 0$) assuming that the cable is infinite permits to obtain the membrane potential depending on the distance from the stimulus (eq. 112) [271]:

$$V_m(x) = V_0 e^{\frac{-|x|}{\lambda}} \; with \; V_0 = \frac{I_0 \lambda r_m}{2} \quad \text{EQ. } 112$$

where V_m is the membrane potential, x is the distance from the stimulus, λ is the space constant controlling the membrane potential decay toward the x direction and I_0 is the injected current [271]. In the cable model theory [269]λ is defined as:

$$\lambda = \sqrt{\frac{r_m}{r_i}} \quad \text{EQ. } 113$$

Numerical values for those variables are available in [269] and depends on the axon diameter (d).

The sealed end solution is the most relevant in neurons as it assumes that the end of the nerve fiber is covered with a neuronal membrane which is quite similar to reality where neurons end with synapses. However for simplification purposes, the infinite cable model solution study was preferred and reported in this document.

In real neurons, the current injection is not constant meaning that the steady state solution cannot be applied, rather time dependent solutions must be considered. A system can be completely characterized by its impulse response. A solution to the cable model equation depending in both x and t can be found in literature [271] and is rewritten here for reader convenience (eq. 114):

$$V_\delta(x,t) = \frac{I_0 r_m}{2\lambda(\pi t)^{\frac{1}{2}}} e^{\frac{\tau x^2}{4t\lambda^2}} e^{-\frac{t}{\tau}} \quad \text{EQ. } 114$$

where $V_\delta(x,t)$ is the time and space dependent solution of the nerve fiber membrane potential, t is the time variable and τ the time constant ($\tau = r_m * C_m$).

However $V_\delta(x,t)$ cannot be easily separated into the product of two expression with separate variable, making this expression more difficult to manipulate. Furthermore this time solution is significantly distinct from the time response of an AP. In fact the time response obtained by the cable theory model is divergent from the time response of an excited nerve fiber (which produces an AP). This is caused by the physics of the cable model equation which supposes that a diffusion occur (of Na^+ ions from the site of injection to the extremity of the cable). However the diffusion process is repeated in each neighboring area of the nerve cell. A real AP is supposed regenerating in each neighboring area with only small decrease in the membrane voltage amplitude along the x position [254]. The physical mechanism involved is self regenerating hence acts as a wave propagating inside the nerve cell, not a diffusion from a single stimulus point.

Further models (non linear cable theory for example) have been proposed to overcome the inaccuracies of the linear cable model. The assumptions underlying the cable model theory and limiting its physical meaning are reported in [272].

Besides the velocity of electrons propagation in the cable model solution which is close to the light velocity is several orders of magnitude greater than the AP propagation velocity in nerve cells, rendering this model inappropriate for neurons study.

b) Wave model of action potential propagation

Another new model for AP propagation was proposed in[269], based on wave propagation theory. An AP was considered as a transverse wave which starts at a point of stimulus, runs through the nerve membrane to the synapse, with a nearly constant propagation velocity.

A little remembering of wave theory is provided in this document, allowing better comprehension of the wave model of an AP. Every solution of the D' Alembert equation [273] can be considered as a wave (the spatial position must vary with time). Applying this equation to the membrane potential was performed in[269], and is recalled in eq. 115

$$\frac{\partial^2 V_m}{\partial x^2} = \frac{1}{k}\frac{\partial^2 V_m}{\partial t^2} \qquad \text{EQ. } 115$$

where k is the wave number. The solution of this equation is indicated in eq. 116, made of the forward propagating wave V_{m1} and the backward propagating wave V_{m2}:

$$V_m(x,t) = V_{m1}(x-kt) + V_{m2}(x+kt) \qquad \text{EQ. 116}$$

We considered only V_{m1} in the following development, as it is the forward propagating wave and aimed to construct a wave V_{m1} with the time response and spatial responses close to a real AP.
Using the Hodgkin Huxley equations permitted to obtain a waveform in relation with the mechanisms involved in AP generation, as defined by eq. 117, extracted from [269]

$$\frac{\partial^2 V_m}{\partial t^2} = K * \left(\frac{\partial V_m}{\partial t} + \frac{1}{C_m} * \left(-\overline{g_{Na}} * m^3 * h^1 * (V_m - V_{Na}) + \overline{g_k} * n^4 * (V_m - V_k) + g_l * (V_m - V_l)\right)\right) \qquad \text{EQ. 117}$$

where the variables m, h, n, V_{Na}, V_k and V_l were already defined in Section III.G.5.d)
This mathematical model describes with great precision the AP movement through the nerve fiber. However it is often discarded for practical AP simulations in neuronal network as it is very resources consuming.

3. Electromagnetic wave analogy limits

As partly pointed out by the cable model theory, the electromagnetic theory of AP propagation is not suitable directly as the propagation velocity of an AP (which is around 20m/s depending on the nerve fiber diameter) is by several order of magnitude lower than the electromagnetic wave propagation velocity. Moreover the mean AP duration is around 3ms and its generation time interval is around 15ms (please refer to Inter Spike Delay (ISD) in [160, 185, 274]), which corresponds to a wavelength in electromagnetic theory of several meters, hence making it impossible to propagate in a thin neuron cell. Remembering that the AP waveform represents the membrane potential variation over time, the electromagnetic representation of the AP should display an electric field with similar propagation characteristics. In the electromagnetic theory developed in the following Sections, the electric field is of known form whereas the waveform can be related to it using the Maxwell's equations as indicated in [275], [276]

The mean refractive index computation from the nerve tissue permittivity and conductivity is performed in eq. 118. The permittivity and conductivity curves depending on frequency for nerve tissue are extracted from [53]

$$n_{nerve} = \sqrt{\mu\,\varepsilon} = \sqrt{\mu_0\varepsilon_0} * \sqrt{\mu_{relative}\varepsilon_{relative}} \qquad \text{EQ. } 118$$

$$where\ \varepsilon_{relative} = \varepsilon' - i\varepsilon'' - i\,\frac{\sigma}{\omega\,\varepsilon_0}$$

$$\rightarrow\ n_{nerve}(1000Hz)\ \approx\ 130\ - i * 120$$

where μ is the nerve permeability, $\mathcal{E}$ the dielectric permittivity which is a complex number composed of the real part which is the energy stored in the medium and the complex part made of the energy losses inside the medium. Part of these losses may be related to the material conductivity σ. $\mathcal{E}_0$ is the vacuum permittivity and ω is the pulsation.

The electromagnetic wave velocity (phase velocity v_ϕ) is related to the light velocity in free space (c) by the refractive index as described in eq. 119

$$v_\varphi = \frac{\lambda * \omega}{2 * \pi} = \frac{c}{n_{AP}} \approx 20\ m/s \qquad \text{EQ. } 119$$

$$\rightarrow\ n_{AP}\ \approx\ 1.5e7 - i * 1.69e7$$

where λ is the wavelength, n_{AP} is the theoretical refractive index that should have the nerve tissue to propagate the electromagnetic wave at the AP velocity. Obtaining physically this refractive index is nowadays illusory.

From eq. 118 and eq. 119, it can be deduced that the refractive index required for an electromagnetic wave propagation with the same wavelength, frequency and mostly the same velocity has unrealistic values and may not be found nowadays on a created physical material.

4. Mathematical function describing an action potential

We hence propose a new model for AP propagation. We considered an AP as a transverse wave which starts at a point of stimulus and runs through the nerve membrane to the synapse. The propagating wave aimed to have a time and spatial responses close to a real AP.

A nerve AP has three main phases: depolarization, hyperpolarization and repolarization whereas in AP running through skeletal muscle time response is different due to different physiological

processes occurring [277]. We modeled only the AP relative to cochlear nerve response but similar development can be followed to obtain cardiac AP generation for instance.

The mathematical function we developed, aimed to model the three phases of the AP generation and used exponential functions to duplicate the general AP shape and a sinus function to sketch the hyperpolarization region, similarly as Ultra Wide Band (UWB) mathematical modeling. The forward propagating electronic field expression we developed (called $f_1(x,t)$) is indicated in eq. 120

$$\forall\, t \geq \frac{x}{v_\varphi}, \qquad f_1(x,t) = A_0 \sin\left(\omega_0 (t - \frac{x}{v_\varphi})\right) e^{-\omega_1 (t - \frac{x}{v_\varphi}) + \frac{1}{\omega_2}\left|(t - \frac{x}{v_\varphi})\right|} e^{\frac{-x}{\lambda}} \qquad \text{EQ. } 120$$

where ω_0 and ω_1 were pulsations obtained to fit the AP values obtained from experiments. We chose ω_0 = 1200 rad/s, ω_1 = 2000 rad/s and ω_2 = 1/3000 rad/s. These values were determined to fit experimental AP behavior. The last term in eq. 120, which represents the AP energy damping among the nerve fiber distance, may be neglected in practice. λ is extracted from experiments on single nerve fiber [44, 278-280]

V_ϕ is the velocity of propagation of the AP along the axon. This velocity has been proved to be dependent on the nerve fiber diameter, although neglected in this Section to permit easier implementation.

It must be noticed that the equation $f_1(x,t)$ gives the AP propagation in the forward direction with a temporal response very accurate (because designed mathematically), but the spatial propagation response (along the x direction) is correct only as long as $e^{\frac{-x}{\lambda}}$ is greater than the other terms, thus as long as:

$$\left|\frac{x}{\lambda}\right| \gg \frac{\omega_1}{v_\varphi} \quad and \quad \left|\frac{x}{\lambda}\right| \gg \frac{1}{\omega_1 v_\varphi} \qquad \text{EQ. } 121$$

The values used for the pulsations ω_0 and ω_1 and the values extracted from the cable model theory verify the above equations.

The spatial propagation of the wave, implemented using the software Maple® is presented in Figure 76, which displays the same wave at two different times. The mathematical model of the AP will be used in the next Sections to theoretically simulate nerve cells responses from acoustic wave amplitude.

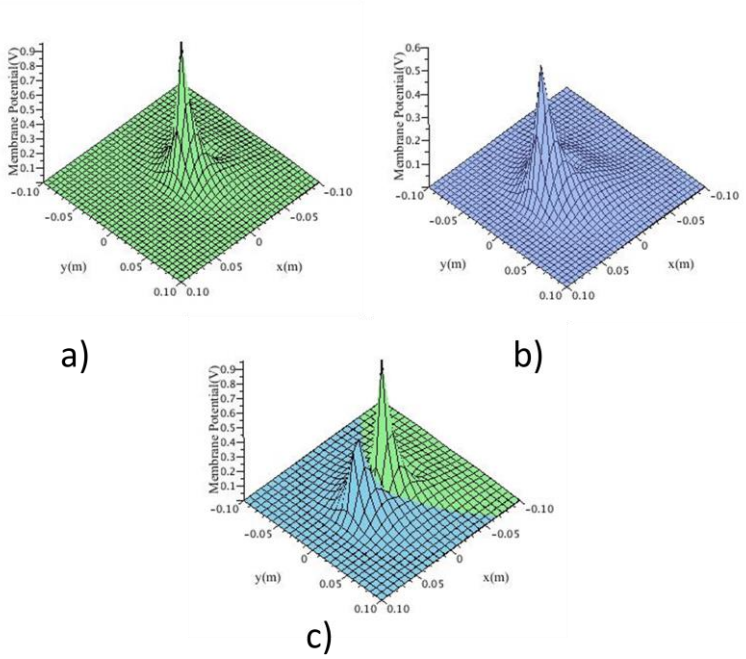

FIGURE 76: AT A DISTINCT TIME, THE MEMBRANE IS DEPOLARIZED AT DIFFERENT POSITION.3.A) NERVE FIBER MEMBRANE POTENTIAL AT T=1E-3S, B) NERVE FIBER MEMBRANE POTENTIAL AT T=5E-2S, C) SUPERPOSITION OF THE TWO MEMBRANE POTENTIALS, INDICATING A PROPAGATION OF THE AP ALONG THE NERVE FIBER

5. Electric analog circuit used for action potential propagation modeling

a) A. Pulse generator

By noticing that the temporal behavior of the mathematical function used to model the AP ($f_1(x,t)$) is very similar to an Ultra Wide Band (UWB) pulse time response or to a Gaussian pulse time response, which are used in telecommunication domain, we decided to create an electric analog of an AP using a UWB pulse generators circuitry.

The time domain waveform for a UWB signal is based on a basic pulse shape often called monocycle [166, 281]. We recreated a similar basic pulse based on this theory (proposed in Figure 77)

The UWB pulse generator is excited by cyclical input waveforms (square waves or sinusoidal waves). Diverse technologies may be used to generate a Gaussian pulse: a tunnel diode or an

avalanche transistor may be used [282] or four differential pairs made of NMOS transistors as explained in [283].

The band pass filter after the pulse generator does not need to be included for AP generation (in UWB it ensures that the pulse is transmitted in the frequency band in accordance with the country transmission standards).

AP time length is around 4ms [265] which corresponds to a frequency of 250Hz. For such low frequency, even more simple circuits may be used such as a RC circuit instead of the more complex UWB pulse generator circuitry described.

The electrical circuit presented above, generates a pulse (with shape similarities of the AP generated in nerve fibers as indicated in Figure 80) and may model AP propagation. The physical connections of this circuit with the events generating the AP are approximate and better physical matching is provided by complex models such as in Hodgkin Huxley model.

This circuit description is close to the Integrate and Fire model which permits fast simulations and is currently used to model neuronal networks [192, 217]. The dot lined circled elements in Figure 77 gather the pulse generation circuitry from a Square Voltage generator for instance. This pulse is the input of the circuit, acting as the stimulus that may result from different inputs such as from mechanosensory cells or a synaptic transmission, etc. The varying resistance models the inertia of the ionic channels disclosure, the capacitor models the difference in ionic concentration between the outside of the cell and the inside. This interpretation is similar with the Hodgkin Huxley model. The inductor, which is specific to our model, is associated with the K^+ escape of the cell following the Na^+ entry (details of the AP generation are provided in Section I.B.1). The ionic K^+ current may be interpreted as an induced current associated with the Na^+ subsequent accumulation inside the cell. The diode, which allows only positive current to propagate aims to model the inactivation time (avoiding the negative peak creation in the electrical circuit). The diode may hence model the single direction of the ionic currents due to ionic concentration differences between the extracellular and intracellular compartments.

Hence an electrical system aiming to produce a similar function is drawn in Figure 77:

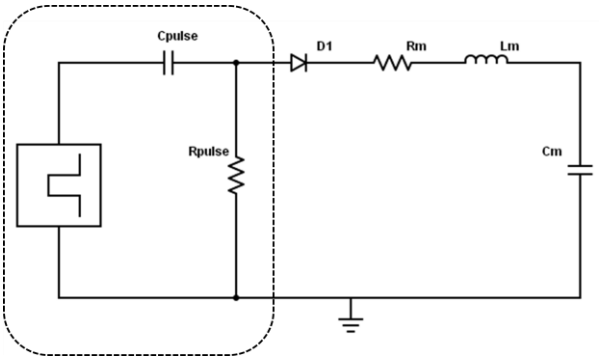

FIGURE 77: ULTRA WIDE BAND CIRCUIT REUSED FOR ACTION POTENTIAL MODELING AND TRANSMISSION THROUGH NERVE FIBERS.

b) Delays incorporation

The direct electromagnetic wave propagation model is not directly suitable with the AP propagation due to the very low velocity of the electromagnetic field during AP propagation. We hence decided to recreate the mechanical process done in nerve cells that was at the roots of the AP generation. In order to obtain an electric field velocity similar to the one produced during AP generation, we introduced delays between the pulse propagation.

Several pulse generators were required, depending on the length of nerve fiber that we wanted to model as indicated in eq. 122. For a nerve fiber of length L, the number of pulse generators required to obtain the experimental AP propagation are:

$$N = \frac{L}{v_{\varphi} * f} \qquad \text{EQ. } 122$$

$$if\ L = 1m \ \rightarrow \ N \approx 100$$

where f is the AP generation frequency and v_{ϕ} is the AP velocity.

However these pulse generators have to start at different times to model the AP propagation from an area of the nerve cell to another area. A first pulse is sent then it is delayed by a delay block which output value is connected to the enable entry of the second pulse generator and the same process is repeated for each N pulse generators. The enable function ensures that the pulse starts only after the previous pulse is delayed.

The electrical implementation of a delay block associated with an enable function however does not precisely gives the same waveform between two consecutive pulse as enable entry are used to receive Transistor-Transistor Logic (TTL) signals. Another way to create a delay is to detect a

particular value (which should correspond to the membrane voltage at which Na_v channels open but for simplicity purposes was set to the maximum of the pulse) of the AP using a comparator for instance. A system similar to logical cascaded gates was selected. When the first pulse is generated the other ones are switched off. This mechanism is repeated for all the pulse generators as described in Figure 78. Another RC filter was required as the comparator detection returned to '0' when the pulse voltage failed after the detected value. Hence the comparator signal was lengthen to the pulse duration using a RC filter. The Operational Amplifier after the comparator block aimed to increase the filtered signal amplitude.

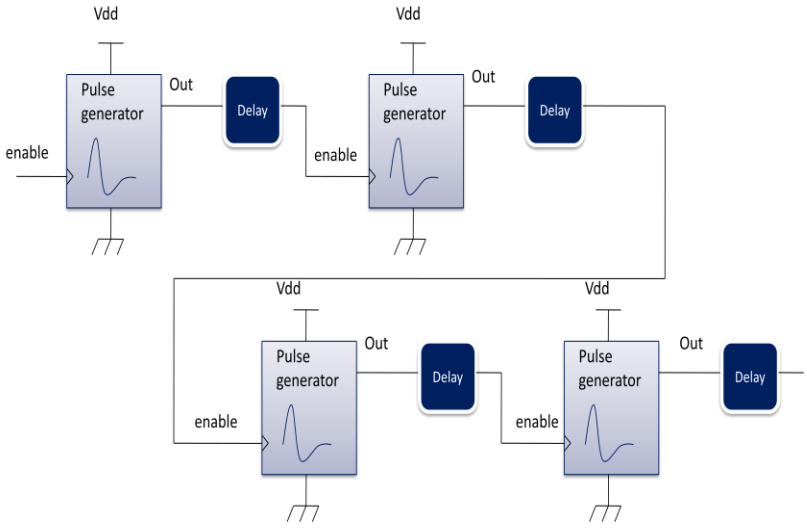

FIGURE 78: ELECTRIC MODEL OF AP GENERATION, CONSERVING THE AP TIME CHARACTERISTICS

The AP electric analog was implemented with PSpice® and the simplified electric schematic (with only the two first stages) is presented in Figure 79. Developing such an analog model may allow faster and more complex simulations than theoretical and computer based models. Other modeling environments such as VHDL-AMS could have been utilized for such modeling but we preferred the PSpice® environment since the development time needed was reduced.

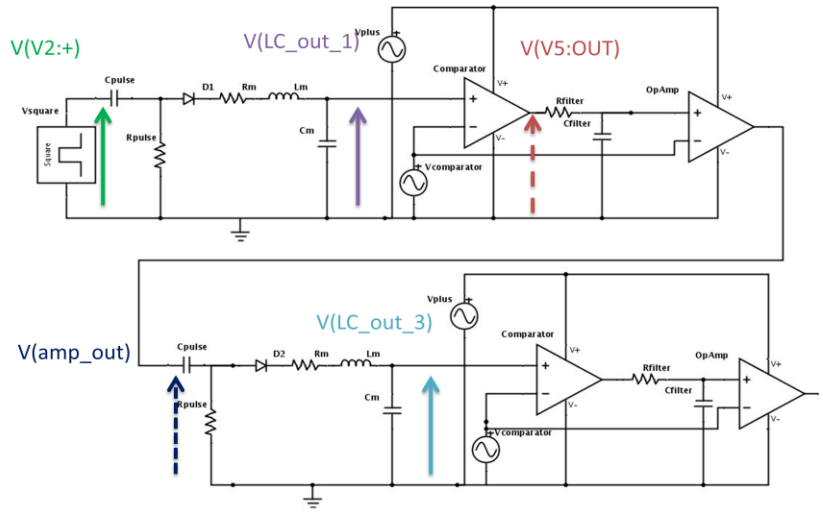

FIGURE 79: ELECTRIC MODEL OF ACTION POTENTIAL GENERATION (ONLY TWO STAGES). THE VARIABLES REPORTED ARE THE ONES THAT ARE USED IN THE SIMULATION WITH PSPICE®

It should be specified that the electromagnetic field propagation of each stage before the delay is at the velocity of the light in free space, however the delays permit to stop the electric field propagation for a certain amount of time resulting in an overall electric field propagating close to the AP velocity.

6. Simulation results

Running transient simulations of the electric schematic presented above (limited to 2 stages) showed that the delay introduced by each stage (which is dependent on the comparator value) is approximately 200µs. If we assume a mean AP propagation velocity of 20m/s, that means that each stage models around 1cm of nerve fiber.

As previously indicated, the second amplifier aims to lengthen the time during which the second pulse generator is enabled (V(amp_out) in the Figure 79). The amplitude variation of an AP is respected in this electric model (corresponding to a membrane depolarization of 100mV) but not its real value (the resting membrane potential of a nerve fiber is around -70mV). An electric block performing a subtraction operation may be included to obtain the precise AP voltage.

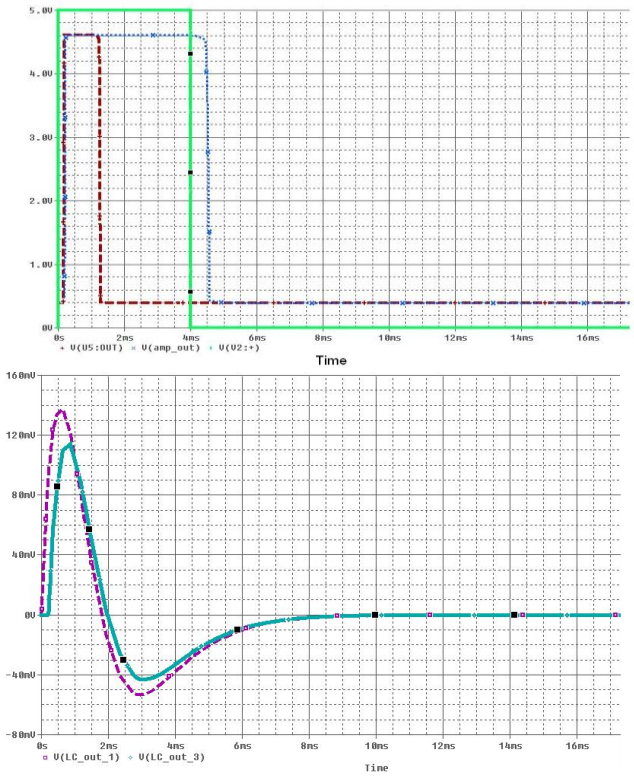

FIGURE 80: TIME SIMULATIONS OBTAINED WITH THE SOFTWARE PSPICE®

The amplitude damping between the two pulses is introduced by tuning the supply source of the Operational Amplifier (OpAmp). A mathematical function may be used to define this amplitude in relation to the nerve distance (that is modeled by pulse generators). In such a way, the amplitude of the following pulse would be decreased exactly as the AP amplitude decreases during its propagation

Figure 81 represents the analogy between the created model and the nerve fiber for AP propagation.

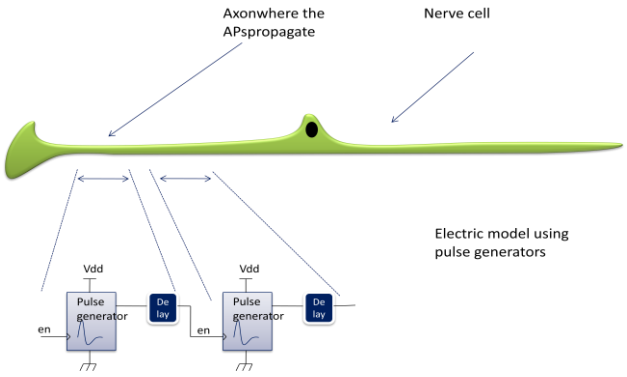

FIGURE 81: PROPOSED ELECTRIC MODEL OF THE NERVE CELLS

It should be further emphasized that the electric model we propose for AP propagation, respects the AP practical velocity, the AP electric field wavelength and the AP frequency. This new model is hence very adapted for nerve cell propagation study, and may further be used to propose new mechanisms for neurons communication or memory mechanisms understanding.

C. Spike trains model

1. Spike trains generation

Dendrites are branched projections of the nerve fibers hence resulting in a nerve fiber modeling with multiple inputs and multiple outputs. They were not taken into consideration as this greatly complicate the model. Consequently, we considered only a single axon propagating APs.

In diverse patch clamp experiments, it has been noted that when the nerve fiber potential is hold to a value greater than the Na_v conduction threshold, APs are generated randomly and the time interval between two APs is called the Inter Spike Delay (ISD) [284]. These notions are further extended in the Section I.C.2.

Spikes train is a time series of discrete APs from same or a group of neurons[285]. Neural spikes train analysis often referred as the neural code is a vast area of research [286, 287].

To mathematically describe a spikes train diagram, several APs starting at different times must be generated. Hence the starting time of each AP must be different and the minimum time length between two consecutive APs corresponds to the absolute refractory period at least (more details in Section I.C.2). eq. 123 shows the mathematical expression of the n-order AP (called V_{swn}) that is delayed by a time $t_p(n)$ compared to the first AP (called V_{sw0}) :

$$V_{sw0} = f_1(x,t) = f_1(t - \frac{x}{v_\varphi}) \qquad \text{EQ. 123}$$

$$V_{swn} = f_1(x,\left(t - t_p(n)\right) = f_1\left(\left(t - t_p(n)\right) - \frac{x}{v_\varphi}\right)$$

where f_1 is the function defined in the previous Section. $t_p(n) - t_p(n-1)$ is the time interval between the n-order spike and the (n-1) order spike. It was shown in experiments [285] that spikes train can be modeled as a Poisson process. Hence the Inter Spike Delay (ISD) can be modeled using an

exponential distribution [285]. However this assumption is sometimes controversial [288] and more complex ISD models have been proposed but were discarded to ease the computations.

We implemented an exponential distribution generator by using a random generator which was used to select the time interval given by the exponential distribution. eq. 124 gives the probability distribution of an exponential distribution.

$$F(t) = \lambda_p e^{-\lambda_p t} \qquad \text{EQ. } 124$$

where λ_p is a parameter of the exponential distribution and is equal to the expected value of the probability distribution ($E[F(t)] = \lambda_p$)

λ_p can be extracted from physical measures [289, 290] and was found around 15ms for a typical stimulus.

Hence the reverse function (F^{-1}) gives the time associated with a probability p and is expressed in eq. 124

$$F^{-1}(p) = \frac{-1}{\lambda_p}\ln(\frac{p}{\lambda_p}) \qquad \text{EQ. } 125$$

We generated the probability p using a random generator provided by Matlab® creating uniformly distributed pseudorandom numbers.

The ISD is given by the eq. 126

$$t_p(n) = F^{-1}\big(random(n)\big) \qquad \text{EQ. } 126$$

$$\Leftrightarrow t_p(n) = F^{-1}\left(\frac{-1}{\lambda_p}\ln(\frac{random\,(\,n\,)}{\lambda_p})\right)$$

Figure 82 represents the simulation results of the developed theory. The time interval was the same in both experiments (3s) but the stimulus amplitude was different (30 or 50dB of input sound power). It can be noted that the ISD is lower for the stronger nerve stimulus and consequently that the number of spikes is more important for this stimulus as the experiment time was the same in both experiments.

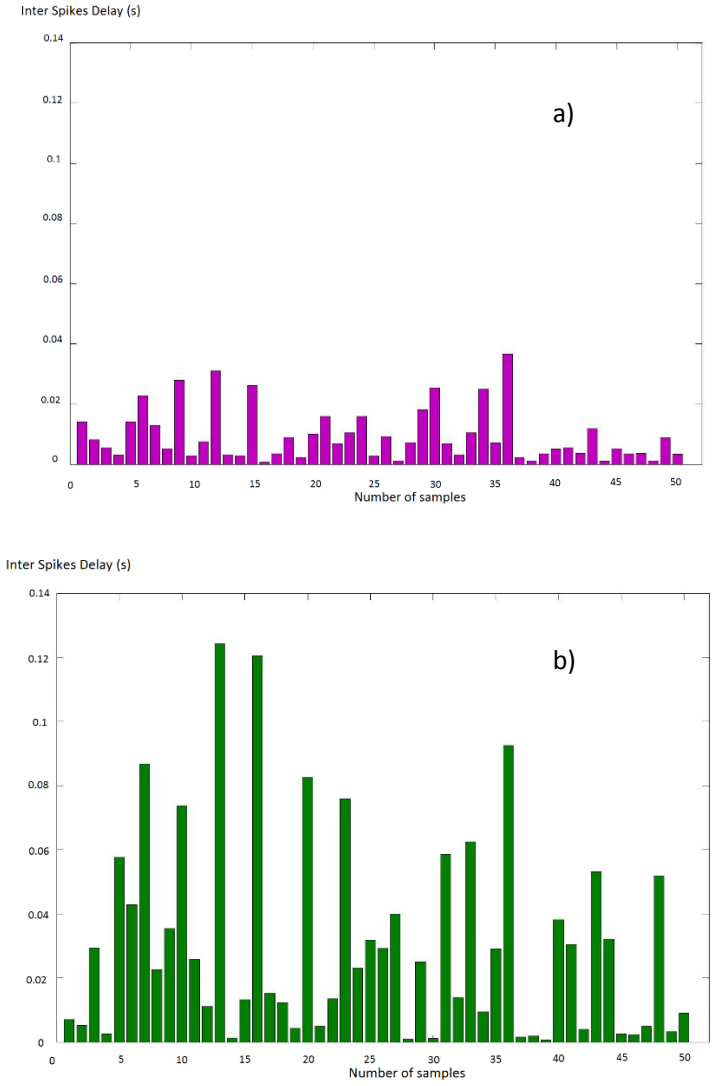

FIGURE 82: INTER SPIKES DELAY GENERATED WITH THE POISSON GENERATOR PRESENTED IN EQ. 126 FOR A 50DB SOUND WAVE AS INPUT (A) OR A 30 DB SOUND WAVE AS INPUT (B)

2. Spikes train frequency rate:

As previously described, spike trains are time series of multiple waves starting at different times (t_p). We hence defined a spikes train ($V_{MW}(x, t)$) as the addition of non-overlapping waves starting at different times (eq. 127):

$$V_{MW}(x,t) = f_1\left(t - \frac{x}{v_\varphi}\right) + f_1\left(\left(t - t_p(1)\right) - \frac{x}{v_\varphi}\right) + f_1\left(\left(t - t_p(2)\right) - \frac{x}{v_\varphi}\right) + \cdots \quad \text{EQ. 127}$$

$$V_{MW}(x,t) = \sum_{n=1}^{Nb_{spikes}} f_1\left(\left(t - \sum_{m=1}^{n} t_p\,(m)\right) - \frac{x}{v_\varphi}\right)$$

where Nb_{spikes} is the number of spikes generated and $t_p(m)$ is the inter spikes delay defined in the previous Section. This number depends on the wave amplitude as shown by diverse measurements [39, 186]where further details are available to define precisely the number of spikes associated with the amplitude of the membrane depolarization.

The mathematical function described above does not perfectly model spike train as overlapping between two spikes is hence possible. However for simplification purposes we presented the general form of the equation which, once restricted the interval of t_p, gives realistic spikes train.

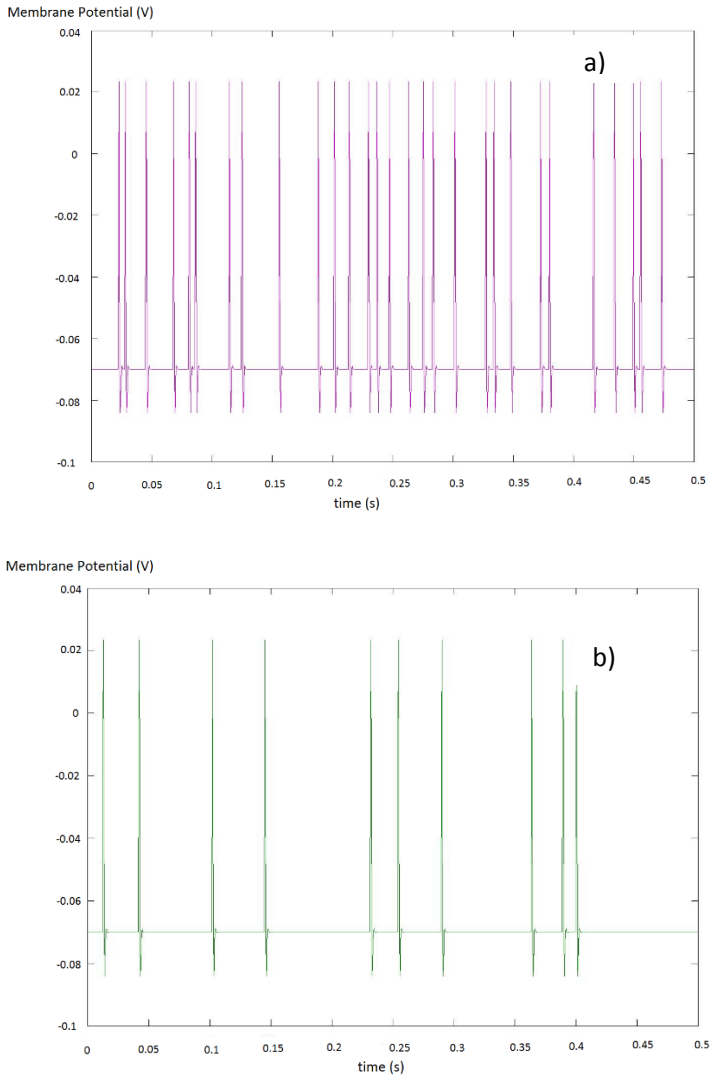

FIGURE 83: SPIKES TRAIN GENERATED IN A UNIQUE NERVE FIBER FOR A 50DB SOUND WAVE AS INPUT (A) OR A 30 DB SOUND WAVE AS INPUT (B)

The addition of AP function delayed by the ISD defined in Figure 82, permitted to generate a theoretical spike trains running on a single nerve fiber (Figure 83). These results are in accordance with simulations results obtained from auditory nerve fibers of animals presented in [291, 292], where the frequency of spikes for same amplitude and frequency stimuli is comparable with our simulations data.

As outlined in the Zalewska and Hausmanowa-Petrusewicz experiment [293], the amplitude of the APs may also vary depending on the nerve fiber diameter (d). The relation extracted from [187] is shown eq. 128 (we considered the relation as almost linear, so we performed a first order polynomial extraction):

$$\alpha = k\, d \qquad \text{EQ. } 128$$

where d is the fiber diameter, α is the amplification factor and k a scalar evaluated to be around 0.01.

Once the Basilar Membrane is excited due to a mechanical wave, a special place is excited in relation to the wave frequency. The BM excitation results in variation of several IHC membrane potential, resulting in a packet of nerve fibers firing.

The sum of all the APs generated in the different nerve fibers is of importance in the computation of the Compound Action Potential (CAP) (later described in Section I.D.2).
This packet of single fiber waves (called $V_{AN}(x,t)$ or CAP) is expressed in eq. 129

$$V_{AN}(x,t,d) = \sum_{n=1}^{Nb_{fibers}} \alpha(d) f_1\left(t - \frac{x}{v_\varphi(d)}\right) \qquad \text{EQ. } 129$$

where α is the amplitude factor associated with the fiber diameter d, v_ϕ is the wave velocity which also depends on the fiber diameter d and Nb_{fibers} is the number of nerve fibers stimulated by the mechanical wave with the same diameter (more information about this number can be found in Section I.D.1).

APs propagation on several nerve fibers due to the same excitation phenomenon (hence starting at the same time), which represents a packet of nerve fibers excited, should not be confused with spike trains, which represent the consecutive excitement (at various time interval) of a single or multiple nerve fibers.

The mathematical series of the multiple excited nerve fibers (V_{AN}) starting at different time intervals is used to model spike trains of several nerve fibers. Delays between parallel nerve fibers excited from the same stimulus may also exist in practice as the AP generation is probabilistic but is poorly described in current literature. Hence this phenomena was discarded in our nerve model.

This mathematical description permits to model theoretical cochlea nerve stimulation over time and is expressed in eq. 130. Furthermore this mathematical description can also be used to compare the auditory nerve fibers output with experimental data (as eCAPs on overall or fractions of the auditory nerve are usually measured in practice), possibly detecting nerve fiber damages.

$$V_{AST}(x,t,d) = \sum_{n=1}^{Nb_{fibers}} \alpha(d) \left\{ \sum_{k=1}^{Nb_{spikes}} f_1 \left(\left(t - \sum_{m=1}^{n} t_p\,(m) \right) - \frac{x}{v_p(d)} \right) \right\} \qquad \text{EQ. } 130$$

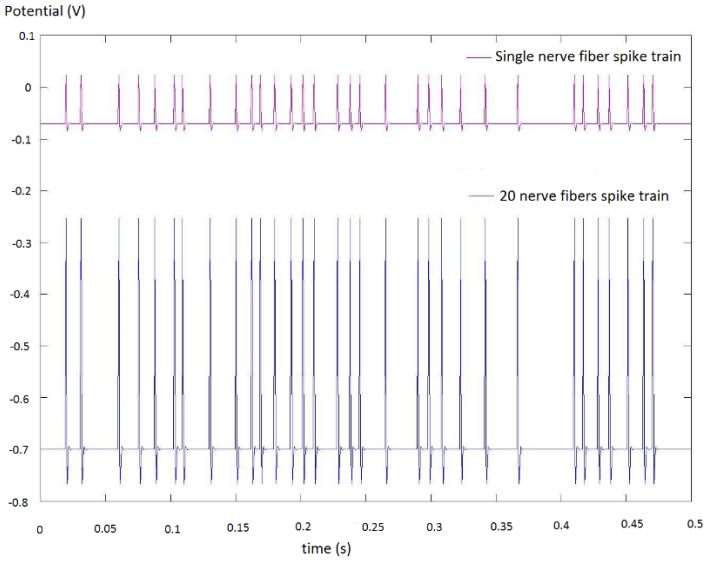

FIGURE 84: SPIKE TRAINS GENERATED AS A RESULT OF MULTIPLE NERVE FIBERS FIRING IN THE SAME TIME FOR A 50DB SOUND WAVE AS INPUT. THE AMPLITUDE AND THE VELOCITY OF THE ACTION POTENTIALS PROPAGATION CHANGE AS MULTIPLE NERVE FIBERS ARE INCLUDED.

Single cell neural spike recording using a microelectrode is often challenging due to local neurons activity. Single nerve cell activity determination often requires spike sorting algorithms in order to separate the recorded electric signal into different nerve cells potential. In that intent this sorting often uses the main feature of spike shape: the spike amplitude (or the ratio between its maximum and minimum values) [294]. In consequence to measure the activity of a neuron, a voltage threshold trigger may be used to separate the nerve cell activity from other neurons activity. However in case of synchronous firing of multiple nerve fibers or if the nerve cell recorded has a small diameter

compared to its neighboring cells for instance, clustering algorithms (such as k-clustering or Bayesian clustering for instance) are employed to extract the targeted neuronal activity [294].

Several different neurons may generate action potentials having very similar shapes in the recorded waveform such as when the neurons are similar in morphology and about equally distant from the recording electrode [294]. Dendritic action potentials may also mix with axonal action potentials making much more complex single neuron activity extraction. For more accurate spikes clustering, the number of recording electrodes may be increased, each electrode having different locations (as with tetrodes for instance) [295]. In fact if multiple recording electrodes are used, neighboring cells will be less likely to be equidistant from both electrodes [295]. Furthermore multiple electrodes also permit to study the activity of local population of neurons, provided efficient spike sorting and nerve cells characterization.

Many of the spike-sorting techniques for single electrodes extend naturally to multiple electrodes. Besides other methods, initially developed for multiple source analysis, may also be applied such as Principal Component Analysis (PCA) and Independent Component Analysis (ICA) [294, 296, 297]. ICA have been used successfully in various analysis of EletroEncephaloGrams (EEG), however it requires a greater (or equal) number of electrodes than the number of neurons studied [298, 299]. Other techniques based on wavelet transform are also available in literature [300].

Various issues are still difficult to address such as burst firing neurons, electrode drifts or non stationary background noise [288]. Figure 84 shows the simulation result of eq. 130 with a packet of 20 nerve fibers which diameter varies linearly from 5µm to 15 µm (and with corresponding AP propagation velocities varying from 17 m/s to 52 m/s according to [187]). The mathematical expectancy of the exponential generator was set to 15ms.

To get closer to practical measurements neuronal noise has to be included. Sources of neuronal noises are reviewed in the following documents [301-303] and only the most significant ones will be described in this Section.

Thermal noise is present in every biological systems due to thermal carriers agitation and is probably contributing to most of the noises presented thereafter. In the model developed, we included two sources of thermal noise, the one associated with nerve cells (that we supposed myelinated) and the one associated with the electrodes (made of platinum or tungsten). The standard deviation mathematical expression of the thermal noise (σ_{WN}) and the associated numerical values can be found in eq. 131.

$$\sigma_{WN}^2 = 4kTBR \qquad \text{EQ. } 131$$

where k is the Boltzmann constant, T the absolute temperature in Kelvin, B the noise bandwidth supposed equal to 1KHz (close to AP generation frequency) and R the resistivity of the material which was extracted from [304] for myelinated nerve fibers or from [305] for tungsten electrode

Channel shot noise is also present due to variation in the number of ions entering the postsynaptic channels as this number is discrete and fluctuating around a mean value [306]. Mathematical formulas of channel shot noise mean (μ_{SN}) and standard deviation (σ_{SN}) can be found in [307] and are recalled in eq. 132

$$\mu_{SN} = \lambda_{Poisson} * \int_0^\infty I(t)dt \qquad \text{EQ. } 132$$

$$\sigma_{SN} = \lambda_p * \int_0^\infty I^2(t)dt$$

where λ_p is the mathematical expectancy of the Poisson generator presented in Section I.C.1 and I is the current caused by the movement of one ion across the membrane. To simplify we supposed that I has the same shape of the resulting AP and its maximal value was fixed to 20mA.

Probabilistic gating of voltage-gated ion channels generate voltage noise in neuronal membranes which is called channel noise [308, 309]. It was determined that this noise may limit the reliability of neuronal responses to identical stimuli, as this noise is able to generate post synaptic APs. Channel noise has been shown to have a 1/f noise PSD [306]. The variance associated with channel noise is described in [310, 311] and rewritten in eq. 133

$$S_{CN} = \frac{S_{C0}}{f^\alpha} \qquad \text{EQ. } 133$$

$$\sigma_{CN}^2 = \int_0^\infty S_{CN}(f)df$$

restricting the computation of the variance in the $[f_l;f_h]$ interval, gives:

$$\sigma_{CN}^2(f_l, f_h) = \int_{f_l}^{f_h} S_{CN}(f)df \approx \ln(\frac{f_h}{f_l}) \qquad \text{EQ. } 134$$

where S_X is the PSD of the channel noise integrated from frequency f_l to f_h. f_l was fixed by the simulation time and f_h by the refractory period of the AP. S_{C0} is the maximum amplitude reached by the noise PSD and α the slope of the PSD in a logarithmic scale. We used a Matlab® pink noise generator with a filter in $\sqrt{\frac{S_{C0}}{f^\alpha}}$ to model channel noise.

Synaptic noise is the most influencing noise in nervous tissues. It is caused by packets of neurotransmitters released in the synapse from presynaptic networks. It is often described as stochastic with a PSD (S_{SN}) with Lorentzian shape such as indicated in [312-314] and reminded in eq. 135. The variance of a such stochastic process can be approximated to the integral of its PSD as described in [312].

$$S_{SN} = \frac{S_{S0}}{1 + \frac{f}{fc}^{m}} \qquad \text{EQ. 135}$$

$$\sigma_{SN}^2 = \int_0^{\infty} S_{SN}(f)df = \frac{\pi f_c S_{S0}}{2}$$

where S_{S0} is the maximum amplitude of the PSD, f_c is the cutoff frequency and m a scalar coefficient. According to [312], S_{S0} was fixed to 0.1, f_c to 70Hz and m to 2.25.

Synaptic noise is caused in part by channel noise as the channel density fluctuations in the presynaptic cell results in change in vesicles release in the synaptic cleft. In addition carrier agitations due to thermal noise participates to channel noise and synaptic noise generation. In consequence those different noises are highly correlated.

Figure 85 shows the neuronal noises we simulated. The inclusion of these noises to the simulated spike train is displayed in Figure 86, which is comparable to experimental auditory nerve fibers spike trains fulfilled in [315-321]. The amplitude of the simulated signals is often different from the measured ones since it greatly relates on the measurement technique used.

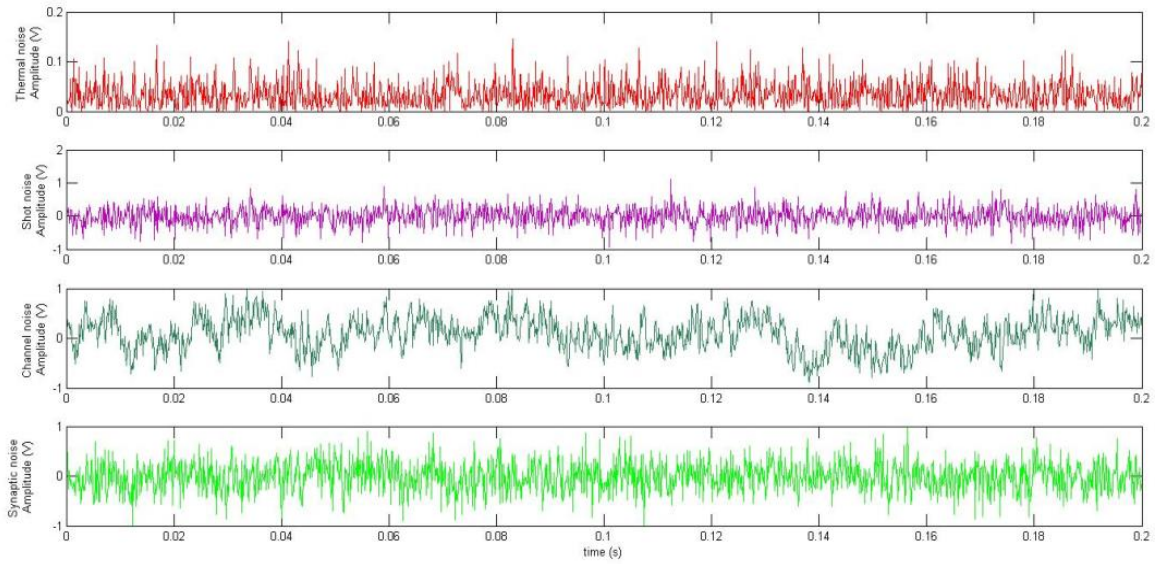

FIGURE 85: NEURONAL NOISES SIMULATED

The developed neuronal noises model is still incomplete and under study. In fact synaptic noise or channel noise are able to generate spikes which increases the unpredictability of spikes generation timing. By modifying synaptic channels dynamics including such noises as performed in [309], spike train generation could also depends on these noises.

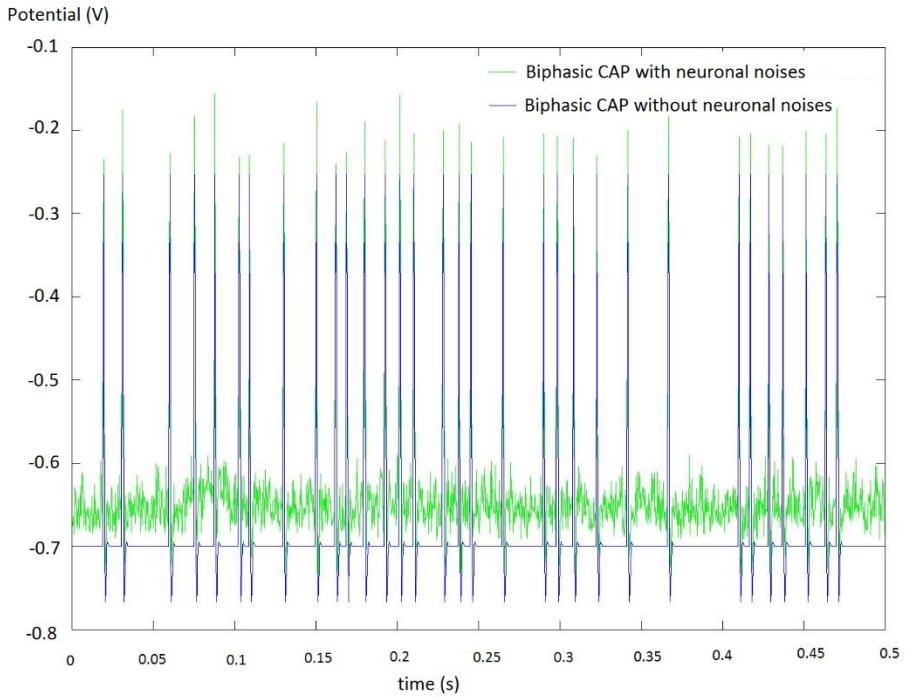

FIGURE 86: SPIKE TRAIN SIMULATED WITH NEURONAL NOISES INCLUSION

It has been shown that spontaneous activity can facilitate neuronal information transmission. The discovery of stochastic resonance in non linear systems using a threshold for information transmission such as neurons, has suggested that unpredictable noise is beneficial [252]. Subthreshold stimuli which cannot stimulate a nerve response may, given an optimal noise level, reach the threshold value and result in a spike production. Furthermore it has been advanced that the nervous transmission is more efficient when the signal is multi-frequential and not periodic, hence suggesting an advantageous role for the noise in enhancing sensory information transmission [252].

D. Cognitive science and electrophysiolological recording techniques

1. Electrophysiological recording techniques

The complete list of recordings procedures is outside the scope of this document. The classification and presentation of some of the nowadays commonly used electrophysiological recording techniques is proposed in this Section.

Ions channels protein are usually studied with patch clamp or voltage clamp experiments [322]. Current clamps are used mainly to study postsynaptic membrane potential variations following neurotransmitter introduction in the synapse [323].

Amperometry major utility is the study of vesicles release from the intracellular space to the extracellular space. This technique is of particular value in studying cell chemical communications and may be used to study vesicles release in the presynaptic cells [324].

Optical physiological techniques are also available and use fluorescent proteins or voltage sensitive drugs to provide measurements of neuronal firing activity of single or multiple cells [325]. Voltage sensitive drugs are used to detect membrane voltage change and provide information of the AP duration and velocity.

To better monitor electrical activity inside cell organelles where electrode insertion is not possible (as in mitochondria), potentiometric drugs may be used. They also permit the study of the spatial propagation of the AP on the surface of a single neuron[326].

The study of neurons activity can be performed in vivo (with surgical insertion of electrodes close to the neurons as in ElectroCorticoGraphy (ECoG) for instance) or in vitro.

Single nerve recordings gather the techniques used to record a single neuron frequently employing one microelectrode insertion inside the intracellular space.

Multi unit recordings are made by often larger electrodes inserted in the extracellular space. It is a less precision requiring method, which may be used in living animals, but often require spikes sorting in order to obtain the diverse neurons proper activity.

Then extracellular field potentials recordings techniques such as ElectroEncephaloGraphy (EEG), ElectroCorticoGraphy (ECoG) or MagnetoEncephaloGraphy (MEG) permit to study relations between different nerve cell groups and are of great interest for brain comprehension. However these

recordings involve summation of different neuron activities and are hence prone to noise corruption.

The propagation of a single AP or several APs running on nerve fibers belonging to the same nerve may also be investigated in order to detect nerve ruptures or myelinations defects. Packet of nerves fibers depolarization due to the same stimulus is called Compound Action Potential (CAP). The recording of the propagation of an AP or a CAP may be performed by putting both the recording electrodes close to the nerve fiber (biphasic recording) at different places along it. In monophasic recording one electrode is inserted inside of the nerve or in the extracellular space and the other one is at the ground.

Communication process by which measurements are made and data transmitted from inaccessible locations is called telemetry. Using voltage telemetry, voltages between electrodes can be recorded. The Modiolus current model (defined in [327]) permits to characterize intracochlear impedances.

Neural Response Telemetry (NRT) circuitry and associated software may also be used to send a stimulus to an electrode and records the evoked Compound Action Potential (eCAP) produced [328], which is defined as a CAP recorded from a sensory receptor such as the Spiral Ganglions Cells. Some CIs also included electric filed recording in these neighboring electrodes after central electrode activity. Using telemetry techniques, included in a great majority of modern CIs, facilitates device fitting and parameters tuning especially in young patients not able to communicate [327].

2. Compound action potential mathematical characterization

Physical experiments involving nerve fibers transmission often use compound action potential recording as it is often difficult to isolate only one nerve fiber. CAP results from the addition of simultaneous APs generated at the same time, in the same area, of several nerve fibers (CAP are usually recorded from an entire nerve). Each CAP contains the electric stimulation of several axons in parallel with different diameters, threshold and degree of myelination [329].

In this Section, only biphasic CAP recording is studied and mathematically defined. When a large stimulus is delivered to the nerve by electrode A, many axons fire and the signal recorded by two electrodes (B_1 and B_2 with B_1 placed very close to A and with B_2 placed farer in the axon) is used to measure a CAP [330]. CAP biphasic recording and measurement results expected are reported in Figure 87.

Spikes train are not included in the CAP simulation because the time needed for an AP to propagate from B_1 to B_2 (called t_{B1B2} which is defined in eq. 136) is much lower than the mean Inter Spike Delay which is around 15ms (cf Section I.C). To avoid unnecessary simulation time and because the spike train generation principle can be applied to CAP generation, we discarded inclusion of multiple spikes in biphasic CAP generation. In consequence we defined CAP by several APs, once per nerve fiber stimulated, but all starting at the same time.

$$t_{B1B2} = v_{\varphi} d_{B1B2} \qquad \text{EQ. } 136$$

where v_ϕ is the propagation velocity of an AP (cf Section I.H) and d_{B1B2} is the distance between the two electrodes B_1 and B_2

As a starting point we considered that only one AP defines a CAP (biphasic recording). Recalling that at time t_0, AP is generated at electrode B_1 and that at time t_{B1B2}, the same AP is received by electrode B_2, the potential between electrode B_1 and electrode B_2 (called V_{B1B2}) is equal to $V_{B1} - V_{B2}$. This potential (V_{B1B2}) is expressed in eq. 137

$$At\ t_0, \qquad V_{B1} = f_1(0,0), \quad V_{B2} = f_1(d_{B1B2}, 0) \sim 0 \qquad \text{EQ. } 137$$

$$At\ t_x > t_0, \qquad V_{B1} = f_1(t_x, 0), \quad V_{B2} = f_1(d_{B1B2}, t_x) \sim 0$$

$$\Rightarrow \forall\, t > O, \qquad V_{B1B2} = V_{CAP-1F-BI} = f_1(d_{B1B2}, t_x) - f_1(0, t_x)$$

where $V_{CAP\text{-}1F\text{-}BI}$ is the CAP produced by a biphasic recording in the case where only one nerve fiber was firing, and is equal to the potential difference between electrode B1 and electrode B2. f_1 is the forward propagation wave function defining an AP propagation (cf Section I.H).

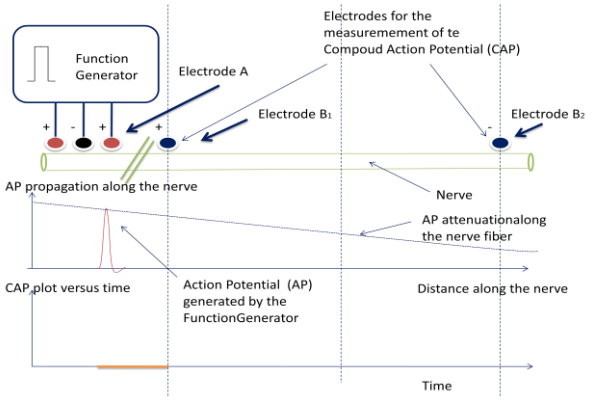

a)

b)

c)

d)

FIGURE 87: BASIC EXPLANATION DIAGRAM OF A CAP (BIPHASIC RECORDING). THE PROPAGATION OF AN AP ALONG A NERVE FIBER PERMITS TO RECORD A CAP. A PEAK STIMULUS IS SENT TO ELECTRODE A. THE RECORDED POTENTIAL OVER TIME (CAP) IS THE POTENTIAL DIFFERENCE BETWEEN THE RECORDING ELECTRODE B_1 AND ELECTRODE B_2, DURING THE AP PROPAGATION. THIS FIGURE SHOWS THE DIFFERENT TIME STEPS OF THE BIPHASIC CAP CREATION (ELECTRICAL SYSTEM REPRODUCED FROM [331])

As a nerve is composed of several nerve fibers, the previous equation was modified as exhibited by eq. 138

$$V_{CAP-BI}(x,t,d) = \sum_{n=1}^{Nb_{nfc}} \alpha(d)\left(f_1\left(t - \frac{xd_{B1B2}}{v_{\varphi}(d)}\right) - f_1(t - 0)\right) \quad \text{EQ. 138}$$

where $V_{CAP\text{-}BI}$ is the theoretical potential of the theoretical biphasic recorded CAP, which depends on t and on the distance between the two electrodes. Nb_{nfc} is the number of nerve fibers with the same diameter d included in the CAP. α is the gain in amplitude associated with the fiber diameter (d) and v_ϕ is the velocity of the AP propagation both defined in Section I.C.

It should be indicated that a CAP can represent the APs propagation of a packet of nerve fibers excited (V_{AN} in eq. 129 (monophasic recording)) or the potential variation between the two recording electrodes during APs propagation (biphasic CAP recording).

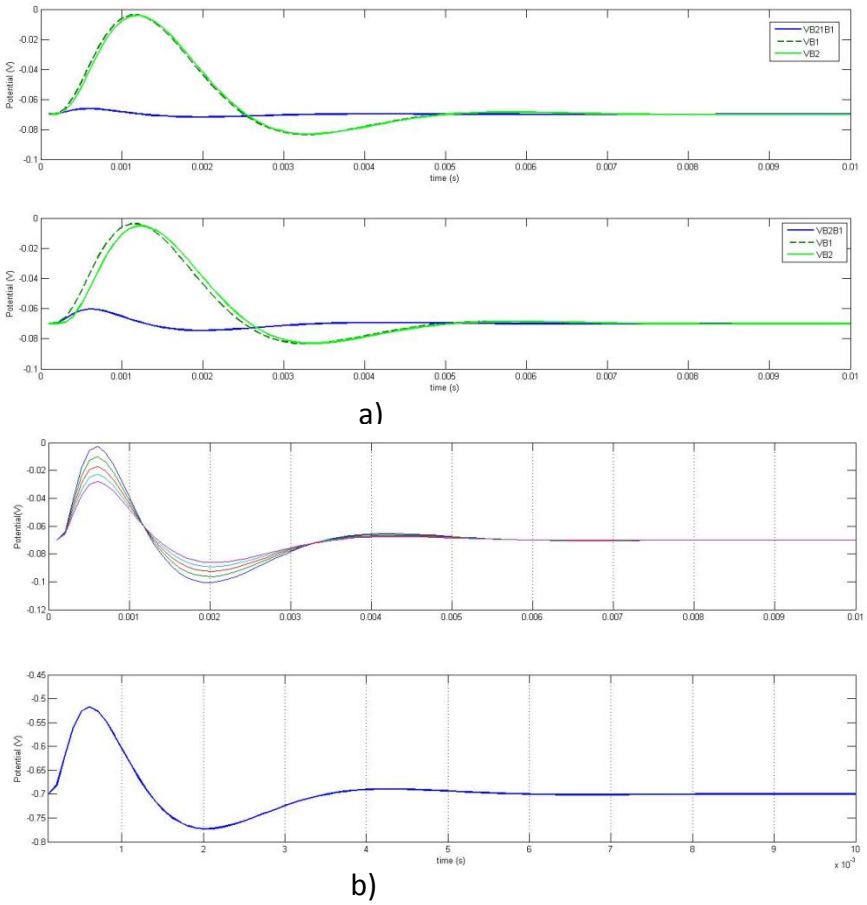

FIGURE 88.A) BIPHASIC CAP CONSTRUCTION FOR A SINGLE NERVE FIBER. BIPHASIC RECORDED CAP IS DEFINED AS THE DIFFERENCE POTENTIAL BETWEEN ELECTRODE B1 AND ELECTRODE B2.B) CAP SIMULATION FOR MULTIPLE NERVE FIBERS WITH DIFFERENT DIAMETERS HENCE DIFFERENT PROPAGATION VELOCITIES AND AMPLITUDE OF THE APS.

Figure 88.acompares the theoretical CAP (biphasic recording) obtained with a single nerve fiber. The electrode B1 was suppose at a distance of 10µm from the stimulating electrode and the electrode B2 was at a distance of 53µm from electrode B1. In a second experiment, electrode B1 and B2 were separated by 106µm and the resulting biphasic CAP value was increased as shown in the Figure.

Just as pointed out in Figure 88.b as 20 nerve fibers with different diameters varying linearly from 6µm to 15µm (hence with different velocities) were included in the multiple fibers CAP computation, the multiple nerve fibers CAP resulted in a smooth version with greater amplitude of the single fiber CAP. It should be specified that for such electrode distance, the different velocities of the nerve fibers have almost no influence on the overall CAP.

E. Closure remarks

The development of a new analog model for action potential propagation along the nerve fibers membrane is proposed. This new propagation model (presented in Section IV.B) depicts same wave properties of measured action potentials and may be of interest in brain cognition studies. In addition the spike train modeling based on statistical neuronal properties was performed. This model can further be refined in future work by including more nerve fibers diameters (hence nerve fibers velocity) as well as asynchronous delays between spikes resulting in more realistic spike train diagram. Adding neuronal noise to our ideal spike train model improved spike trains diagrams that fitted with actual measurements.

Summing Action Potentials propagation of different nerve fibers permitted to estimate the evoked compound action potential produced which is commonly used as a metric in cochlear implant back telemetry.

F. Work submitted

- New electric system analog of Action Potential propagation with equivalent wave dynamics, U. Cerasani, W. Tatinian, IEEE Communications Magazine, 2014

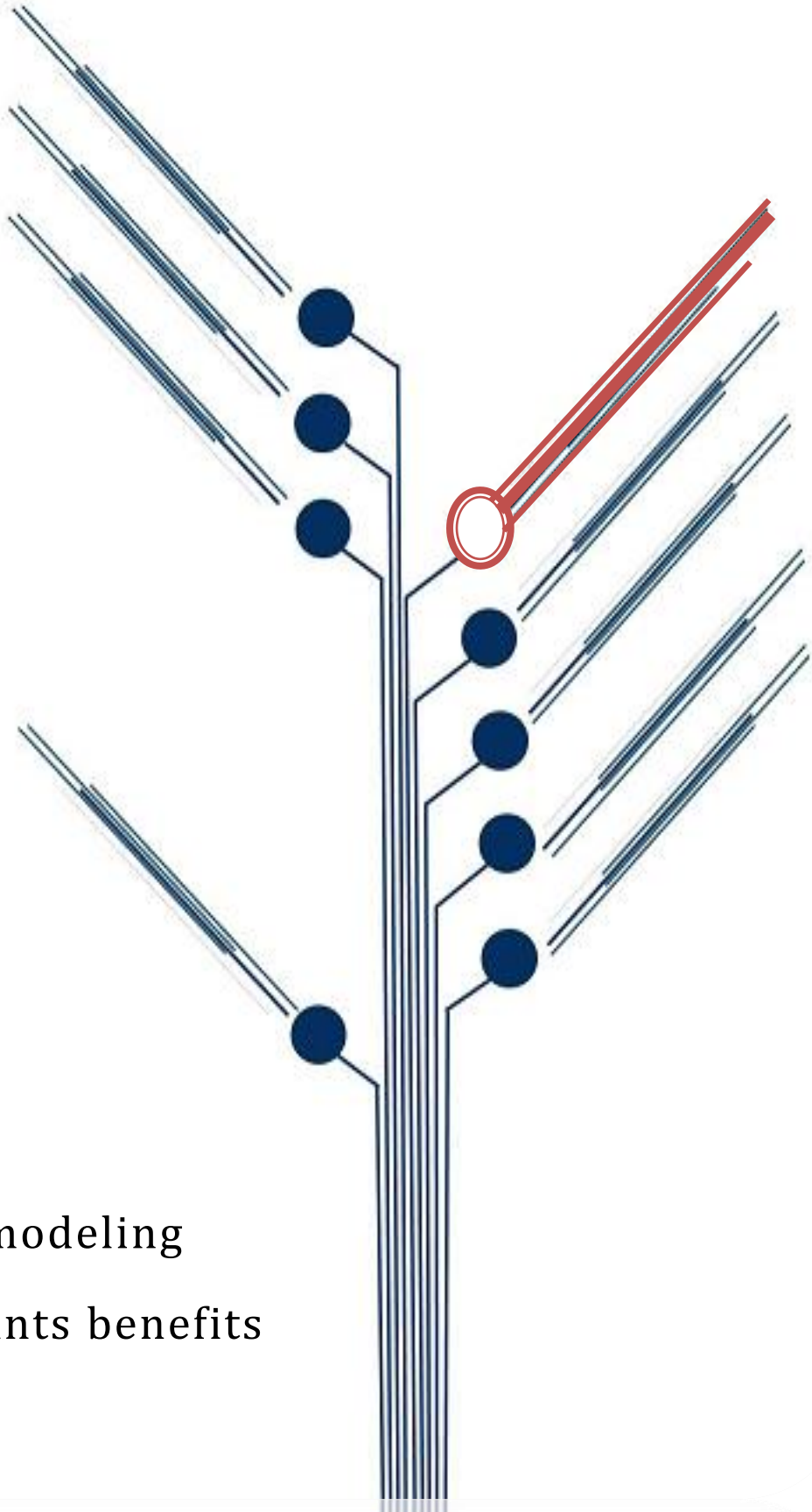

Chapter V:

Damaged cochlea modeling and cochlear implants benefits

A. Opening notifications

Cochlear Implants (CIs) are very efficient neurostimulating prosthesis. However CIs still present many drawbacks and the hearing sensation brought to these patients is often restricted to a close frequency range, requiring a significant learning process. The review of the major limitations of CIs is proposed in this Chapter such as the electrodes and nerve fibers rough interface resulting in limited number of stimulating channels. Based on this review, we proposed a new electrical model of this interfacing based on the physiology of the cochlea which may define the electrode array electric specifications. Furthermore we reused the Spiral Ganglions Cells (SGC) repartition map inside the cochlea, to express the number of nerve fibers stimulated by each electrodes. This map was of importance to permit amplitude sound restitution in cochlear implants. Then, using a modified Discrete Fourier Transform (DFT) expression, we developed a program reproducing the sound that may be heard by deaf people using cochlear implants. Successively a hypothetical algorithm for electrodes selection is discussed.

B. Introduction to cochlear implants

CIs are used to remedy partial or complete hearing loss. They allow direct stimulation of the auditory fibers with an electrodes array designed to reproduce the stimulus that would be generated by a healthy cochlea.

Only current commercially available CIs architectures are reviewed in this Section.

To do so, the behind-the-ear part of the CI contains a microphone that captures the acoustic waves and transforms them into an electrical signal. Then, this signal is processed by a Digital Signal Processing Unit (DSP) which uses speech coding strategies in order to produce the currents that will be sent to the electrodes [332]. The frequency of the sound determines the electrodes to stimulate and the sound intensity is directly proportional to the current sent to these electrodes. This signal is then transferred to the receiver using a RF link composed mainly of a PA (as there is not battery in the stimulator) and a coil antenna. The transmit frequency is defined by the chosen ISM standard (for instance 13,56MHz, 433MHz, 866MHz, 2.45GHz). Both Figure 89 and Figure 90 which display the general components of the Cochlear implant were inspired by Cochlear® available products and modeled using the 3D modeling software Autocad®. The external part of the ear was provided from [71]

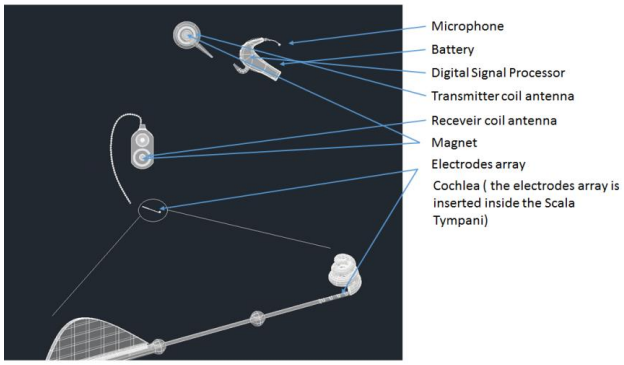

FIGURE 89: X-RAY REPRESENTATION OF THE COCHLEAR IMPLANT (INSPIRED BY COCHLEAR® DEVICES AND MODELED WITH AUTOCAD®)

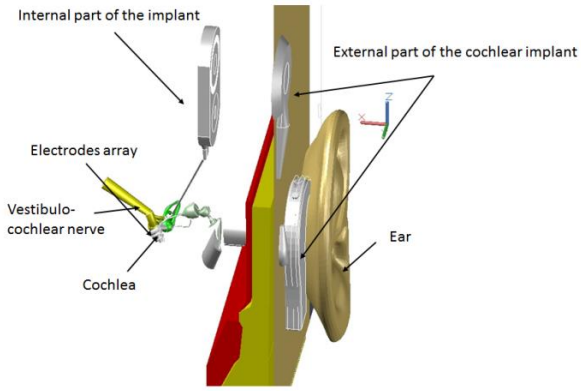

FIGURE 90: COCHLEAR IMPLANT (MODELED WITH AUTOCAD®)

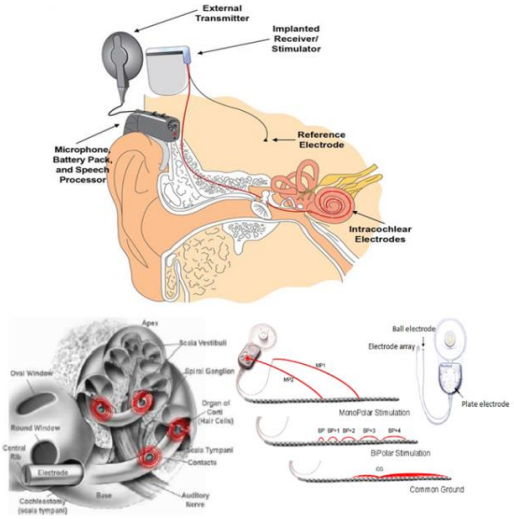

FIGURE 91: COCHLEAR IMPLANT OVERVIEW. ELECTRODES ARRAY ARE INSERTED INSIDE THE SCALA TYMPANI OF THE COCHLEA. VARIOUS TYPES OF ELECTRODES ARRAY EXIST, THE CURRENT ONES ARE USING BIPOLAR STIMULATION FOR MORE ACCURATE NERVE STIMULATION. THE FIGURES ARE ATTRIBUTED TO [1], [333] AND TO [334]

An hermetically sealed stimulator located within the patient's head, close to the skull, is held in place by a magnet. This device is composed of active electronic circuitry [332] (containing a data decoder, a data distributor, a Programmable Gain Amplifier (PGA), …) which derives power from the RF signal and converts it into electric current sent to a set of electrodes (contracting the cochlea and stimulating the auditory nerve) [11, 12, 332].

The integrated part is encapsulated into biocompatible materials (further details in [332]).

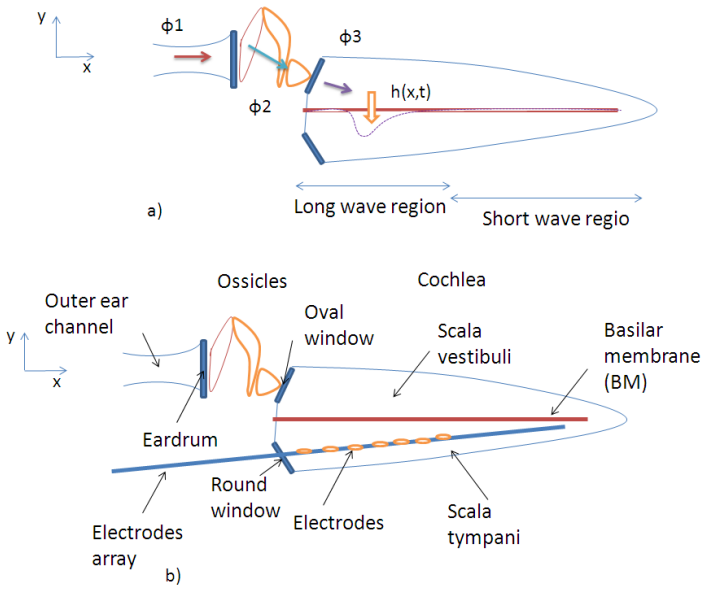

FIGURE 92.A) EAR SCHEMATIC WITH INCLUSION OF THE ELECTRODES ARRAY INSIDE THE COCHLEA. B) EAR SCHEMATIC AND THE WAVE PROPAGATION LEADING TO A BASILAR MEMBRANE HEIGHT CHANGE (H(X,T))

1. Coding strategies and electrodes array design

Improvements in coding strategies have produced large ameliorations in speech reception performances in CIs users [1, 335]. The use of multiple sites of stimulation also called channels have ensured higher scores in words perception tests. However the use of active channels is currently fixed to 6-8 in current CIs (cf [6]). In fact various studies have shown that the increase in channels number does not produce better hearing perception and may eventually degrade it [1, 336]. Similarly increasing the number of electrodes from 8 to 20 does not improve the hearing accuracy in CIs patients [337], [336]. It may be deduced and further demonstrated by various authors [338], [339], [333], that the very strong electrical coupling between electrodes (electric field interferences between neighboring electrodes) is responsible for the lack of precision of cochlea area stimulation.

To overcome this issue, the electrodes array have evolved. First ground based stimulation showed very high coupling between electrodes, this coupling was reduced using monopolar stimulation where the ground wire is separated from the electrode array wire, increasing electric field directivity and hence nerve fibers targeting. Best stimulation was achieved with the help of multipolar stimulation (in bipolar stimulation the nearest electrode to the firing electrode is used as ground electrode. Another technique termed "field steering" uses the two nearest neighboring electrodes as ground electrodes. As noted in [1], field steering may result in more accurate nerve stimulation allowing more channels recognition by CI patients).

Electrodes array associated with Acoustic Stimulation (EAS) are also commercially available, increasing the sound perception in low frequencies. As the low frequencies are detected by the apex of the cochlea, this part of the cochlea should be intact and working for the success of this system. As demonstrated by various studies such as [1], [340], the hearing amelioration in low frequencies and the noise distinction for these frequencies are indicated by numerous patients testing the EAS system. Binaural stimulation also offers great advantages facilitating sound localization and hearing perception as the cochlea may be damaged at different places in the two ears.

Currently implemented speech coding strategies use parallel bandpass filter bank to extract the frequency components of the sound signal recorded by the microphone. Then the envelope of these signals are retained using lowpass filters. It was demonstrated by various authors [341] that Hilbert Transformation can be applied to sound waves allowing its splitting into envelope and fine structure. As envelope was found to be the main carrier of voice information, only the envelope of the sound is further processed. Fine structure appears to be of importance in music perception, better noise separation,… [1]. The Spectral Peak (SPEAK) or Advanced Combination Encoder (ACE) strategies selects the n-signals among the m channels with the highest amplitude (n-of-m strategies). The stimulus are sent only to the electrodes that correspond to the n-channels selected. Differences between the stimulation rates, number of channels selected and other parameters distinguish these n-of-m speech coding strategies. More information are available in [1], [332]. Other speech coding strategies implemented in present day are the Continuous Interleaved Sampling (CIS) or HiRes. These strategies use all the envelope extracted outputs and each of these are directed toward a single electrodes. Using delayed biphasic pulse for each single electrodes, the corresponding electrodes are interleaved in time, ensuring non simultaneous electrodes stimulation [1], [334], [342].

Because the number of electrodes is greater than the number of active channels available, various authors decided to simultaneously stimulate electrodes with varying intensity to achieve better spatial resolution. Although arguable, when two neighboring electrodes (HiRes 120 coding strategy) or more electrodes (hybrid stimulating strategies) are stimulated in a particular way, it seems to narrows the stimulation area, allowing more precise nerve fibers selectivity. These new intermediate channels created, also called virtual channels, may allow more precise cochlea stimulation increasing the frequency selectivity reached by the implant. Currently there are 120 virtual channels in the HiRes120, which uses only two neighboring electrodes to create these channels whereas 300 virtual channels can be reached using 4 consecutive electrodes stimulation (FECSS strategy not currently implemented in commercially available CIs) [1, 338, 343]. Results using these virtual channels are very encouraging (approaching 100% recognition scores in white noise) [338]. It should be noted that the virtual channels can be created with a single current source as nerve fibers stimulation duration is about 4ms (absolute refractory period of the nerve fiber), consequently neighboring electrodes stimulation time lower than nerve fiber absolute refractory period but with added delay between the electrodes stimulation will result as a single stimulation for the nerve fibers selected.

Then amplitude mapping is performed, which permits to convert acoustic levels into current amplitudes [334]. The diverse steps of the signal transformation in the CI are indicated in Figure 93.

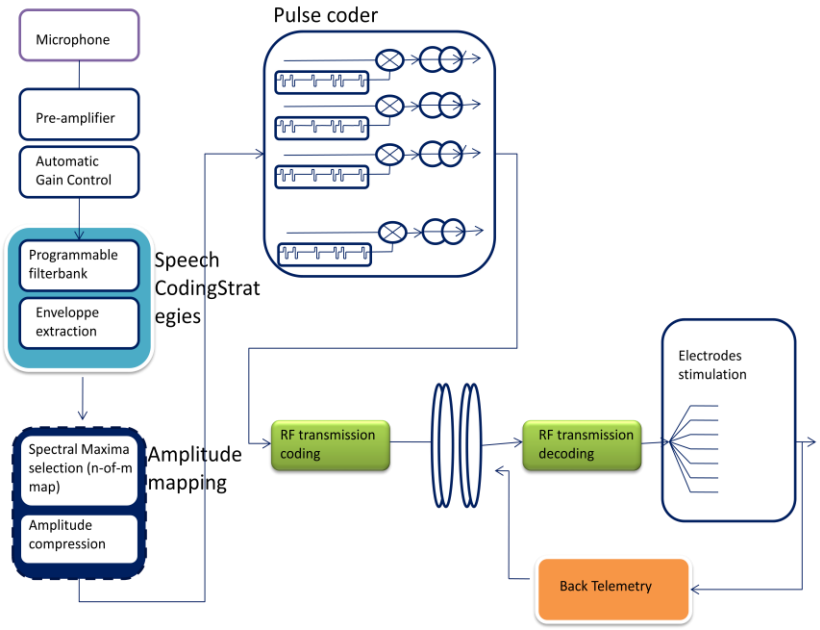

FIGURE 93: CURRENT COCHLEAR IMPLANTS ARCHITECTURE OVERVIEW. MAINLY BASED ON THE STUDY OF [255] AND [254]

Other architectures such as Asynchronous Interleaved Sampling (AIS) has been proposed. They associate an Integrate-and-Fire block to each channel where the first channel to fire is the one with the highest average amplitude (more information about this architecture may be found in [344, 345]). Traveling wave based architectures [346], which are closer to the biophysical processes operating inside the cochlea, have also been developed.

The study of stimulation rate of electrodes is complicated by the number of different CIs available and shows important variations between patients. As stated in Section I.B, CIs directly stimulate the nerve fibers. Considering the absolute refractory period of the action potentials as around 4ms, we may expect no further improvement with a stimulation rate greater than 250 pulses per channel (pps/ch). Higher stimulation rates may reproduce the stochastic stimulation of the nerve fibers, decreasing the Inter Spikes Delay (ISD), and hence resulting in a stimulation perceived with higher magnitude by the brain. Results from various documents [334, 347] showed an optimum in hearing restoration for stimulation rates between 350 pps/ch to 500pps/ch, although it was greatly varying between patients. Stimulation rates above 1500 pps/ch may result in some patients in disturbances such as tinnitus [347].

Biphasic current pulse is preferred for electrode stimulation because there is not net current, avoiding long lasting residual currents [327]. As previously stated in Section I.B.1, the negative value of the biphasic peak may decrease the absolute refractory time of the Action Potential (AP), maybe explaining why rates of stimulation superior to 250 pps/ch are optimal.

2. RF transmission link in cochlear implants

Wireless inductive power link brings energy to the internal part of the implant as current CI contains no battery. Data telemetry and power transfer uses the same pair of inductively coupled coils[14]. Bit coding is usually required for wireless transmission robustness (and is different among commercially available CIs, some of them relying on On OFF Keying (OOK), others on Pulse Width Coding (PWC), etc.)[332]. Nowadays most of the CIs utilize the Amplitude Shift Keying (ASK) modulation for RF transmission, but the carrier frequencies used are diverse. This modulation is preferred because of easier implementation and lower power consumption. Furthermore frame coding is required to transmit functional information such as pulse amplitude or pulse duration [332].

3. Power consumption of the implant

As CIs must hold behind the ear, it should be as light as possible. This requirement greatly impacts the battery size and hence the battery lifetime [14]. Power consumption reported on commercially available CIs with present days are between 20mW and 100mW for the three different major brands of CIs manufacturing companies [332]. The current typical power consumption associated with the electrodes stimulation varies between 1mW to 10mW, the power dissipated in the RF link is around 10-20mW and the most consuming part of the implant is associated with signal processing and is around 20mW [348]. However electronic technology is evolving amazingly fast and CIs significant improvements are expected, as described by modern research.

In [349], a DSP architecture for use in CIs consuming around 1.7mW (with a standby power dissipation of 330µW) is described. Recently CIs processors with 250µW of signal computing power have been created. Besides ultra low power Biomedical Signal Processors (BSP) are being developed consuming few µW at MHz frequencies when running basic algorithms [350-352]. RF link efficiency is very impacted by the reduction in power consumption. Low RF power consumption (by appropriate class E amplifier conception) of around 100µW with 60% of link efficiency is presented in [353]. Ultra Wide Band (UWB) transmission may be used instead allowing reduced power consumption (below 100µW), low spectral perturbations and increased robustness against interferences [354, 355].

Low consuming power electrodes (dissipating only 750µW of power) are presented in [356]

A recent implantable chip consuming less than 1mW is proposed in [357]. Other documents indicate that bionic ear circuitry consuming less than 3mW of power with a coil separation distance of 5mm can be elaborated [353].

In addition, micropower designs are also available for various blocks of the CI such as microphone, preamplifier, AGC and VGA. These might be adapted and integrated to the overall system [353, 358].

C. Electrical analog of electrodes and nerve fiber interface and associated equations

The aim of the electrodes inserted inside the cochlea is to generate an AP once a sound is perceived. Their selection mainly depends on the wave frequency.

Consequently to obtain the same AP at the nerve fiber using only electrodes stimulation, two possibilities exist. First the direct nerve fiber stimulation can be made by changing the nerve membrane potential in order to produce a membrane depolarization above the threshold of Voltage Sensitive Na+ Channels (Na_v) to create an AP [359]. The second solution consists in opening the potassium channels of the stereocilia to recreate the complete stimulation process. As Hair Cells (HC) or stereocilia are dysfunctional in the vast majority of implanted patients, only the first mechanism was considered in this work.

Electrical model of electrodes inserted within the cochlea have been proposed by Hartmann *et al.*[360], where the spatial distribution of electrical potential was measured for intracochlear stimulation. In addition, electronic model of electrode/neuron coupling is available in [361] in order to reveal the most efficient coupling conditions. However, both models lack of physical connection with AP generation. In this document, we present an electrical description of the electrodesclose to the organ of Corti in order to obtain theoretical minimal stimulation voltage sent to the electrodes for AP generation. Furthermore, this model allowed us to link the stimulation voltage with the duration of the nerve fibers stimulation. Then the impact of surrounding electrodes were theoretically investigated. We developed a theoretical model developed for the organ of Corti associated with the electrodes. Thereafter, simulation results from SPICE software were presented.

1. Organ of Corti electrical analog

The electrical equivalent circuit of human tissue used in this paper is the one presented in Figure 94 and extracted from Cole and Cole impedance model [362], which has been shown to fit experimental data (cf Section I.D.1 for extended precisions). The human tissues considered were the ones presented in Figure 48. The value of R_s, R_p, $C_p$and C_h (defined in Section I.D.1) were obtained using available literature on impedance spectroscopy applied to human tissues. As the maximum hearing frequency is 22kHz, it was considered in this paper that R_p and C_p could be neglected as their model the energy loss and tissue response in high frequencies.

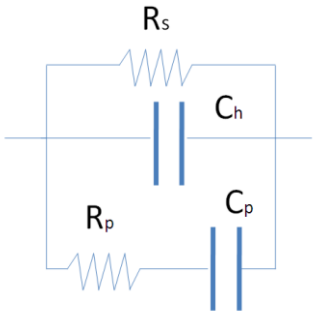

FIGURE 94: HUMAN TISSUE ELECTRICAL ANALOG [362]

To obtain the numerical values for R_s and C_h for all the tissues or interfaces, we used the physical equations for the capacitance (parallel-plate capacitor) and for the resistance computation (cylindrical resistor model) [30, 363].

The values of the relative permeability and electrical conductivity for the nerves were extracted from [364] or from [365] for platinum as electrodes are mainly composed of it. However as far as the author knows, no relative permeability or electrical conductivity was available for Deiter cells or Basilar Membrane (BM) tissue. As Deiter cells are mainly composed of microtubules[366], which are involved in mechanical transport as actin proteins found in muscles cells and because the width of the BM is negligible compared to the Deiter cell height, we chose to take the relative permeability and electrical conductivity of muscle cells to characterize those two tissues.

On the other hand, the computation of the capacitance and the resistances (C_{patch}, Rp_{patch}, Rs_{patch}) between two electrodes is more complex, as highlighted in Figure 95, those variables depend on the distance between the two electrodes. The cable model theory was used to compute those variables as the current can return to the ground in every place in its way to the neighboring electrodes, similar to the current that can return to the ground during its propagation inside a cable, as expressed in Figure 95.

We simplified the tissue between two electrodes as only made of Deiter cells, then we implemented the cable model theory in order to obtain a general impedance depending on the electrodes distance.

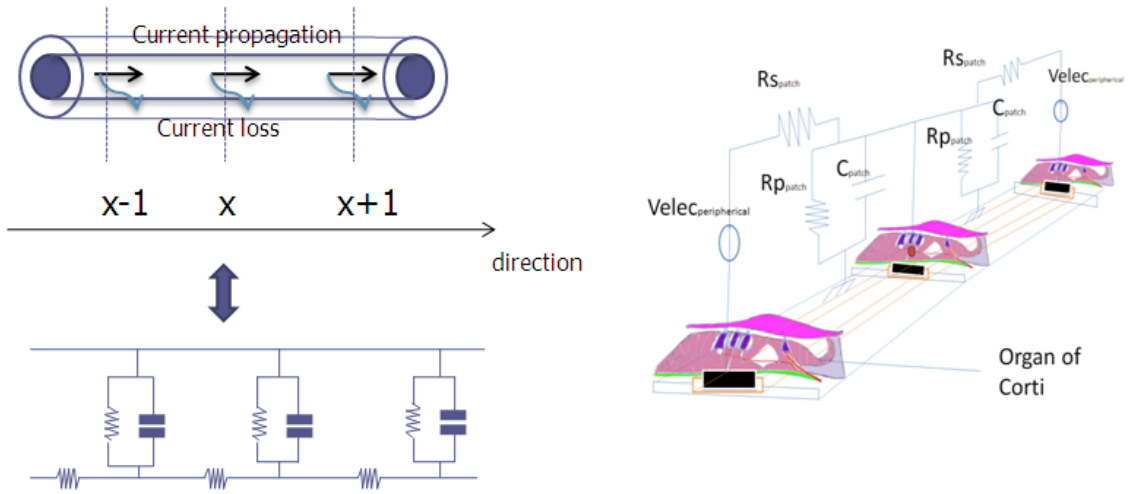

FIGURE 95. TWO SURROUNDING ELECTRODES INFLUENCES THE NERVE FIBERS TARGETED. WE USED THE CABLE MODEL THEORY TO ACCOUNT FOR THE CURRENT RETURNING TO THE GROUND BETWEEN THE TWO ELECTRODES.

To compute Rs_{patch}, the cylindrical model of resistance was considered. The cylinder going from the first electrode to the second electrode, as defined in Figure 96.a, was used to compute Rs_{patch} (expressed in eq. 139)

$$R_{spatch} = \frac{1}{\sigma_M} * \frac{l_{spatch}}{S_{spatch}} \qquad \text{EQ. 139}$$

$$with \quad l_{spatch}(y) = \int_0^{Y_{tot}} y * dy$$

$$and \quad S_{spatch}(y) = \int_0^{2*\pi} \int_{-\frac{X_1}{2}}^{\frac{X_1}{2}} \rho * d\rho * d\theta$$

where Y_{tot} is the distance between the two electrodes, X_1 is the distance between one electrode and the corresponding nerve fibers. Those values were respectively extracted from {, #400} and[227]. y is the variable shown in Figure 96.a, Figure 96.b and Figure 96.c. σ_M is the electrical conductivity of muscle cells.

Rp_{patch} models the resistance between the two longitudinal edges of the cylinder defined previously. Hence, this computation changes as expressed in eq. 140, since it models all the losses through the ground from one electrode to another one.

$$R_{ppatch} = \frac{1}{\sigma_M} * \frac{l_{ppatch}}{S_{ppatch}} \qquad \text{EQ. 140}$$

$$with \quad l_{ppatch}(y) = \int_0^{Z1} dz$$

$$and \quad S_{spatch}(y) = \int_0^{2*\pi} \int_0^{y} \rho * d\rho * d\theta$$

where we supposed Z_1 equal to X_1 for simplification purposes (X1 and Z1 correspond to the distances indicated in Figure 96).

We defined Cp_{patch} as a squared parallel plate capacity (Figure 96.c) (developed in eq. 126):

$$C_p = \mathcal{E}_0 \mathcal{E}_M \frac{A_{patch}}{d_{patch}} \qquad \text{EQ. } 141$$

$$with \quad d_{patch}(y) = \int_0^{Z_1} dz$$

$$and \quad A_{patch}(y) = \int_0^{y} dy_1 \int_0^{X_1} dx$$

where $\mathcal{E}_M$ is the muscle relative permeability.

For reader's convenience, the value of the capacitances and resistances described previously are summarized in Table 9.

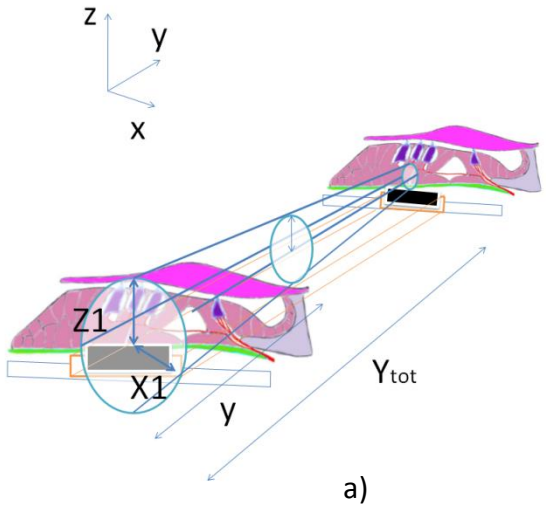

a)

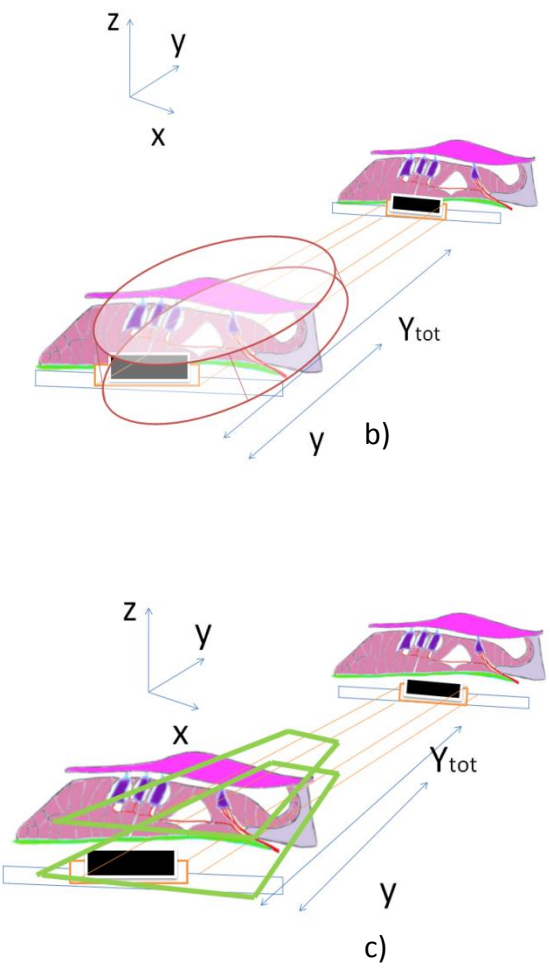

FIGURE 96. PHYSICAL MODEL OF RS_{PATCH} (A), RP_{PATCH} (B) AND CP_{PATCH} (C)

The electrical description containing only a single electrode is shown in Figure 97. The input voltage generator is directly connected to the electrodes analog model (low frequencies model), which can be eventually considered as a perfect conductor compared to the other resistance values.

The electrodes array configuration implemented here is the common ground electrodes array (where the wire is working as the ground) which is usually not found in modern CIs as it is associated with increased power loss and hence electrodes consumption. However with this common ground electrode array, the model created is more precise than considering a monopolar stimulation (as the distance from the two wire is not known) or a bipolar stimulation (the electrodes working as ground in bipolar stimulation may depend on the CI system used).

Then the current can flow to the nerve cell or can go back to the ground. The current loss through the physical isolation between the electrode and the ground is neglected as the insulator has a low loss tangent (high resistivity). The membrane rest potential of a nerve cell is around -70mV, explaining the two -70mV voltage generators, in Figure 97. We defined the analog equivalent circuit of a nerve cell using a resistance (R_n) in parallel with a capacitor (C_n). This electrical description should not be confused with the Hodgkin-Huxley model [367], which is used to model ions flow through the nerve cell membrane and not the electron flow.

In addition, the electrical description of the system starting from the nerve and going through all the body to the ground was not considered because very little electrical current is going through this pathway.

Usually longitudinal impedances are included in propagation channel modeling associated with layers of diverse tissues resulting in a mesh of complex impedances [368]. In the propagation channel modeling of biological tissue associated with a single electrode, longitudinal impedances were not included because we supposed that membrane properties were similar between different tissues (we used a single wire instead). However we included the impedances associated with the cable theory model, in the propagation channel modeling of biological tissues associated with multiple electrodes.

TABLE 9: RESISTANCES AND CAPACITANCES USED IN THE ELECTRICAL MODEL

Electrodes	**Re= 1.5 Ω, Ce=11 fF**
Basilar Membrane and Deiter cells	R_{bc}= 933 Ω, C_{bc}= 300 nF
Nerve fibers	R_n= 1076Ω, C_n= 3µF
Cable Model Theory	Rs_{patch}= 8 MΩ, Rp_{patch}= 1265 Ω Cp_{patch}= 92.6 nF

Figure 97 exhibits the electrical description of the overall system with two surrounding electrodes added. They are composed of a voltage generator, the platinum electrode equivalent circuit and the cable model (Rs_{patch}, Rp_{patch} and C_{patch}), to connect the peripheral electrodes with the nerve fibers that we want to activate.

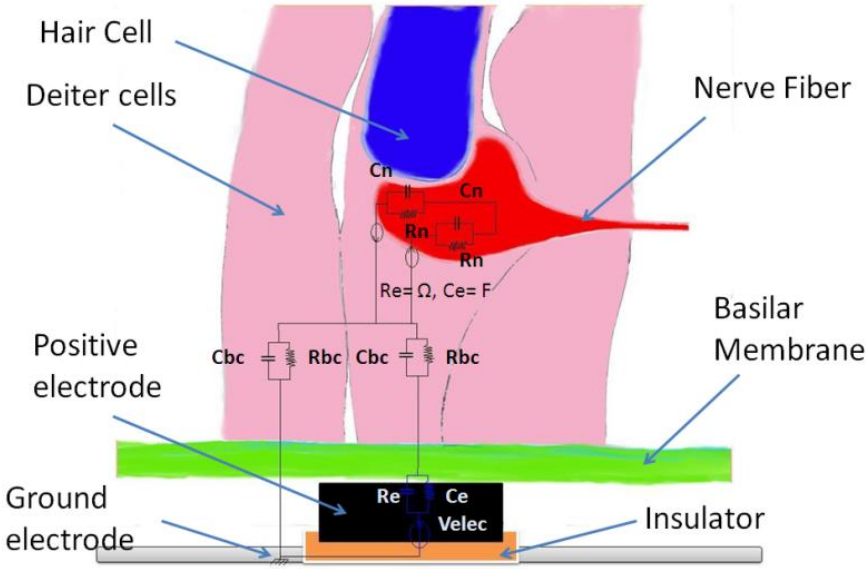

a)

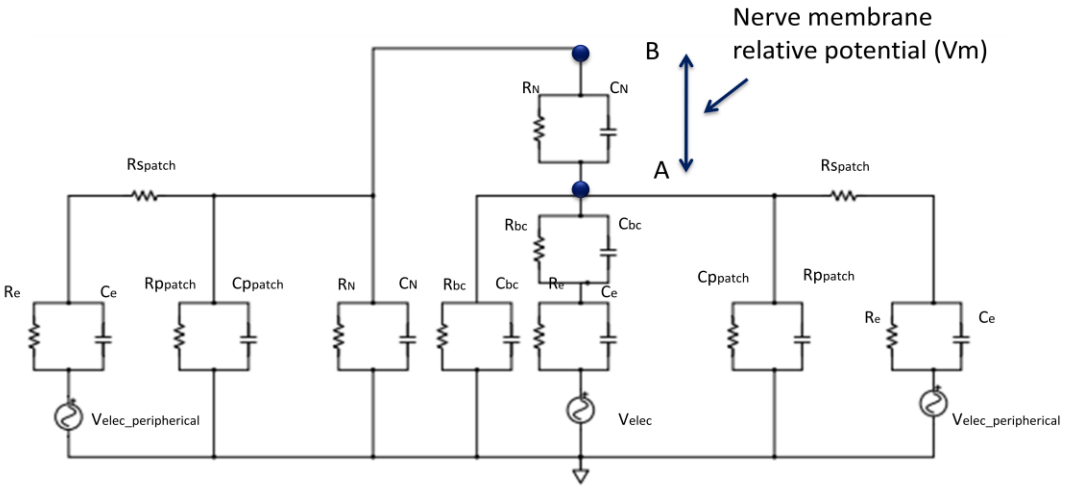

b)

FIGURE 97.A. ELECTRICAL ANALOG OF THE ELECTRODE AND NERVE (NOT AT THE RIGHT SCALE FOR BETTER UNDERSTANDING).

B. ELECTRICAL ANALOG WITH THREE ELECTRODES

The main goal of the addition of the two surrounding electrodes was to study theoretically the influence of these on the stimulation of selected nerve fibers (or more precisely of the packet of nerve fibers that should only be stimulated by the central electrode). These perturbations, if significant, could make the sound reconstitution inaccurate.

2. Interpretation of this electrical analog

The membrane potential (V_m) which corresponds to the difference of potential between point A and point B in Figure 97, have to vary of 30mV to generate an AP. The electrode stimulation (V_{elec}) was made using first a DC source. Neglecting the effect of the capacitors, V_m varied linearly with V_{elec} and the variation of 30mV was reached for an electrode stimulus around 0.9V.

When a nerve fiber is stimulated constantly, it will not produce an AP indefinitely but rather produce a succession of randomly spaced AP called spike trains. The spike train length that could be produced by a sound of given intensity has to be reproduced with the electrodes of the cochlear implant. We performed transient simulation including the capacitors effects by injecting a square voltage with a period of 15ms. This experiment was repeated for input square voltages varying from 1V to 5V (Figure 98). The aim of this simulation was to study if the voltage amplitude sent to the electrode would affect the spike train duration and starting time. Figure 98 reveals that the delays for V_m potential to reach its maximum value were around 0.1µs, which were small compared to the duration of a nerve AP (few ms). This result pointed out that theoretically the electrode voltage magnitude had a very insignificant effect on the spike train duration. In addition, the recreated spike train starting time has negligible delay with the electrode stimulation starting time.

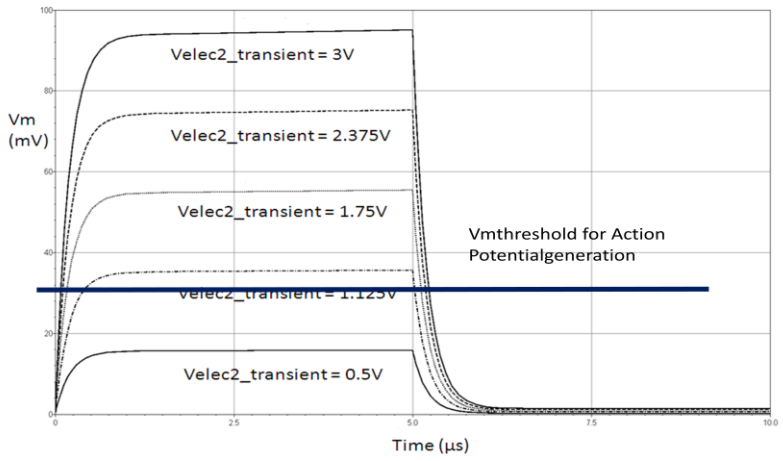

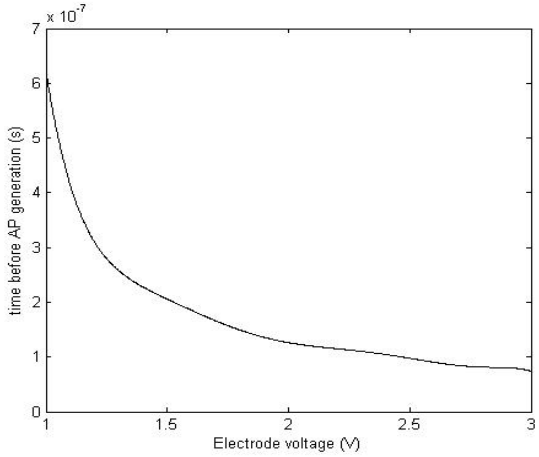

FIGURE 98.A. TRANSIENT SIMULATION WITH DIFFERENT ELECTRODE VOLTAGE AS INPUT AND VM VOLTAGE AS OUTPUT.

B. TIME BEFORE AP GENERATION DEPENDING ON THE ELCTRODE VOLTAGE

A general overview of the spike train related to the V_m amplitude is presented in Figure 99. The AP generated were obtained from basic mathematical functions in order to model the nerve fiber AP created after square voltage electrode stimulation. The Inter Spike Delay (ISD) was taken randomly and greatly depends on the amplitude of the stimulus[285]. However, the electrical analog presented in this document does not account for this effect.

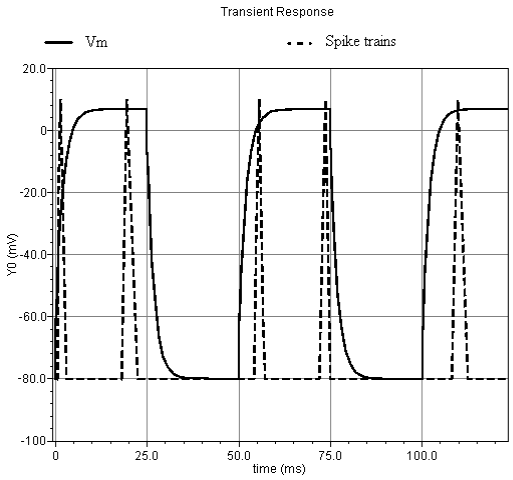

FIGURE 99. SPIKE TRAIN GENERATED BY THE ELECTRODE INPUT VOLTAGE

We performed also a parametric simulation using the electrical description ofFigure 97, where the surrounding electrodes were added. The central electrode had a DC amplitude of 1V and we

varied the voltage of the surrounding electrodes between 0.9 and 5V. According to RC values used in Figure 97, analytical computation showed that when the voltage of the surrounding electrodes was maximum (5V), the nerve fibers (above the central electrode) membrane potential V_m variation was 0.5mV, which was not high enough to stimulate these nerve fibers (the ones that should be stimulated only by the central electrode).

The overall system consumption is of great significance as cochlear implants are not convenient for the users to recharge. The study of the power consumption is presented in Figure 100.

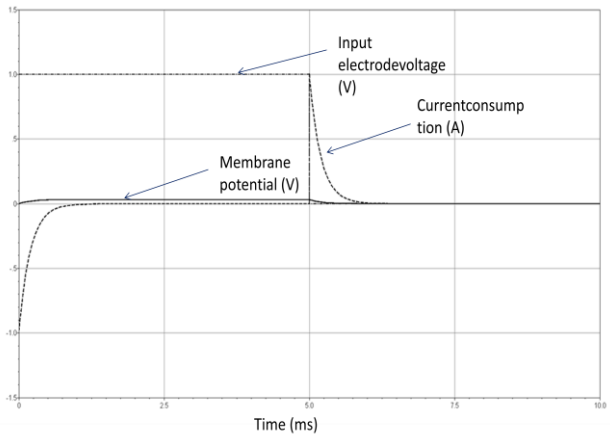

FIGURE 100. CURRENT CONSUMPTION DURING ONE STIMULATION PERIOD

The current peaks during each input signal transitions could reach 1A. Consequently, the maximum power consumed during a square input signal generation by the electrodes was around 1W (peak value), whereas the mean power consumed per period was around 50mW. These results may be used for the electrodes array conception to define battery size as well as electrode minimum width.

3. Limits of the model created

The electrodes array power consumption mean value is by far more important than the one reported in current CIs (cf Section II.B.3 for more details). This may be explained by the fact that we implemented an old stimulating electrode technology (common ground electrodes array) rather than the one used in modern CIs which is more directive and hence less power consuming (bipolar

electrodes array). This modeling choice was made for the precise restitution of the physical phenomenon involved as indicated the previous Section.

Besides in commercially available CIs, the number of channels (with distinct stimulation area of the cochlea) is lower than the total number of electrodes as indicated in Section I.B, possibly caused by strong electric field coupling between the electrodes, which disagrees profoundly with our model. The main explication is that the scala tympani, where the electrodes array is inserted, is filled with perilymph, hence there is conductive fluid between all the electrodes (explaining why very poor accuracy is associated with common ground technology). We did not account for perilymph perturbation in our study, maybe explaining the model disagreement with experimental results. However, if this conclusion were true, that would suggest that reducing the perilymph perturbations may result in very precise nerve stimulation.

D. Nerve fibers selected by the electrodes array

1. Nerve repartition map

The biomechanical most widespread theory of BM vibration is the traveling wave theory: following acoustic vibrations, the BM is excited and vibrates at a particular place inside the cochlea. This place depends on the sound wave frequency as well as sound amplitude [164, 369]. CIs aim to recreate the neural stimuli of a healthy cochlea using a wired electrodes array inserted inside the scala tympani, close to the BM. As each electrode is at a fixed place inside the cochlea, electrode stimulation will excite only a limited region of the cochlea which will be further interpreted in the brain as a sound of a certain frequency. Consequently sound division into single frequency using the Fast Fourier Transform (FFT) algorithm for instance or using more complex algorithms based on the BM width motion (as presented in Section VI.B.1) are necessary to select the right electrodes to activate, which then stimulate their surrounding nerve fibers.

In order to better reproduce the original sound amplitude with functioning Hair Cells (HC), we created an afferent nerve fiber map of the cochlea including the frequency selective mechanisms of the ear.

2. Spiral ganglions

There are between 30000 to 40000 nerve fibers in the cochlea of a healthy adult [370]. Three types of nerve fibers innervate the cochlea: autonomic (associated with blood vessels for example), afferent (conducting information from the cochlea to the brain) and efferent (conducting information from the brain to the cochlea, especially to the Outer Hair Cells (OHC)). Afferent nerve fibers are produced by Spiral Ganglions Cells (SGC) [160]. Spiral ganglions are synaptically connected to the IHC and OHC as indicated in Figure 102.

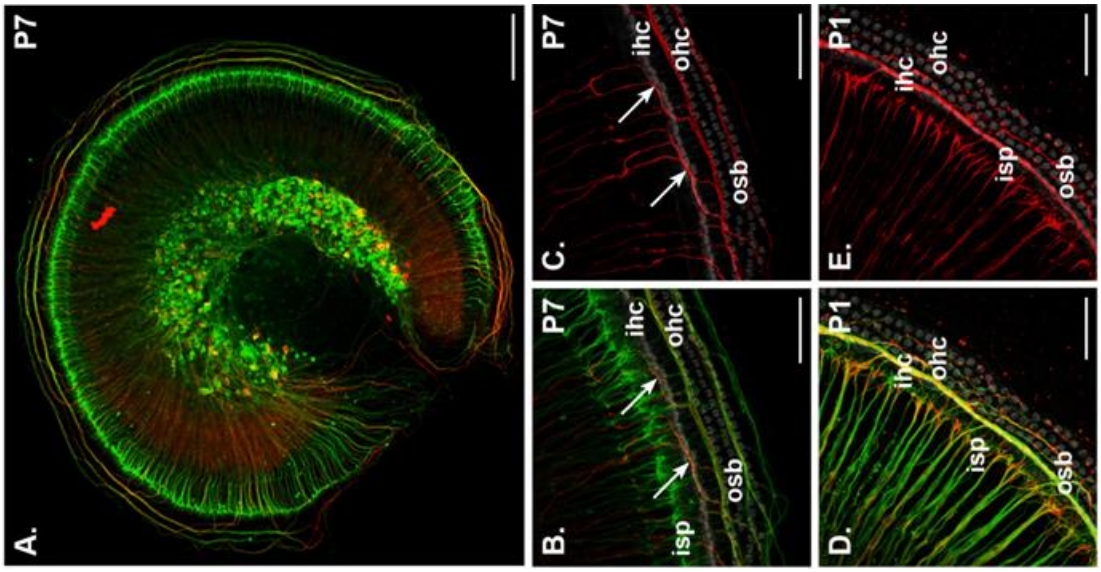

FIGURE 101: IMMUNOFLUORESCENT LABELING OF NEURAL PROTEINS, SHOWING THE NERVE FIBERS, INNER HAIR CELLS (IHC) AND OUTER HAIR CELLS (OHC). MORE DETAILS ARE AVAILABLE AT[142] . THE PICTURE IS ATTRIBUTED TO [142]

Type I SGC represent 95% of the SGC and each one connects to a single IHC whereas a single IHC is connected to 10-20 type I SGC [160]. There are around 15 nerve fibers per IHC in the lower second turn of the cochlea and this number changes from the base to the apex, most probably slightly contributing the cochlea sensitivity toward certain frequencies as explained in [246, 247, 286].

Type II Spiral Ganglions Cells (SGC) are smaller and unmyelinated and mostly connect OHC.

It may be deduced that IHC are surrounded by almost all the afferent nerve fibers, therefore they are thought to function primarily as sensory receptors [371]. OHC otherwise are more connected with motor properties of the stereocilia [180], they may permit an higher accuracy in sound perception.

In [372], the Spiral Ganglions repartition over the cochlea distance from the base is presented for cats. We assumed that the spiral ganglions cochlea distribution for other terrestrial mammal

species was similar [160, 373] (this assumption may be inaccurate as the cat hearing frequency range is often larger than the other species, but may be used as first approximation).

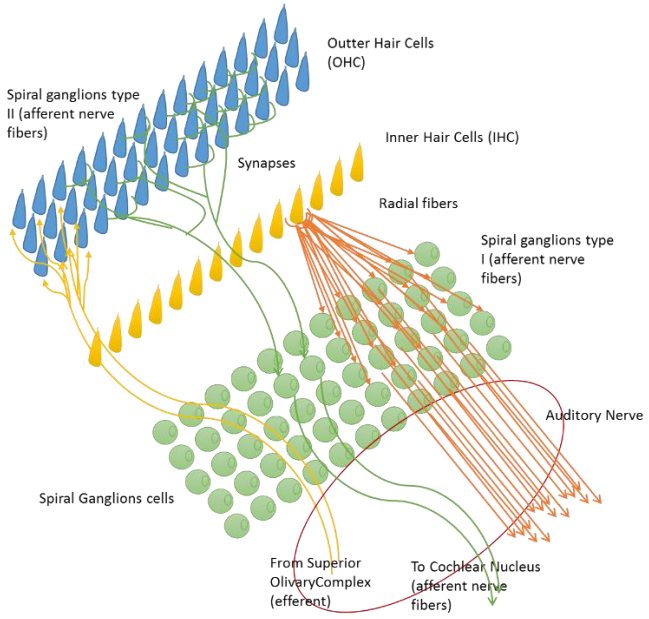

FIGURE 102: AUDITORY NERVE FIBERS AND HAIR CELLS. REDRAWN FROM [374]

As type II SGC function in hearing sensation has been partially understood and because their number is limited compared to type I SGC number, we neglected type II SGC, and supposed in this model that:

- the total SGC number and repartition was entirely defined by type I SGC.
- the total afferent nerve cell number and repartition inside the cochlea was therefore similar to type I SGC number and repartition.

3. Ear frequency sensitivity hypothesis

The human ear is composed of the outer ear, the medium ear and the inner ear (where BM makes the organ of Corti oscillates)[126]. When the eardrum is stimulated, the nerve response over frequency presents a peak amplitude around 4kHz [375]. This particular human hearing frequency sensitivity may result from the combined effects of outer ear resonance, the middle ear resonance and the cochlea sound filtering and amplification.

It has been suggested that the outer ear and the medium ear contribute to frequency sensitivity in mammalian hearing, especially for frequencies around 3kHz [375-379].

The cochlea frequency sensitivity may also result from other various mechanisms still controversial. Considering only the cochlea biophysics, the Intracochlear/eardrum magnitude of the scala tympani over frequency found in [380] may indicate varying vibrations amplitude depending on the sound wave frequency. The BM displacement (when stimulated by a mechanical wave) contributes to produce the frequency sensitivity of the cochlea due to the BM different physical properties (stiffness, mass) inside the cochlea (distance from the base).

The cochlea sensitivity toward certain frequencies may be further affected by other physiological factors, such as different afferent nerve fibers repartition and stimulation, depending on the position on the cochlea. Several mechanisms have been proposed such as:

- IHCs frequency response which is similar to a low pass filter with a resonating pulse around 10kHz [274, 381]. The IHCs frequency response may result from different IHCs length inside the cochlea or to their stereocilia and cellular mechanical properties. Furthermore gradient of IHC ionic channels along the cochlea length exist and increase the frequency hearing sensitivity of the cochlea [382]. Besides ribbon synaptic contacts with type II SGC are diverse with respect to their cochlea location with highest numbers (15 contacts) for frequencies in the 8kHz-16kHz range [199].
- Spiral ganglions density increases slowly and linearly with the cochlea position with respect of the cochlea location hence spiral ganglions repartition is related to the frequency of the sound wave but fails to explain the 4kHz frequency peak (cf spiral ganglions frequency map, presented in Figure 104) [372, 380]. Furthermore AMPA Receptors density of type II SGC is changing depending on their place inside the cochlea.

To the author's personal interpretation the frequency selectivity of the cochlea is greatly linked to biophysics of the cochlea, to IHCs potential change and repartition and ear/middle ear resonance rather than nerve fiber topography (as they seem to contribute less to the amplification peak in the 3-4kHz range [380]).

4. Afferent nerve fibers repartition inside the cochlea

As indicated in [370], the number of afferent nerve fibers in the cochlea is around 40000 and their effective stimulation is depending on the sound wave frequency. We hence decided to create an afferent nerve repartition map already including all the physical or anatomical mechanisms presented in the above Section (that we called Afferent Nerve Fibers Repartition Map Including Ear Frequency Selection Mechanisms or MEFFRINAM map), in order to roughly define the number of afferent nerve fibers affected by a sound wave. This map presents great interest for cochlear implants application as the electrodes array are directly stimulating these nerve fibers and the outer/middle ear resonance, the BM variations depending on wave frequencies, the organ of Corti selective mechanisms,… are bypassed in cochlear implants, making the use of this map fundamental to recreate a realistic hearing.

To develop this topographic map we took first the reverse function of the human hearing threshold over frequencies [383] to get the human ear sensitivity toward the frequencies.

By making this function linear (R(f)) and then reversing it ($I_R(f)$), it allowed us to estimate the cochlea sensitivity toward frequency.

Transforming the $I_R(f)$ function into a probability density function ($P_{IR}(f)$) and multiplying it with the total number of afferent nerves in the cochlea ($Nb_{afferentnerves}$) resulted in the Afferent Nerve Fibers Repartition Map Including Ear Frequency Selection Mechanisms (MEFFRINAM map) of the cochlea as expressed in eq. 142. The afferent nerve cells inside the cochlea are weighted by healthy hearing responsiveness as only nerve fibers are involved in sound perception in CIs users.

$$Threshold\ of\ hearing = 10\log|R(f)| \qquad \text{EQ. } 142$$

$$\rightarrow 10\log|I_R(f)| = -10\log|R(f)|$$

$$P_{IRT}(f) = \frac{I_R(f)}{\int_{f_{min}}^{f_{max}} I_R(f)} Nb_{afferentnerves}$$

where $P_{IRT}(f)$ is the equivalent afferent nerve stimulated repartition map over the frequencies (f).

The Greenwood function [384] was used to change from the resonant frequency into a position in the cochlea between the base and the apex[384]. Therefore $P_{IRT}(f)$ can be transformed into $P_{IRT}(d_A)$ where d_A is the distance from the apex as described in eq. 143

$$f = 165.4\,(10^{2.1\,d_A} - 1) \qquad \text{EQ. } 143$$

$$P_{IRT}(f) = P_{IRT}\left(165.4\,(10^{2.1\,d_A} - 1)\right)$$

According to Greenwood parameters for human ear fitting [384].

Figure 103 displays the afferent nerve fibers stimulated map including ear amplification mechanisms (MEFFRINAM map) compared to cochlea position. The comparison between the spiral ganglions topographic map (attributed to [372]) and the created topographic map is presented in Figure 104. Based on the assumptions presented in the above Section, both maps have the same number of cells but these are differently affected over frequencies.

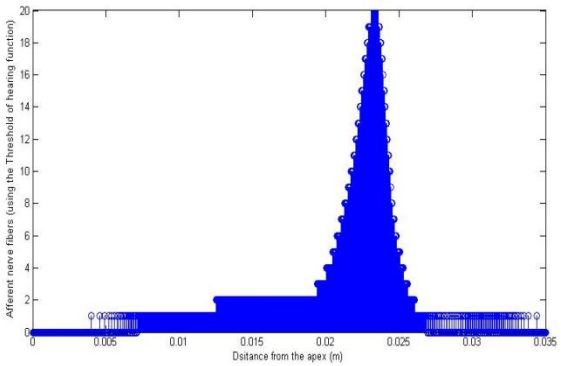

FIGURE 103: AFFERENT NERVE FIBERS REPARTITION MAP INCLUDING EAR FREQUENCY SELECTION MECHANISMS (MEFFRINAM MAP) IN RELATION TO THE DISTANCE FROM THE APEX

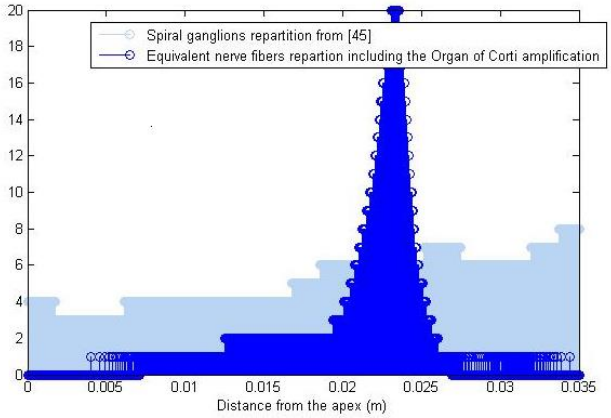

FIGURE 104: COMPARISON OF SPIRAL GANGLIONS REPARTITION MAP (ATTRIBUTED TO [372]) AND EQUIVALENT AFFERENT NERVE FIBERS STIMULATED MAP DEPENDING ON THE COCHLEA AND EAR BIOPHYSICS (MEFFRINAM MAP IN DARK BLUE)

5. Benefits of the created topographic map for cochlear implants

In severely deaf people the use of cochlear implants helps to partially recover the hearing function. In implanted patients the afferent nerve fibers stimulation is directly done through electrodes and does not require the organ of Corti. By remembering that we made the

approximation that the afferent nerve fibers were equivalent to the SGC, the afferent nerve fibers selected by the electrodes is given by the spiral ganglions repartition map.

We use CI422® device characteristics with an insertion depth of 20-25mm, a mean diameter of the electrodes around 0.35mm and a spacing between the electrodes around 0.45mm {, #400}. As explained in {, #400} the number of nerve fibers stimulated by an electrode is a function of the power magnitude as well as the proximity of the electrodes with the SGC.

We supposed that the electrodes are very close to the SGC, resulting in a window type selection (very accurate) of the afferent nerve fibers stimulation by the electrodes ($H_{implants.}$) displayed in Figure 105. In practice, this may be inexact as the insertion of the electrode array inside the scala tympani is difficult and usually result in spacing between the electrodes array and the Spiral ganglions [385]. In consequence, in practice, the nerve fibers selection mathematical description is closer to a Gaussian function.

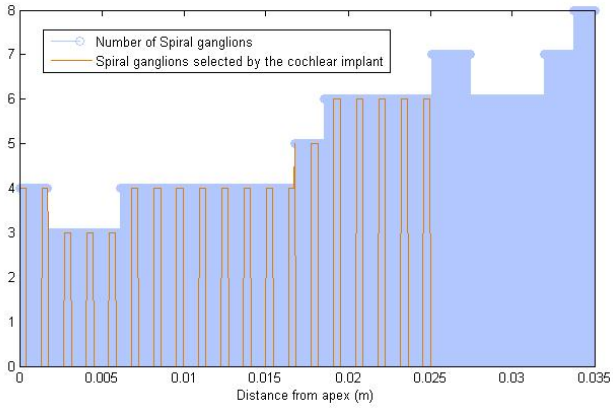

FIGURE 105: PACKET OF AFFERENT NERVE FIBERS SELECTED BY THE ELECTRODES OF THE COCHLEAR IMPLANTS. THE NUMBER OF SPIRAL GANGLIONS REPARTITION IS ATTRIBUTED TO [372]

From Figure 104 and Figure 105, it can be easily deduced that the cochlear implant electrodes do not provide the required amplification in the 2kHz – 6kHz frequency range (corresponding to distances from the apex in the 19-24mm interval according to Greenwood function [384]) as cochlear amplification is not done. Algorithmic correction by modifying the energy sent to the electrodes may be used to correct this defective amplification. This algorithmic correction should be based on the human hearing threshold or similarly on the equivalent afferent nerve fibers stimulated map which takes into consideration the amplification mechanisms of a healthy cochlea.

Using the mathematical logarithmic spiral representation presented in [386], the spatial representation of the cochlea can be performed. The mathematical equation in the cited document describes a flat spiral disagreeing with a real cochlea, however we may use the z direction to plot information such as the nerve fiber topographic map or the nerve fibers selected by the electrodes array, as indicated in Figure 107 and Figure 108.

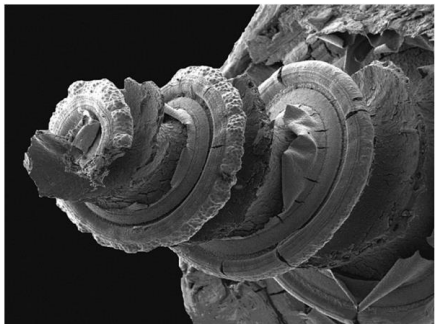

FIGURE 106: SNAIL LIKE STRUCTURE OF THE COCHLEA (ATTRIBUTED TO [387])

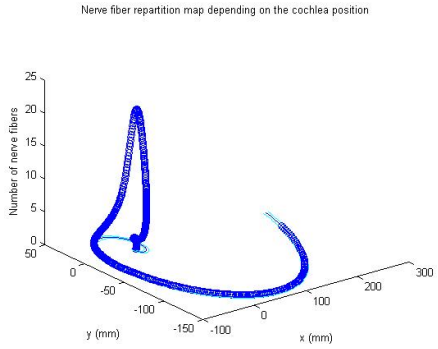

FIGURE 107: AFFERENT NERVE FIBERS REPARTITION MAP INCLUDING EAR FREQUENCY SELECTION MECHANISMS INSIDE THE COCHLEA DEPENDING ON THE COCHLEA SPATIAL POSITION

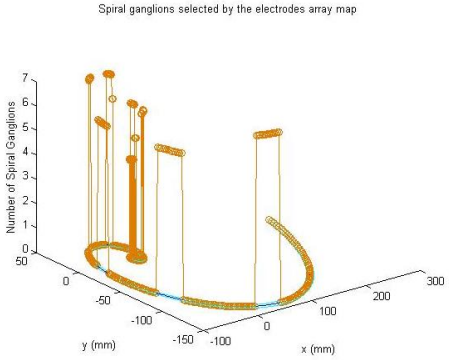

FIGURE 108: PORTION OF THE AFFERENT NERVE FIBERS INSIDE THE COCHLEA STIMULATED BY THE COCHLEAR IMPLANT ELECTRODES

6. Amplification coefficients associated with the topographic maps comparison

CI electrodes should hence be multiplied by scalar coefficients to correctly model the frequency sensitivity of a healthy ear. This correction is required as the central nervous system interprets neuronal signals already amplified in some particular frequencies (though it may partially adapt to distorted sounds). If the frequency amplitude dependence is not reproduced in cochlear implants it may result in inability to correctly hear certain frequencies (especially in the 3-4kHz band), ultimately resulting in sound distortion.

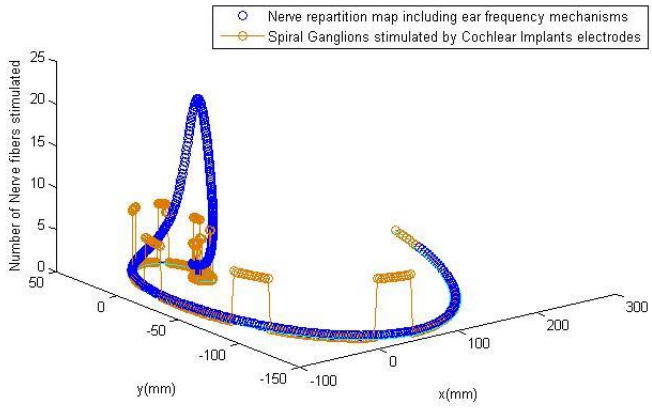

FIGURE 109: COMPARISON BETWEEN THE SPIRAL GANGLIONS STIMULATED BY THE ELECTRODES AND THE CREATEDMEFFRIMAM MAP

Comparison between the MEFFRIMAM map and the Spiral Ganglions topographic map selected by the cochlear implants is exposed in Figure 109. To correctly model the frequency response of an healthy ear, each electrode should be multiplied with the coefficient indicated in Figure 110. We further supposed that the number of nerve fibers stimulated is linearly increasing with the amplitude of the electrode. This may be inaccurate for high voltage stimulus or very low voltage stimulus due to saturation mechanisms [152, 158, 159]. To compute this average coefficient a simple division was performed between the afferent nerve fibers number in the MEFFRIMAM map and the afferent nerve fibers number defined by the spiral ganglions map for the same position inside the cochlea. The average value of this coefficient was retained for each electrode.

The multiplication of these coefficients with the voltage value, which must be sent at an electrode to stimulate an afferent nerve fiber response, could be done in the processing unit of the

cochlear implant. However due to strong electrode coupling in modern CIs, these coefficients should rather be used to correct the channel amplitude rather than the electrode amplitude. The computing technique still apply for such modifications.

Furthermore coefficients amplitude tuning tests (using back telemetry) performed in deaf people using cochlear implants for each electrode may add precision in the hearing response of these patients.

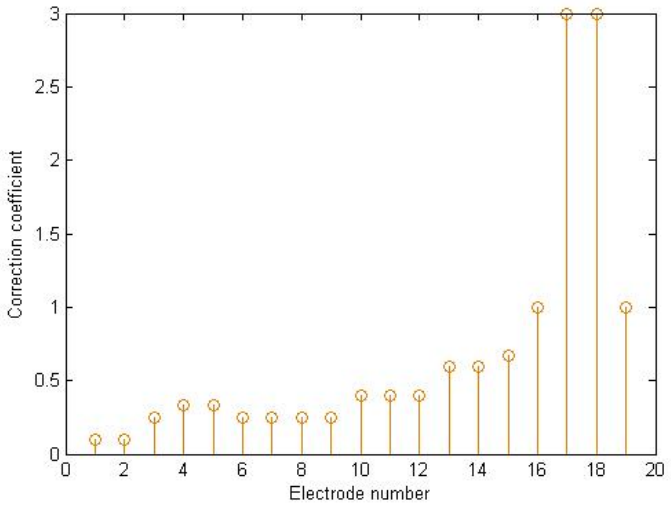

FIGURE 110: ELECTRODES AMPLIFICATION COEFFICIENTS TO ENSURE SIMILAR FREQUENCY RESPONSE WITH AN HEALTHY COCHLEA

E. New algorithmic model developed for electrodes array stimulation

As previously stated in Section I.D, we supposed that the electrodes array is very close to the SGC resulting in a rectangular window-like function called $H_{implants}(x)$.

The selection and the power sent to the electrodes may use the function h(x,t) and w(x) (described in Section III.E) as depicted in Figure 111. Such speech coding strategy is called traveling wave based stimulation [346]. The basilar membrane width excitement (w(x)), following a sound wave perception in an healthy cochlea may be recreated by selecting the right electrodes to stimulate as indicated in Figure 111, and the amplitude of the electrodes may be found using the function h(x).

As indicated in the previous Section, the Greenwood function [140]permits the easy conversion of the central resonant frequency of the cochlea with the BM distance from the apex. $H_{implants}(x)$ can be converted into $H_{implants}(f)$ by using the Greenwood function.

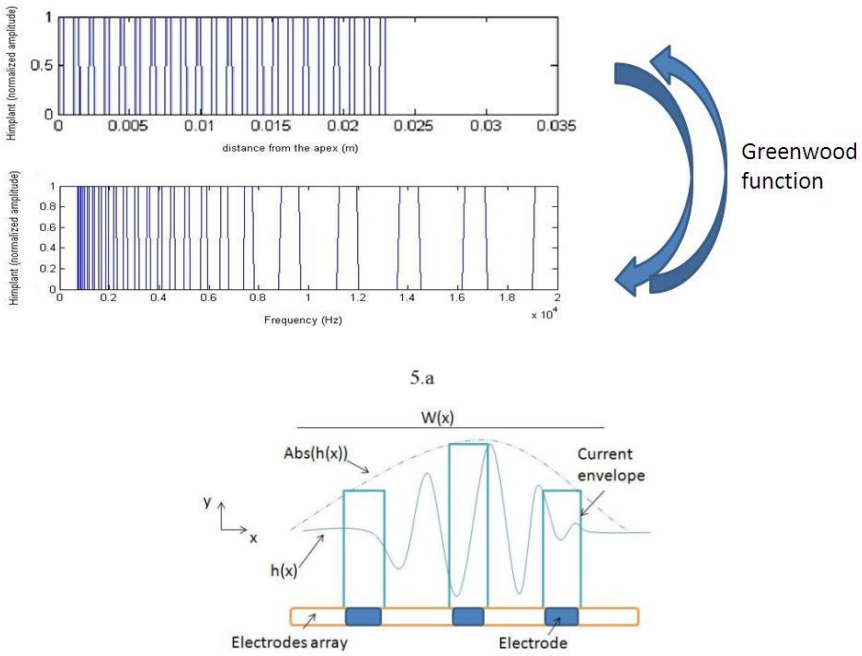

FIGURE 111.A: HIMPLANTS FUNCTION WHICH INDICATES THE POSITION IN THE COCHLEA OR THE FREQUENCIES STIMULATED BY THE ELECTRODES ARRAY. B: USING BASILAR MEMBRANE MOVEMENT FOR ELECTRODES STIMULATION DEPENDING ON THE FUNCTION H(X) AND ON THE STIMULATION WIDTH (W(X)) IS PROPOSED IN TRAVELING WAVE BASED SPEECH CODING STRATEGIES

Figure 112 shows that not all the frequencies can be stimulated by the electrodes and the main limitation of this electrode array is that the input frequency must match with the frequencies coverage by the implant, which is rarely the case for high frequencies. In consequence we proposed an alternative model.

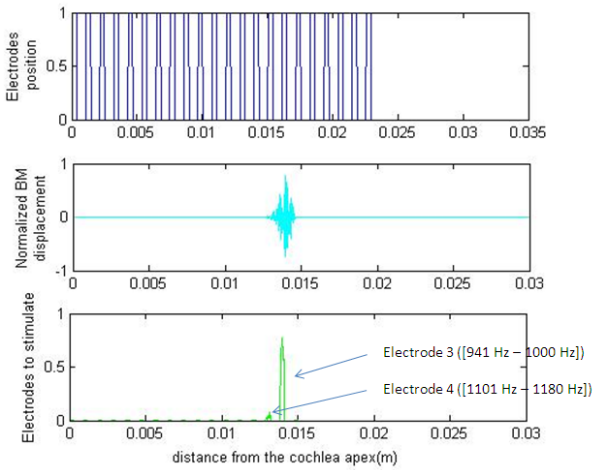

FIGURE 112.A: THE AUDITORY NERVE FIBERS POSITION STIMULATED BY THE ELECTRODES ARRAY. B: BM DISPLACEMENT FOR A 1250HZ SINE WAVE. C: RESULTING ELECTRODES STIMULATED BY THE 1250 HZ SINE WAVE BASED ON THE BM SPEECH CODING STRATEGY

1. Created algorithm for numerous electrodes selection

The function $H_{implants}$ selects the frequencies stimulated by the electrodes array. We chose to only compute the Fourier Transform (FT) on the frequencies which can be stimulated by the cochlear implants. Speech coding strategies such as SPEAK (developed in Section I.B.1) also uses the band pass filtering for electrode selection similar to applying the FT on an infinite number of points (as the signal is still analog). However our algorithm is diverse, the FT is not applied to a very large number of points and its result mapped to the electrodes, rather we directly computes the FT on only 22 frequencies associated with each electrode central estimated stimulation frequency.

Hence we obtain the following equations for the FT computation (eq. 144):

$$X_k = \sum_{n=0}^{N-1} x_n * e^{-\frac{i2\pi f_{central}(k)n}{N}} \quad \text{EQ. } 144$$

and

$$x_n = \frac{1}{N} \sum_{f_{central}(k=0)}^{f_{central}(N-1)} X_k * e^{\frac{i2\pi f_{central}(k)n}{N}}$$

where X_k are normalized frequencies (the normalizing frequency is the sampling frequency chosen at 44KHz, similar to audio formats as .wav or .mp3),$f_{central}$ is the central frequency of each rectangular sub window of $H_{implants}(f)$ as one electrode can only have one voltage value and N is the number of electrodes.

As time signals after sampling largely exceeded N, the time signal was buffered and cut into M frames of length N. The FT and the IFT computation were performed over these M frames before concatenating the results (similar to the Short Time Fourier Transform (STFT) principle [388, 389], [390] but different to the Sliding DFT principle where all the FT of the different windows computed are superimposed [391]). The corresponding results for a 1250 Hz sine wave stimulus is shown in Figure 113.

Each time a sound wave is received, the STFT is performed only on the frequencies stimulated by the cochlear implants. These STFT coefficients directly gives the amplification coefficient for the electrodes stimulation. In such a way with this created algorithm, only one electrode is stimulated if the signal frequency is exactly the same as the one associated with the electrode position or several

electrodes may be stimulated if the frequency is outside a specific frequency associated with an electrodes.

2. Created algorithm testing

As the frequency of 1250Hz does not match with a frequency covered by one electrode, in the traveling wave speech coding strategy used for instance as a comparison, the signal power is distributed to the two closest frequencies covered by the electrodes, causing distortion in the reconstructed signal. Reversely in our new algorithm, the signal power is distributed over all the electrodes, resulting in less distortion. As electrodes coupling is significant in modern CIs, time interleaved electrode stimulation is required after such algorithmic calculus for stimulating only one electrode at a time.

Transient simulations were completed and the reconstructed signal from the STFT model was significantly less distorted than the other one (Figure 113). This test signal stimulates only two electrodes (in the actual physical model as presented Figure 112) or all the electrodes (in the STFT model).

However when the frequency of the test input signal was inside the frequency range corresponding to the electrodes position shown in Figure 112, both models gave approaching results (not shown in this document). In that case the most efficient model in terms of processing resources should be selected.

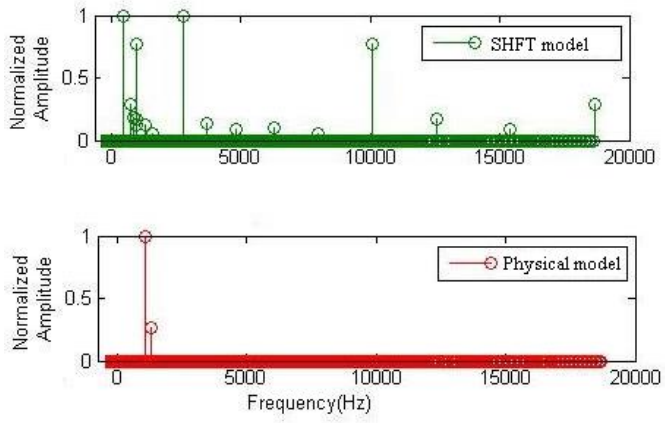

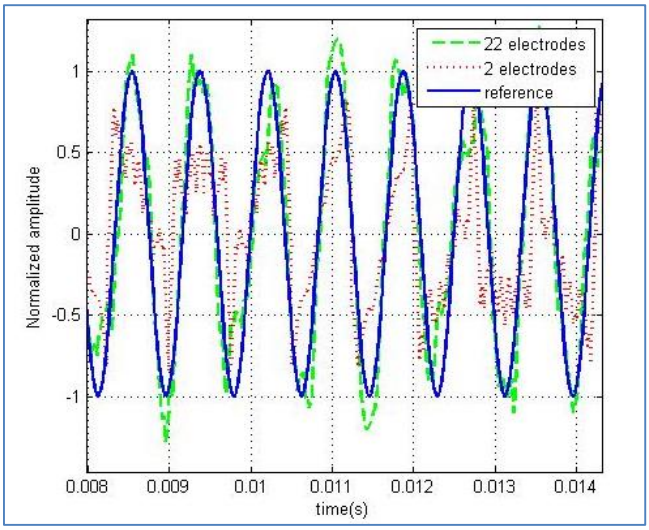

FIGURE 113.A: NORMALIZED VOLTAGE SENT TO THE ELECTRODES FOR A 1250HZ INPUT AUDITORY WAVE (USING THE STFT MODEL).B: NORMALIZED VOLTAGE SENT TO THE ELECTRODES FOR A 1250HZ INPUT AUDITORY WAVE (USING THE TRAVELING WAVE STRATEGY).C: COMPARISON BETWEEN THE TWO TEMPORAL SIGNALS RELATED TO THESE TWO TYPES OF STIMULATION

Testing this hypothesis may provide new insights of the hearing process. Tests require CIs users with a reprogrammed implant following speech perception assessments such as Word Identification by Picture Identification, Grammatical Analysis of Elicited Language-Presentence Level, Phonetic task evaluation, Sentence in Noise test, etc. In fact if the STFT model would give better results in person using cochlear implants than the algorithms that might be implemented at present, this could mean that the brain could adapt to these new nerve stimulation.

The brain adaptation to these stimulus may probably not happen in people who became deaf as the signal received in the central nervous system is very different in the case of a sound frequency not covered by the electrode array. Taking the previous example (1250 Hz sound wave stimulation), the nerve fibers stimulated by an healthy cochlea will be localized in a similar area (traveling wave theory) whereas the nerve fibers stimulated by cochlear implants using the STFT algorithm will be stimulated in very heterogeneous locations of the cochlea resulting in differently nerve fibers locations that the brain could not interpret (illustrated in Figure 114). If this algorithm would be implemented and utilized in very young implanted patients (maximal brain plasticity and with extended learning process), this could give new insights in the brain nerve adaptation and possibly provide better results than the algorithms used commercially. In all the case animal models may allow efficient testing without affecting or confusing the learning capacities of young implanted patients.

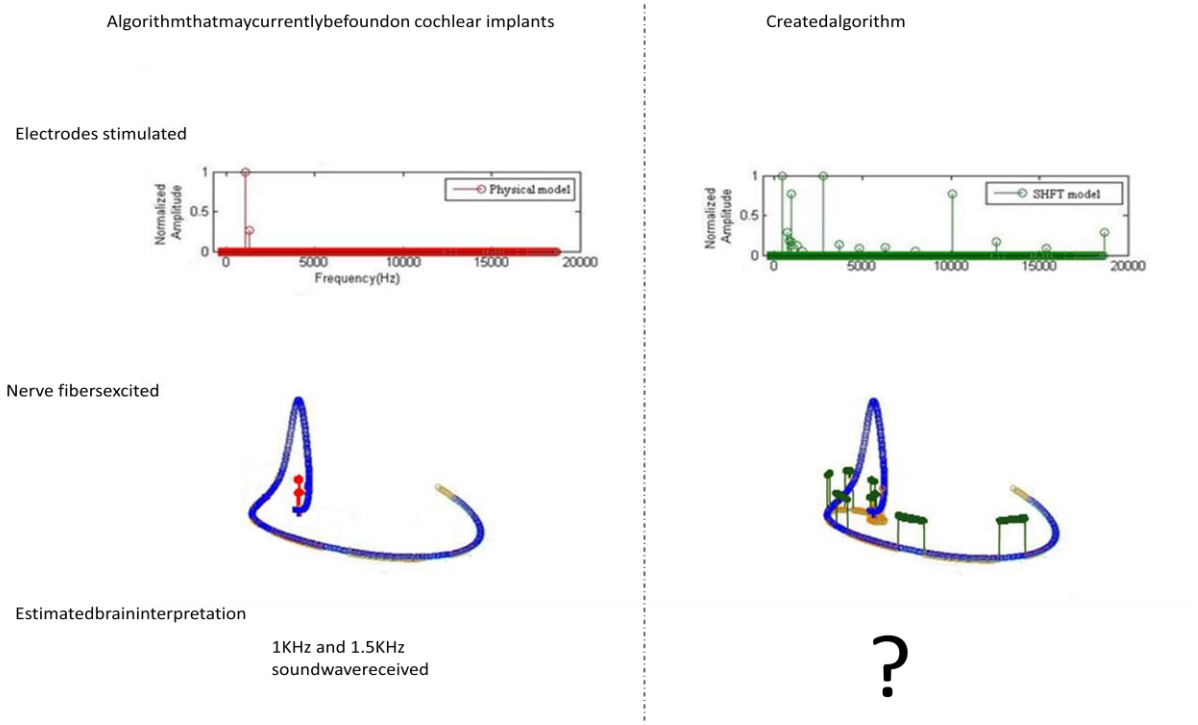

FIGURE 114: OUR NEW ALGORITHM FOR ELECTRODE SELECTION MAY LEAD TO INCORRECT BRAIN INTERPRETATION. TESTING THIS HYPOTHESIS MAY BRING NEW INSIGHTS ON BRAIN SIGNALS COGNITION AND INTERPRETATION

F. Reconstructed sound perceived by a damaged cochlea with cochlear implant

1. Hearing loss filters

The five main factors causing hearing loss are heredity, infections like meningitis, acute or chronic exposure to loud sounds, age and ototoxic antibiotics or chemotherapeutic drugs [392]. Outer ear and middle ear pathologies are nowadays easier to correct as they involve mainly the eardrum and the ear ossicles.

Cochlea dysfunction is associated with inner ear malfunction and is very common in elderly people. Furthermore, the majority of hearing loss implicates loss of Hair Cells (HC). Hearing aids such as amplifiers can help when the HC loss is moderate whereas cochlear implants are used to correct severe or absence of HC.

We created filters based on hearing reduction or hearing loss associated with different causes, permitting to model the hearing capacity in these situations. The filters were designed using the Hair

Cell Loss (HCL) plot over the auditory frequency range. In this document only two cases were developed from mice experiments attributed to [393]: hearing loss filters due to loud noise damage with Octave band noise (centered at 4KHz, 120 dB SPL for 5 hours) and the hearing loss associated with Octave band noise (centered at 4KHz, 105 dB SPL for 6 hours). These two hearing loss are both associated with loud noise damage as it is a quick way to damage HC experimentally and both centered at 4Khz as the cochlea amplification is maximal in this frequency area. The HCL plots and the reconstructed signal after filtering are shown Figure 115.

Cochlear implants bypass the non-functional HC by directly stimulating the auditory nerves. It is commonly reported [394] that the surgery needed to enclose the electrode array inside the scala tympani of the cochlea damages the hearing mechanism hence in this case the HC stimulation can be supposed negligible.

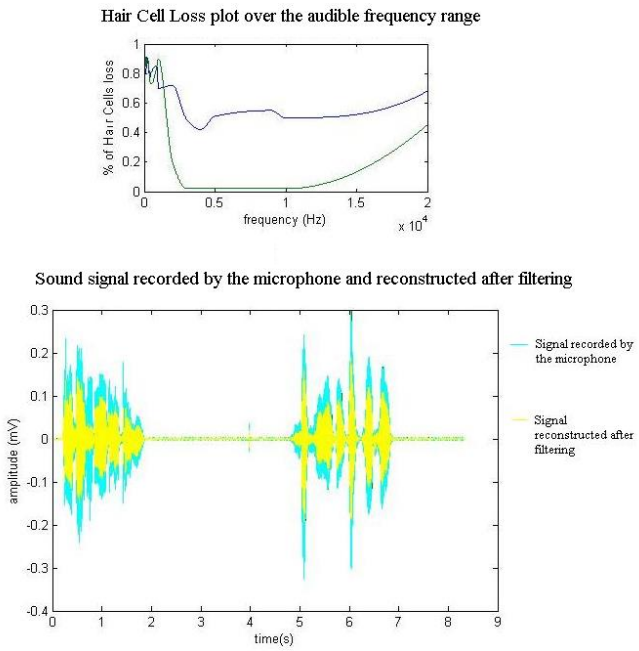

FIGURE 115.A: HAIR CELL LOSS CORRESPONDING TO THE TWO CASES OF LOUD DAMAGES PRESENTED IN SECTION V.F.1. B: DIFFERENCES BETWEEN THE TIME SIGNAL RECORDED BY THE MICROPHONE AND THE TIME SIGNAL AFTER FILTERING WITH ABOVE BLUE FILTER

Following the previous hypothesis, after the patient implantation, the hearing capacity resides almost exclusively on the electric stimulation of the electrodes array (except for low frequencies as the electrodes array is less long than the entire cochlea, resulting in preservation of the apex structure). Consequently we supposed that for a patient using a cochlear implant, only the nerve fibers near the electrodes will be stimulated.

2. Electrodes based Fourier transform

Systems using band pass filters applied to the signal recorded by the microphone have been developed to estimate sound perception in CIs patients. Simple FT algorithms have also been implemented in that intent.

The function $H_{implants}$ presented in Section I.E.1 selects the frequencies stimulated by the electrodes array. We chose to only compute the FT on the frequencies which can be stimulated by the cochlear implants, applying the same algorithm presented in Section I.E.2. It should be emphasized that this methodology is different from simple FT computation over an important number of points and selection of several amplitudes peaks.

The FT and the IFT involve same number of frequency samples and time samples, explaining the use of STFT computation as already indicated.

This theoretical model was not confirmed in practice as tests were difficult to perform and to the authors knowledge no precise model of hearing after implantation is now available. As previously stated in Section I.E.1, the main drawback of this model is the stimulation of all the electrodes for every sound.

3. Created models

Two models were created, one for hearing reduction and the other for severe or total hearing loss with cochlear implants use (presented Figure 116). The aim of these models was to evaluate the hearing restitution brought by CIs on a damaged ear. For real time application such as direct speech decoding, rendering this algorithm parallel may be necessary with the use of filter bank for instance. The power estimation of this algorithm was not performed since no implementation platform was fixed yet.

Besides these models can be easily modified to estimate the hearing improvement associated with the use of hearing prosthesis utilized by mild hearing loss patients.

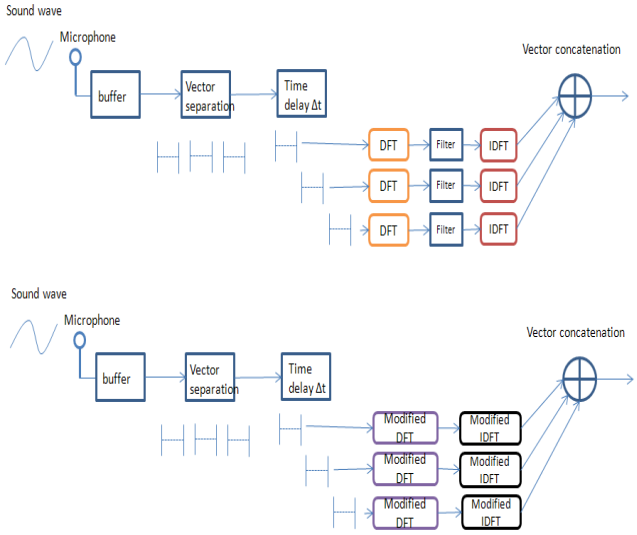

FIGURE 116: SYSTEM CREATION TO MODEL THE SOUNDS PERCEIVED BY DEAF PEOPLE IN THE CASE OF LOUD SOUNDS DAMAGE (A) OR IN THE CASE OF SEVERELY DEAF PEOPLE USING COCHLEAR IMPLANTS (B)

It is worth notifying that it was really difficult to quantify mathematically the loss of hearing perception in the two models. A temporal correlation or a frequency signals superposition could be used to quantify the loss of hearing but the better evaluation remains the hearing difference between the original sound signal and the reconstructed one by a functional ear.

As the results were difficult to describe, a specific experiment we performed is available in [1], comparing an historic speech sequence and a famous music track without an with CIs.

G. Closure remarks

Cochlear implanted patients with best auditory tests are able to follow a conversation in a noisy environment and understand a telephonic discussion. However they still suffer from drawbacks such as battery frequent reloading and approximate speech restitution. The work proposed in this chapter is aiming at possible enhanced audio signal reconstruction.

We enriched the theoretical electrical model of the organ of Corti stimulated by electrodes. The results obtained are slightly different from experiment outputs found in literature possibly indicating modeling inaccuracies but are still encouraging for first electrical model attempt. We further

[1] Example of audio signal reconstruction are available at http://youtu.be/x5o4jeTZt5M ("cochlear implants estimation film")

developed two algorithms for speech perception improvement; one permitting an adapted electrode stimulation amplitude depending on electrode position, the other more speculative and related to the use of a modified STFT applied only to the frequencies covered by the electrodes array. A testing environment was developed to theoretically validate our hypothesis.

It should be notified that to verify audio signal integrity, we preferred hearing the audio signal reconstructed rather than mathematical comparative functions such as least squares method [2]

H. Work published

- Audio signal reconstruction for a damaged cochlea model, U. Cerasani, W. Tatinian, DATE, March 2013, Grenoble (FRANCE)
- Electrical analog of the organ of Corti stimulated by the cochlear implant electrodes, U. Cerasani, W. Tatinian, CENTRIC, October 2013 ,Venice (ITALY)
- Study of cochlear implants electrodes stimulation based on the physics of the ear for audio signal integrity improvement, U. Cerasani, W. Tatinian, CENTRIC, October 2013 ,Venice (ITALY)
- Modeling of the organ of Corti Stimulated by Cochlear Implant Electrodes and electrodes potential definition based on their part inside the cochlea, U. Cerasani, W. Tatinian, International Journal On Advances in Life Sciences, v 6 n 1&2 2014.

[2] Example of audio signal reconstruction are available at http://youtu.be/x5o4jeTZt5M ("cochlear implants estimation film")

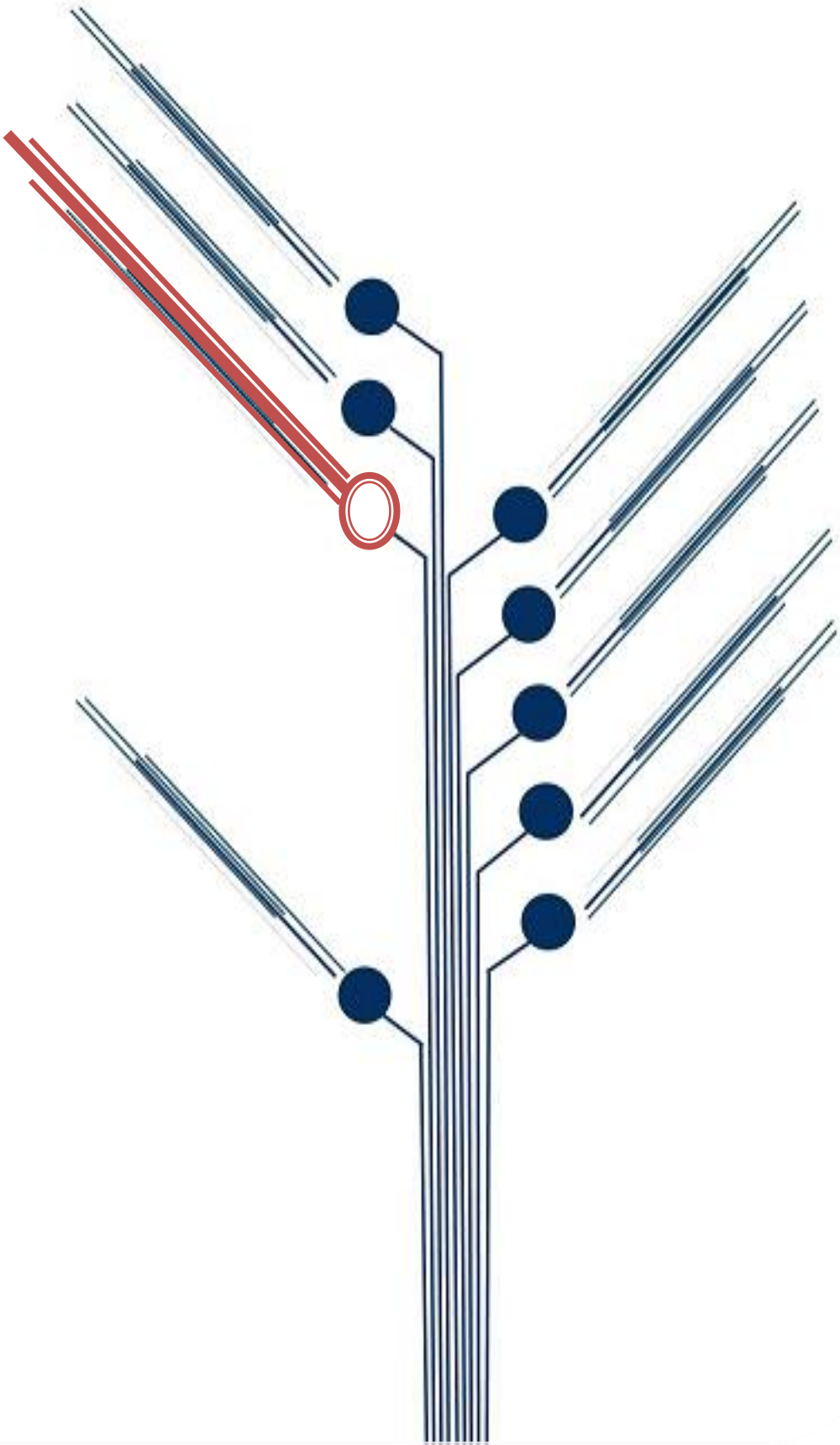

Conclusion

CIs are one of the most successful prosthesis of modern medicine, restoring with very high rate the hearing function.

The heterogeneous modeling of the CIs and cochlea interface is proposed in this document. This modeling ensures accurate understanding of the mechanisms involved in hearing and pointed out the limitations of cochlear implants at present, possibly suggesting new solutions to test for CIs system improvement.

As CIs manufacturing companies are currently developing less noticeable devices, the electrical system architecture redesign may be obligatory. Using the transmitter design of Y. Vaiarello [24] for these new types of CIs as a basis to this work, we then proposed a complete behavioral model of this entire transmitter. The propagation channel between the transmitter and the receiver was also modeled using a simplified Cole and Cole [49, 362] impedance model which is an electric description of biological tissue that has been proven to match physical experiments. Concatenating those models allowed us to estimate the power received in the receiver and the noise introduced. However these values have still to be confirmed by physical measurements.

The transmitter behavioral model was concatenated with the propagation channel model and the simulation results defined the specifications of the receiver. As the receiver will be implanted inside the patient skull, robust design and low power consumption are required. The noise power introduced by the propagation channel was found a little lower than the power received, adding more constraints on the receiver LNA design. In order to correctly design the LNA, a mathematical optimization algorithm developed by P. Ndungidi [395] was utilized before its SPICE implementation and refinement.

Three common receiver architectures were compared in terms of power consumption and Noise Figure, using a SPICE simulator. The receiver architecture composed of a LNA and a power detector was found the most suitable with the receiver specifications and its behavioral modeling was realized.

The entire behavioral modeling of the transceiver was hence performed permitting extended simulations. The most sensitive parameters extraction was investigated selecting a set of critical parameters and defining a minimum, a typical and a maximum value of them. However this testing was not covering all the possible cases combinations. From this study it resulted that the preamplifier gain, the comparator offset, the antenna efficiency and the LNA output dynamics were fundamental in the transceiver output signal integrity.

The receiver layout was not done, neither was the receiver physical realization and testing. This could further bring new issues about the receiver specifications and disagreements on the entire transceiver architecture imposed by the transmitter part.

As the transmitter performed PWM modulation before sending the signal to the RF band, the study of phase noise is of capital importance for the overall signal integrity as well as the ISM band specifications respect. However the study of phase noise was statistical and could hardly be incorporated into transient simulation models. Jitter extraction from phase noise models was performed and applied to the oscillators of the transmitter. The PWM signal accuracy was greatly reduced based on the simulation results obtained, suggesting that control systems such as PLL may be necessary for efficient signal encoding and transmission.

After reviewing the mathematical basis of stochastic process and systems, the review of the current understanding and description of noise types was proposed. Two major theories describing phase noise were discussed, Leeson model and Hajimiri and Lee model, both interpreting phase noise as white and 1/f noise entering inside a physical system. We then proposed a new model combining both the Lesson model and the Hajimiri and Lee model of phase noise. The model was tested on two different oscillator topologies and gave satisfying accuracy. This model permitted a system creation which ensures consequent simulation time gain. We are currently extending this system to avoid running SPICE simulation for system parameters extraction, rendering our model of great convenience.

Conversion of phase noise into timing jitter theories were discussed before computing the timing jitter introduced by the oscillators of the transmitter by two diverse methodologies. The timing jitter introduced by the ramp creating oscillator significantly restricted the PWM accuracy, suggesting oscillator design optimization.

Besides hearing is a very complex mechanism and understanding it deeply may bring new solutions for cochlear implant system. The external ear, middle ear and the propagation biomechanics occurring inside the cochlea were quickly reviewed. We also decided to implement the traveling wave theory, which is the most accepted theory describing the pressure propagation inside the cochlea. This implementation led to BM vibrations, which excites the organ of Corti. We proposed a mechanical model of the organ of Corti, close to literature available one, and completed this model with the HCs study. Two theoretical sound wave of 300 Hz and 600 Hz respectively and with an amplitude of 50 dB were used for model verification.

Then HC depolarization occurs and we modeled the complex mechanism of synaptic transmission which probably result in SGCs depolarization and APs generation. We gather into a single mathematical model some of the current understanding of ribbon synapse, synaptic transmission and synaptic receptors, to explain the AP generation following a HC membrane depolarization.

Following SGCs excitation, different part of the brain, still partly understood, are stimulated resulting in the hearing perception.

We proposed a new analog model of AP propagation on nerve cells. The two main literature available models of AP propagation along a nerve fiber were reviewed and theirs advantages and theirs limitations were pointed out. This new model was mimicking very closely to the physics of the events occurring during AP propagation. We were able to obtain a model with similar velocity, wavelength and frequency like an experimental AP. This model may be of importance for brain study of more complex mechanisms.

The consecutive firing of nerve cells following a maintained stimulus, called spikes train, can be recorded using multiple microelectrodes, requiring spikes sorting. We first mathematically defined the single spikes train generation which indicated single nerve cell activity, based on the AP propagation function that we defined. The ISD statistics were also reviewed. ISD is often modeled by various authors with an exponential distribution, and has been shown to be inversely proportional to the nerve fiber stimulus.

To monitor the activity of the auditory nerve *in vivo*, the total or partial auditor nerve activity is generally measured by electroencephalograhy. The study of the AP creation and propagation involving many nerve fibers was then performed, with the mathematical description of the CAP propagation (biphasic recording only).

The understanding of the physiological description of the cochlea is of great value in order to analyze cochlear implants and to propose possible improvements.

We performed the study of the interface between the electrodes and the organ of Corti and we proposed an electrical analog of this interface. After running SPICE simulations, we obtained the theoretical minimum voltage and power needed for a single electrode to stimulate a packet of nerve fibers and we also studied the influence of neighboring electrodes.

Besides the threshold of hearing describes the hearing sensitivity toward the sound frequencies. This function is not constant, meaning that amplification of certain frequency bands is achieved by the ear, mainly associated with the cochlea physical properties. We hence created a topographic map of the SGCs as a function of their place inside the cochlea and weighted by the threshold of

hearing function. This map may be of importance in order to restitute the hearing sensitivity toward certain frequency in cochlear implants. In fact we defined scalar coefficients associated with this map that we multiplied to the standard voltage sent to the electrodes and needed to stimulate the nerve fibers.

We further developed a new algorithm for electrodes selection, based on STFT, that may increase the hearing sensation when the frequency of the sound received is not directly covered or close to frequencies covered by the electrodes. The implementation of this algorithm in cochlear implanted people was not done and the benefits are however highly hypothetical. As described in details in Section I.E, when a sound wave frequency is not inside the frequency set associated with the electrodes, our new algorithm may lead to stimulation of spaced electrodes. The brain interpretation of such signals may not be optimal and may even result in patient discomfort.

Finally we also proposed a system attempting to define sound perception in deaf people (using filters to model hearing loss) or in deaf people with CIs (using DFT applied only on the frequencies activated by the electrodes). The mathematical results obtained were less concluding than the analysis by an healthy hear of the sound reconstructed after signal processing.

This work was mainly driven by the application and we aimed to propose new hypothesis in area partly characterized in literature and also to expose solutions for better signal transmission or sound perception in people using cochlear systems.

The various theoretical models presented were mainly based on data extracted from physical experiments. The inclusion of these diverse models into two single parametric models may be envisaged and is currently under study: one system gathering all the models associated with a healthy ear and a second system bringing together all the CIs modeling works and their effect on auditory nerve fibers. The comparison of these two global system results may permit to quantify theoretically the gap in sound perception between a healthy ear and a CI sound production. Furthermore, if verified by physical experiments, it may also allow extending tests of this device which could be of significance as they are surgically implanted inside the patient's skull and hence hard to remove or upgrade.

CIs are among the best prostheses available to date and many improvements may appear in future, especially associated with a nerve cells profound understanding and very accurate stimulation. Besides research on stem cells and regenerative medicine is currently exploding, and that may bring new hope for deaf people. Furthermore, manipulations of the human genome, which

started around 50 years ago with the discovery of DNA structure and various genetic techniques may also be exploited in few decades to cure genetic illnesses leading to deafness.

For now, genetic, biochemical and microelectronic technologies just begin to be combined and may one day permit very efficient and convenient hearing restitution.

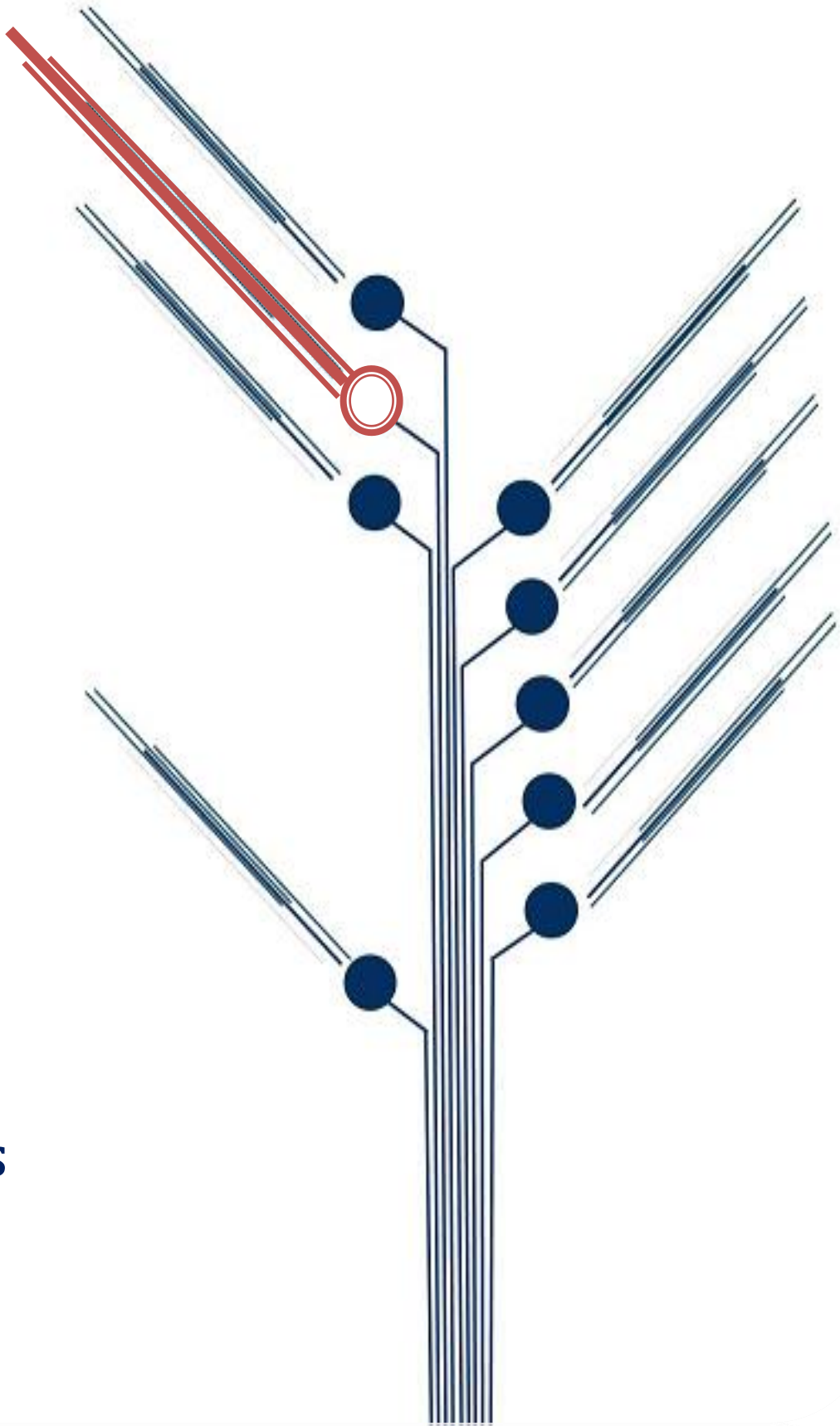

References

[1] B. S. Wilson and M. F. Dorman, "Cochlear implants: current designs and future possibilities", *J Rehabil Res Dev, Vol.* 45-5, pp. 695-730, (2008)
[2] J. Rouger and et. al., "Evidence that cochlear-implanted deaf patients are better multisensory integrators"*, Vol.* 104-17, pp. 7295-7300, (2007)
[3] O. Bø Wie, E.-S. Falkenberg, O. Tvete and B. Tomblin, "Children with a cochlear implant: Characteristics and determinants of speech recognition, speech-recognition growth rate, and speech production: Niños con Implante Coclear: Características y determinantes del reconocimiento, de la tasa de crecimiento del reconocimiento y de la producción de lenguaje", *International Journal of Audiology, Vol.* 46-5, pp. 232-243, (2007)
[4] M. Burger, "Biosciences in the 21st century, Lecture 2: Innovations and Challenges", *LeHigh University*, Online: *http://www.lehigh.edu/~inbios21/PDF/Fall2008/Burger_08292008.pdf*
[5] "Cochlear Implant 1", *common.wikipedia.org*,
[6] A. N. P. Fan-Gang Zeng, Richard R. Fay, "Cochlear Implants: Auditory Prostheses and Electric Hearing", *ed. Springer*. (21 avr. 2004 - 437 pages)
[7] M. Carlberg and e. al., "BioInitiative 2012: A Rationale for Biologically Exposure Standards for Low Electromagnetic Radiation", (December 31, 2012)
[8] H. P. Schwan and K. R. Foster, "RF-field interactions with biological systems: electrical properties and biophysical mechanisms", *Proceedings of the IEEE, Vol.* 68-1, pp. 104-113, (1980)
[9] L. Challis, "Mechanisms for interaction between RF fields and biological tissue", *Bioelectromagnetics, Vol.* 26-S7, pp. S98-S106, (2005)
[10] U. Møller, D. G. Cooke, K. Tanaka and P. U. Jepsen, "Terahertz reflection spectroscopy of Debye relaxation in polar liquids", *Advances in Optics and Photonics, Vol.* 26, pp. A113-A125 (2009)
[11] J. K. Niparko, "Cochlear Implants: Principles and Practices (chapter 7)". (2009)
[12] G. Clark, "Cochlear Implants: Fundamentals and Applications (ch. 4-8)", *ed. Springer-Verlag*. (2003)
[13] M. Bond, S. Mealing, R. Anderson, J. Elston, G. Weiner, R. Taylor, M. Hoyle, Z. Liu, A. Price and K. Stein, "The effectiveness and cost-effectiveness of cochlear implants for severe to profound deafness in children and adults: a systematic review and economic model", *Health technology assessment, Vol.* 13-44, pp. 1-330, (2009)
[14] A. Moctezuma and J. Tu, "An overview of cochlear implant systems", *USA: University of Illinois, Urbana-Champaign*, (2011), Online: *https://wiki.engr.illinois.edu/download/attachments/48137228/ECE+415+Cochlear+Implant+Final.pdf*
[15] P. Senn, "Making deaf people hear (better?) European project ", *University Department of Otorhinolaryngology, Head & Neck Surgery, Inselspital, Bern, Switzerland*, (2013), Online: *http://www.euronanoforum2013.eu/wp-content/uploads/2013/07/P-Senn-ENF2013.pdf*
[16] J. Spitzer, "Evaluation of decisions regarding candidates for cochlear implants", *Archives of oto-rhino-laryngology, Vol.* 245-2, pp. 92-97, (1988)
[17] J. Nancy and M. Roizen, "ETIOLOGY OF HEARING LOSS IN CHILDREN, Nongenetic Causes , HEARING LOSS IN CHILDREN", *Department of Pediatrics, University of Chicago Pritzker School of Medicine*,
[18] P. M. Carter and e. al., "Cochlear implant system with soft turn on electrodes", *Patent US5755747 A, USA*, (2008),
[19] R. Nowak, "Light opens up a world of sound for the deaf", *Newscientist.com*, (21 November 2008),
[20] A. Wheeler, S. Archbold, S. Gregory and A. Skipp, "Cochlear implants: The young people's perspective", *Journal of Deaf Studies and Deaf Education, Vol.* 12-3, pp. 303-316, (2007)
[21] R. J. Briggs, H. C. Eder, P. M. Seligman, R. S. Cowan, K. L. Plant, J. Dalton, D. K. Money and J. F. Patrick, "Initial clinical experience with a totally implantable cochlear implant research device", *Otology & Neurotology, Vol.* 29-2, pp. 114-119, (2008)
[22] D. A. Chen, D. D. Backous, M. A. Arriaga, R. Garvin, D. Kobylek, T. Littman, S. Walgren and D. Lura, "Phase 1 clinical trial results of the Envoy System: a totally implantable middle ear device for sensorineural hearing loss", *Otolaryngology--Head and Neck Surgery, Vol.* 131-6, pp. 904-916, (2004)
[23] Y. Vaiarello, Y. Leduc, N. Veau and G. Jacquemod, "Ultra Low Power Transmitter for Cochlear Implant Application", *IEEE Circuits and Systems Society Forum on Emerging and Selected Topics (CAS-FEST)*, (2011)
[24] R. Roby, "Roby Institute - Advanced treatment for a healthy living", (2011), Online: *http://onlineallergycenter.com/dr_roby.php*

[25] J. K. Kevin D Jones, Victor Konrad, "Some "Real World" Problems in the Analog and Mixed Signal Domains ", *Malta*, (2008),
[26] K. Kundert, "Informative note: Simulation of Analog and Mixed Signal Circuits", (1998),
[27] X. Zhou and T. Tang, "Accurate Timing Simulation of Mixed-Signal Circuits with a Dynamic Delay Model", *Proceedings of the Int. Workshop on Computer-Aided Design, Test, and Evaluation for Dependability*, pp. 309-311, (1996)
[28] S. B. Bibyk, "Mixed-Signal IC Design Kit Training Manual", *Ohio*, (2003),
[29] N. Padmaraju, "Analog and Mixed Signal Modeling Approaches", *MindTree Limited*, Online: *http://www.design-reuse.com/articles/22773/analog-mixed-signal-modeling.html*
[30] K. Kundert, "Introduction to The Design of Mixed-Signal Systems on Chip, MS-SOC", (1998),
[31] J. L. T. Elisabeth M. S. J. Van Gennip, "Assessment and Evaluation of Information Technologies in Medicine", *ed. IOS Press*. (1995)
[32] C. M. Macal, "Model Verififcation and Validation", *Threat Anticipation: Social Science Methods and Models*, (2005)
[33] R. G. Sargent, "Verification and Validation of simulation models", *Simulation Conference (WSC)*, pp. 166 - 183 (2010)
[34] J. A. Sokolowski and C. M. Banks, "Principles of Modeling and Simulation: A Multidisciplinary Approach", *ed. John Wiley & Sons*. (2009)
[35] Y. Vaiarello, "Étude et conception d'un microphone sans fil très faible onception d'un microphone sans fil très faible onception d'un microphone sans fil très faible onception d'un microphone sans fil très faible onception d'un microphone sans fil très faible o", *LEAT, Sophia Antipolis*, (2012),
[36] Fang Lin Luo, Hong Ye and M. H. Rashid, "Digital Power Electronics and Applications", *ed. Elsevier, USA*. (2005)
[37] A. Bell, "A Resonance Approach to Cochlear Mechanics", *PloS one, Vol.* 7-11, pp. e47918, (2012)
[38] E. S. Ferre-Pikal and e. al., " Draft revision of IEEE std 1139- 1988 standard definitions of physical quantities for fundamental frequency and time metrology – random instabilities", *IEEE international, Frequency control symposium*, pp. 338 - 357, (1997)
[39] L. A. Werner and L. Gray, "Behavioral studies of hearing development",in *Development of the auditory system*, *ed. Springer*. 12-79, (1998)
[40] K. Kundert, "Accurate and rapid measurement of IP2 and IP3", *The designer guide to SPICE and Spectre, Version 2b*, (2002)
[41] N. Pernick, "Ear Anatomy", (2013), Online: *http://www.pathologyoutlines.com/topic/earnormalanatomy.html*
[42] R. Arvind, Nuttapong, Srirattana and Joy Laskar, "Modeling and design techniques for RF power amplifier", *ed. John Wiley & Sons*. (2008)
[43] R. A. Bergman, A. K. Afifi and P. M. Heidger, "Plate 16.312 Organ of Corti", *http://www.anatomyatlases.org/MicroscopicAnatomy/Section16/Plate16312.shtml*, Online: *Anatomy Atlas*
[44] M. M. Radmanesh, "Advanced RF and microwave circuit design: the ultimate guide to superior design". *I. 978-1-4259-7243-1*, (2009)
[45] J. Prikkel, "Modelling cochlear mechanics", *Order, Vol.* 501, pp. 2395, (2009)
[46] G. Vasilescu, "Electronic Noise and Interfering Signals: Principles and Applications", *ed. Springer*. (1999)
[47] M. Hubin, "Propriétés des milieux biologiques", (22 Mars 2013),
[48] S. M. Sze, & Ng, K. K., "Physics of semiconductor devices", (2006), Online: *maktabkhooneh.org/files/library/eng/electrical/5.pdf*
[49] P. B. Filho, "Tissue Characterisation using an Impedance Spectrosocpy probe", (2002),
[50] S. M. Sze and K. K. Ng, "Physics of semiconductor devices in *Chapter V: Investigation of ac conductivity and electronic modulus of LBS, LPBS and LVBS samples*", (2006),
[51] H. L. Friedman, "Theory of the dielectric constant of solutions ", *The Journal of Chemical Physics, Vol.* 2, (1976)
[52] D. Andreuccetti, "Dielectric Properties of Biologic Tissues in the frequency range of 10 Hz - 100 GHz", *IFAC*,

[53] S.Grimnes, Ø.G.Martinsen, J.Malmivuo, R.Plonsey, D. S. Holder and J. G. Webster, "Measurement of Electrical Bio-Impedance (the EBI) and its diagnostical applications", *Thomas Johann Seebecki elektroonikainstituut*, Online: *http://www.elin.ttu.ee/mesel/Study/Courses/Biomedel/Content/BioImped/BioImped.htm*

[54] S. Ueno, "Biological effects of magnetic and electromagnetic fields", *ed. Springer*. (1996)

[55] R. Sarpeshkar, T. Delbruck and C. A. Mead, "White noise in MOS transistors and resistors", *Circuits and Devices Magazine, IEEE, Vol.* 9-6, pp. 23-29, (1993)

[56] J. Johnson and H. Nyquist, "Thermal Agitation of Electricity in Conductors - details of the experiment", *Phys. Rev., Vol.* 32-97, (1928)

[57] Y. Vaiarello, W. Tatinian, Y. Leduc, N. Veau and G. Jacquemod, "Ultra low power radio microphone for cochlear implant application", *IEEE Journal of Emerging and Selected Topics in Circuits And Systems Vol.* 1-4, pp. 622-630, (2011)

[58] O. Diop, "Study and optimisation of the quality factor of small antennas", (2013), Online: *LEAT, Sophia Antipolis*

[59] O. Diop and e. al., "Planar antennas on Integrated Passive Device technology for biomedical applications", *IEEE International Workshop on Antenna Technology (iWAT)*, pp. 217 - 220, (2012)

[60] R. A. York, "Noise and radiating systems", *Microwave Electronics Laboratory of the University of California in Santa Barbara*, (2014), Online: *http://my.ece.ucsb.edu/York/Bobsclass/201C/Handouts/chap4.pdf*

[61] T. H. Lee, "The Design of CMOS Radio-Frequency Integrated Circuits", *ed. Cambridge*. (2003)

[62] "Low Noise Amplifier (LNA)", *University of California San Diego, Computer Science and Engeneering*, Online: *http://www-cse.ucsd.edu/*

[63] W.-H. Cho and S. S. Hsu, "An ultra-low-power 24 GHz low-noise amplifier using 0.13 CMOS technology", *Microwave and Wireless Components Letters, IEEE, Vol.* 20-12, pp. 681-683, (2010)

[64] M.-T. Lai and H.-W. Tsao, "Ultra-Low-Power Cascaded CMOS LNA With Positive Feedback and Bias Optimization", (2013)

[65] J. Jeong, J. Kim, D. S. Ha and H.-s. Lee, "A reliable ultra low power merged LNA and Mixer design for medical implant communication services", *Life Science Systems and Applications Workshop (LiSSA), 2011 IEEE/NIH*, pp. 51-54, (2011)

[66] P.-Y. Chang, S.-H. Su, S. S. Hsu, W.-H. Cho and J.-D. Jin, "An ultra-low-power transformer-feedback 60 GHz low-noise amplifier in 90 nm CMOS", *Microwave and Wireless Components Letters, IEEE, Vol.* 22-4, pp. 197-199, (2012)

[67] "Presentation on Fundamentals of Mixer Design", *Agilent Technologies*, (2001),

[68] A. Helmy and M. Ismail, "On Chip Inductors Design Flow", *Substrate Noise Coupling in RFICs Analog Circuits And Signal Processing Series*, pp. 63 - 86, (2008)

[69] P. Ndungidi, H. García-Vázquez, J. d. Pino, F. Dualibe and C. Valderrama, "RF specification driven by Multi-Objective Optimization Method", *DCIS*, (November, 2012)

[70] B. Vigraham and P. R. Kinget, "An ultra low power, compact UWB receiver with automatic threshold recovery in 65 nm CMOS", *Radio Frequency Integrated Circuits Symposium (RFIC), 2012 IEEE*, pp. 251-254, (2012)

[71] A. C. W. Wong, G. Kathiresan, C. K. T. Chan, O. Eljamaly, O. Omeni, D. McDonagh, A. J. Burdett and C. Toumazou, "A 1 V wireless transceiver for an ultra-low-power SoC for biotelemetry applications", *IEEE JOURNAL OF SOLID-STATE CIRCUITS, Vol.* 43-7, pp. 1511-1521, (2008)

[72] P. D. Bradley, "An ultra low power, high performance medical implant communication system (MICS) transceiver for implantable devices", *Biomedical Circuits and Systems Conference, 2006. BioCAS 2006. IEEE*, pp. 158-161, (2006)

[73] W. Wu, M. A. Sanduleanu, X. Li and J. R. Long, "17 GHz RF front-ends for low-power wireless sensor networks", *IEEE JOURNAL OF SOLID-STATE CIRCUITS, Vol.* 43-9, pp. 1909-1919, (2008)

[74] J. Jin and K. Fu, "An Ultra-low-power Integrated RF Receiver for Multi-standard Wireless Applications", *IETE Journal of Research, Vol.* 59-4, (2013)

[75] X. Huang, A. Ba, P. Harpe, G. Dolmans, H. de Groot and J. R. Long, "A 915 MHz, ultra-low power 2-tone transceiver with enhanced interference resilience", *Solid-State Circuits, IEEE Journal of, Vol.* 47-12, pp. 3197-3207, (2012)

[76] M. Lont, D. Milosevic, A. van Roermund and G. Dolmans, "Ultra-low power FSK wake-up receiver front-end for body area networks", *Radio Frequency Integrated Circuits Symposium (RFIC), 2011 IEEE*, pp. 1-4, (2011)
[77] L. Huang, M. Ashouei, R. F. Yazicioglu, J. Penders, R. J. Vullers, G. Dolmans, P. Merken, J. Huisken, H. de Groot and C. Van Hoof, "Ultra-Low Power Sensor Design for Wireless Body Area Networks-Challenges, Potential Solutions, and Applications", *JDCTA, Vol.* 3-3, pp. 136-148, (2009)
[78] H.-H. Hsieh, H.-S. Chen, P.-H. Hung and L.-H. Lu, "Experimental 5-GHz RF frontends for ultra-low-voltage and ultra-low-power operations", *Very Large Scale Integration (VLSI) Systems, IEEE Transactions on, Vol.* 19-4, pp. 705-709, (2011)
[79] M. Camus, B. Butaye, L. Garcia, M. Sie, B. Pellat and T. Parra, "A 5.4 mW/0.07 mm 2.4 GHz front-end receiver in 90 nm CMOS for IEEE 802.15. 4 WPAN standard", *Solid-State Circuits, IEEE Journal of, Vol.* 43-6, pp. 1372-1383, (2008)
[80] X. Hua, W. Lei, S. Yin and D. F. Foster, "Design and optimization of a 2.4 GHz RF front-end with an on-chip balun", *Journal of Semiconductors, Vol.* 32-9, pp. 095004, (2011)
[81] J.-F. Chang and Y.-S. Lin, "3.15 dB NF, 7.2 mW 3–9 GHz CMOS ultra-wideband receiver front-end", *Electronics letters, Vol.* 47-25, pp. 1401-1402, (2011)
[82] L. Thede, "Practical Analog and Digital filter design", (2004), Online: *http://dsp-book.narod.ru/PADFD.pdf*
[83] S. Larribe, "Le filtrage analogique", *CNAM Saclay*, (2005), Online: *http://sylvain.larribe.free.fr/CNAM/2004-2005/CNAM_2005_Filtrage.pdf*
[84] C. G. Dunenberg, "Filter Approximation Theory: Butterworth, Chebyshev, and Elliptic Filters", Online: *http://doctord.dyndns.org/courses/topics/Circuits/Filter_Approximation_Theory.pdf*
[85] A. D. Poularikas, "The handbook of formulas and tables for signal processing, Analog Filter Approximations", *ed. A. D. Poularikas*. (1999)
[86] V. Meghdadi, "Première partie: le filtrage analogique, Chapitre 2: Approximations", *ENSIL*,
[87] E. Sanchez, "A Designer's Guide To Filter Approximations", (Fall 2004),
[88] S. Icart, "Elec 4: Automatique", *Polytech Nice Sophia Antipolis University*, Online: *http://users.polytech.unice.fr/~icart/*
[89] D. Earl, "Möbius transformations and the extended complex plane", (2007), Online: *http://people.maths.ox.ac.uk/earl/G2-lecture4.pdf*
[90] C. Mello, "IIR filter design example", *Carnegie Mellon University*, (2005), Online: *https://www.ece.cmu.edu/~ee791/lectures/L22/IIRDesign.pdf*
[91] K. K. Parhi, "Chapter 11: Scaling and Round-off Noise", *University of Minnesota , Department of Electrical and Computer Engineering*, Online: *http://www.ece.umn.edu/users/parhi/SLIDES/chap11.pdf*
[92] O. Hinton, "Chapter 5 Design of IIR Filters ", *Newcasle University*, (2001), Online: *http://www.staff.ncl.ac.uk/oliver.hinton/eee305/Chapter5.pdf*
[93] A. kolesnikov, "Efficient algorithms for vectorization and polygonal approximation ", *Universityof joensuu computer science dissertations*, (2005),
[94] D. B. Leeson, "A simple model of feedback oscillator noise spectrum", *Proceedings IEEE, Vol.* 54, pp. 329–330, (1966)
[95] G. Sauvage, "Phase noise in oscillators: a mathematical nalysis of Leeson' smodel", *IEEE Transactions on instrumentation and measurments, Vol.* IM-26-4, (1977)
[96] A. Hajimiri and T. Lee, "Oscillator Phase Noise: A Tutorial", *IEEE J. Solid-State Circuits,* -35, (2000)
[97] T. Lee and A. Hajimiri, "A general theory of phase noise in electrical oscillators", *IEEE JOURNAL OF SOLID-STATE CIRCUITS, Vol.* 33, pp. 179-194, (1998)
[98] M. S. Keshner, "1/f noise", *Proceedings of the IEEE, Vol.* 70-3, pp. 212-218, (1982)
[99] Y. Jia and J. Li, "Stochastic system with colored correlation between white noise and colored noise", *Physica A: Statistical Mechanics and its Applications, Vol.* 252-3, pp. 417-427, (1998)
[100] E. Milotti, "1/f noise: a pedagogical review", *Corwnell University Library, classical physics*, (2002)
[101] J. A. Gubner, "Probability and Random Processes for Electrical and Computer Engineers, Chap. 10: Introduction to Random Processes", *ed. Cambridge University Press*. (2006)
[102] E. Rubiola, *FEMTOST Institute*, (2006), Online: *http://www.ieee-uffc.org/frequency-control/learning/pdf/Rubiola.pdf*

[103] A. M. Niknejad, "Oscillator Phase Noise", *University of Berkley*, (2009),
[104] H. Abidi and A. Asad, "How phase noise appears in oscillators",in *Analog Circuit Design*, *ed. Springer*. 271-290, (1997)
[105] J. Phillips and K. Kundert, "Noise in Mixers, Oscillators, Samplers & Logic, an introduction to Cyclostationary noise", *Cadence Design Systems*,
[106] A. Hajimiri and H. Donhee, "Virtual damping in oscillators", *Proceedings of the IEEE*, pp. 213-216, (2002)
[107] A. Hajimiri, S. Limotyrakis and T. H. Lee, "Jitter and Phase Noise in Ring Oscillators", *IEEE JOURNAL OF SOLID-STATE CIRCUITS, Vol.* 34-6, (2006)
[108] B. L. a. A. Lowenberger, "Understanding Jitter Requirements of PLL-Based Processors Rev 1 ", *Analog Devices, Engineer-to-engineer note*, (January 20, 2005),
[109] C. Emmerich, "Introduction to Jitter", *Iowa State University, Department of Electrical and Computer Engineering*
(October 23), Online: *http://class.ee.iastate.edu/mmina/ee418/Notes/Introduction_to_Jitter.pdf*
[110] M. Zielinski, M. Kowalski, D. Chaberski and S. Grzelak, "Estimation of the Clock Signal Jitter Using the Time-Interval Measurement System", *Proc. of XVIII IMEKO World Congress Metrology for a Sustainable Development*, (2006)
[111] A. Hajimiri, S. Limotyrakis and T. H. Lee, "Jitter and phase noise in ring oscillators", *Solid-State Circuits, IEEE Journal of, Vol.* 34-6, pp. 790-804, (1999)
[112] M. Grozing and M. Berroth, "The Effect of 1/f Noise on the Spectrum and the Jitter of a Free Running Oscillator", *Research in Microelectronics and Electronics 2006*, pp. 485-488, (2006)
[113] M. R. Khanzadi, A. Panahi, D. Kuylenstierna and T. Eriksson, "A model-based analysis of phase jitter in RF oscillators", *Frequency Control Symposium (FCS), 2012 IEEE International*, pp. 1-4, (2012)
[114] D. Howe and T. Tasset, "Clock jitter estimation based on PM noise measurements", *ed. IEEE*. 541-546, (2003)
[115] R. Poore, "Phase Noise and Jitter", *Agilent*, Online: *http://www.keysight.com/upload/cmc_upload/All/phase_noise_and_jitter.pdf?&cc=FR&lc=fre*
[116] A. Zanchi, "How to Calculate the Period Jitter σT from the SSCR L(fn) with Application to Clock Sources for High-Speed ADCs", *Texas Instruments*, (December 2003), Online: *http://www.ti.com/lit/an/slwa028/slwa028.pdf*
[117] A. Chorti and M. Brookes, "A spectral model for RF oscillators with power-law phase noise", *Circuits and Systems I: Regular Papers, IEEE Transactions on, Vol.* 53-9, pp. 1989-1999, (2006)
[118] M. Mansuri and C.-K. Ken, "Jitter optimization based on phase-locked loop design parameters", *Solid-State Circuits, IEEE Journal of, Vol.* 37-11, pp. 1375-1382, (2002)
[119] M. J. Rossano, "Chapter 10: Perception of sounds", *Southeaster Louisiana University*, Online: *https://www2.southeastern.edu/Academics/Faculty/mrossano/perception/index.html*
[120] J. O. Pickles, "An introduction to the physiology of hearing", Vol. 2, *ed. Academic press London*. (1988)
[121] W. A. Yost, "Fundamentals of hearing: An introduction", *ed. Academic Press*. (1994)
[122] R. E. Turner, "An introduction to hearing", *University of Cambridge*, (2013), Online: *https://camtools.cam.ac.uk/access/content/group/d4fe6800-4ce2-4bad-8041-957510e5aaed/Public/3G3/RET/2013/hearing.pdf*
[123] P. A. Santi and P. Mancini, "Chapter 140: Cochlear Anatomy and Central Auditory Pathways", *Predrag M. Maksimović Web Site*, Online: *http://famona.tripod.com/ent/cummings/cumm140.pdf*
[124] Nicole, "Anatomy of the Ear", *Yournursingtutor.com*, (2012), Online: *http://www.yournursingtutor.com/ANATOMY-OF-THE-EAR/*
[125] P. W. Alberti, "The anatomy and physiology of the ear and hearing", *University of Toronto, Canada*, Online: *http://www.who.int/occupational_health/publications/noise2.pdf*
[126] J. Whittaker, "Physics of the ear, Comps II presentation", *John Hopkins University*, (2006),
[127] H. Kurokawa and R. L. Goode, "Sound pressure gain produced by the human middle ear"*, Vol.* 113 -4, pp. 349-355, (1995)
[128] J. P. Wilson and B. M. Bull, "Mechanics of middle and inner ear"*, Vol.* 43-4, pp. 821-837, (1987)
[129] J. E. Roeckelein, "Dictionary of theories, laws, and concepts in psychology", *ed. Greenwood Publishing Group*. (1998)

[130] B. H. J. Runsung Munkong, "Auditory perception and cognition", *IEEE SIGNAL PROCESSING MAGAZINE*, pp. 98-108, (2008)
[131] S. K. Griffiths, "Inner ear", *University of Florida, Department of Communication Sciences and Disorders*, (2010), Online: *http://web.clas.ufl.edu/users/sgriff/A&P.html*
[132] J. Tobias, "Foundations of modern auditory theory, Volume 1", *ed. Elsevier*. (2012)
[133] Kewley-Port, "S 319 Auditory system ", *Indiana University*, (2012), Online: *http://www.indiana.edu/~acoustic/*
[134] E. S. Olson, H. Duifhuis and C. R. Steele, "Von Békésy and cochlear mechanics", *Hearing research, Vol.* 293-1, pp. 31-43, (2012)
[135] J. Ashmore, P. Avan, W. Brownell, P. Dallos, K. Dierkes, R. Fettiplace, K. Grosh, C. Hackney, A. Hudspeth and F. Jülicher, "The remarkable cochlear amplifier", *Hearing research, Vol.* 266-1, pp. 1-17, (2010)
[136] C. A. M. Richard F. Lyon, "Cochlear hydrodynamics demystified", *Caltech-CS-TR-88-4*,
[137] C. Kubisch and e. al., "KCNQ4, a Novel Potassium Channel Expressed in Sensory Outer Hair Cells, Is Mutated in Dominant Deafness", *Cell, Vol.* 96-3, pp. 437–446, (5 February 1999)
[138] C. A. S. Stephen J Elliott, "The cochlea as a smart structure "*, Vol.* 21-6, (2012)
[139] D. D. Greenwood, "A cochlea frequency position function for several species – 29 years late"*, Vol.* 87-6, pp. 2592-2605, (1991)
[140] E. L. LePage, "The mammalian cochlear map is optimally warped", *The Journal of the Acoustical Society of America, Vol.* 114-2, pp. 896-906, (2003)
[141] M. Barclay, A. F. Ryan and G. D. Housley, "Type I vs type II spiral ganglion neurons exhibit differential survival and neuritogenesis during cochlear development", *Neural Dev, Vol.* 6-33, pp. 101-186, (2011)
[142] G. V. Békésy, "Experiments in Hearing, part 3. Chap 12-14". (1989)
[143] F. N. F. Mammano, "Biophysics of the cochlea: linear approximation"*, Vol.* 93-6, (June 1993)
[144] L. Trussel, "Mutant ion channel in cochlear hair cells"*, Vol.* 97-8, pp. 3786 –3788, (2000)
[145] B. A. H. a. R. M. O. Steven K. Juhn, "Blood-Labyrinth Barrier and Fluid Dynamics of the Inner Ear"*, Vol.* Vol. 7-nº 2, pp. 78-83, (Jul/ Dec de 2001)
[146] R. Yehoash and R. A. Altschuler, "Structure and innervation of the cochlea"*,* -60, pp. 397 - 422, (15 January 2003)
[147] M. F. Bear, "Neuroscience, Chapter 4, The Action Potential", *ed. Lippincott Williams & Wilkins*. (2007)
[148] "Essential Neuroscience, Section II The Neuron", *ed. Lippincott Williams & Wilkins*. (April 2010)
[149] R. Nobili, F. Mammano and J. Ashmore, "How well do we understand the cochlea?", *Trends in neurosciences, Vol.* 21-4, pp. 159-167, (1998)
[150] A. Saremi and S. Stenfelt, "A physiological signal-transmission model of cochlea", *Linkoping University*, Online: *https://www.liu.se/ihv/head/mobility/1.288026/Amin_poster_mechanics.pdf*
[151] S. J. Elliott and C. A. Shera, "The cochlea as a smart structure", *Smart Materials and Structures, Vol.* 21-6, pp. 064001, (2012)
[152] S. Ramamoorthy and A. L. Nuttall, "Outer hair cell somatic electromotility in vivo and power transfer to the organ of Corti", *Biophysical journal, Vol.* 102-3, pp. 388-398, (2012)
[153] J. A. Vernon and A. R. Møller, "A model for cochlear origin of subjective tinnitus: Excitatory drift in operating point of inner hair cells",in *Mechanisms of Tinnitus, Chapter 11*
ed. Jack A. Vernon, Aage R. Møller.
[154] P. Martin, "Negative hair-bundle stiffness betrays a mechanism for mechanical amplification by the hair cell", *Proceedings of the National Academy of Sciences, Vol.* 97-22, pp. 12026-12031, (2000)
[155] J. R. Cotton and J. W. Grant, "A finite element method for mechanical response of hair cell ciliary bundles", *Journal of biomechanical engineering, Vol.* 122-1, pp. 44-50, (2000)
[156] S. T. Smith, Chadwick, Richard S, "Simulation of the response of the inner hair cell stereocilia bundle to an acoustical stimulus", *PloS one, Vol.* 6-3, pp. e18161, (2011)
[157] R. Zelick, "Vertebrate Hair Cells", *Randy Zelick's laboratory at Portland State University*, Online: *http://web.pdx.edu/~zelickr/sensory-physiology/lecture-notes/OLDER/L12b-hair-cells.pdf*
[158] A. W. Peng, F. T. Salles, B. Pan and A. J. Ricci, "Integrating the biophysical and molecular mechanisms of auditory hair cell mechanotransduction", *Nature communications, Vol.* 2, pp. 523, (2011)

[159] J. R. Ison, "Auditory Nerve I, Innervation of the Cochlea, Frequency and Level Coding", *University of Rochester, Brain and Cognitive Sciences*, (1999), Online: *http://www.bcs.rochester.edu/courses/crsinf/221/ARCHIVES/S11/Auditory_Nerve1.pdf*
[160] R. Fettiplace and C. M. Hackney, "The sensory and motor roles of auditory hair cells", *Nature Reviews Neuroscience, Vol.* 7-1, pp. 19-29, (2006)
[161] H. Cai, B. Shoelson and R. S. Chadwick, "Evidence of tectorial membrane radial motion in a propagating mode of a complex cochlear model", *Proceedings of the National Academy of Sciences of the United States of America, Vol.* 101-16, pp. 6243-6248, (2004)
[162] K. G. a. N. Deo, "Mechanical-electrical-acoustical modeling of the cochlea", *Institute of Pure and Apllied Mathematics*, (2005), Online: *www.ipam.ucla.edu/publications/.../es2005_5406.ppt*
[163] R. F. Lyon and C. A. Mead, "Cochlear Hydrodynamics demystified
", *Department of Computer Sciences, California Institute of Technology*, (1989)
[164] K. L. Tsang, "Determination of effective masses and parametric study of the organ of Corti", (2012), Online: *http://www.rochester.edu/college/kearnscenter/pdf/Xerox_2013/Ka_Lai_Tsang.pdf*
[165] T. Kato, S. Omachi and H. Aso, "Asymmetric gaussian and its application to pattern recognition",in *Structural, Syntactic, and Statistical Pattern Recognition*, *ed. Springer*. 405-413, (2002)
[166] F. Chen, D. Zha, A. Fridberger, J. Zheng, N. Choudhury, S. L. Jacques, R. K. Wang, X. Shi and A. L. Nuttall, "A differentially amplified motion in the ear for near-threshold sound detection", *Nature neuroscience, Vol.* 14-6, pp. 770-774, (2011)
[167] D. Zha, F. Chen, S. Ramamoorthy, A. Fridberger, N. Choudhury, S. L. Jacques, R. K. Wang and A. L. Nuttall, "In vivo outer hair cell length changes expose the active process in the cochlea", *PloS one, Vol.* 7-4, pp. e32757, (2012)
[168] C. Q. Davis and D. M. Freeman, "Direct observations of sound-induced motions of the reticular lamina, tectorial membrane, hair bundles, and individual stereocilia", *Department of Physiology at the University of Wisconsin - Madison*, (1995), Online: *http://www.neurophys.wisc.edu/auditory/qdavis/talk.html*
[169] S. T. Smith and R. S. Chadwick, "Simulation of the response of the inner hair cell stereocilia bundle to an acoustical stimulus", *PloS one, Vol.* 6-3, pp. e18161, (2011)
[170] A. Pierre, "Cours de Trigonométrie", *ed. Éditions Aurélien PIERRE*. (2013)
[171] A. Jilkine and K. Leiderman, "Modeling Length Regulation of Stereocilia", *Park City Mathematics Institute*, (2005), Online: *pcmi.ias.edu/2005/documents/K2.ppt*
[172] A. Fridberger, I. Tomo, M. Ulfendahl and J. B. de Monvel, "Imaging hair cell transduction at the speed of sound: dynamic behavior of mammalian stereocilia", *Proceedings of the National Academy of Sciences of the United States of America, Vol.* 103-6, pp. 1918-1923, (2006)
[173] K. Grosh and N. Deo, "Mechanical-electrical-acoustical modeling of the cochlea", *Institute of Pure and Apllied Mathematics*, (2005), Online: *www.ipam.ucla.edu/publications/.../es2005_5406.ppt*
[174] Y.-W. Liu and S. T. Neely, "Outer hair cell electromechanical properties in a nonlinear piezoelectric model", *The Journal of the Acoustical Society of America, Vol.* 126, pp. 751, (2009)
[175] D. Purves, G. Augustine, D. Fitzpatrick and e. al., "Hair Cells and the Mechanoelectrical Transduction of Sound Waves",in *Neuroscience. 2nd edition*, *ed. http://www.ncbi.nlm.nih.gov/books/NBK10867/*. (2001)
[176] C. M. Hackney and D. N. Furness, "Mechanotransduction in vertebrate hair cells: structure and function of the stereociliary bundle", *American Journal of Physiology-Cell Physiology, Vol.* 268-1, pp. C1-C13, (1995)
[177] J. L. Fitzakerley, "Stereocilia tiplinks & transduction channels, Inner Ear Physiology ", *University of Minnesota Duluth*, (2013), Online: *http://www.d.umn.edu/~jfitzake/Lectures/DMED/InnerEar/Transduction/TipLinks.html*
[178] P. Fuchs, "Hair Cell Mechanotransduction - Neurobiology of Hearing, Neurobiology of Hearing MEDS 5377", *UConn health Center*, (2011), Online: *http://neurobiologyhearing.uchc.edu/Course_Content_Library/Auditory_Periphery/Fuchs%20Salamanca2%20handout.pdf*
[179] J. Zheng, W. Shen, D. Z. He, K. B. Long, L. D. Madison and P. Dallos, "Prestin is the motor protein of cochlear outer hair cells", *Nature, Vol.* 405-6783, pp. 149-155, (2000)
[180] P. Brodal, "The central nervous system: structure and function", *ed. Oxford University Press*. (2004)

[181] F. Lang, V. Vallon, M. Knipper and P. Wangemann, "Functional significance of channels and transporters expressed in the inner ear and kidney", *American Journal of Physiology-Cell Physiology, Vol.* 293-4, pp. C1187-C1208, (2007)
[182] Y. Raphael and R. A. Altschuler, "Structure and innervation of the cochlea", *Brain research bulletin, Vol.* 60-5, pp. 397-422, (2003)
[183] F. Mammano, M. Bortolozzi, S. Ortolano and F. Anselmi, "Ca2+ signaling in the inner ear", *Physiology, Vol.* 22-2, pp. 131-144, (2007)
[184] L. A. Werner, "The auditory nerve response", *Introduction to Hearing Science*, Online: *http://depts.washington.edu/*
[185] C. Darwin, "Ear and Auditory Nerve", *Hearing Lecture Notes (2)*, (1994), Online: *http://www.lifesci.sussex.ac.uk/*
[186] D. B. Koch and E. H. Overstreet, "Neural Response Imaging: Measuring Auditory-Nerve Responses from the Cochlea with the HiResolution™ Bionic Ear System",
[187] C. J. Sumner, E. A. Lopez-Poveda, L. P. O'Mard and R. Meddis, "A revised model of the inner-hair cell and auditory-nerve complex", *The Journal of the Acoustical Society of America, Vol.* 111, pp. 2178, (2002)
[188] R. Dingledine, K. Borges, D. Bowie and S. F. Traynelis, "The glutamate receptor ion channels", *Pharmacological reviews, Vol.* 51-1, pp. 7-62, (1999)
[189] O. A. Petroff, "Book Review: GABA and glutamate in the human brain", *The Neuroscientist, Vol.* 8-6, pp. 562-573, (2002)
[190] S. G. Tewari and K. K. Majumdar, "A mathematical model of the tripartite synapse: astrocyte-induced synaptic plasticity", *Journal of biological physics, Vol.* 38-3, pp. 465-496, (2012)
[191] R. Jolivet, T. J. Lewis and W. Gerstner, "Generalized integrate-and-fire models of neuronal activity approximate spike trains of a detailed model to a high degree of accuracy", *Journal of Neurophysiology, Vol.* 92-2, pp. 959-976, (2004)
[192] A. Destexhe, Z. F. Mainen and T. J. Sejnowski, "Synthesis of models for excitable membranes, synaptic transmission and neuromodulation using a common kinetic formalism", *Journal of computational neuroscience, Vol.* 1-3, pp. 195-230, (1994)
[193] H. von Gersdorff, "Synaptic ribbons: versatile signal transducers", *Neuron, Vol.* 29-1, pp. 7-10, (2001)
[194] E. Glowatzki, L. Grant and P. Fuchs, "Hair cell afferent synapses", *Current opinion in neurobiology, Vol.* 18-4, pp. 389-395, (2008)
[195] D. Lenzi and H. von Gersdorff, "Structure suggests function: the case for synaptic ribbons as exocytotic nanomachines", *Bioessays, Vol.* 23-9, pp. 831-840, (2001)
[196] E. Glowatzki, "The Auditory Periphery 4 – Afferent synaptic transmission by cochlear hair cells Structure and Function", *Johns Hopkins School of Medicine*, (2011), Online: *http://pages.jh.edu/~strucfunc/strucfunc/2011_files/2011_09_13.pdf*
[197] L. D. Liberman, H. Wang and M. C. Liberman, "Opposing gradients of ribbon size and AMPA receptor expression underlie sensitivity differences among cochlear-nerve/hair-cell synapses", *The Journal of Neuroscience, Vol.* 31-3, pp. 801-808, (2011)
[198] T. Moser, "The hair cell ribbon synapse", *Ludwig Maximilians Universitat Munchen*, Online: *http://www.bio.lmu.de/~benda/teaching/mnsws07/Moser-RibbonSynapse.pdf*
[199] P. Sterling and G. Matthews, "Structure and function of ribbon synapses", *Trends in neurosciences, Vol.* 28-1, pp. 20-29, (2005)
[200] L. Grant, E. Yi and E. Glowatzki, "Two modes of release shape the postsynaptic response at the inner hair cell ribbon synapse", *The Journal of Neuroscience, Vol.* 30-12, pp. 4210-4220, (2010)
[201] T. Parsons and P. Sterling, "Synaptic ribbon: conveyor belt or safety belt?", *Neuron, Vol.* 37-3, pp. 379-382, (2003)
[202] M. H. Hennig, "Modeling Synaptic Transmission", *ANC, Informatics, University of Edinburgh*,
[203] A. R. Sargsyan, A. A. Melkonyan, C. Papatheodoropoulos, H. H. Mkrtchian and G. K. Kostopoulos, "A model synapse that incorporates the properties of short-and long-term synaptic plasticity", *Neural networks, Vol.* 16-8, pp. 1161-1177, (2003)
[204] C. Koch and I. Segev, "Methods in neuronal modeling: from synapses to networks", *ed. The MIT Press*. (1998)

[205] S. H. Koslow, S. Subramaniam and S. Subramaniam, "Databasing the Brain: From Data to Knowledge (Neuroinformatics)", *ed. Wiley-Liss*. (2005)
[206] R. Veltz and O. Faugeras, "Introduction to the biology of synapses", *INRIA*, (2013), Online: *http://www-sop.inria.fr/members/Olivier.Faugeras/MVA/Slides13/lecture5.pdf*
[207] A. Roth and M. C. van Rossum, "Modeling Synapses", *University of Edinburgh, School of Informatics*, (2009), Online: *http://homepages.inf.ed.ac.uk/mvanross/reprints/roth_mvr_chap.pdf*
[208] T. Yu and G. Cauwenberghs, "Biophysical synaptic dynamics in an analog VLSI network of Hodgkin-Huxley neurons", *Engineering in Medicine and Biology Society, 2009. EMBC 2009. Annual International Conference of the IEEE*, pp. 3335-3338, (2009)
[209] M. Xiao, M. Karpefors, B. Gustafsson and H. Wigstrom, "On the linkage between AMPA and NMDA receptor-mediated EPSPs in homosynaptic long-term depression in the hippocampal CA1 region of young rats", *The Journal of Neuroscience, Vol.* 15-6, pp. 4496-4506, (1995)
[210] J. Ruel, C. Chen, R. Pujol, R. P. Bobbin and J.-L. Puel, "AMPA-preferring glutamate receptors in cochlear physiology of adult guinea-pig", *The Journal of Physiology, Vol.* 518-3, pp. 667-680, (1999)
[211] J.-H. Cho, I. T. Bayazitov, E. G. Meloni, K. M. Myers, W. A. Carlezon Jr, S. S. Zakharenko and V. Y. Bolshakov, "Coactivation of thalamic and cortical pathways induces input timing-dependent plasticity in amygdala", *Nature neuroscience, Vol.* 15-1, pp. 113-122, (2012)
[212] D. F. de Sevilla, M. Fuenzalida, A. B. P. Pazos and W. Buño, "Selective shunting of the NMDA EPSP component by the slow afterhyperpolarization in rat CA1 pyramidal neurons", *Journal of Neurophysiology, Vol.* 97-5, pp. 3242-3255, (2007)
[213] M. A. Sikora, J. Gottesman and R. F. Miller, "A computational model of the ribbon synapse", *Journal of neuroscience methods, Vol.* 145-1, pp. 47-61, (2005)
[214] R. Rao-Mirotznik, G. Buchsbaum and P. Sterling, "Transmitter concentration at a three-dimensional synapse", *Journal of Neurophysiology, Vol.* 80-6, pp. 3163-3172, (1998)
[215] A. Borisyuk and e. al., "Modeling Synaptic Plasticity", *Mathematical Biosciences Institute*, (2004),
[216] N. Shepard, "Integrate and Fire Model", *www.nathanshepard.net*, (2007), Online: *http://www.nathanshepard.net/documents/Integrate_and_Fire_Model.pdf*
[217] R. Vandiver, "Hodgkin-Huxley Model of Action Potentials", *Bryn Mawer College*, (201O), Online: *http://www.brynmawr.edu/math/people/vandiver/documents/HodgkinHuxley.pdf*
[218] J. Selgrade, "Hodgkin-Huxley and Fitzhugh-Nagumo Models", *North Carolina State University*, (2005), Online: *http://www.phaser.com/modules/maa05/h-h_model.ppt%E2%80%8E*
[219] F. Fröhlich and S. Jezernik, "Feedback control of Hodgkin–Huxley nerve cell dynamics", *Control engineering practice, Vol.* 13-9, pp. 1195-1206, (2005)
[220] "From Hodgkin-Huxley to Integrate-and-Fire", *University of Paris V, Laboratory of Neurophysics and Physiology*, (2011), Online: *http://neurophys.biomedicale.univ-paris5.fr/~brunel/tutorial.pdf*
[221] W. Heitler, "The Hodgkin-Huxley Model for the Generation of Action Potentials", *School of Biology, University of St Andrews*, Online: *http://www.st-andrews.ac.uk/~wjh/hh_model_intro/*
[222] D. Zhou, D. Cai, S. Li and Y. Xiao, "Mathematical Modeling of Biological Neurons", (2012)
[223] M. Chung, B. Göbel, A. Peters, K. M. Oltmanns and A. Moser, "Mathematical modeling of the biphasic dopaminergic response to glucose", *Journal Biomedical Science Engineering, Vol.* 4, pp. 36-145, (2011)
[224] N. S. Imennov and J. T. Rubinstein, "Stochastic population model for electrical stimulation of the auditory nerve", *Biomedical Engineering, IEEE Transactions on, Vol.* 56-10, pp. 2493-2501, (2009)
[225] "Topic 11: Nerve Conduction", *Centenary College of Luisiana*, Online: *http://www.centenary.edu/attachments/biophysics/bphy304/11a.pdf*
[226] Y. J and W. JB, "Morphological observation and electrophysiological properties of isolated Deiters' cells from guinea pig cochlea"*, Vol.* 14-1, pp. 29-31, (2000)
[227] T. Fujikawa, R. S. Petralia, T. S. Fitzgerald, Y.-X. Wang, B. Millis, J. A. Morgado-Díaz, K. Kitamura and B. Kachar, "Localization of kainate receptors in inner and outer hair cell synapses", *Hearing research, Vol.* 314, pp. 20-32, (2014)
[228] J. Ruel, C. Chabbert, R. Nouvian, R. Bendris, M. Eybalin, C. L. Leger, J. Bourien, M. Mersel and J.-L. Puel, "Salicylate enables cochlear arachidonic-acid-sensitive NMDA receptor responses", *The Journal of Neuroscience, Vol.* 28-29, pp. 7313-7323, (2008)

[229] B. Peng, Q. Li, T. Ren, S. Ahmad, S. Chen, P. Chen and X. Lin, "Group I metabotropic glutamate receptors in spiral ganglion neurons contribute to excitatory neurotransmissions in the cochlea", *Neuroscience, Vol.* 123-1, pp. 221-230, (2004)
[230] G. Burnstock and A. N. Verkhratskiĭ, "Purinergic signalling and the nervous system", *ed. Springer*. (2012)
[231] E. Oestreicher, W. Arnold and D. Felix, "Neurotransmission of the cochlear inner hair cell synapse-implications for inner ear therapy", (2004)
[232] T. Honoré, J. Lauridsen and P. Krogsgaard-Larsen, "The binding of [3H] AMPA, a structural analogue of glutamic acid, to rat brain membranes", *Journal of neurochemistry, Vol.* 38-1, pp. 173-178, (1982)
[233] S. R. Platt, "The role of glutamate in central nervous system health and disease–a review", *The Veterinary Journal, Vol.* 173-2, pp. 278-286, (2007)
[234] C. Rosenmund, Y. Stern-Bach and C. F. Stevens, "The tetrameric structure of a glutamate receptor channel", *Science, Vol.* 280-5369, pp. 1596-1599, (1998)
[235] T. Otis, I. Raman and L. Trussell, "AMPA receptors with high Ca2+ permeability mediate synaptic transmission in the avian auditory pathway", *The Journal of Physiology, Vol.* 482-Part 2, pp. 309-315, (1995)
[236] A. Destexhe, Z. F. Mainen and T. J. Sejnowski, "Fast kinetic models for simulating AMPA, NMDA, GABA A and GABA B receptors",in *The Neurobiology of Computation*, *ed. Springer*. 9-14, (1995)
[237] C. S. a. Engineering, "Modeling single neurons", *University of Washingthon*, (2013), Online: *http://courses.cs.washington.edu/courses/cse528/05wi/Lect5.pdf*
[238] E. Yi, I. Roux and E. Glowatzki, "Dendritic HCN channels shape excitatory postsynaptic potentials at the inner hair cell afferent synapse in the mammalian cochlea", *Journal of Neurophysiology, Vol.* 103-5, pp. 2532-2543, (2010)
[239] E. Glowatzki and P. A. Fuchs, "Transmitter release at the hair cell ribbon synapse", *Nature neuroscience, Vol.* 5-2, pp. 147-154, (2002)
[240] L. Grant, E. Yi, J. D. Goutman and E. Glowatzki, "Postsynaptic recordings at afferent dendrites contacting cochlear inner hair cells: monitoring multivesicular release at a ribbon synapse", *Journal of visualized experiments: JoVE,* -48, (2011)
[241] A. I. S. Darwish, "Central and Peripheral N-methyl-D-aspartate (NMDA) Receptors: Sites, Actions, Modulators and Possible Clinical Applications", (2009)
[242] D. C. Cooper, "Introduction to neuroscience I", *ed. Donald C. Cooper Ph. D.*, (2011)
[243] S. Coombes, "Synapses", *The University of Nottingham Department of Mathematical Sciences B12412: Computational Neuroscience and Neuroinformatics*, Online: *https://www.maths.nottingham.ac.uk/personal/sc/cnn/CNN6ToDo.pdf*
[244] S. S. Kumar and J. R. Huguenard, "Properties of excitatory synaptic connections mediated by the corpus callosum in the developing rat neocortex", *Journal of Neurophysiology, Vol.* 86-6, pp. 2973-2985, (2001)
[245] R. Jonsson, "Field interactions in the peripheral auditory neural system with reference to cochlear implants", *University of Pretoria, Electrical, Electronic and Computer Engineering*, (2011),
[246] A. F. Jahn and J. Santos-Sacchi, "Physiology of the Ear", *ed. Cengage Learning*. (2001)
[247] J. C. Fiala, S. Grossberg and D. Bullock, "Metabotropic glutamate receptor activation in cerebellar Purkinje cells as substrate for adaptive timing of the classically conditioned eye-blink response", *The Journal of Neuroscience, Vol.* 16-11, pp. 3760-3774, (1996)
[248] M. Masugi-Tokita, E. Tarusawa, M. Watanabe, E. Molnár, K. Fujimoto and R. Shigemoto, "Number and density of AMPA receptors in individual synapses in the rat cerebellum as revealed by SDS-digested freeze-fracture replica labeling", *The Journal of Neuroscience, Vol.* 27-8, pp. 2135-2144, (2007)
[249] Z. Nusser, R. Lujan, G. Laube, J. D. B. Roberts, E. Molnar and P. Somogyi, "Cell type and pathway dependence of synaptic AMPA receptor number and variability in the hippocampus", *Neuron, Vol.* 21-3, pp. 545-559, (1998)
[250] L. O. Trussell, A. N. Popper and R. R. Fay, "Synaptic Mechanisms in the Auditory System", *ed. Springer*. (2012)
[251] S. F. Traynelis and F. Jaramillo, "Getting the most out of noise in the central nervous system", *Trends in neurosciences, Vol.* 21-4, pp. 137-145, (1998)

[252] L. Abbott, "Realistic synaptic inputs for model neural networks", *Network: Computation in Neural Systems, Vol.* 2-3, pp. 245-258, (1991)
[253] D. Purves, G. Augustine, D. Fitzpatrick and e. al., "Neuroscience: The Ionic Basis of the Resting Membrane Potential", *ed. Sinauer Associates, Sunderland (MA)*. (2001)
[254] J. Koester and S. A. Siegelbaum, "Membrane Potential", *http://www.bioltis.fmed.edu.uy/*,
[255] R. Rhoades and D. R. Bell, "Medical Physiology: Principles of Clinical Medicine, Chapter 3: Action Potential, Synaptic Transmission, and Maintenance of Nerve Function", *ed. Lippincott Willams and Wilkins*. *C. Forehand*,
[256] V. Weerasinghe, "Excitable Tissues, Resting Membrane Potential & Action Potential", *Faculty of Medicine, University of Peradenyia*,
[257] "Ionic Basis of Action Potentials", *Medical University of South California (MUSC), Woodward Lab: Department of Neurosciences*,
[258] L. H, Berk A, Z. SL and e. al., "The Action Potential and Conduction of Electric Impulses",in *Molecular Cell Biology*, Vol. Section 21.2. *http://www.ncbi.nlm.nih.gov/books/NBK21668/*, (2000)
[259] M. F. Bear, B. W. Connors and M. A. Paradiso, "Neuroscience: Exploring the Brain plus CD Rom Testbank", *Neuroscience research*, (2000)
[260] N. Yang, R. Kondo, J. Dolzer and D. Yamane, "Analysis Of The Biophysical Properties Of Sodium Channel Na", *moleculardevices.com*,
[261] M. D. Mann, "Properties of excitable cell membranes: the spike", (2013), Online: *http://michaeldmann.net/mann3b.html*
[262] C. J. Forehand, "The action potential, synaptic transmission, and maintenance of nerve function", *Medical Physiology: Principles for Clinical Medicine, Rhoades RA, Bell DR, eds., Lippincott Williams & Wilkins, a Wolters Kluwer business, Philadelphia, USA*, pp. 38-64, (2009)
[263] B. Alberts, "Essential cell biology: an introduction to the molecular biology of the cell", Vol. 1, *ed. Taylor & Francis*. (1998)
[264] B. Alberts, A. Johnson, J. Lewis, M. Raff, K. Roberts and P. Walter, "Ion Channels and the Electrical Properties of Membranes", (2002)
[265] N. Al-Shorbaji, "Health and medical informatics", *World Health Organisation, Cairo*, (2001)
[266] C. Koch, "Biophysics of Computation: Information Processing in Single Neurons (Computational Neuroscience)", Vol. Chapter 2: Linear Cable theory. (1999)
[267] E. Young, "Models of the Neuron (580.439/639)", *John Hopkins University*, (Fall 2013), Online: *http://www.jhu.edu/motn/*
[268] F. Rieke, "Action potential propagation", *University of Washington*, Online: *http://rieke-server.physiol.washington.edu/People/Fred/Classes/532/HH408.pdf*
[269] E. Young, "Lecture 9, Nonlinear cable theory in *Systems Biology II: Neural Systems (580.422)*", (2006), Online: *http://www.shadmehrlab.org/Courses/physfound_files/Eric_5.pdf*
[270] E. Young, "Systems Biology II: Neural Systems (580.422), Lecture 9, Nonlinear cable theory", Online: *http://www.shadmehrlab.org/Courses/physfound_files/Eric_5.pdf*
[271] R. Rhoades and D. R. Bell, "Medical Physiology: Principles of Clinical Medicine", Vol. Chapter 3: Action Potential, Synaptic Transmission, and Maintenance of Nerve Function, C. Forehand, *ed. Lippincott Willams and Wilkins*.
[272] D. Mittleman, "Waves and the wave equation", *ECE Department at Rice University*,
[273] "Auditory Nerve Processing", *University of Rochester, Brain and Cognitive Sciences*, (2013), Online: *http://www.bcs.rochester.edu/courses/crsinf/504/ARCHIVES/F05/audition2.pdf*
[274] Tschang, "Chapter 34 Maxwell's Equations, Electromagnetic Waves", *Department of Physics at National Tsing Hua University* Online: *http://www.phys.nthu.edu.tw/~thschang/notes/GP34.pdf*
[275] Orfanidi, "Maxwell' s equations", *Information, Networks, and Signal Processing Research (INSPIRE) Lab*, Online: *http://www.ece.rutgers.edu/~orfanidi/ewa/ch01.pdf*
[276] W. F. Boron and E. L. Boulpaep, "Medical Physiology, 2e Updated Edition: with STUDENT CONSULT Online Access", *ed. Elsevier Health Sciences*. (2012)
[277] S. Kim, S. J. Guzman, H. Hu and P. Jonas, "Active dendrites support efficient initiation of dendritic spikes in hippocampal CA3 pyramidal neurons", *Nature neuroscience, Vol.* 15-4, pp. 600-606, (2012)

[278] B. Sivyer and S. R. Williams, "Direction selectivity is computed by active dendritic integration in retinal ganglion cells", *Nature neuroscience, Vol.* 16-12, pp. 1848-1856, (2013)
[279] A. Destexhe, "High-conductance state", *Scholarpedia, 2(11):1341*, (2007),
[280] X. Chen and S. Kiaei, "Monocycle shapes for ultra wideband system", *Circuits and Systems, 2002. ISCAS 2002. IEEE International Symposium on, Vol.* 1, pp. I-597-I-600, (2002)
[281] Y. Yeap, "Ultra wideband signal generation", *Microwave Journal, Vol.* 48-9, pp. 172, (2005)
[282] M. Dhieb, M. Lahiani and H. Ghariani, "Pulse generator monocycle Gaussian for UWB applications", *WSEAS Transactions on Circuits and Systems, Vol.* 9-12, pp. 756-766, (2010)
[283] G. J. Goodhill, "A theoretical model of axon guidance by the robo code", *Neural computation, Vol.* 15-3, pp. 549-564, (2003)
[284] X. Wang, "Neural representation of Sensory Stimuli: Properties of Spike Trains", *Biosystem II: Neuroscience*, Online: *http://www.shadmehrlab.org/*
[285] L. A. Werner, "inner ear anatomy", *Introduction to Hearing Science*, Online: *http://depts.washington.edu/*
[286] P. Dayan, L. F. Abbott and L. Abbott, "Theoretical neuroscience: Computational and mathematical modeling of neural systems", (2001)
[287] C. Pouzat, "Extracellular Recording and Spike Train Analysis", *CNRS UMR 8118 and Paris-Descartes University Paris*, (2009), Online: *http://www.biomedicale.univ-paris5.fr/SpikeOMatic/Papers_folder/Pouzat_ENP_2009.pdf*
[288] J. Laudanski, S. Coombes, A. R. Palmer and C. J. Sumner, "Mode-locked spike trains in responses of ventral cochlear nucleus chopper and onset neurons to periodic stimuli", *Journal of Neurophysiology, Vol.* 103-3, pp. 1226-1237, (2010)
[289] N. X. Tritsch, A. Rodríguez-Contreras, T. T. Crins, H. C. Wang, J. G. G. Borst and D. E. Bergles, "Calcium action potentials in hair cells pattern auditory neuron activity before hearing onset", *Nature neuroscience, Vol.* 13-9, pp. 1050-1052, (2010)
[290] I. C. Bruce, "Spatiotemporal coding of sound in the auditory nerve for cochlear implants", *ed. University of Melbourne, Department of Otolaryngology*. (1998)
[291] T. Hromádka, "Representation of Sounds in Auditory Cortex of Awake Rats", *Cold Spring Harbor Laboratory*, (2008),
[292] E. Zalewska and I. Hausmanowa-Petrusewicz, "Approximation of motor unit structure from the analysis of motor unit potential", *Clinical Neurophysiology, Vol.* 119-11, pp. 2501-2506, (2008)
[293] M. S. Lewicki, "A review of methods for spike sorting: the detection and classification of neural action potentials", *Network: Computation in Neural Systems, Vol.* 9-4, pp. R53-R78, (1998)
[294] J. S. Pezaris, M. Sahani and R. A. Andersen, "Tetrodes for monkeys",in *Computational Neuroscience*, *ed. Springer*. 937-942, (1997)
[295] M. Laubach, M. Shuler and M. A. Nicolelis, "Independent component analyses for quantifying neuronal ensemble interactions", *Journal of neuroscience methods, Vol.* 94-1, pp. 141-154, (1999)
[296] C. Savin, P. Joshi and J. Triesch, "Independent component analysis in spiking neurons", *PLoS computational biology, Vol.* 6-4, pp. e1000757, (2010)
[297] S. Takahashi, Y. Anzai and Y. Sakurai, "A new approach to spike sorting for multi-neuronal activities recorded with a tetrode—how ICA can be practical", *Neuroscience research, Vol.* 46-3, pp. 265-272, (2003)
[298] S. Takahashi, Y. Anzai and Y. Sakurai, "Automatic sorting for multi-neuronal activity recorded with tetrodes in the presence of overlapping spikes", *Journal of Neurophysiology, Vol.* 89-4, pp. 2245-2258, (2003)
[299] E. Hulata, R. Segev and E. Ben-Jacob, "A method for spike sorting and detection based on wavelet packets and Shannon's mutual information", *Journal of neuroscience methods, Vol.* 117-1, pp. 1-12, (2002)
[300] W. Gerstner and W. M. Kistler, "Spiking neuron models: Single neurons, populations, plasticity", *ed. Cambridge university press*. (2002)
[301] M. N. Shadlen and W. T. Newsome, "Noise, neural codes and cortical organization", *Current opinion in neurobiology, Vol.* 4-4, pp. 569-579, (1994)
[302] J. Rinzel, "Computational Modeling of Neuronal Systems (Advanced Topics in Mathematical Physiology)", *The Center for Neural Science at New York State University*, Online: *http://www.cns.nyu.edu/~rinzel/CMNSF07/Neuronal%20dyns%20cell_CMNSF07.pdf*

[303] "Nerve Conduction", *Centenary College of Louisiana*, Online: *http://www.centenary.edu/attachments/biophysics/bphy304/11a.pdf*
[304] A.-M. Systems, "Tungsten electrodes", (2014), Online: *http://www.a-msystems.com/s-70-tungsten.aspx*
[305] L. M. Ward and P. E. Greenwood, "1/f noise", *Scholarpedia, Vol.* 2-12, pp. 1537, (2007)
[306] A. Longtin, "Neuronal noise", *Scholarpedia, Vol.* 8-9, pp. 1618, (2013)
[307] J. A. White, J. T. Rubinstein and A. R. Kay, "Channel noise in neurons", *Trends in neurosciences, Vol.* 23-3, pp. 131-137, (2000)
[308] M. Kearns, S. Solla and D. Cohn, "Advances in Neural Information Processing Systems 10", *Cambridge, MA*, (1999)
[309] S. Roy, "The role of noise in living systems", *Universita degli studi di Palermo*, Online: *http://www.unipa.it/daa_erice11/DAA2011_Conference/Speakers_files/Roy.pdf*
[310] T. Markl, "1/f noise, telegraph noise", *Karlsruher Institut für Technologie*, Online: *http://www.phi.kit.edu/noise/abbildungen/Noise-03_Non-Thermal_Noise_1_over_f_Noise.pdf*
[311] A. Destexhe and M. Rudolph-Lilith, "Neuronal noise", Vol. 8, *ed. Springer*. (2012)
[312] H. Feldwisch-Drentrup, A. B. Barrett, M. T. Smith and M. C. van Rossum, "Fluctuations in the open time of synaptic channels: An application to noise analysis based on charge", *Journal of neuroscience methods, Vol.* 210-1, pp. 15-21, (2012)
[313] D. A. Stanley, "Synaptic Noise-Like Activity in Hippocampal Interneurons", *University of Toronto*, (2009),
[314] B. Delgutte, "Auditory Nerve Laboratory: What was the Stimulus?", *Massachusetts Institute of Technology* Online: *web.mit.edu/hst.723/www/Labs/ANF%20Lab.ppt*
[315] D. Johnson and N. Kiang, "Analysis of discharges recorded simultaneously from pairs of auditory nerve fibers", *Biophysical journal, Vol.* 16-7, pp. 719-734, (1976)
[316] B. L. Tempel, "The auditory system", *Washington University*,
[317] A. R. Palmer, "The basic physiology of the auditory nerve ", *MRC Institute of Hearing Research, University of Nottingham*, Online: *http://neurobiologyhearing.uchc.edu/Course_Content_Library/Auditory_nerve/PALMER%20Auditory%20Nerve%20Physiology-ARP.pdf*
[318] A. M. Simmons, J. J. Schwartz and M. Ferragamo, "Auditory nerve representation of a complex communication sound in background noise", *The Journal of the Acoustical Society of America, Vol.* 91-5, pp. 2831-2844, (1992)
[319] I. Fukui, T. Sato and H. Ohmori, "Improvement of phase information at low sound frequency in nucleus magnocellularis of the chicken", *Journal of Neurophysiology, Vol.* 96-2, pp. 633-641, (2006)
[320] R. Roeser and M. Valente, "Audiology diagnosis", *ed. Thieme*. (2007)
[321] E. R. Kandel, J. H. Schwartz and T. M. Jessell, "Principles of neural science", Vol. 4, *ed. McGraw-Hill New York*. (2000)
[322] P. Revest, "Neuroscience Methods: A Guide for Advanced Students", *ed. Elsevier*. (1998)
[323] D. C. Johnson and W. R. LaCourse, "Liquid chromatography with pulsed electrochemical detection at gold and platinum electrodes", *Analytical Chemistry, Vol.* 62-10, pp. 589A-597A, (1990)
[324] "Electrophysiology", *wikipedia.org*, (2014), Online: *http://en.wikipedia.org/wiki/Electrophysiology*
[325] B. Singhal, "Drug Analysis: A Perspective of Potentiometric Sensors", *World Journal of Chemistry, Vol.* 6-2, pp. 59-74, (2011)
[326] R. v. Rohr, "Cochlear Implant Impedance Telemetry Measurements and Model Calculations to Estimate Modiolar Currents", *Swiss Federal Institute of Technology Zurich*, (2011),
[327] N. Dillier, W. K. Lai, B. Almqvist, C. Frohne, J. Muller-Deile, M. Stecker and E. Von Wallenberg, "Measurement of the electrically evoked compound action potential via a neural response telemetry system", *Annals of Otology Rhinology and Laryngology, Vol.* 111-5, Part 1, pp. 407-414, (2002)
[328] J. Mitchell, "Conduction/Synapse, Chapter 4, Neurophysiology II courses", *University of Vermont*, Online: *http://www.uvm.edu/~biology/Classes/255/Lab3.pdf*
[329] J. M. Simone Helluy, Jocelyne Dolce, Emily A. Buchholtz, "Lab 9: Conduction Velocity of Nerves in *BISC 111/113: Introductory Organismal Biology*", *OpenWetWare*, (July 2012), Online: *http://openwetware.org/wiki/Lab_9:_Conduction_Velocity_of_Nerves*

[330] Y.-A. Song, R. Melik, A. N. Rabie, A. M. Ibrahim, D. Moses, A. Tan, J. Han and S. J. Lin, "Electrochemical activation and inhibition of neuromuscular systems through modulation of ion concentrations with ion-selective membranes", *Nature Materials, Vol.* 10-12, pp. 980-986, (2011)
[331] F.-G. Zeng, S. Rebscher, W. Harrison, X. Sun and H. Feng, "Cochlear implants: system design, integration, and evaluation", *Biomedical Engineering, IEEE Reviews in, Vol.* 1, pp. 115-142, (2008)
[332] N. S. Lawand, J. van Driel and P. French, "Electric Field Density Distribution for Cochlear Implant Electrodes", *COMSOL Conference*, (2012)
[333] A. Komal, R. Dowell and P. Dawson, "Cochlear Implant Stimulation Rates and Speech Perception", (2012)
[334] B. Somek, S. Fajt, A. Dembitz, M. Ivković and J. Ostojić, "Coding strategies for cochlear implants", *AUTOMATIKA: časopis za automatiku, mjerenje, elektroniku, računarstvo i komunikacije, Vol.* 47-1-2, pp. 69-74, (2006)
[335] "Cochlear implant simulation", *University of Canada*, (2006), Online: *http://www.ugr.es/~atv/web_ci_SIM/en/seccion_4_en.htm*
[336] L. M. Friesen, R. V. Shannon, D. Baskent and X. Wang, "Speech recognition in noise as a function of the number of spectral channels: comparison of acoustic hearing and cochlear implants", *The Journal of the Acoustical Society of America, Vol.* 110-2, pp. 1150-1163, (2001)
[337] C. T. Choi and Y.-H. Lee, "A Review of Stimulating Strategies for Cochlear Implants", *Intechopen*, Online: *http://cdn.intechopen.com/pdfs-wm/36343.pdf*
[338] J. D. Falcone, "Validation of high density electrode arrays for cochlear implants: a computational and structural approach", (2011)
[339] T. Rader, "Speech Perception of Cochlear Implanted Patients with Combined Electric-Acoustic Stimulation", *ed. Verlag Dr. Hut*. (2012)
[340] "FineHearing™ Technology - Med-El", *Med-El*, Online: *http://www.medel.com/data/pdf/20287.pdf*
[341] M. Y. Srinivas, M. P. Darwin and V. Sailja, "Continuous Interleaved Sampled (CIS) Signal Processing Strategy for Cochlear Implants MATLAB Simulation Program", *International Journal of Scientific & Engineering Research, Vol.* 3-12, (2012)
[342] M. Vondrášek, P. Sovka and T. Tichý, "ACE Strategy with Virtual Channels", *Radioengineering, Vol.* 17-4, (2008)
[343] T. Zajdel, "Asynchronous Stimulation for Cochlear Implants", *The Ohio State University*, (2012),
[344] J.-J. Sit and R. Sarpeshkar, "A cochlear-implant processor for encoding music and lowering stimulation power", *Pervasive Computing, IEEE, Vol.* 7-1, pp. 40-48, (2008)
[345] H. P. Wolmarans, "Cochlear implant speech processing, based on the cochlear travelling wave", *University of Pretoria*, (2005),
[346] A. E. Vandali, L. A. Whitford, K. L. Plant and G. M. Clark, "Speech perception as a function of electrical stimulation rate: using the Nucleus 24 cochlear implant system", *Ear and hearing, Vol.* 21-6, pp. 608-624, (2000)
[347] R. Saba, "Cochlear implant modelling: stimulation and power consumption", *University of Southampton*, (2012),
[348] E. D. Marsman, R. M. Senger, G. A. Carichner, S. Kubba, M. S. McCorquodale and R. B. Brown, "DSP architecture for cochlear implants", *ISCAS ed. Citeseer*, (2006)
[349] T. Instrument, "C5000™ Ultra Low Power DSPs Datasheet",
[350] CSEM, "icyflex4 Datasheet", Online: *http://www.capdigital.com/wp-content/uploads/2012/11/icycom_CapDigital_121205-pdf.pdf*
[351] X. L. e. al., "Ultra-Low-Energy Near-Threshold Biomedical Signal Processor for Versatile Wireless Health Monitoring", *IEEE Asian Solid-State Circuits Conference*, (Kobe, Japan)
[352] M. W. Baker and R. Sarpeshkar, "Feedback analysis and design of RF power links for low-power bionic systems", *Biomedical Circuits and Systems, IEEE Transactions on, Vol.* 1-1, pp. 28-38, (2007)
[353] T. Buchegger, G. Ossberger, E. Hochmair, U. Folger, A. Reisenzahn and A. Springer, "An ultra low power transcutaneous impulse radio link for cochlea implants", *Ultra Wideband Systems, 2004. Joint with Conference on Ultrawideband Systems and Technologies. Joint UWBST & IWUWBS. 2004 International Workshop on*, pp. 356-360, (2004)

[354] T. Buchegger, G. Oß, A. Reisenzahn, E. Hochmair, A. Stelzer and A. Springer, "Ultra-wideband transceivers for cochlear implants", *EURASIP Journal on Advances in Signal Processing, Vol.* 2005-18, pp. 3069-3075, (1900)
[355] J.-J. Sit, A. M. Simonson, A. J. Oxenham, M. A. Faltys and R. Sarpeshkar, "A low-power asynchronous interleaved sampling algorithm for cochlear implants that encodes envelope and phase information", *Biomedical Engineering, IEEE Transactions on, Vol.* 54-1, pp. 138-149, (2007)
[356] N. M. Neihart and R. R. Harrison, "Micropower circuits for bidirectional wireless telemetry in neural recording applications", *Biomedical Engineering, IEEE Transactions on, Vol.* 52-11, pp. 1950-1959, (2005)
[357] A. Yodtean and A. Thanachayanont, "A Micropower CMOS Preamplifier for Cochlear Implant System", *ITC-CSCC: International Technical Conference on Circuits Systems, Computers and Communications*, pp. 997-1000, (2008)
[358] Charand and K. Xiong, "Action Potentials", *Hyperphysics and Biology*, Online: *http://hyperphysics.phy-astr.gsu.edu/hbase/biology/actpot.html*
[359] A. Kral, R. Hartmann, D. Mortazavi and R. Klinke, "Spatial resolution of cochlear implants: the electrical field and excitation of auditory afferents"*, Vol.* 121-1-2, pp. 11-28, (1998)
[360] M. C. e. al., "BioInitiative 2012: A Rationale for Biologically Exposure Standards for Low Electromagnetic Radiation", (December 31, 2012)
[361] H. Solmaz, Y. Ülgen and M. Tümer, "Design of A Microcontroller Based Cole-Cole Impedance Meter for Testing Biological Tissues"*, Vol.* 25-7, pp. 488-491, (September 7-12 2009)
[362] P. Glover, "Resistivity theory", *Petrophysics MSc Course Notes*, Online: *http://www2.ggl.ulaval.ca/personnel/paglover/CD%20Contents/GGL-66565%20Petrophysics%20English/Chapter%2017.PDF*
[363] "The Electrical Conductivity of Tissues ",in *The Biomedical Engineering Handbook: Second Edition*, *ed. Joseph D. Bronzino*. (2000)
[364] N. Ida, "9.2 electromagnetic properties of materials",in *Engineering Electromagnetics*, *ed. Springer*. (2003)
[365] "Microtubules and Filaments", *Scitable by Nature education*, Online: *http://www.nature.com/scitable/topicpage/microtubules-and-filaments-14052932*
[366] A. L. Hodgkin and A. F. Huxley, " A quantitative description of membrane current and its application to conduction and excitation in nerve"*, Vol.* 117-4, pp. 500-544, (1952)
[367] M. Wegmuller, "Intra-Body Communication for Biomedical Sensor Networks", *ETH Zurich Library Collection*, (2007), Online: *http://e-collection.library.ethz.ch/eserv/eth:29911/eth-29911-02.pdf*
[368] L. Watts, "Cochlear mechanics: Analysis and analog VLSI", *California Institute of Technology*, (1992),
[369] E. Mancall and D. Brock, "Gray's clinical neuroanatomy", *ed. Elsevier Health Sciences*. (2011)
[370] M. Deol and S. Gluecksohn-Waelsch, "The role of inner hair cells in hearing", *Nature, Vol.* 278, pp. 250-252 (1979)
[371] I. Chen, C. J. Limb and D. K. Ryugo, "The effect of cochlear-implant-mediated electrical stimulation on spiral ganglion cells in congenitally deaf white cats", *Journal of the Association for Research in Otolaryngology, Vol.* 11-4, pp. 587-603, (2010)
[372] R. R. Fay, "Structure and function in sound discrimination among vertebrates",in *The evolutionary biology of hearing*, *ed. Springer*. 229-263, (1992)
[373] "Innervation of the organ of Corti. Afferent fibres arise from nerve cell bodies within the spiral ganglion", Online: *http://dspace.jorum.ac.uk/*
[374] S. Errede, "The Human Ear Hearing, Sound Intensity and Loudness Levels ", *http://courses.physics.illinois.edu*,
[375] D. Purves, G. J. Augustine, D. Fitzpatrick, L. C. Katz, A.-S. LaMantia, J. O. McNamara and S. M. Williams, "The External Ear in *Neuroscience. 2nd edition*", *ed. Sinauer Associates*. (2001)
[376] S. S. Stevens and H. Davis, "Hearing: Its psychology and physiology", *ed. Wiley New York*. (1938)
[377] "All about ears in *Physics of the Human Body - Physics 3110*", *University of Utah*, (2013),
[378] "IV. Functions and pathphysiology of the middle ear", *University of Wisconsin, Departement of Neurophysiology*, (1996),
[379] "Coclia Anatomy and physiology of hearing ", *University of Vermont, College of Medicine*, (2012),

[380] P. Dallos, "Response characteristics of mammalian cochlear hair cells", *The Journal of Neuroscience, Vol.* 5-6, pp. 1591-1608, (1985)
[381] J. Ashmore, "Biophysics of the cochlea–biomechanics and ion channelopathies", *British medical bulletin, Vol.* 63-1, pp. 59-72, (2002)
[382] C. Fielding, "Lecture 007 Hearing II", *Colege of Santa Fe Auditory theory*, Online: *http://www.feilding.net/sfuad/musi3012-01/html/lectures/007_hearing_II.htm*
[383] D. D. Greenwood, "A cochlear frequency-position function for several species—29 years later", *The Journal of the Acoustical Society of America, Vol.* 87, pp. 2592, (1990)
[384] R. Shepherd, S. Hatsushika and G. Clark, "Electrical stimulation of the auditory nerve: the effect of electrode position on neural excitation", *Hearing research, Vol.* 66-1, pp. 108-120, (1993)
[385] K. Cheng, V. Cheng and C.-H. Zou, "A logarithmic spiral function to plot a Cochleaogram", *Trends in Medical Research, Vol.* 3-1, pp. 36-40, (2008)
[386] D. Furness, "Cochlea of the inner ear", *Welcome Images*,
[387] P. Bebis, "Short Time Fourier Transform (STFT)", *University of Nevada, Computer Sciences and Engineering*, Online: *http://cse.unr.edu*
[388] R. G. Osuna, "L6: Short time Fourier analysis and synthesis in *Introduction to Speech Processing*", *Computer Science & Engeneering, Texas A&M University*, Online: *http://research.cs.tamu.edu/prism/lectures/sp/l6.pdf*
[389] T. F. Quatieri, "SHORT-TIME FOURIER TRANSFORM in *Discrete-Time Speech Signal Processing, Principles and Practice. PHI, 2002. (Chapter 7)*", *University of Hong Kong, Department of Electrical and Electronic Engineering*, Online: *http://www.eee.hku.hk/~work3220/Speech%20analysis%20and%20synthesis-2%20STFT.pdf*
[390] R. Bradford, R. Dobson and J. ffitch, "Sliding is smoother than jumping", *University of Bale, Department of Computer Science*, Online: *http://quod.lib.umich.edu/cgi/p/pod/dod-idx/sliding-is-smoother-than-jumping.pdf?c=icmc;idno=bbp2372.2005.086*
[391] I. Shipsey, "Bionic Hearing: the science and the experience", *University of Minnesota*, (2010),
[392] K. Kawamoto, S.-H. Sha, R. Minoda, M. Izumikawa, H. Kuriyama, J. Schacht and Y. Raphael, "Antioxidant gene therapy can protect hearing and hair cells from ototoxicity", *Molecular Therapy, Vol.* 9-2, pp. 173-181, (2004)
[393] M. O'Leary, J. Fayad, W. House and F. Linthicum Jr, "Electrode insertion trauma in cochlear implantation", *The Annals of otology, rhinology, and laryngology, Vol.* 100-9 Part 1, pp. 695-699, (1991)
[394] P. Ndungidi, H. García-Vázquez, J. d. Pino, F. Dualibe and C. Valderrama, "RF specification driven by Multi-Objective Optimization Method", *DCIS*, (2012)

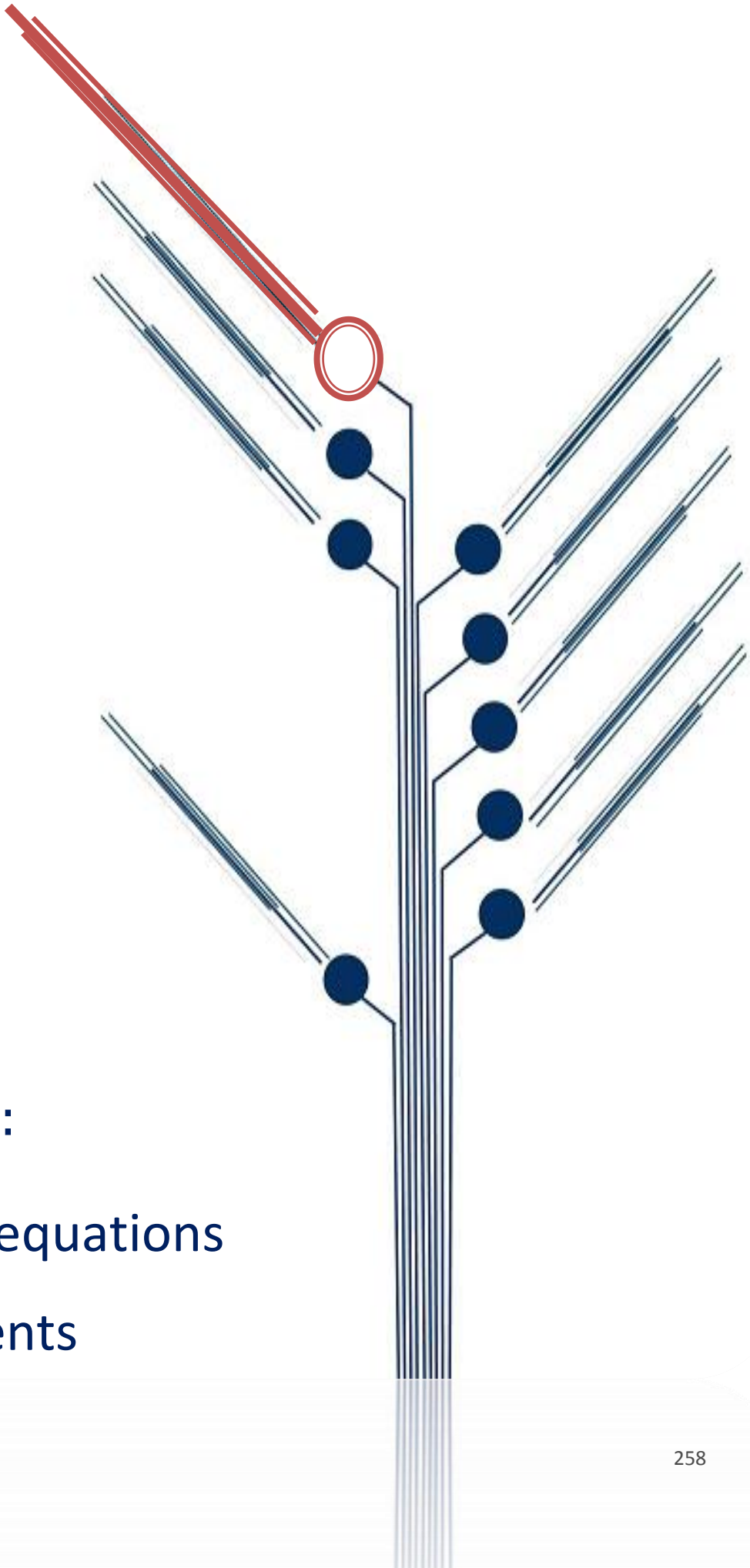

Annex A:

Maxwell equations and currents

Considering the Bohr atomic model [150, 396], and the free electron model [151, 397], in metals, if sufficient energy is applied, the valence electrons of the metals become conducing electrons and move freely through the metals. The free electrons may hence be oversimplified as gas [152, 398].

In the Bohr atomic model, positive atom nucleus are surrounded by negatively charged electrons. If the electrons are averaged in space and time and no electric field is applied, the center of gravity of the atom will coincide exactly with the center of gravity of the electrons sum. If an electrical field is applied, the centers of charge will be changed: the electrons sum will be pulled in the direction of the positive pole of the field and the nucleus to the negative one [399], leading to a dipole moment. The charges of opposite sign hence appear on each surface of the capacitor plate, due to this dipole moment. The charges brought by polarization due to the electric filed, define the displacement current. Applying an electric field to the extremities of two parallel plates of a capacitor without any dielectric between them, result in increased charge surface density in these plates (cf Figure 117). The charge accumulation per unit area present in both extremities of the capacitor due to an electric field is called the displacement current, as indicated in eq. 145:

$$D = \sigma = \epsilon_0 E \qquad \text{EQ. } 145$$

where σ is the charge density on the capacitor plate, $\mathcal{E}_0$ is the vaccum permittivity and E is the applied electric field (equation extracted from[400]).

If a dielectric material is introduced between the plates, the free charges on the plates are now neutralized by the polarization charges contained in the dielectric, as shown in Figure 117.
Because of dielectric insertion, eq. 145 then becomes eq. 146:

$$\sigma = \epsilon_0 E + \sigma_p = \epsilon E \qquad \text{EQ. } 146$$

where σ_p represents the polarization charge density (also called P)and $\mathcal{E}$ the electronic permittivity (equation extracted from [400]). Hence the dielectric polarization is decreasing the net force of the electric field proportionally as expressed in eq. 147

$$P = \epsilon_0 \chi_e E \qquad \text{EQ. } 147$$

where χ_e is called the electronic polarizability or electronic susceptibility [401].

Equating eq. 146 and eq. 147 leads to the relation between the electric permittivity and the electric susceptibility as described in eq. 148

$$\epsilon = 1 + \chi_e \qquad \text{EQ. } 148$$

Because of the causality property of polarization, as well as the electric field, these variables are complex and hence the electric permittivity is complex (eq. 149):

$$\epsilon = \epsilon' - j\,\epsilon'' \qquad \text{EQ. } 149$$

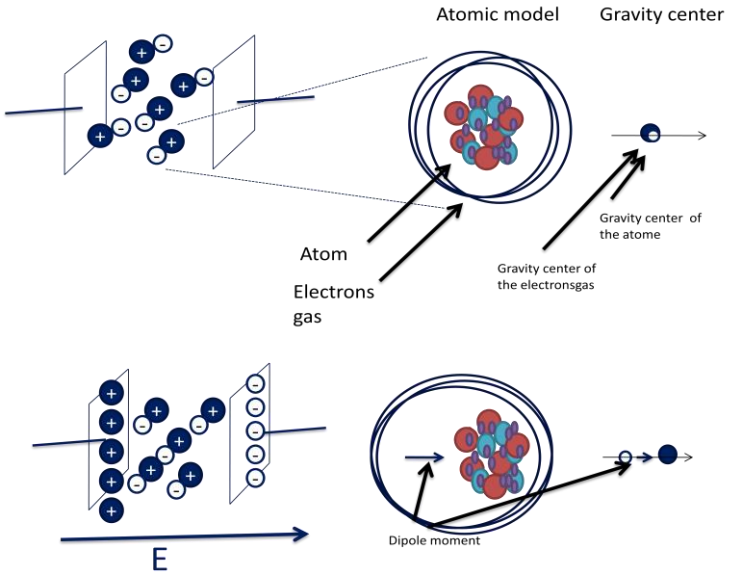

FIGURE 117: DISPLACEMENT CURRENT AND POLARIZATION OF THE MIDDLE[399]. THE POLARIZATION IS LOWERING THE EFFECT OF THE ELECTRIC FIELD

The electric field is generated by any charge particle or magnetic field and describes the electric attractive force applied at any point in space experienced by a secondary particle[402]. By applying the Maxwell Faraday equation, the Maxwell Ampere law and supposing that the electric filed E propagates into the single direction x, the following relation can be extracted (eq. 150)[403]:

$$\frac{\partial^2 E_x}{\partial x^2} = \mu_0 \epsilon_0 \frac{\partial^2 E_x}{\partial t^2} \qquad \text{EQ. } 150$$

where μ_0 is the vaccum permeability. This equation is referred as a De D' Alembert equation and it can be verified that the function $f\left(-\vec{k}.\vec{r} + \omega t\right)$ verifies this equation ([403, 404]). This leads to an electric field function expressed as a mathematical wave function as indicated by eq. 151

$$E_x = f\left(-\vec{k}.\vec{r} + \omega t\right) \qquad \text{EQ. } 151$$

where f represents the electric field propagating in the x direction (as the D' Alembert equation Is linear, electric fields verify the superposition principles) and r is the direction of the wave propagation. ω is the wave pulsation and k is the wave number depending on the refractive index of

the material (eq. 153). Therefore a wave corresponds to periodic time based space translation function. Discarding the vectors and the phase delay, the electric field may be expressed as (eq. 152):

$$E_x(r,t) = E_0 e^{j((\omega t - kr))} \quad \text{EQ. } 152$$

The relation between the wave number, the refractory index and the electric permittivity are recalled in eq. 153 (from [405] and[406])

$$n = \frac{c\,k}{\omega} \;\; and\; k = \sqrt{\mu\,\epsilon}\frac{\omega}{c} \;\; \approx \;\; \sqrt{\epsilon}\frac{\omega}{c} \;\; (for\ most\ transparent\ material) \quad \text{EQ. } 153$$

where n is the refractory index, μ the complex permeability, $\mathcal{E}$ the complex permittivity and c the light velocity in free space.

Once the electric filed mathematically characterized, the Ampere Maxwell law is applied in eq. 152, to obtain a general expression for the complex permittivity (eq. 154)

$$J = J_c + J_D = \sigma\,E_x + \epsilon\,\frac{\partial\,E_x}{\partial t} \quad \text{EQ. } 154$$

$$\Rightarrow J = \sigma\,E_x + j\,\omega\,\epsilon\,E_x$$

where j is the total current density, J_c is the conduction current density, J_D is the displacement current density, σ Is the electrical conductivity and $\mathcal{E}$ the electrical permittivity as defined above. Replacing complex permittivity by its expression in eq. 20, gives eq. 155[407]:

$$J = \sigma\,E_x + j\,\omega\,\epsilon' E_x + \omega\,\epsilon'' E_x \quad \text{EQ. } 155$$

In several documents the conductivity σ is named abusively and rather corresponds to the effective conductivity $\sigma_{eff} = \sigma + \omega\,\epsilon''$[407].

The complex permittivity expression may be further refined in [405] or in [275] where it is shown to be dependent on the pulsation ω (dispersion phenomenon). As depicted in Figure 118, in low frequency region, the permittivity is high because of the dielectric polarization (as the electrons have sufficient time to rotate around the atomic nucleus and reach their optimal dipole moment). At moderate frequency, molecules does not have the time to polarize and the energy is too low to be absorbed by the electrons. This energy causes molecules vibrations (leading to bond breakage and hence heat generation) as electrons and atoms are constantly affected by the electric field (but not reaching their optimal dipole moment) before returning to their initial position. Finally at very high

frequencies, energy is directly absorbed by the atomic structure exciting electron energy levels (ionizing radiations)[408].

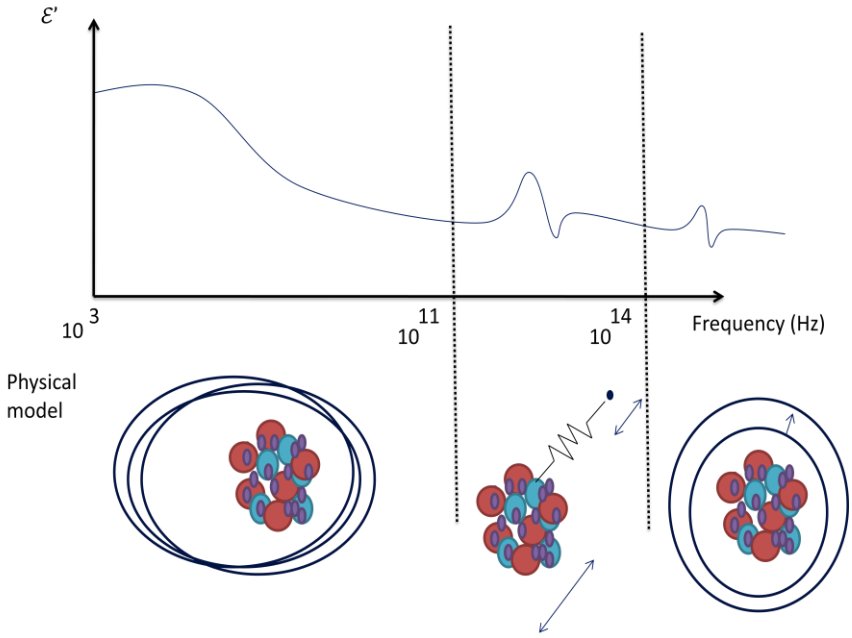

FIGURE 118: GENERAL SHAPE OF THE PERMITTIVITY RESPONSE OVER FREQUENCIES AND ASSOCIATION WITH CHANGE IN THE PHYSICAL MODEL OF THE ATOMIC STRUCTURE DUE TO ENERGY ABSORPTION[409]

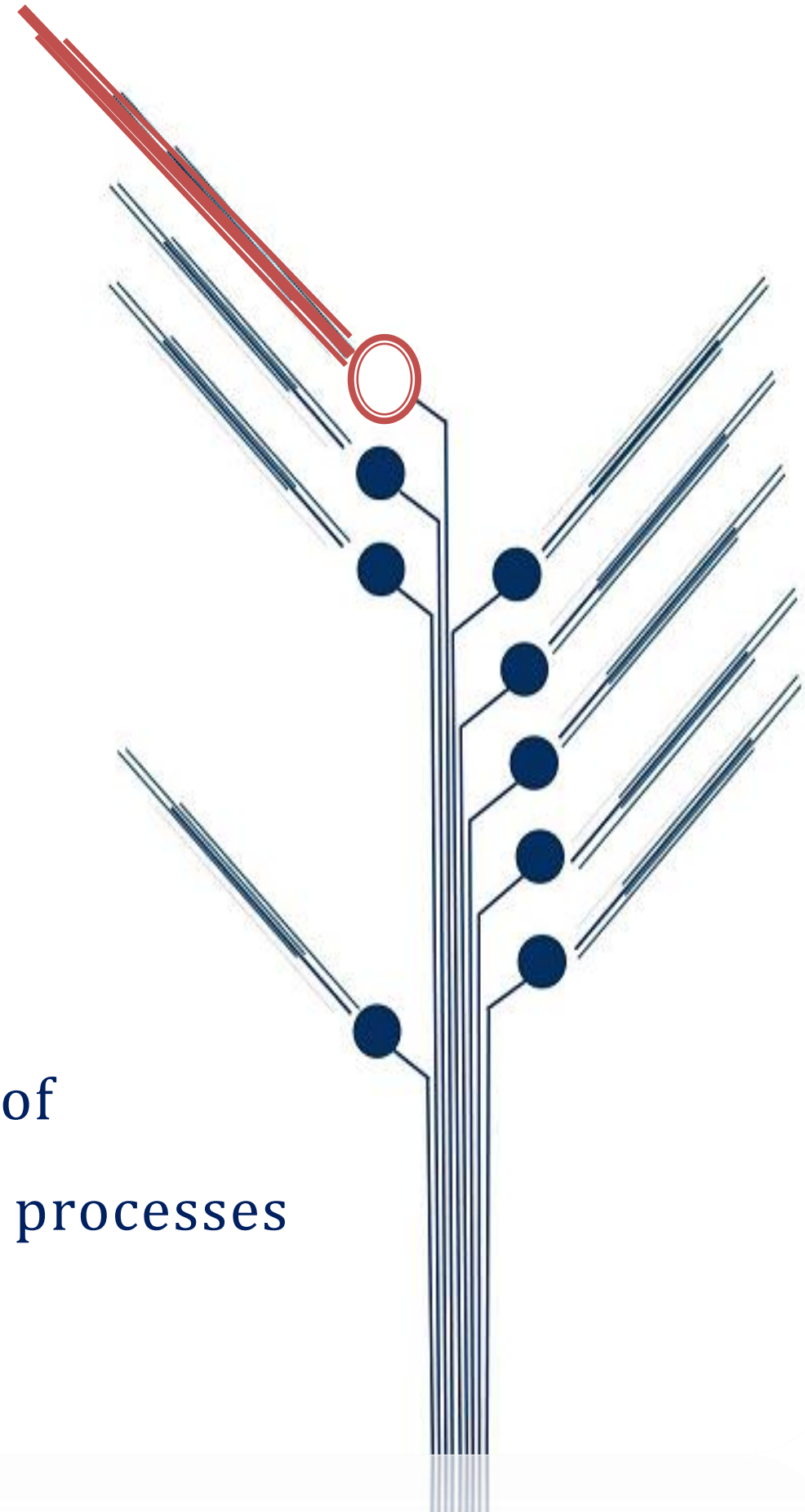

Annex B:

Overview of stochastic processes

1. General properties of stochastic processes:

Precise definition of random variables and extended theory review of stochastic processes can be found in [410, 411]. Mathematical description of probability and measures can be found in [412-418]. A stochastic process is a collection of random variable {X(t1), X(t2), X(t3), X(t4), X(t5),… } often described as the random transient evolution of the process. The study of the evolution of a stochastic process is performed by repeating the same experiment with the same initial conditions. This allows to study the process statistically. A stochastic process is fully characterized by the absolute probability of the process giving the probability of its trajectory, as described in eq. 98 extracted from [3]:

$$P(x_1, t_1, x_2, t_2, \dots, x_n, t_n) = dx_1 dx_2 \dots dx_n \qquad \text{EQ. } 156$$

$$P(x_1, t_1, x_2, t_2, \dots, x_n, t_n) = Probability\ to\ found\ \{x(t_1) = I_1, x(t_2) = I_2, \dots, x(t_n) = I_n\}$$

$$P(x_1, t_1, x_2, t_2, \dots, x_n, t_n) = \frac{Nb\ of\ realizations\ passing\ throught\ I_1,\ I_2, \dots, I_n}{Total\ Number\ of\ realizations} = f_{X(t_1)X(t_2),\dots,X(t_n)}(x_1, x_2, \dots, x_n)$$

where x_i are the random variables associated with time t_i and P is the probability of the event. f is the distribution function(also called density function) associated with the random process X(t)

A stochastic process that can be thought of as 'memoryless' is called a Markov process. In fact if predictions for the future of the process can be made, based solely on its present state, the process is Markovian. Markov process hence satisfies the following property (eq. 157 obtained in [4]):

$$\forall\, t_1, t_2, \dots, t_{n-1} < t_n \quad P(x_1, t_1; x_2, t_2; x_{n-1}, t_{n-1} | x_n, t_n) = P(\, x_{n-1}, t_{n-1} \mid x_n, t_n\,) \qquad \text{EQ. } 157$$

where $P(x_{n-1}, t_{n-1} \mid x_n, t_n)$ is the probability that $x(t_n) = x_n$ knowing that $x(t_{(n-1)}) = x_{n-1}$

Sometimes only one realization of the process is available. In this case the stochastic process study is made possible through the assumption of stationarity. A process is called stationary when this process does not change when temporal translations are applied i.e. (eq. 158 extracted from [410]):

$$\forall\, \tau \in R, \forall\, n \geq 1 \quad P(x_1, t_1, x_2, t_2, \dots, x_n, t_n) = P(x_1, t_1 + \tau, x_2, t_2 + \tau, \dots, x_n, t_n + \tau) \qquad \text{EQ. } 158$$

A weaker form of stationarity is the weak sense stationarity (WSS) that only requires that the first and the second order moments do not vary with respect to the time [5]. A process is WSS if it has the following restrictions:

$$\forall\, t, \tau \in IR \quad , E[X(t)] = E[X(t + \tau)] \qquad \text{EQ. } 159$$

$$and\ \forall\ t_1, t_2\ \in\ IR\ , E[X(t_1)X(t_2)] = E[X(t_1 - t_2), X(0)]$$

where E is the expectancy operator.

A process X is said cyclostationary if it is invariant under time shift for some period T [419]

$$\forall\ t_1 \dots t_n\ \in\ IR, \qquad \exists\ T\ \in\ IR\ \ such\ as\ \{X(t_1), \dots, X(t_n)\} = \{X(t_1 + T), \dots, X(t_n + T)\} \qquad \text{EQ. } 160$$

The following properties hence results from a cyclostationary process:

$$\forall\ t_1, t_2\ \in\ IR, \qquad \exists\ T\ \in\ IR\ such\ as\ E[X(t_1)] = E[X(t_1 + T)] \qquad \text{EQ. } 161$$

$$and\ E[X(t_1)X(t_2)] = E[X(t_1 + T)X(t_2 + T)]$$

The study of a stochastic process is made by statistical properties. Of particular importance are the correlation functions, as explained in [7]. The n-th order correlation function of the stochastic process is given by eq. 162

$$C(t_1, t_2, \dots, t_n) \equiv \ \langle X(t_1)X(t_2) \dots X(t_n)\rangle \qquad \text{EQ. } 162$$

$$= \int_{Rn} dx_1 dx_2 \dots dx_n x_1 x_2 \dots x_n\ P(x_1,\ t_1,\ x_2,\ t_2,\ \dots,\ x_n,\ t_n)$$

The main correlation functions used are the mean (1th order moment) and the autocorrelation function that can be described with correlation functions as shown in eq. 186 [416, 420]:

$$C(t_1) = \qquad \langle X(t_1)\rangle \qquad = \int_{\{X_1(t)\}} dx_1 x_1\ P(x_1,\ t_1) \qquad \text{EQ. } 186$$

$$R_{XX}(t_1, t_2) = \ \langle (X(t_1) - \langle X(t_1)\rangle)(X(t_2) - \langle X(t_2)\rangle\rangle = C(t_1, t_2) - C(t_1)C(t_2)$$

$$R_{XX}(t_1, t_2) = \int\limits_{\{X_1(t)\}} \int\limits_{\{X_{2(t)}\}} x_1 x_2 P(x_1, t_1, x_2, t_2) dx_1 dx_2$$

$$R_{XX}(t_1, t_2) = \int\limits_{\{X_1(t)\}} \int\limits_{\{X_{2(t)}\}} x_1 x_2 f_{X(t_1)X(t_2)}(x_1, x_2) dx_1 dx_2$$

where $\{X(t_1)\}$ and $\{X(t_2)\}$ are the definition domains associated with $X(t_1)$ and $X(t_2)$ respectively.

When the time average of a random process (horizontal mean) is equal to the vertical mean of process, the process is ergodic (interested reader can refer to [421] for complementary information) and is defined as:

$$< X(t) > = \lim_{T \to \infty} \frac{1}{T} \int_{-T}^{T} x(t) dt \qquad \text{EQ. } 163$$

In the following development, the random process are described using lower case letter, to avoid misunderstanding between Fourier Transforms (in upper case letters)

The Fourier Transform of a signal x(t) is defined as:

$$FT[x(t)] = \chi(f) = \int_{-\infty}^{\infty} x(t)e^{j\omega t}\,dt \qquad \text{EQ. } 164$$

where ω is the varying pulsation. The inverse Fourier Transform of the χ(f) signal is defined as:

$$FT^{-1}[\chi(f)] = x(t) = \int_{-\infty}^{\infty} \chi(f)e^{j\omega t}\,df \qquad \text{EQ. } 165$$

In some other definition a normalization factor (2π) may also be found.

The energy and power definition of a deterministic signal or a random one will be reminded in this Section, introducing the theoretical basis of the Power Spectral Density (PSD) analysis.

The total energy of a deterministic signal x(t) is defined by eq. 166[422]:

$$E_n = \int_{-\infty}^{\infty} x(t)^2 dt \qquad \text{EQ. } 166$$

There is energy conservation between the time domain and the frequency domain such as indicated in the Perceval's theorem, which is recalled in eq. 167:

$$E_n = \int_{-\infty}^{\infty} x(t)^2 dt = \int_{-\infty}^{\infty} |\chi(2\pi f)|^2 df \qquad \text{EQ. } 167$$

where $|\chi(f)|^2$ is the Energy Density Spectrum (ESD) of the deterministic signal x(t) and is expressed in Joules/Hz.

For communication signals, the energy is effectively infinite (the signals are of unlimited duration), so power quantities are usually used. The average power of a deterministic signal is defined by eq. 168[422]:

$$Average\ Power = \overline{P_T} = \lim_{T\to\infty} \frac{1}{T} \int_{-T/2}^{T/2} x(t)^2 dt = \lim_{T\to\infty} \frac{1}{T} \int_{-T/2}^{T/2} x_T(t)^2 dt \qquad \text{EQ. } 168$$

where $x_T(t)$ is the x(t) truncated signal in the [-T/2;T/2] interval

Using the Parseval's theorem, the Power Spectral Density (PSD) of a deterministic signal could be extracted [422]:

$$\begin{aligned} \overline{P_T} &= \lim_{T\to\infty} \frac{1}{T} \int_{-T/2}^{T/2} x_T(t)^2 dt \\ &= \lim_{T\to\infty} \frac{1}{T} \int_{-\infty}^{\infty} |\chi_T(2\pi f)|^2 df \\ &= \int_{-\infty}^{\infty} \lim_{T\to\infty} \frac{|\chi_T(2\pi f)|^2}{T} df \end{aligned} \qquad \text{EQ. } 169$$

where $\lim_{T\to\infty} \frac{|\chi_T(2\pi f)|^2}{2T}$ also noted $S_{xx}(f)$ is the PSD of the $x_T(t)$ signal. $S_{xx}(f)$ is expressed in Watts/Hz and $\chi_T(2\pi f)$ is the Fourier Transform of the truncated signal $x_T(t)$ and is

defined as $\int_{-T/2}^{T/2} x_T(2\pi f) e^{j2\pi f t}\, dt$

The above definitions apply to random signals by replacing the signal by the vertical mean of it. In consequence for random signals, the energy and the PSD are defined by eq. 170[422]:

$$E_n = \int_{-\infty}^{\infty} E[(x(t))^2] dt \qquad \text{EQ. } 170$$

$$S_{xx}(f) = \lim_{T \to \infty} \frac{E[|\chi_T(2\pi f)|^2]}{T}$$

The computation of the PSD for stochastic processes is simplified in the particular case of WSS and much more complex when the following assumption does not hold true.

The PSD of WSS processes can be simplified using the Wiener Khintchine theorem (the proof is developed in [423, 424]) which states that the PSD of a WSS is equal to the Fourier Transform of its autocorrelation function as expressed by eq. 171:

$$S_{xx}(f) = FT[R_{xx}(t)] = \int_{-\infty}^{\infty} R_{xx}(t)\, e^{-j\omega t}\, dt \qquad \text{EQ. } 171$$

And

$$R_{xx}(t) = \int_{-\infty}^{\infty} S_{xx}(f) e^{j\omega t}\, df \qquad \text{EQ. } 172$$

In consequence, the relation between variance and PSD which is always true for WSS processes is reminded in eq. 173 (taking τ = 0 in eq. 171):

$$Var[x(t)] = R_{xx}(0) = \int_{-\infty}^{\infty} S_{xx}(f) e^{j\omega t}\, df \qquad \text{EQ. } 173$$

The PSD of non WSS is much more complex as the autocorrelation of the process depends on two time variables and not on their difference. Following the general formula for PSD computation reminded in eq. 170, the Fourier Transform of the vertical expectancy of the random process should be computed first, but does not always converge[425]. Although several authors proposed an extension of the Wiener Khintchine theorem for non WSS processes using the 2 dimensional Fourier Transform [23]or the Short Time Fourier Transform (SHFT) [426], the physical interpretation of the resulting PSD is often complicated. In[427], the extension of Wiener Khintchine theorem for non WSS processes conserving an unique PSD dependency into the single frequency variable f is presented. In order to obtain such result, the mean autocorrelation function over a 2T interval is computed before evaluating its Fourier Transform as expressed in eq. 174

$$\overline{R_{xx}}(\tau) = \lim_{T \to \infty} \frac{1}{2T} \int_{-T}^{T} R_{yy}(t, t - \tau) dt \qquad \text{EQ. } 174$$

The following discussion summarizes the main findings extracted from[428]. Non stationary process often has a time-dependent spectrum. There are at least two different possibilities to construct the time-dependent spectrum. Primarily it is to impose a linear relation between the PSD of the random process and its covariance function. Secondly, it may be possible to create a time-dependent spectrum directly from the process itself. Time-dependent spectrum estimations based on these theories are presented below.

- The Evolutionary Spectra aimed to describe the temporal evolution of spectral contributions, frequency by frequency. Supposing that $A_t(\lambda)$ are slowly time varying function, the evolutionary spectra is defined byeq. 175:

$$x(t) = \int_{-\infty}^{\infty} A_t(f) dZ(f) \qquad \text{EQ. } 175$$

with

$$E[|dZ(f)|^2] = d\mu(f) \qquad \text{EQ. } 176$$

and

$$S_{xx}(t, f) = |A_t(f)|^2 \frac{d\mu(f)}{df} \qquad \text{EQ. } 177$$

where $S_{xx}(t,f)$ is the PSD of the x(t) process around t, Z(f) is an orthogonal process and $A_t(f)$ is an admissible modulation function. The measure dμ is absolutely continuous with respect to f. Complementary information can be found in [428].

- According to[428], the Wigner-Ville distribution is defined as:

$$W_x(t, \omega) = \int_{-\infty}^{\infty} x(t + \frac{\tau}{2}) \overline{x(t - \frac{\tau}{2})} e^{-i\omega\tau} d\tau \qquad \text{EQ. } 178$$

Calling

$$Y_t(\tau) = x(t + \frac{\tau}{2}) \overline{x(t - \frac{\tau}{2})} \qquad \text{EQ. } 179$$

and supposing that the absolute value of the autocorrelation of $Y_t(\tau)$ is finite, the expected value of the Wigner-Ville distribution can be defined (and is called the Wigner-Ville spectrum), such as described byeq. 180:

$$E[W_x(t, \omega)] = S_{WV}(t, \omega) \qquad \text{EQ. } 180$$

The variance and its two-dimensional spectral distribution function along the principal diagonal is developed ineq. 181[428]:

$$Var[x(t)] = \frac{1}{2\pi}\int_{-\frac{\pi}{2}}^{\frac{\pi}{2}} S_{WV}(t,\omega)d\omega \qquad \text{EQ. } 181$$

- The evolutive spectrum of Tjostheim and Melard is based on the decomposition of a random process into a stationary gaussian process(x(t)) entering into a LTV system, such as indicated by eq. 182[428]:

$$y(t,\tau) = h(t,\tau) * x(t) \qquad \text{EQ. } 182$$

where * denotes the convolution product. The evolutive spectrum of Tjostheim and Melard is defined by the general definition of the PSD already presented in eq. 170 and rewritten below for reader's convenience:

$$S_{TM}(\omega,t) = \lim_{t\to\infty}\frac{1}{T}E[|TF(y(t,\tau)|^2] \qquad \text{EQ. } 183$$

However if h is supposed LTI rather than LTV, and if x(t) is a stationary gaussian process with variance σ_{WN} the evolutive Tjostheim and Melard spectrum simplifies into[428]:

$$S_{TM}(t,\omega) = \frac{\sigma_{WN}^2}{2\pi}.\left|\sum_{s=-\infty}^{t} h(t,s)e^{i\omega s}\right| \qquad \text{EQ. } 184$$

The variance of y(t) is obtained by integrating the Tjostheim and Melard spectrum over a 2π interval, as described by eq. 185[428]:

$$Var[y(t)] = \frac{1}{2\pi}\int_{-\pi}^{\pi} S_{TM}(t,\omega)d\omega \qquad \text{EQ. } 185$$

2. Mathematical operations associated with systems

As one goal of phase noise modeling was to express phase noise as input noises entering inside a system and resulting in phase noise, the mathematical theory of systems is quickly reviewed in this document. The stochastic processes generally introduced in Section I.H.1, will be the 'input' of a system for phase noise study. The only systems considered are determinist and causal as they are supposed to model physical systems. A system can be defined by a function h : C^{IR} -> C^{IR} that maps an input {x(t), - ∞< t <∞ } into an output {y(t), - ∞< t <∞ } [8].

Important properties that will lead to simplified relations are the system linearity and the time-invariance. A system is said to be linear if[429]:

$$\forall\, x_1, x_2 \; in \; C^{IR} \; and \; \forall\, a_1, a_2 \; in \; C^2 \; h(ax_1 + bx_2) = ah(x_1) + bh(x_2) \qquad \text{EQ. } 187$$

A system is time-invariant if[429]:

$$h(\{x(t+\tau)\,, -\infty < t < \infty\}) = \{h(x, t+\tau), -\infty < t < \infty\} \quad \text{EQ. } 188$$

It is shown in [9] that if h is a linear system and x € C^{IR} is an input function, its output is given by the eq. 189 reminded from [10]:

$$y(x,t) = \int_{-\infty}^{\infty} x(u)h(t,u)du \quad \text{EQ. } 189$$

However these notations are far from the usual covariance definition. It can be shown in [430], [431], [432] than the above definition can be rewritten in a more conventional way, closer to the usual one dimension covariance definition:

$$y(x,t) = \int_{-\infty}^{\infty} x(u)h(t,u-t)du \quad \text{EQ. } 190$$

If h is a Linear Time Invariant system (LTI) and the input x(t)=exp(j2πft), the output of the system is[429]:

$$H(f) = \int_{-\infty}^{\infty} h(u-t)\exp(2j\pi f\,(u-t))du \quad \text{EQ. } 191$$

where H(f) is the Fourier Transform of the impulse response h(t) also called system transfer function. Useful Fourier or Laplace transform of LTI systems can be easily found on literature. Lotfi and Zahed extended the Fourier/Laplace transform theory for Linear Time Variant systems (LTV) study. For a LTV system the system transfer function H(f,t) is given by the following equation[429]:

$$H(f,t) = \int_{-\infty}^{\infty} h(t,u-t)\exp(2j\pi f\,(u-t))du \quad \text{EQ. } 192$$

For an input x(t)=exp(j2πft) feeding a LTV system, the output is then obtained by eq. 193[10], defining the inverse Fourier Transform operation [10, 425]:

$$h(x,t) = \int_{-\infty}^{\infty} H(f,t)X(f)\exp(-2j\pi ft)\,df \quad \text{EQ. } 193$$

where X(f) is the Fourier Transform of the input function x(t)

Although some authors questioned the utility of these definitions [429], the system transfer function H(f,t) is only valid around t.

The study of LTV system is further simplified if the system is Linear Periodically Time Varying system (LPTV) with an impulse response which satisfies[429]:

$$\forall\, t,u \in IR^2, for\ some\ period\ T > 0\ h(t,u) = h(t+T, u+T) \quad \text{EQ. } 194$$

The impulse response of a LPTV system is hence periodic and can be decomposed using the Fourier series. It can be shown in [11] that the LPTV system function is also periodic in t, as described in eq. 195 :

$$H(f,t) = \int_{-\infty}^{\infty} h(t, t-\tau)\exp(-2j\pi f\tau)d\tau \quad \text{EQ. } 195$$

This system transfer function can be hence decomposed using the Fourier series [12], as defined by equation eq. 196 [429]:

$$H(f,t) = \sum_{n=-\infty}^{\infty} H_n(f + nfc)\exp(j2\pi nfct) \quad \text{EQ. } 196$$

where

$$H_n(f) = \int_{-\infty}^{\infty} h_n(\tau)\exp(-j2\pi f\tau)d\tau$$

The output of the system to a LPTV system can be found in [13] and is reminded in eq. 197

$$y(x,t) = \int_{-\infty}^{\infty} \sum_{n=-\infty}^{\infty} H_n(f + nfc)\, exp(j2\pi fct)\, X(f)\, exp(j2\pi ft)\, df \quad \text{EQ. } 197$$

$$h(x,t) = TF^{-1}\left\{ \sum_{n=-\infty}^{\infty} H_n(f)X(f + nfc) \right\}$$

Assuming that the above integrals are well defined for all t in some rigorous sense, the mean and the autocorrelation of the output signal y(x,t) are defined by the eq. 198.

$$m_y(t) = \int_{-\infty}^{\infty} m_x(u)h(t,u)du \quad \text{EQ. } 198$$

$$R_{yy}(t_1,t_2) = \int_{-\infty}^{\infty}\int_{-\infty}^{\infty} R_{xx}(r,s)h(t_1,r)h(t_2,s)drds$$

where m_x is the esperance of the x(t) process and R_{xx} its autocorrelation function. For further development of these equations, interested readers should refer to [432], [431] for additional information.

The statistic properties of the system output and well as its PSD are greatly simplified on the following special cases and are the basis of the current noise analysis.

- If the input X is a WSS process and the system is a stable LTI system (the condition of stability can be found in [11]), the cross correlation of the input X and the output Y are given by eq. 199:

$$R_{YX}(\tau) = R_X(\tau) * h(\tau) \quad \text{EQ. } 199$$

$$R_{XY}(\tau) = R_X(\tau) * h(-\tau)$$

where * is the convolution operator. The PSD of the output Y is hence obtained by eq. 200 and is of great importance in system study:

$$S_{YY}(f) = |H(f)|^2 S_{XX}(f) \qquad \text{EQ. } 200$$

- Another special case that is commonly found in literature and extracted from [13] is when a cyclostationary process is the input of a stable LPTV system. Assuming that the fundamental frequency of the cyclostationary process is equal to the fundamental frequency of the LPTV system, it can be shown [433] that the output of the system is also cyclostationary with the same fundamental frequency. The autocorrelation function and the output PSD can be found in [433].
- Other special cases include the LTI system with a cyclostationary process in input or the opposite case a WSS process feeding a LPTV system. The autocorrelation function and the output PSD in these cases are detailed in [410].
- More general cases are however more difficult to handle. The following development is based on the author's personal computations.
    - If h(t, τ) is a Linear Time Varying (LTV) system and the input process x(t) is WSS:

$$R_{yy}(\alpha, t) = E[y(t), y(t+\alpha)] \qquad \text{EQ. } 201$$

$$R_{yy}(\alpha, t) = E[\int_{-\infty}^{\infty} h^*(\tau_1, t)\, x^*(t - \tau_1) d\tau_1 \,.\, \int_{-\infty}^{\infty} h(\tau_2,\ t + \alpha) x(t + \alpha - \tau_2) d\tau_2]$$

$$R_{yy}(\alpha, t) = \int_{-\infty}^{\infty} \int_{-\infty}^{\infty} E[h^*(\tau_1, \quad t) h(\tau_2, t + \alpha)] R_{xx}(\alpha - \tau_1 - \tau_2) d\tau_1 d\tau_2$$

If h(t,τ) is LTV, its Fourier Transform has two variables. The understanding of the PSD computed is difficult implying both STFT (only valid around t) and the 2 dimensions Fourier Transform of the system transfer function. The Wiener Khintchine theorem can be applied as the process is WSS, greatly simplifying the PSD computation.

$$S_{yy}(f, t) = \int_{-\infty}^{\infty} R_{yy}(\tau, t) e^{-j2\pi f \tau}\, d\tau \qquad \text{EQ. } 202$$

$$S_{yy}(f, t) = \int_{-\infty}^{\infty} \int_{-\infty}^{\infty} \int_{-\infty}^{\infty} E[h^*(\tau_1, t) h(\tau_2, t + \tau)] R_{xx}(\tau - \tau_1 - \tau_2) d\tau_1 d\tau_2\, e^{-j2\pi f \tau}\, d\tau$$

Naming the following expressions:

$$H^*(F, t) = \int_{-\infty}^{\infty} h^*(\tau_1, t)\, e^{-j2\pi F \tau_1} d\tau_1 \qquad \text{EQ. } 203$$

$$and\ H(F, f) = \int_{-\infty}^{\infty} \int_{-\infty}^{\infty} h(\tau_2, \quad \alpha) e^{-j2\pi F \tau_2} e^{-j2\pi f \alpha} d\tau_2\, d\alpha$$

$$\rightarrow S_{yy}(f,t) = \int_{-\infty}^{\infty} S_{xx}(F) e^{j2\pi f t} H^*(F,t)\, H(F,f)\, dF$$

This result is very difficult to interpret and is only valid close to t.

- The general case is to consider h(t,τ) has a Linear Time Variant (LTV) process and x(t) is a non WSS process. As the input process is not WSS, the Wiener Khintchine theorem cannot be applied. However a generalization of the Wiener Khintchine theorem for nonstationary process already discussed above, can be used to greatly ease the calculus. Other development to compute the PSD of the overall process such as proposed in Annex B.1, may be utilized also but render the result interpretation more complex as many independent variables are involved.

  Noting the mean autocorrelation function of the non WSS x(t) process around t as:

$$\overline{R_{yy}}(\tau) = \lim_{T \to \infty} \frac{1}{2T} \int_{-T}^{T} R_{yy}(t, t-\tau) dt \qquad \text{EQ. } 204$$

  Taking the mean of the autocorrelation function permits to express the autocorrelation only depending on a single variable, hence the definition for the PSD still holds true. $R_{yy}(t,\tau)$ is the autocorrelation of the x(t) process defined in eq. 197 (however the simplification of the autocorrelation into one single variable cannot be made for non WSS). Using both eq. 201and eq. 204, the mean autocorrelation function can be defined such as:

$$\overline{R_{yy}}(\tau) = \lim_{T \to \infty} \frac{1}{2T} \int_{-T}^{T} E\Big[\int_{-\infty}^{\infty} h^*(\tau_1, t)\, x^*(t - \tau_1) d\tau_1 \,.\, \int_{-\infty}^{\infty} h(\tau_2,\ t+\tau) x(t+\tau-\tau_2) d\tau_2 \Big]\, dt \qquad \text{EQ. } 205$$

  The PSD of this process can be defined by eq. 206, according to the Wiener Khintchine theorem extended to non WSS processes:

$$S_{yy}(f) = \int_{-\infty}^{\infty} \overline{R_{yy}}(\tau) e^{-j2\pi f \tau} d\tau \qquad \text{EQ. } 206$$

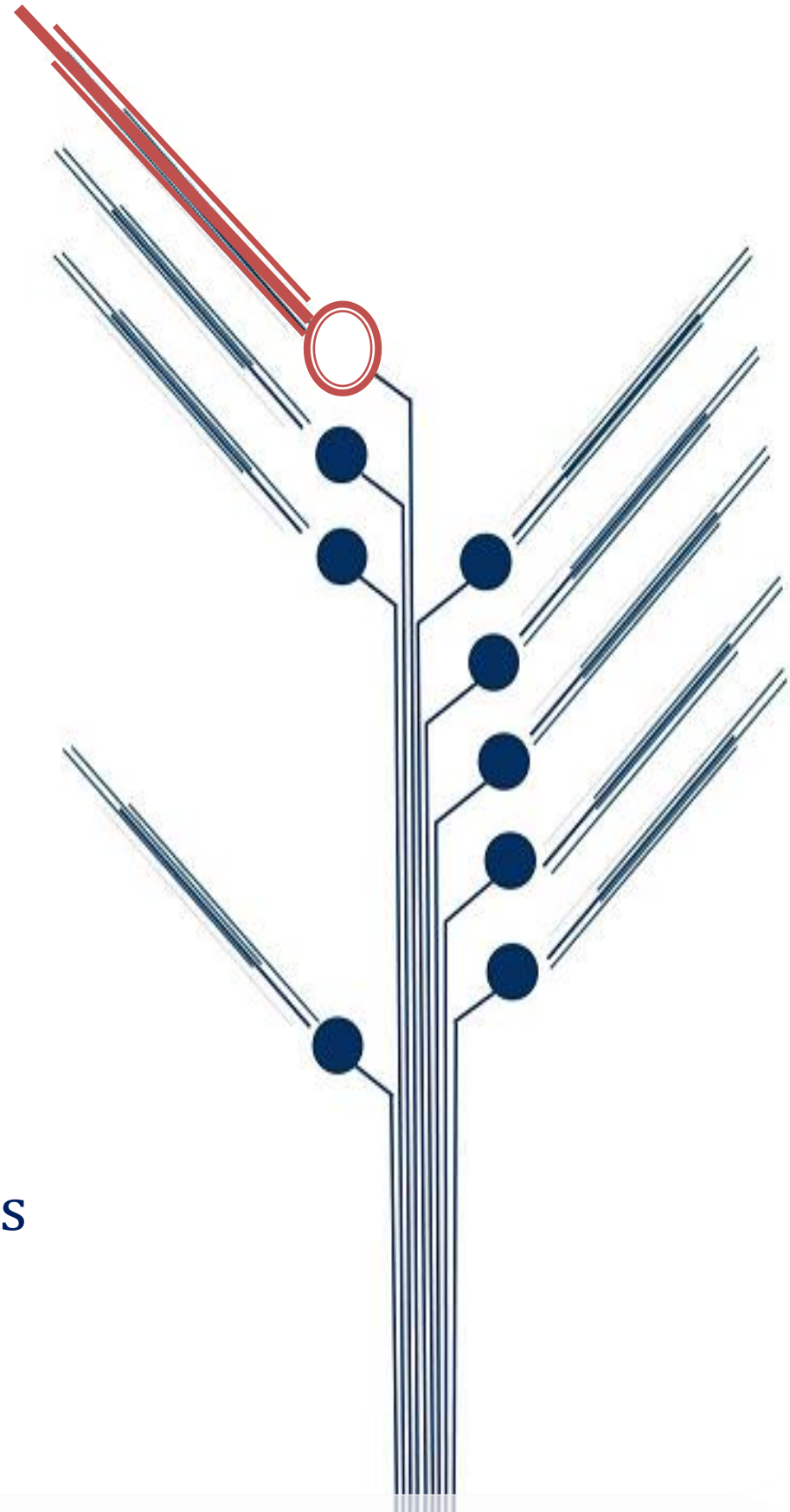

Annex C:

Input noises

The noise description is still an vast area of research in physics, not restricted to electronic. Physical description of the different types of noise is of value to understand its origins to permit more efficient correction.

In common description of phase noise[434], input noises such as thermal noise, shot noise are responsible for phase perturbations in an oscillator.

3. White noise general introduction

White noise has the same energy over all the frequencies (constant PSD) [435]. White noise is a Gaussian process defined with a null mean and with a covariance$C(t_1, t_2) = \Gamma\delta(t_2 - t_1)$, where δ is the delta function and Γ is its associated energy. The covariance is hence non null when t_1 is very close to t_2 meaning that the white noise f(t_1) is uncorrelated to f(t_2) except when $t_1 \approx t_2$[435].

Thermal noise is associated with carrier agitations which increase with temperature and is described mathematically as white noise.

We used the Matlab® function *randn* to generate a white Gaussian noise.

4. Higher order noises

a) Introduction to the Fokker Plank equation

The theory presented in this section is mostly derived from [435]. This theory is of importance to define the physical processes associated with higher order noises than white noise.

To study diffusive Markovian process, the probability of transition P(x_0|x,t) is defined as the probability of a particle to be at a position x at a given t, knowing that its initial position was x0.The three properties given by eq. 207defines completely a diffusive process [435].

$$\langle \Delta x \rangle x_0 = \int_R dx\,(x - x_0) P(x_0|x,t) =^{t\to 0}\ a(x_0)t + \theta(t^\alpha)\,, \alpha > 1 \qquad \text{EQ. } 207$$

$$\langle (\Delta x)^2 \rangle x_0 = \int_R dx\,(x - x_0)^2 P(x_0|x,t) =^{t\to 0} b(x_0)t + \theta(t^\alpha)\,, \alpha > 1$$

$$\langle (\Delta x)^k \rangle x_0 = \int_R dx\,(x - x_0)^k P(x_0|x,t) =^{t\to 0}\ \theta(t^\alpha)\,, \alpha > 1 \quad , \qquad k > 2$$

where a(x) is the derive function and b(x) is the diffusion function of the process

The properties presented in eq. 207leads to the Fokker-Plank equation (eq. 208):

$$\frac{\partial}{\partial t}P(x_0|x,t) = -\frac{\partial}{\partial x}\big(a(x)P(x_0|x,t)\big) + \frac{1}{2}\frac{\partial^2}{\partial x^2}\big(b(x)P(x_0|x,t)\big) \qquad \text{EQ. } 208$$

The solution of this equation can be found in [435] and will give the $P(x_0|x,t)$ function.

b) Wiener process

A special case of the diffusion equation is the Wiener process taking a = 0 and b = 2D $=2\frac{K_b T}{m\gamma}$ (Einstein relation [434]) where m is the mass of the particle, γ is the friction coefficient K_b is the Boltzmann constant and T the absolute temperature. The Wiener process is used to describe the diffusion process called Brownian motion (or random walk of a particle) and also the Brownian noise.

The main relations useful for noise description are available in [435] and are recalled in eq. 209

$$P(x,t) = \frac{1}{\sqrt{4\pi D t}} e^{\frac{-x^2}{4Dt}} \qquad t > 0 \qquad \text{EQ. } 209$$

$$\langle x(t) \rangle = 0$$

$$\langle x(t_1) x(t_2) \rangle = 2Dt_1$$

$$Sxx(\omega) = \int_R C(t)\, e^{i\omega t} dt = \frac{D}{-2\pi^2 w^2}$$

where C(t) is the autocorrelation function. A Wiener process has hence a PSD proportional to $\frac{1}{\omega^2}$

c) I.5 Ornstein-Uhlenbeck process

This process represents a second well known particular case of the diffusion equation, with $a(v)=-\gamma v$ and $b(v)=2\gamma^2 D$ which describes the particle movement due to thermal agitation in a fluid. As for the Wiener process, the mean, covariance and DSP are significant and presented in eq. 210 (extracted from [435])

$$P(v,t) = \sqrt{\frac{m}{2\pi KbT}} e^{\frac{-mv^2}{2KbT}} \quad \text{EQ. 210}$$

This process is stationary, Gaussian and with null mean, in consequence:

$$\langle v(t) \rangle = 0 \quad \text{EQ. 211}$$

$$\langle v(t_0) v(t) \rangle = \frac{KbT}{m} e^{-\gamma(t-t_0)}$$

Because the process is stationary, the simplification of the PSD formula can be applied and the PSD of this process is given by eq. 212

$$Svv(w) \quad = \quad \frac{KbT}{m} \frac{1}{(2\pi i\omega - \gamma)^2} \quad \text{EQ. 212}$$

Hence the magnitude of the PSD of this process is proportional to $\frac{1}{w^2}$

It must be noted that the PSD considered is the PSD of the velocity of the particle and not the PSD of its position. Integrating the velocity to obtain the position will give $Sxx(f)$ proportional to $\frac{1}{\omega^4}$

5. 1/f noise general overview

The other type of electronic noise which mainly influences phase noise is the Flicker noise (also called pink noise or 1/f noise) related to the shape of its PSD. However the integration of white noise leads to the Wiener process also called Brownian motion (which PSD is in $1/f^2$).

1/f noise has been intensively studied in an attempt to find a physical explanation with a mathematical description but there is not yet an unified theory [98, 100, 436]. Mathematical models have been proposed such as recurrence models, non linear differential equation stochastic models, reversible Markov chain models,… (summarized in [100]). The early description of the 1/f noise in vacuum tubes was made by Johnson and described mathematically by Schottky and presented in eq. 213

Suppose that $\{t_k\}$ with k> 0 is a Poisson process. Shot noise process is obtained by attaching to each t_k, an exponential relaxation law and summing on k [100]:

$$Sn(t,tk) = \sum_k N_0 e^{-\lambda(t-tk)} \quad \text{EQ. 213}$$

where N_0 is the initial number of electrons and λ the relaxation constant of the exponential law. The Fourier Transform (FT) of shot noise is given by eq. 214[100]

$$F(\omega) = \int_{-\infty}^{\infty} \sum_k N(t, t_k) e^{-i\omega t} dt = \frac{N_0}{\lambda + i\omega} \sum_k e^{i\omega t_k} \qquad \text{EQ. } 214$$

Applying the general equation for the PSD computation, the PSD of the shot noise is given by the Lorentzian function shown in eq. 215[100]

$$S_{nn}(\omega) = \frac{{N_0}^2}{\lambda^2 + \omega^2} \qquad \text{EQ. } 215$$

where n is the average pulse rate of electrons before being captured by the trapping sites. However this mathematical description felt to describe the 1/ω behavior. Superposing such process with a distribution of the relaxation rate uniformly distributed can conduce to the 1/ω if some assumptions are made [100]:

$$S_{nn}(w) = \frac{1}{\lambda_2 - \lambda_1} \int_{\lambda_1}^{\lambda_2} \frac{{N_0}^2}{\lambda^2 + \omega^2} \, d\lambda = \frac{{N_0}^2 n}{\omega\,(\lambda_2 - \lambda_1)} \left[\arctan\frac{\lambda_1}{\omega} - \arctan\frac{\lambda_2}{\omega}\right] \qquad \text{EQ. } 216$$

$$S_{nn}(\omega) = \begin{cases} {N_0}^2 n & 0 < \omega \ll \lambda_1 \ll \lambda_2 \\ \dfrac{{N_0}^2 n \pi}{2\omega\,(\lambda_2 - \lambda_1)} & \lambda_1 \ll \omega \ll \lambda_2 \\ \dfrac{{N_0}^2 n}{\omega^2} & \lambda_1 \ll \lambda_2 \ll \omega \end{cases}$$

Making these assumptions permit to obtain the 1/ω behavior, more details are available in[100].

In electronics field the two most significant descriptions are attributed to McWhorther (which associated 1/f noise with random surface trapping and detrapping of the mobile carriers of the channel [30, 437]) and to Hooges (which attributed Flicker noise to mobility fluctuations of the charge carriers[438]).

Generating pink noise was made by using a white noise generator as input of a $\frac{1}{\sqrt{f}}$ transfer function which has a $\frac{1}{f}$ PSD not achievable with common filters. For instance, this transfer function can be created using the fracpole suite [439]. However this algorithmic description of 1/f noise, has no physical meaning.

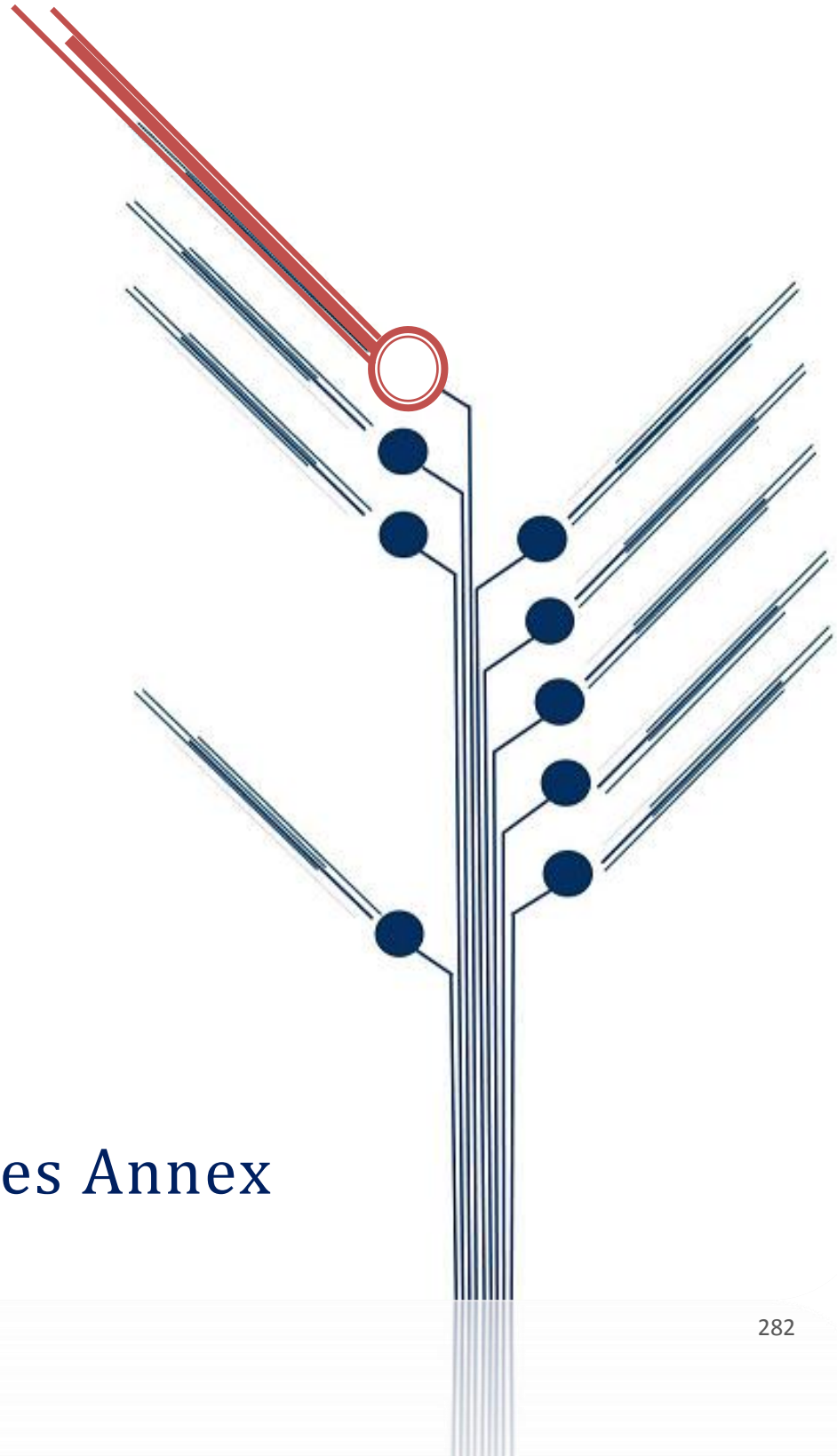

References Annex

[1] B. S. Wilson and M. F. Dorman, "Cochlear implants: current designs and future possibilities", *J Rehabil Res Dev, Vol.* 45-5, pp. 695-730, (2008)
[2] J. Rouger and et. al., "Evidence that cochlear-implanted deaf patients are better multisensory integrators"*, Vol.* 104-17, pp. 7295-7300, (2007)
[3] O. Bø Wie, E.-S. Falkenberg, O. Tvete and B. Tomblin, "Children with a cochlear implant: Characteristics and determinants of speech recognition, speech-recognition growth rate, and speech production: Niños con Implante Coclear: Características y determinantes del reconocimiento, de la tasa de crecimiento del reconocimiento y de la producción de lenguaje", *International Journal of Audiology, Vol.* 46-5, pp. 232-243, (2007)
[4] M. Burger, "Biosciences in the 21st century, Lecture 2: Innovations and Challenges", *LeHigh University*, Online: *http://www.lehigh.edu/~inbios21/PDF/Fall2008/Burger_08292008.pdf*
[5] "Cochlear Implant 1", *common.wikipedia.org*,
[6] A. N. P. Fan-Gang Zeng, Richard R. Fay, "Cochlear Implants: Auditory Prostheses and Electric Hearing", *ed. Springer*. (21 avr. 2004 - 437 pages)
[7] M. Carlberg and e. al., "BioInitiative 2012: A Rationale for Biologically Exposure Standards for Low Electromagnetic Radiation", (December 31, 2012)
[8] H. P. Schwan and K. R. Foster, "RF-field interactions with biological systems: electrical properties and biophysical mechanisms", *Proceedings of the IEEE, Vol.* 68-1, pp. 104-113, (1980)
[9] L. Challis, "Mechanisms for interaction between RF fields and biological tissue", *Bioelectromagnetics, Vol.* 26-S7, pp. S98-S106, (2005)
[10] U. Møller, D. G. Cooke, K. Tanaka and P. U. Jepsen, "Terahertz reflection spectroscopy of Debye relaxation in polar liquids", *Advances in Optics and Photonics, Vol.* 26, pp. A113-A125 (2009)
[11] J. K. Niparko, "Cochlear Implants: Principles and Practices (chapter 7)". (2009)
[12] G. Clark, "Cochlear Implants: Fundamentals and Applications (ch. 4-8)", *ed. Springer-Verlag*. (2003)
[13] M. Bond, S. Mealing, R. Anderson, J. Elston, G. Weiner, R. Taylor, M. Hoyle, Z. Liu, A. Price and K. Stein, "The effectiveness and cost-effectiveness of cochlear implants for severe to profound deafness in children and adults: a systematic review and economic model", *Health technology assessment, Vol.* 13-44, pp. 1-330, (2009)
[14] A. Moctezuma and J. Tu, "An overview of cochlear implant systems", *USA: University of Illinois, Urbana-Champaign*, (2011), Online: *https://wiki.engr.illinois.edu/download/attachments/48137228/ECE+415+Cochlear+Implant+Final.pdf*
[15] P. Senn, "Making deaf people hear (better?) European project ", *University Department of Otorhinolaryngology, Head & Neck Surgery, Inselspital, Bern, Switzerland*, (2013), Online: *http://www.euronanoforum2013.eu/wp-content/uploads/2013/07/P-Senn-ENF2013.pdf*
[16] J. Spitzer, "Evaluation of decisions regarding candidates for cochlear implants", *Archives of oto-rhino-laryngology, Vol.* 245-2, pp. 92-97, (1988)
[17] J. Nancy and M. Roizen, "ETIOLOGY OF HEARING LOSS IN CHILDREN, Nongenetic Causes , HEARING LOSS IN CHILDREN", *Department of Pediatrics, University of Chicago Pritzker School of Medicine*,
[18] P. M. Carter and e. al., "Cochlear implant system with soft turn on electrodes", *Patent US5755747 A, USA*, (2008),
[19] R. Nowak, "Light opens up a world of sound for the deaf", *Newscientist.com*, (21 November 2008),
[20] A. Wheeler, S. Archbold, S. Gregory and A. Skipp, "Cochlear implants: The young people's perspective", *Journal of Deaf Studies and Deaf Education, Vol.* 12-3, pp. 303-316, (2007)
[21] R. J. Briggs, H. C. Eder, P. M. Seligman, R. S. Cowan, K. L. Plant, J. Dalton, D. K. Money and J. F. Patrick, "Initial clinical experience with a totally implantable cochlear implant research device", *Otology & Neurotology, Vol.* 29-2, pp. 114-119, (2008)
[22] D. A. Chen, D. D. Backous, M. A. Arriaga, R. Garvin, D. Kobylek, T. Littman, S. Walgren and D. Lura, "Phase 1 clinical trial results of the Envoy System: a totally implantable middle ear device for sensorineural hearing loss", *Otolaryngology--Head and Neck Surgery, Vol.* 131-6, pp. 904-916, (2004)
[23] Y. Vaiarello, Y. Leduc, N. Veau and G. Jacquemod, "Ultra Low Power Transmitter for Cochlear Implant Application", *IEEE Circuits and Systems Society Forum on Emerging and Selected Topics (CAS-FEST)*, (2011)

[24] Y. Vaiarello, "Étude et conception d'un microphone sans fil très faible comsommation pour implants cochléaires", *LEAT, Sophia Antipolis*, (2012),
[25] R. Roby, "Roby Institute - Advanced treatment for a healthy living", (2011), Online: *http://onlineallergycenter.com/dr_roby.php*
[26] J. K. Kevin D Jones, Victor Konrad, "Some "Real World" Problems in the Analog and Mixed Signal Domains ", *Malta*, (2008),
[27] K. Kundert, "Informative note: Simulation of Analog and Mixed Signal Circuits", (1998),
[28] X. Zhou and T. Tang, "Accurate Timing Simulation of Mixed-Signal Circuits with a Dynamic Delay Model", *Proceedings of the Int. Workshop on Computer-Aided Design, Test, and Evaluation for Dependability*, pp. 309-311, (1996)
[29] S. B. Bibyk, "Mixed-Signal IC Design Kit Training Manual", *Ohio*, (2003),
[30] N. Padmaraju, "Analog and Mixed Signal Modeling Approaches", *MindTree Limited*, Online: *http://www.design-reuse.com/articles/22773/analog-mixed-signal-modeling.html*
[31] K. Kundert, "Introduction to The Design of Mixed-Signal Systems on Chip, MS-SOC", (1998),
[32] J. L. T. Elisabeth M. S. J. Van Gennip, "Assessment and Evaluation of Information Technologies in Medicine", *ed. IOS Press*. (1995)
[33] C. M. Macal, "Model Verififcation and Validation", *Threat Anticipation: Social Science Methods and Models*, (2005)
[34] R. G. Sargent, "Verification and Validation of simulation models", *Simulation Conference (WSC)*, pp. 166 - 183 (2010)
[35] J. A. Sokolowski and C. M. Banks, "Principles of Modeling and Simulation: A Multidisciplinary Approach", *ed. John Wiley & Sons*. (2009)
[36] Fang Lin Luo, Hong Ye and M. H. Rashid, "Digital Power Electronics and Applications", *ed. Elsevier, USA*. (2005)
[37] A. Bell, "A Resonance Approach to Cochlear Mechanics", *PloS one, Vol.* 7-11, pp. e47918, (2012)
[38] E. S. Ferre-Pikal and e. al., " Draft revision of IEEE std 1139- 1988 standard definitions of physical quantities for fundamental frequency and time metrology – random instabilities", *IEEE international, Frequency control symposium*, pp. 338 - 357, (1997)
[39] L. A. Werner and L. Gray, "Behavioral studies of hearing development",in *Development of the auditory system*, *ed. Springer*. 12-79, (1998)
[40] K. Kundert, "Accurate and rapid measurement of IP2 and IP3", *The designer guide to SPICE and Spectre, Version 2b*, (2002)
[41] N. Pernick, "Ear Anatomy", (2013), Online: *http://www.pathologyoutlines.com/topic/earnormalanatomy.html*
[42] R. Arvind, Nuttapong, Srirattana and Joy Laskar, "Modeling and design techniques for RF power amplifier", *ed. John Wiley & Sons*. (2008)
[43] R. A. Bergman, A. K. Afifi and P. M. Heidger, "Plate 16.312 Organ of Corti", *http://www.anatomyatlases.org/MicroscopicAnatomy/Section16/Plate16312.shtml*, Online: *Anatomy Atlas*
[44] M. M. Radmanesh, "Advanced RF and microwave circuit design: the ultimate guide to superior design". *I. 978-1-4259-7243-1*, (2009)
[45] J. Prikkel, "Modelling cochlear mechanics", *Order, Vol.* 501, pp. 2395, (2009)
[46] G. Vasilescu, "Electronic Noise and Interfering Signals: Principles and Applications", *ed. Springer*. (1999)
[47] M. Hubin, "Propriétés des milieux biologiques", (22 Mars 2013),
[48] S. M. Sze, & Ng, K. K., "Physics of semiconductor devices", (2006), Online: *maktabkhooneh.org/files/library/eng/electrical/5.pdf*
[49] P. B. Filho, "Tissue Characterisation using an Impedance Spectrosocpy probe", (2002),
[50] S. M. Sze and K. K. Ng, "Physics of semiconductor devices in *Chapter V: Investigation of ac conductivity and electronic modulus of LBS, LPBS and LVBS samples*", (2006),
[51] H. L. Friedman, "Theory of the dielectric constant of solutions ", *The Journal of Chemical Physics, Vol.* 2, (1976)
[52] D. Andreuccetti, "Dielectric Properties of Biologic Tissues in the frequency range of 10 Hz - 100 GHz", *IFAC*,

[53] S.Grimnes, Ø.G.Martinsen, J.Malmivuo, R.Plonsey, D. S. Holder and J. G. Webster, "Measurement of Electrical Bio-Impedance (the EBI) and its diagnostical applications", *Thomas Johann Seebecki elektroonikainstituut*, Online: *http://www.elin.ttu.ee/mesel/Study/Courses/Biomedel/Content/BioImped/BioImped.htm*

[54] S. Ueno, "Biological effects of magnetic and electromagnetic fields", *ed. Springer*. (1996)

[55] R. Sarpeshkar, T. Delbruck and C. A. Mead, "White noise in MOS transistors and resistors", *Circuits and Devices Magazine, IEEE, Vol.* 9-6, pp. 23-29, (1993)

[56] J. Johnson and H. Nyquist, "Thermal Agitation of Electricity in Conductors - details of the experiment", *Phys. Rev., Vol.* 32-97, (1928)

[57] Y. Vaiarello, W. Tatinian, Y. Leduc, N. Veau and G. Jacquemod, "Ultra low power radio microphone for cochlear implant application", *IEEE Journal of Emerging and Selected Topics in Circuits And Systems Vol.* 1-4, pp. 622-630, (2011)

[58] O. Diop, "Study and optimisation of the quality factor of small antennas", (2013), Online: *LEAT, Sophia Antipolis*

[59] O. Diop and e. al., "Planar antennas on Integrated Passive Device technology for biomedical applications", *IEEE International Workshop on Antenna Technology (iWAT)*, pp. 217 - 220, (2012)

[60] R. A. York, "Noise and radiating systems", *Microwave Electronics Laboratory of the University of California in Santa Barbara*, (2014), Online: *http://my.ece.ucsb.edu/York/Bobsclass/201C/Handouts/chap4.pdf*

[61] T. H. Lee, "The Design of CMOS Radio-Frequency Integrated Circuits", *ed. Cambridge*. (2003)

[62] "Low Noise Amplifier (LNA)", *University of California San Diego, Computer Science and Engeneering*, Online: *http://www-cse.ucsd.edu/*

[63] W.-H. Cho and S. S. Hsu, "An ultra-low-power 24 GHz low-noise amplifier using 0.13 CMOS technology", *Microwave and Wireless Components Letters, IEEE, Vol.* 20-12, pp. 681-683, (2010)

[64] M.-T. Lai and H.-W. Tsao, "Ultra-Low-Power Cascaded CMOS LNA With Positive Feedback and Bias Optimization", (2013)

[65] J. Jeong, J. Kim, D. S. Ha and H.-s. Lee, "A reliable ultra low power merged LNA and Mixer design for medical implant communication services", *Life Science Systems and Applications Workshop (LiSSA), 2011 IEEE/NIH*, pp. 51-54, (2011)

[66] P.-Y. Chang, S.-H. Su, S. S. Hsu, W.-H. Cho and J.-D. Jin, "An ultra-low-power transformer-feedback 60 GHz low-noise amplifier in 90 nm CMOS", *Microwave and Wireless Components Letters, IEEE, Vol.* 22-4, pp. 197-199, (2012)

[67] "Presentation on Fundamentals of Mixer Design", *Agilent Technologies*, (2001),

[68] A. Helmy and M. Ismail, "On Chip Inductors Design Flow", *Substrate Noise Coupling in RFICs Analog Circuits And Signal Processing Series*, pp. 63 - 86, (2008)

[69] P. Ndungidi, H. García-Vázquez, J. d. Pino, F. Dualibe and C. Valderrama, "RF specification driven by Multi-Objective Optimization Method", *DCIS*, (November, 2012)

[70] B. Vigraham and P. R. Kinget, "An ultra low power, compact UWB receiver with automatic threshold recovery in 65 nm CMOS", *Radio Frequency Integrated Circuits Symposium (RFIC), 2012 IEEE*, pp. 251-254, (2012)

[71] A. C. W. Wong, G. Kathiresan, C. K. T. Chan, O. Eljamaly, O. Omeni, D. McDonagh, A. J. Burdett and C. Toumazou, "A 1 V wireless transceiver for an ultra-low-power SoC for biotelemetry applications", *IEEE JOURNAL OF SOLID-STATE CIRCUITS, Vol.* 43-7, pp. 1511-1521, (2008)

[72] P. D. Bradley, "An ultra low power, high performance medical implant communication system (MICS) transceiver for implantable devices", *Biomedical Circuits and Systems Conference, 2006. BioCAS 2006. IEEE*, pp. 158-161, (2006)

[73] W. Wu, M. A. Sanduleanu, X. Li and J. R. Long, "17 GHz RF front-ends for low-power wireless sensor networks", *IEEE JOURNAL OF SOLID-STATE CIRCUITS, Vol.* 43-9, pp. 1909-1919, (2008)

[74] J. Jin and K. Fu, "An Ultra-low-power Integrated RF Receiver for Multi-standard Wireless Applications", *IETE Journal of Research, Vol.* 59-4, (2013)

[75] X. Huang, A. Ba, P. Harpe, G. Dolmans, H. de Groot and J. R. Long, "A 915 MHz, ultra-low power 2-tone transceiver with enhanced interference resilience", *Solid-State Circuits, IEEE Journal of, Vol.* 47-12, pp. 3197-3207, (2012)

[76] M. Lont, D. Milosevic, A. van Roermund and G. Dolmans, "Ultra-low power FSK wake-up receiver front-end for body area networks", *Radio Frequency Integrated Circuits Symposium (RFIC), 2011 IEEE*, pp. 1-4, (2011)
[77] L. Huang, M. Ashouei, R. F. Yazicioglu, J. Penders, R. J. Vullers, G. Dolmans, P. Merken, J. Huisken, H. de Groot and C. Van Hoof, "Ultra-Low Power Sensor Design for Wireless Body Area Networks-Challenges, Potential Solutions, and Applications", *JDCTA, Vol.* 3-3, pp. 136-148, (2009)
[78] H.-H. Hsieh, H.-S. Chen, P.-H. Hung and L.-H. Lu, "Experimental 5-GHz RF frontends for ultra-low-voltage and ultra-low-power operations", *Very Large Scale Integration (VLSI) Systems, IEEE Transactions on, Vol.* 19-4, pp. 705-709, (2011)
[79] M. Camus, B. Butaye, L. Garcia, M. Sie, B. Pellat and T. Parra, "A 5.4 mW/0.07 mm 2.4 GHz front-end receiver in 90 nm CMOS for IEEE 802.15. 4 WPAN standard", *Solid-State Circuits, IEEE Journal of, Vol.* 43-6, pp. 1372-1383, (2008)
[80] X. Hua, W. Lei, S. Yin and D. F. Foster, "Design and optimization of a 2.4 GHz RF front-end with an on-chip balun", *Journal of Semiconductors, Vol.* 32-9, pp. 095004, (2011)
[81] J.-F. Chang and Y.-S. Lin, "3.15 dB NF, 7.2 mW 3–9 GHz CMOS ultra-wideband receiver front-end", *Electronics letters, Vol.* 47-25, pp. 1401-1402, (2011)
[82] L. Thede, "Practical Analog and Digital filter design", (2004), Online: *http://dsp-book.narod.ru/PADFD.pdf*
[83] S. Larribe, "Le filtrage analogique", *CNAM Saclay*, (2005), Online: *http://sylvain.larribe.free.fr/CNAM/2004-2005/CNAM_2005_Filtrage.pdf*
[84] C. G. Dunenberg, "Filter Approximation Theory: Butterworth, Chebyshev, and Elliptic Filters", Online: *http://doctord.dyndns.org/courses/topics/Circuits/Filter_Approximation_Theory.pdf*
[85] A. D. Poularikas, "The handbook of formulas and tables for signal processing, Analog Filter Approximations", *ed. A. D. Poularikas*. (1999)
[86] V. Meghdadi, "Première partie: le filtrage analogique, Chapitre 2: Approximations", *ENSIL*,
[87] E. Sanchez, "A Designer's Guide To Filter Approximations", (Fall 2004),
[88] S. Icart, "Elec 4: Automatique", *Polytech Nice Sophia Antipolis University*, Online: *http://users.polytech.unice.fr/~icart/*
[89] D. Earl, "Möbius transformations and the extended complex plane", (2007), Online: *http://people.maths.ox.ac.uk/earl/G2-lecture4.pdf*
[90] C. Mello, "IIR filter design example", *Carnegie Mellon University*, (2005), Online: *https://www.ece.cmu.edu/~ee791/lectures/L22/IIRDesign.pdf*
[91] K. K. Parhi, "Chapter 11: Scaling and Round-off Noise", *University of Minnesota , Department of Electrical and Computer Engineering*, Online: *http://www.ece.umn.edu/users/parhi/SLIDES/chap11.pdf*
[92] O. Hinton, "Chapter 5 Design of IIR Filters ", *Newcasle University*, (2001), Online: *http://www.staff.ncl.ac.uk/oliver.hinton/eee305/Chapter5.pdf*
[93] A. kolesnikov, "Efficient algorithms for vectorization and polygonal approximation ", *Universityof joensuu computer science dissertations*, (2005),
[94] D. B. Leeson, "A simple model of feedback oscillator noise spectrum", *Proceedings IEEE, Vol.* 54, pp. 329–330, (1966)
[95] G. Sauvage, "Phase noise in oscillators: a mathematical nalysis of Leeson' smodel", *IEEE Transactions on instrumentation and measurments, Vol.* IM-26-4, (1977)
[96] A. Hajimiri and T. Lee, "Oscillator Phase Noise: A Tutorial", *IEEE J. Solid-State Circuits,* -35, (2000)
[97] T. Lee and A. Hajimiri, "A general theory of phase noise in electrical oscillators", *IEEE JOURNAL OF SOLID-STATE CIRCUITS, Vol.* 33, pp. 179-194, (1998)
[98] M. S. Keshner, "1/f noise", *Proceedings of the IEEE, Vol.* 70-3, pp. 212-218, (1982)
[99] Y. Jia and J. Li, "Stochastic system with colored correlation between white noise and colored noise", *Physica A: Statistical Mechanics and its Applications, Vol.* 252-3, pp. 417-427, (1998)
[100] E. Milotti, "1/f noise: a pedagogical review", *Corwnell University Library, classical physics*, (2002)
[101] J. A. Gubner, "Probability and Random Processes for Electrical and Computer Engineers, Chap. 10: Introduction to Random Processes", *ed. Cambridge University Press*. (2006)
[102] E. Rubiola, *FEMTOST Institute*, (2006), Online: *http://www.ieee-uffc.org/frequency-control/learning/pdf/Rubiola.pdf*

[103] A. M. Niknejad, "Oscillator Phase Noise", *University of Berkley*, (2009),
[104] H. Abidi and A. Asad, "How phase noise appears in oscillators",in *Analog Circuit Design*, *ed. Springer*. 271-290, (1997)
[105] J. Phillips and K. Kundert, "Noise in Mixers, Oscillators, Samplers & Logic, an introduction to Cyclostationary noise", *Cadence Design Systems*,
[106] A. Hajimiri and H. Donhee, "Virtual damping in oscillators", *Proceedings of the IEEE*, pp. 213-216, (2002)
[107] A. Hajimiri, S. Limotyrakis and T. H. Lee, "Jitter and Phase Noise in Ring Oscillators", *IEEE JOURNAL OF SOLID-STATE CIRCUITS, Vol.* 34-6, (2006)
[108] B. L. a. A. Lowenberger, "Understanding Jitter Requirements of PLL-Based Processors Rev 1 ", *Analog Devices, Engineer-to-engineer note*, (January 20, 2005),
[109] C. Emmerich, "Introduction to Jitter", *Iowa State University, Department of Electrical and Computer Engineering*
(October 23), Online: *http://class.ee.iastate.edu/mmina/ee418/Notes/Introduction_to_Jitter.pdf*
[110] M. Zielinski, M. Kowalski, D. Chaberski and S. Grzelak, "Estimation of the Clock Signal Jitter Using the Time-Interval Measurement System", *Proc. of XVIII IMEKO World Congress Metrology for a Sustainable Development*, (2006)
[111] A. Hajimiri, S. Limotyrakis and T. H. Lee, "Jitter and phase noise in ring oscillators", *Solid-State Circuits, IEEE Journal of, Vol.* 34-6, pp. 790-804, (1999)
[112] M. Grozing and M. Berroth, "The Effect of 1/f Noise on the Spectrum and the Jitter of a Free Running Oscillator", *Research in Microelectronics and Electronics 2006*, pp. 485-488, (2006)
[113] M. R. Khanzadi, A. Panahi, D. Kuylenstierna and T. Eriksson, "A model-based analysis of phase jitter in RF oscillators", *Frequency Control Symposium (FCS), 2012 IEEE International*, pp. 1-4, (2012)
[114] D. Howe and T. Tasset, "Clock jitter estimation based on PM noise measurements", *ed. IEEE*. 541-546, (2003)
[115] R. Poore, "Phase Noise and Jitter", *Agilent*, Online: *http://www.keysight.com/upload/cmc_upload/All/phase_noise_and_jitter.pdf?&cc=FR&lc=fre*
[116] A. Zanchi, "How to Calculate the Period Jitter σT from the SSCR L(fn) with Application to Clock Sources for High-Speed ADCs", *Texas Instruments*, (December 2003), Online: *http://www.ti.com/lit/an/slwa028/slwa028.pdf*
[117] "Noise Modeling in MOSFET and Bipolar Devices", *Silvaco*, Online: *http://www.silvaco.com/content/kbase/noise_modeling.pdf*
[118] A. Chorti and M. Brookes, "A spectral model for RF oscillators with power-law phase noise", *Circuits and Systems I: Regular Papers, IEEE Transactions on, Vol.* 53-9, pp. 1989-1999, (2006)
[119] M. Mansuri and C.-K. Ken, "Jitter optimization based on phase-locked loop design parameters", *Solid-State Circuits, IEEE Journal of, Vol.* 37-11, pp. 1375-1382, (2002)
[120] M. J. Rossano, "Chapter 10: Perception of sounds", *Southeaster Louisiana University*, Online: *https://www2.southeastern.edu/Academics/Faculty/mrossano/perception/index.html*
[121] J. O. Pickles, "An introduction to the physiology of hearing", Vol. 2, *ed. Academic press London*. (1988)
[122] W. A. Yost, "Fundamentals of hearing: An introduction", *ed. Academic Press*. (1994)
[123] R. E. Turner, "An introduction to hearing", *University of Cambridge*, (2013), Online: *https://camtools.cam.ac.uk/access/content/group/d4fe6800-4ce2-4bad-8041-957510e5aaed/Public/3G3/RET/2013/hearing.pdf*
[124] P. A. Santi and P. Mancini, "Chapter 140: Cochlear Anatomy and Central Auditory Pathways", *Predrag M. Maksimović Web Site*, Online: *http://famona.tripod.com/ent/cummings/cumm140.pdf*
[125] Nicole, "Anatomy of the Ear", *Yournursingtutor.com*, (2012), Online: *http://www.yournursingtutor.com/ANATOMY-OF-THE-EAR/*
[126] P. W. Alberti, "The anatomy and physiology of the ear and hearing", *University of Toronto, Canada*, Online: *http://www.who.int/occupational_health/publications/noise2.pdf*
[127] J. Whittaker, "Physics of the ear, Comps II presentation", *John Hopkins University*, (2006),
[128] H. Kurokawa and R. L. Goode, "Sound pressure gain produced by the human middle ear"*, Vol.* 113 -4, pp. 349-355, (1995)
[129] J. P. Wilson and B. M. Bull, "Mechanics of middle and inner ear"*, Vol.* 43-4, pp. 821-837, (1987)

[130] J. E. Roeckelein, "Dictionary of theories, laws, and concepts in psychology", *ed. Greenwood Publishing Group*. (1998)
[131] B. H. J. Runsung Munkong, "Auditory perception and cognition", *IEEE SIGNAL PROCESSING MAGAZINE*, pp. 98-108, (2008)
[132] S. K. Griffiths, "Inner ear", *University of Florida, Department of Communication Sciences and Disorders*, (2010), Online: *http://web.clas.ufl.edu/users/sgriff/A&P.html*
[133] J. Tobias, "Foundations of modern auditory theory, Volume 1", *ed. Elsevier*. (2012)
[134] Kewley-Port, "S 319 Auditory system ", *Indiana University*, (2012), Online: *http://www.indiana.edu/~acoustic/*
[135] E. S. Olson, H. Duifhuis and C. R. Steele, "Von Békésy and cochlear mechanics", *Hearing research, Vol.* 293-1, pp. 31-43, (2012)
[136] J. Ashmore, P. Avan, W. Brownell, P. Dallos, K. Dierkes, R. Fettiplace, K. Grosh, C. Hackney, A. Hudspeth and F. Jülicher, "The remarkable cochlear amplifier", *Hearing research, Vol.* 266-1, pp. 1-17, (2010)
[137] C. A. M. Richard F. Lyon, "Cochlear hydrodynamics demystified", *Caltech-CS-TR-88-4*,
[138] C. Kubisch and e. al., "KCNQ4, a Novel Potassium Channel Expressed in Sensory Outer Hair Cells, Is Mutated in Dominant Deafness", *Cell, Vol.* 96-3, pp. 437–446, (5 February 1999)
[139] C. A. S. Stephen J Elliott, "The cochlea as a smart structure "*, Vol.* 21-6, (2012)
[140] D. D. Greenwood, "A cochlea frequency position function for several species – 29 years late"*, Vol.* 87-6, pp. 2592-2605, (1991)
[141] E. L. LePage, "The mammalian cochlear map is optimally warped", *The Journal of the Acoustical Society of America, Vol.* 114-2, pp. 896-906, (2003)
[142] M. Barclay, A. F. Ryan and G. D. Housley, "Type I vs type II spiral ganglion neurons exhibit differential survival and neuritogenesis during cochlear development", *Neural Dev, Vol.* 6-33, pp. 101-186, (2011)
[143] G. V. Békésy, "Experiments in Hearing, part 3. Chap 12-14". (1989)
[144] F. N. F. Mammano, "Biophysics of the cochlea: linear approximation"*, Vol.* 93-6, (June 1993)
[145] L. Trussel, "Mutant ion channel in cochlear hair cells"*, Vol.* 97-8, pp. 3786 –3788, (2000)
[146] B. A. H. a. R. M. O. Steven K. Juhn, "Blood-Labyrinth Barrier and Fluid Dynamics of the Inner Ear"*, Vol.* Vol. 7-nº 2, pp. 78-83, (Jul/ Dec de 2001)
[147] R. Yehoash and R. A. Altschuler, "Structure and innervation of the cochlea"*,* -60, pp. 397 - 422, (15 January 2003)
[148] M. F. Bear, "Neuroscience, Chapter 4, The Action Potential", *ed. Lippincott Williams & Wilkins*. (2007)
[149] "Essential Neuroscience, Section II The Neuron", *ed. Lippincott Williams & Wilkins*. (April 2010)
[150] R. Nobili, F. Mammano and J. Ashmore, "How well do we understand the cochlea?", *Trends in neurosciences, Vol.* 21-4, pp. 159-167, (1998)
[151] A. Saremi and S. Stenfelt, "A physiological signal-transmission model of cochlea", *Linkoping University*, Online: *https://www.liu.se/ihv/head/mobility/1.288026/Amin_poster_mechanics.pdf*
[152] S. J. Elliott and C. A. Shera, "The cochlea as a smart structure", *Smart Materials and Structures, Vol.* 21-6, pp. 064001, (2012)
[153] S. Ramamoorthy and A. L. Nuttall, "Outer hair cell somatic electromotility in vivo and power transfer to the organ of Corti", *Biophysical journal, Vol.* 102-3, pp. 388-398, (2012)
[154] J. A. Vernon and A. R. Møller, "A model for cochlear origin of subjective tinnitus: Excitatory drift in operating point of inner hair cells",in *Mechanisms of Tinnitus, Chapter 11*
ed. Jack A. Vernon, Aage R. Møller.
[155] P. Martin, "Negative hair-bundle stiffness betrays a mechanism for mechanical amplification by the hair cell", *Proceedings of the National Academy of Sciences, Vol.* 97-22, pp. 12026-12031, (2000)
[156] J. R. Cotton and J. W. Grant, "A finite element method for mechanical response of hair cell ciliary bundles", *Journal of biomechanical engineering, Vol.* 122-1, pp. 44-50, (2000)
[157] S. T. Smith, Chadwick, Richard S, "Simulation of the response of the inner hair cell stereocilia bundle to an acoustical stimulus", *PloS one, Vol.* 6-3, pp. e18161, (2011)
[158] R. Zelick, "Vertebrate Hair Cells", *Randy Zelick's laboratory at Portland State University*, Online: *http://web.pdx.edu/~zelickr/sensory-physiology/lecture-notes/OLDER/L12b-hair-cells.pdf*
[159] A. W. Peng, F. T. Salles, B. Pan and A. J. Ricci, "Integrating the biophysical and molecular mechanisms of auditory hair cell mechanotransduction", *Nature communications, Vol.* 2, pp. 523, (2011)

[160] J. R. Ison, "Auditory Nerve I, Innervation of the Cochlea, Frequency and Level Coding", *University of Rochester, Brain and Cognitive Sciences*, (1999), Online: *http://www.bcs.rochester.edu/courses/crsinf/221/ARCHIVES/S11/Auditory_Nerve1.pdf*
[161] R. Fettiplace and C. M. Hackney, "The sensory and motor roles of auditory hair cells", *Nature Reviews Neuroscience, Vol.* 7-1, pp. 19-29, (2006)
[162] H. Cai, B. Shoelson and R. S. Chadwick, "Evidence of tectorial membrane radial motion in a propagating mode of a complex cochlear model", *Proceedings of the National Academy of Sciences of the United States of America, Vol.* 101-16, pp. 6243-6248, (2004)
[163] K. G. a. N. Deo, "Mechanical-electrical-acoustical modeling of the cochlea", *Institute of Pure and Apllied Mathematics*, (2005), Online: *www.ipam.ucla.edu/publications/.../es2005_5406.ppt*
[164] R. F. Lyon and C. A. Mead, "Cochlear Hydrodynamics demystified
", *Department of Computer Sciences, California Institute of Technology*, (1989)
[165] K. L. Tsang, "Determination of effective masses and parametric study of the organ of Corti", (2012), Online: *http://www.rochester.edu/college/kearnscenter/pdf/Xerox_2013/Ka_Lai_Tsang.pdf*
[166] T. Kato, S. Omachi and H. Aso, "Asymmetric gaussian and its application to pattern recognition",in *Structural, Syntactic, and Statistical Pattern Recognition*, *ed. Springer*. 405-413, (2002)
[167] F. Chen, D. Zha, A. Fridberger, J. Zheng, N. Choudhury, S. L. Jacques, R. K. Wang, X. Shi and A. L. Nuttall, "A differentially amplified motion in the ear for near-threshold sound detection", *Nature neuroscience, Vol.* 14-6, pp. 770-774, (2011)
[168] D. Zha, F. Chen, S. Ramamoorthy, A. Fridberger, N. Choudhury, S. L. Jacques, R. K. Wang and A. L. Nuttall, "In vivo outer hair cell length changes expose the active process in the cochlea", *PloS one, Vol.* 7-4, pp. e32757, (2012)
[169] C. Q. Davis and D. M. Freeman, "Direct observations of sound-induced motions of the reticular lamina, tectorial membrane, hair bundles, and individual stereocilia", *Department of Physiology at the University of Wisconsin - Madison*, (1995), Online: *http://www.neurophys.wisc.edu/auditory/qdavis/talk.html*
[170] S. T. Smith and R. S. Chadwick, "Simulation of the response of the inner hair cell stereocilia bundle to an acoustical stimulus", *PloS one, Vol.* 6-3, pp. e18161, (2011)
[171] A. Pierre, "Cours de Trigonométrie", *ed. Éditions Aurélien PIERRE*. (2013)
[172] A. Jilkine and K. Leiderman, "Modeling Length Regulation of Stereocilia", *Park City Mathematics Institute*, (2005), Online: *pcmi.ias.edu/2005/documents/K2.ppt*
[173] A. Fridberger, I. Tomo, M. Ulfendahl and J. B. de Monvel, "Imaging hair cell transduction at the speed of sound: dynamic behavior of mammalian stereocilia", *Proceedings of the National Academy of Sciences of the United States of America, Vol.* 103-6, pp. 1918-1923, (2006)
[174] K. Grosh and N. Deo, "Mechanical-electrical-acoustical modeling of the cochlea", *Institute of Pure and Apllied Mathematics*, (2005), Online: *www.ipam.ucla.edu/publications/.../es2005_5406.ppt*
[175] Y.-W. Liu and S. T. Neely, "Outer hair cell electromechanical properties in a nonlinear piezoelectric model", *The Journal of the Acoustical Society of America, Vol.* 126, pp. 751, (2009)
[176] D. Purves, G. Augustine, D. Fitzpatrick and e. al., "Hair Cells and the Mechanoelectrical Transduction of Sound Waves",in *Neuroscience. 2nd edition*, *ed. http://www.ncbi.nlm.nih.gov/books/NBK10867/*. (2001)
[177] C. M. Hackney and D. N. Furness, "Mechanotransduction in vertebrate hair cells: structure and function of the stereociliary bundle", *American Journal of Physiology-Cell Physiology, Vol.* 268-1, pp. C1-C13, (1995)
[178] J. L. Fitzakerley, "Stereocilia tiplinks & transduction channels, Inner Ear Physiology ", *University of Minnesota Duluth*, (2013), Online: *http://www.d.umn.edu/~jfitzake/Lectures/DMED/InnerEar/Transduction/TipLinks.html*
[179] P. Fuchs, "Hair Cell Mechanotransduction - Neurobiology of Hearing, Neurobiology of Hearing MEDS 5377", *UConn health Center*, (2011), Online: *http://neurobiologyhearing.uchc.edu/Course_Content_Library/Auditory_Periphery/Fuchs%20Salamanca2%20handout.pdf*
[180] J. Zheng, W. Shen, D. Z. He, K. B. Long, L. D. Madison and P. Dallos, "Prestin is the motor protein of cochlear outer hair cells", *Nature, Vol.* 405-6783, pp. 149-155, (2000)
[181] P. Brodal, "The central nervous system: structure and function", *ed. Oxford University Press*. (2004)

[182] F. Lang, V. Vallon, M. Knipper and P. Wangemann, "Functional significance of channels and transporters expressed in the inner ear and kidney", *American Journal of Physiology-Cell Physiology, Vol.* 293-4, pp. C1187-C1208, (2007)
[183] Y. Raphael and R. A. Altschuler, "Structure and innervation of the cochlea", *Brain research bulletin, Vol.* 60-5, pp. 397-422, (2003)
[184] F. Mammano, M. Bortolozzi, S. Ortolano and F. Anselmi, "Ca2+ signaling in the inner ear", *Physiology, Vol.* 22-2, pp. 131-144, (2007)
[185] L. A. Werner, "The auditory nerve response", *Introduction to Hearing Science*, Online: *http://depts.washington.edu/*
[186] C. Darwin, "Ear and Auditory Nerve", *Hearing Lecture Notes (2)*, (1994), Online: *http://www.lifesci.sussex.ac.uk/*
[187] D. B. Koch and E. H. Overstreet, "Neural Response Imaging: Measuring Auditory-Nerve Responses from the Cochlea with the HiResolution™ Bionic Ear System",
[188] C. J. Sumner, E. A. Lopez-Poveda, L. P. O'Mard and R. Meddis, "A revised model of the inner-hair cell and auditory-nerve complex", *The Journal of the Acoustical Society of America, Vol.* 111, pp. 2178, (2002)
[189] R. Dingledine, K. Borges, D. Bowie and S. F. Traynelis, "The glutamate receptor ion channels", *Pharmacological reviews, Vol.* 51-1, pp. 7-62, (1999)
[190] O. A. Petroff, "Book Review: GABA and glutamate in the human brain", *The Neuroscientist, Vol.* 8-6, pp. 562-573, (2002)
[191] S. G. Tewari and K. K. Majumdar, "A mathematical model of the tripartite synapse: astrocyte-induced synaptic plasticity", *Journal of biological physics, Vol.* 38-3, pp. 465-496, (2012)
[192] R. Jolivet, T. J. Lewis and W. Gerstner, "Generalized integrate-and-fire models of neuronal activity approximate spike trains of a detailed model to a high degree of accuracy", *Journal of Neurophysiology, Vol.* 92-2, pp. 959-976, (2004)
[193] A. Destexhe, Z. F. Mainen and T. J. Sejnowski, "Synthesis of models for excitable membranes, synaptic transmission and neuromodulation using a common kinetic formalism", *Journal of computational neuroscience, Vol.* 1-3, pp. 195-230, (1994)
[194] H. von Gersdorff, "Synaptic ribbons: versatile signal transducers", *Neuron, Vol.* 29-1, pp. 7-10, (2001)
[195] E. Glowatzki, L. Grant and P. Fuchs, "Hair cell afferent synapses", *Current opinion in neurobiology, Vol.* 18-4, pp. 389-395, (2008)
[196] D. Lenzi and H. von Gersdorff, "Structure suggests function: the case for synaptic ribbons as exocytotic nanomachines", *Bioessays, Vol.* 23-9, pp. 831-840, (2001)
[197] E. Glowatzki, "The Auditory Periphery 4 – Afferent synaptic transmission by cochlear hair cells Structure and Function", *Johns Hopkins School of Medicine*, (2011), Online: *http://pages.jh.edu/~strucfunc/strucfunc/2011_files/2011_09_13.pdf*
[198] L. D. Liberman, H. Wang and M. C. Liberman, "Opposing gradients of ribbon size and AMPA receptor expression underlie sensitivity differences among cochlear-nerve/hair-cell synapses", *The Journal of Neuroscience, Vol.* 31-3, pp. 801-808, (2011)
[199] T. Moser, "The hair cell ribbon synapse", *Ludwig Maximilians Universitat Munchen*, Online: *http://www.bio.lmu.de/~benda/teaching/mnsws07/Moser-RibbonSynapse.pdf*
[200] P. Sterling and G. Matthews, "Structure and function of ribbon synapses", *Trends in neurosciences, Vol.* 28-1, pp. 20-29, (2005)
[201] L. Grant, E. Yi and E. Glowatzki, "Two modes of release shape the postsynaptic response at the inner hair cell ribbon synapse", *The Journal of Neuroscience, Vol.* 30-12, pp. 4210-4220, (2010)
[202] T. Parsons and P. Sterling, "Synaptic ribbon: conveyor belt or safety belt?", *Neuron, Vol.* 37-3, pp. 379-382, (2003)
[203] M. H. Hennig, "Modeling Synaptic Transmission", *ANC, Informatics, University of Edinburgh*,
[204] A. R. Sargsyan, A. A. Melkonyan, C. Papatheodoropoulos, H. H. Mkrtchian and G. K. Kostopoulos, "A model synapse that incorporates the properties of short-and long-term synaptic plasticity", *Neural networks, Vol.* 16-8, pp. 1161-1177, (2003)
[205] C. Koch and I. Segev, "Methods in neuronal modeling: from synapses to networks", *ed. The MIT Press*. (1998)

[206] S. H. Koslow, S. Subramaniam and S. Subramaniam, "Databasing the Brain: From Data to Knowledge (Neuroinformatics)", *ed. Wiley-Liss*. (2005)
[207] R. Veltz and O. Faugeras, "Introduction to the biology of synapses", *INRIA*, (2013), Online: *http://www-sop.inria.fr/members/Olivier.Faugeras/MVA/Slides13/lecture5.pdf*
[208] A. Roth and M. C. van Rossum, "Modeling Synapses", *University of Edinburgh, School of Informatics*, (2009), Online: *http://homepages.inf.ed.ac.uk/mvanross/reprints/roth_mvr_chap.pdf*
[209] T. Yu and G. Cauwenberghs, "Biophysical synaptic dynamics in an analog VLSI network of Hodgkin-Huxley neurons", *Engineering in Medicine and Biology Society, 2009. EMBC 2009. Annual International Conference of the IEEE*, pp. 3335-3338, (2009)
[210] M. Xiao, M. Karpefors, B. Gustafsson and H. Wigstrom, "On the linkage between AMPA and NMDA receptor-mediated EPSPs in homosynaptic long-term depression in the hippocampal CA1 region of young rats", *The Journal of Neuroscience, Vol.* 15-6, pp. 4496-4506, (1995)
[211] J. Ruel, C. Chen, R. Pujol, R. P. Bobbin and J.-L. Puel, "AMPA-preferring glutamate receptors in cochlear physiology of adult guinea-pig", *The Journal of Physiology, Vol.* 518-3, pp. 667-680, (1999)
[212] J.-H. Cho, I. T. Bayazitov, E. G. Meloni, K. M. Myers, W. A. Carlezon Jr, S. S. Zakharenko and V. Y. Bolshakov, "Coactivation of thalamic and cortical pathways induces input timing-dependent plasticity in amygdala", *Nature neuroscience, Vol.* 15-1, pp. 113-122, (2012)
[213] D. F. de Sevilla, M. Fuenzalida, A. B. P. Pazos and W. Buño, "Selective shunting of the NMDA EPSP component by the slow afterhyperpolarization in rat CA1 pyramidal neurons", *Journal of Neurophysiology, Vol.* 97-5, pp. 3242-3255, (2007)
[214] M. A. Sikora, J. Gottesman and R. F. Miller, "A computational model of the ribbon synapse", *Journal of neuroscience methods, Vol.* 145-1, pp. 47-61, (2005)
[215] R. Rao-Mirotznik, G. Buchsbaum and P. Sterling, "Transmitter concentration at a three-dimensional synapse", *Journal of Neurophysiology, Vol.* 80-6, pp. 3163-3172, (1998)
[216] A. Borisyuk and e. al., "Modeling Synaptic Plasticity", *Mathematical Biosciences Institute*, (2004),
[217] N. Shepard, "Integrate and Fire Model", *www.nathanshepard.net*, (2007), Online: *http://www.nathanshepard.net/documents/Integrate_and_Fire_Model.pdf*
[218] R. Vandiver, "Hodgkin-Huxley Model of Action Potentials", *Bryn Mawer College*, (201O), Online: *http://www.brynmawr.edu/math/people/vandiver/documents/HodgkinHuxley.pdf*
[219] J. Selgrade, "Hodgkin-Huxley and Fitzhugh-Nagumo Models", *North Carolina State University*, (2005), Online: *http://www.phaser.com/modules/maa05/h-h_model.ppt%E2%80%8E*
[220] F. Fröhlich and S. Jezernik, "Feedback control of Hodgkin–Huxley nerve cell dynamics", *Control engineering practice, Vol.* 13-9, pp. 1195-1206, (2005)
[221] "From Hodgkin-Huxley to Integrate-and-Fire", *University of Paris V, Laboratory of Neurophysics and Physiology*, (2011), Online: *http://neurophys.biomedicale.univ-paris5.fr/~brunel/tutorial.pdf*
[222] W. Heitler, "The Hodgkin-Huxley Model for the Generation of Action Potentials", *School of Biology, University of St Andrews*, Online: *http://www.st-andrews.ac.uk/~wjh/hh_model_intro/*
[223] D. Zhou, D. Cai, S. Li and Y. Xiao, "Mathematical Modeling of Biological Neurons", (2012)
[224] M. Chung, B. Göbel, A. Peters, K. M. Oltmanns and A. Moser, "Mathematical modeling of the biphasic dopaminergic response to glucose", *Journal Biomedical Science Engineering, Vol.* 4, pp. 36-145, (2011)
[225] N. S. Imennov and J. T. Rubinstein, "Stochastic population model for electrical stimulation of the auditory nerve", *Biomedical Engineering, IEEE Transactions on, Vol.* 56-10, pp. 2493-2501, (2009)
[226] "Topic 11: Nerve Conduction", *Centenary College of Luisiana*, Online: *http://www.centenary.edu/attachments/biophysics/bphy304/11a.pdf*
[227] Y. J and W. JB, "Morphological observation and electrophysiological properties of isolated Deiters' cells from guinea pig cochlea"*, Vol.* 14-1, pp. 29-31, (2000)
[228] T. Fujikawa, R. S. Petralia, T. S. Fitzgerald, Y.-X. Wang, B. Millis, J. A. Morgado-Díaz, K. Kitamura and B. Kachar, "Localization of kainate receptors in inner and outer hair cell synapses", *Hearing research, Vol.* 314, pp. 20-32, (2014)
[229] J. Ruel, C. Chabbert, R. Nouvian, R. Bendris, M. Eybalin, C. L. Leger, J. Bourien, M. Mersel and J.-L. Puel, "Salicylate enables cochlear arachidonic-acid-sensitive NMDA receptor responses", *The Journal of Neuroscience, Vol.* 28-29, pp. 7313-7323, (2008)

[230] B. Peng, Q. Li, T. Ren, S. Ahmad, S. Chen, P. Chen and X. Lin, "Group I metabotropic glutamate receptors in spiral ganglion neurons contribute to excitatory neurotransmissions in the cochlea", *Neuroscience, Vol.* 123-1, pp. 221-230, (2004)
[231] G. Burnstock and A. N. Verkhratskiĭ, "Purinergic signalling and the nervous system", *ed. Springer*. (2012)
[232] E. Oestreicher, W. Arnold and D. Felix, "Neurotransmission of the cochlear inner hair cell synapse-implications for inner ear therapy", (2004)
[233] T. Honoré, J. Lauridsen and P. Krogsgaard-Larsen, "The binding of [3H] AMPA, a structural analogue of glutamic acid, to rat brain membranes", *Journal of neurochemistry, Vol.* 38-1, pp. 173-178, (1982)
[234] S. R. Platt, "The role of glutamate in central nervous system health and disease–a review", *The Veterinary Journal, Vol.* 173-2, pp. 278-286, (2007)
[235] C. Rosenmund, Y. Stern-Bach and C. F. Stevens, "The tetrameric structure of a glutamate receptor channel", *Science, Vol.* 280-5369, pp. 1596-1599, (1998)
[236] T. Otis, I. Raman and L. Trussell, "AMPA receptors with high Ca2+ permeability mediate synaptic transmission in the avian auditory pathway", *The Journal of Physiology, Vol.* 482-Part 2, pp. 309-315, (1995)
[237] A. Destexhe, Z. F. Mainen and T. J. Sejnowski, "Fast kinetic models for simulating AMPA, NMDA, GABA A and GABA B receptors",in *The Neurobiology of Computation*, *ed. Springer*. 9-14, (1995)
[238] C. S. a. Engineering, "Modeling single neurons", *University of Washingthon*, (2013), Online: *http://courses.cs.washington.edu/courses/cse528/05wi/Lect5.pdf*
[239] E. Yi, I. Roux and E. Glowatzki, "Dendritic HCN channels shape excitatory postsynaptic potentials at the inner hair cell afferent synapse in the mammalian cochlea", *Journal of Neurophysiology, Vol.* 103-5, pp. 2532-2543, (2010)
[240] E. Glowatzki and P. A. Fuchs, "Transmitter release at the hair cell ribbon synapse", *Nature neuroscience, Vol.* 5-2, pp. 147-154, (2002)
[241] L. Grant, E. Yi, J. D. Goutman and E. Glowatzki, "Postsynaptic recordings at afferent dendrites contacting cochlear inner hair cells: monitoring multivesicular release at a ribbon synapse", *Journal of visualized experiments: JoVE,* -48, (2011)
[242] A. I. S. Darwish, "Central and Peripheral N-methyl-D-aspartate (NMDA) Receptors: Sites, Actions, Modulators and Possible Clinical Applications", (2009)
[243] D. C. Cooper, "Introduction to neuroscience I", *ed. Donald C. Cooper Ph. D.*, (2011)
[244] S. Coombes, "Synapses", *The University of Nottingham Department of Mathematical Sciences B12412: Computational Neuroscience and Neuroinformatics*, Online: *https://www.maths.nottingham.ac.uk/personal/sc/cnn/CNN6ToDo.pdf*
[245] S. S. Kumar and J. R. Huguenard, "Properties of excitatory synaptic connections mediated by the corpus callosum in the developing rat neocortex", *Journal of Neurophysiology, Vol.* 86-6, pp. 2973-2985, (2001)
[246] R. Jonsson, "Field interactions in the peripheral auditory neural system with reference to cochlear implants", *University of Pretoria, Electrical, Electronic and Computer Engineering*, (2011),
[247] A. F. Jahn and J. Santos-Sacchi, "Physiology of the Ear", *ed. Cengage Learning*. (2001)
[248] J. C. Fiala, S. Grossberg and D. Bullock, "Metabotropic glutamate receptor activation in cerebellar Purkinje cells as substrate for adaptive timing of the classically conditioned eye-blink response", *The Journal of Neuroscience, Vol.* 16-11, pp. 3760-3774, (1996)
[249] M. Masugi-Tokita, E. Tarusawa, M. Watanabe, E. Molnár, K. Fujimoto and R. Shigemoto, "Number and density of AMPA receptors in individual synapses in the rat cerebellum as revealed by SDS-digested freeze-fracture replica labeling", *The Journal of Neuroscience, Vol.* 27-8, pp. 2135-2144, (2007)
[250] Z. Nusser, R. Lujan, G. Laube, J. D. B. Roberts, E. Molnar and P. Somogyi, "Cell type and pathway dependence of synaptic AMPA receptor number and variability in the hippocampus", *Neuron, Vol.* 21-3, pp. 545-559, (1998)
[251] L. O. Trussell, A. N. Popper and R. R. Fay, "Synaptic Mechanisms in the Auditory System", *ed. Springer*. (2012)
[252] S. F. Traynelis and F. Jaramillo, "Getting the most out of noise in the central nervous system", *Trends in neurosciences, Vol.* 21-4, pp. 137-145, (1998)

[253] L. Abbott, "Realistic synaptic inputs for model neural networks", *Network: Computation in Neural Systems, Vol.* 2-3, pp. 245-258, (1991)
[254] D. Purves, G. Augustine, D. Fitzpatrick and e. al., "Neuroscience: The Ionic Basis of the Resting Membrane Potential", *ed. Sinauer Associates, Sunderland (MA)*. (2001)
[255] J. Koester and S. A. Siegelbaum, "Membrane Potential", *http://www.bioltis.fmed.edu.uy/*,
[256] R. Rhoades and D. R. Bell, "Medical Physiology: Principles of Clinical Medicine, Chapter 3: Action Potential, Synaptic Transmission, and Maintenance of Nerve Function", *ed. Lippincott Willams and Wilkins*. *C. Forehand*,
[257] V. Weerasinghe, "Excitable Tissues, Resting Membrane Potential & Action Potential", *Faculty of Medicine, University of Peradenyia*,
[258] "Ionic Basis of Action Potentials", *Medical University of South California (MUSC), Woodward Lab: Department of Neurosciences*,
[259] L. H, Berk A, Z. SL and e. al., "The Action Potential and Conduction of Electric Impulses",in *Molecular Cell Biology*, Vol. Section 21.2. *http://www.ncbi.nlm.nih.gov/books/NBK21668/*, (2000)
[260] M. F. Bear, B. W. Connors and M. A. Paradiso, "Neuroscience: Exploring the Brain plus CD Rom Testbank", *Neuroscience research*, (2000)
[261] N. Yang, R. Kondo, J. Dolzer and D. Yamane, "Analysis Of The Biophysical Properties Of Sodium Channel Na", *moleculardevices.com*,
[262] M. D. Mann, "Properties of excitable cell membranes: the spike", (2013), Online: *http://michaeldmann.net/mann3b.html*
[263] C. J. Forehand, "The action potential, synaptic transmission, and maintenance of nerve function", *Medical Physiology: Principles for Clinical Medicine, Rhoades RA, Bell DR, eds., Lippincott Williams & Wilkins, a Wolters Kluwer business, Philadelphia, USA*, pp. 38-64, (2009)
[264] B. Alberts, "Essential cell biology: an introduction to the molecular biology of the cell", Vol. 1, *ed. Taylor & Francis*. (1998)
[265] B. Alberts, A. Johnson, J. Lewis, M. Raff, K. Roberts and P. Walter, "Ion Channels and the Electrical Properties of Membranes", (2002)
[266] N. Al-Shorbaji, "Health and medical informatics", *World Health Organisation, Cairo*, (2001)
[267] C. Koch, "Biophysics of Computation: Information Processing in Single Neurons (Computational Neuroscience)", Vol. Chapter 2: Linear Cable theory. (1999)
[268] E. Young, "Models of the Neuron (580.439/639)", *John Hopkins University*, (Fall 2013), Online: *http://www.jhu.edu/motn/*
[269] F. Rieke, "Action potential propagation", *University of Washington*, Online: *http://rieke-server.physiol.washington.edu/People/Fred/Classes/532/HH408.pdf*
[270] E. Young, "Lecture 9, Nonlinear cable theory in *Systems Biology II: Neural Systems (580.422)*", (2006), Online: *http://www.shadmehrlab.org/Courses/physfound_files/Eric_5.pdf*
[271] E. Young, "Systems Biology II: Neural Systems (580.422), Lecture 9, Nonlinear cable theory", Online: *http://www.shadmehrlab.org/Courses/physfound_files/Eric_5.pdf*
[272] R. Rhoades and D. R. Bell, "Medical Physiology: Principles of Clinical Medicine", Vol. Chapter 3: Action Potential, Synaptic Transmission, and Maintenance of Nerve Function, C. Forehand, *ed. Lippincott Willams and Wilkins*.
[273] D. Mittleman, "Waves and the wave equation", *ECE Department at Rice University*,
[274] "Auditory Nerve Processing", *University of Rochester, Brain and Cognitive Sciences*, (2013), Online: *http://www.bcs.rochester.edu/courses/crsinf/504/ARCHIVES/F05/audition2.pdf*
[275] Tschang, "Chapter 34 Maxwell's Equations, Electromagnetic Waves", *Department of Physics at National Tsing Hua University* Online: *http://www.phys.nthu.edu.tw/~thschang/notes/GP34.pdf*
[276] Orfanidi, "Maxwell' s equations", *Information, Networks, and Signal Processing Research (INSPIRE) Lab*, Online: *http://www.ece.rutgers.edu/~orfanidi/ewa/ch01.pdf*
[277] W. F. Boron and E. L. Boulpaep, "Medical Physiology, 2e Updated Edition: with STUDENT CONSULT Online Access", *ed. Elsevier Health Sciences*. (2012)
[278] S. Kim, S. J. Guzman, H. Hu and P. Jonas, "Active dendrites support efficient initiation of dendritic spikes in hippocampal CA3 pyramidal neurons", *Nature neuroscience, Vol.* 15-4, pp. 600-606, (2012)

[279] B. Sivyer and S. R. Williams, "Direction selectivity is computed by active dendritic integration in retinal ganglion cells", *Nature neuroscience, Vol.* 16-12, pp. 1848-1856, (2013)
[280] A. Destexhe, "High-conductance state", *Scholarpedia, 2(11):1341*, (2007),
[281] X. Chen and S. Kiaei, "Monocycle shapes for ultra wideband system", *Circuits and Systems, 2002. ISCAS 2002. IEEE International Symposium on, Vol.* 1, pp. I-597-I-600, (2002)
[282] Y. Yeap, "Ultra wideband signal generation", *Microwave Journal, Vol.* 48-9, pp. 172, (2005)
[283] M. Dhieb, M. Lahiani and H. Ghariani, "Pulse generator monocycle Gaussian for UWB applications", *WSEAS Transactions on Circuits and Systems, Vol.* 9-12, pp. 756-766, (2010)
[284] G. J. Goodhill, "A theoretical model of axon guidance by the robo code", *Neural computation, Vol.* 15-3, pp. 549-564, (2003)
[285] X. Wang, "Neural representation of Sensory Stimuli: Properties of Spike Trains", *Biosystem II: Neuroscience*, Online: *http://www.shadmehrlab.org/*
[286] L. A. Werner, "inner ear anatomy", *Introduction to Hearing Science*, Online: *http://depts.washington.edu/*
[287] P. Dayan, L. F. Abbott and L. Abbott, "Theoretical neuroscience: Computational and mathematical modeling of neural systems", (2001)
[288] C. Pouzat, "Extracellular Recording and Spike Train Analysis", *CNRS UMR 8118 and Paris-Descartes University Paris*, (2009), Online: *http://www.biomedicale.univ-paris5.fr/SpikeOMatic/Papers_folder/Pouzat_ENP_2009.pdf*
[289] J. Laudanski, S. Coombes, A. R. Palmer and C. J. Sumner, "Mode-locked spike trains in responses of ventral cochlear nucleus chopper and onset neurons to periodic stimuli", *Journal of Neurophysiology, Vol.* 103-3, pp. 1226-1237, (2010)
[290] N. X. Tritsch, A. Rodríguez-Contreras, T. T. Crins, H. C. Wang, J. G. G. Borst and D. E. Bergles, "Calcium action potentials in hair cells pattern auditory neuron activity before hearing onset", *Nature neuroscience, Vol.* 13-9, pp. 1050-1052, (2010)
[291] I. C. Bruce, "Spatiotemporal coding of sound in the auditory nerve for cochlear implants", *ed. University of Melbourne, Department of Otolaryngology*. (1998)
[292] T. Hromádka, "Representation of Sounds in Auditory Cortex of Awake Rats", *Cold Spring Harbor Laboratory*, (2008),
[293] E. Zalewska and I. Hausmanowa-Petrusewicz, "Approximation of motor unit structure from the analysis of motor unit potential", *Clinical Neurophysiology, Vol.* 119-11, pp. 2501-2506, (2008)
[294] M. S. Lewicki, "A review of methods for spike sorting: the detection and classification of neural action potentials", *Network: Computation in Neural Systems, Vol.* 9-4, pp. R53-R78, (1998)
[295] J. S. Pezaris, M. Sahani and R. A. Andersen, "Tetrodes for monkeys",in *Computational Neuroscience*, *ed. Springer*. 937-942, (1997)
[296] M. Laubach, M. Shuler and M. A. Nicolelis, "Independent component analyses for quantifying neuronal ensemble interactions", *Journal of neuroscience methods, Vol.* 94-1, pp. 141-154, (1999)
[297] C. Savin, P. Joshi and J. Triesch, "Independent component analysis in spiking neurons", *PLoS computational biology, Vol.* 6-4, pp. e1000757, (2010)
[298] S. Takahashi, Y. Anzai and Y. Sakurai, "A new approach to spike sorting for multi-neuronal activities recorded with a tetrode—how ICA can be practical", *Neuroscience research, Vol.* 46-3, pp. 265-272, (2003)
[299] S. Takahashi, Y. Anzai and Y. Sakurai, "Automatic sorting for multi-neuronal activity recorded with tetrodes in the presence of overlapping spikes", *Journal of Neurophysiology, Vol.* 89-4, pp. 2245-2258, (2003)
[300] E. Hulata, R. Segev and E. Ben-Jacob, "A method for spike sorting and detection based on wavelet packets and Shannon's mutual information", *Journal of neuroscience methods, Vol.* 117-1, pp. 1-12, (2002)
[301] W. Gerstner and W. M. Kistler, "Spiking neuron models: Single neurons, populations, plasticity", *ed. Cambridge university press*. (2002)
[302] M. N. Shadlen and W. T. Newsome, "Noise, neural codes and cortical organization", *Current opinion in neurobiology, Vol.* 4-4, pp. 569-579, (1994)
[303] J. Rinzel, "Computational Modeling of Neuronal Systems (Advanced Topics in Mathematical Physiology)", *The Center for Neural Science at New York State University*, Online: *http://www.cns.nyu.edu/~rinzel/CMNSF07/Neuronal%20dyns%20cell_CMNSF07.pdf*

[304] "Nerve Conduction", *Centenary College of Louisiana*, Online: *http://www.centenary.edu/attachments/biophysics/bphy304/11a.pdf*
[305] A.-M. Systems, "Tungsten electrodes", (2014), Online: *http://www.a-msystems.com/s-70-tungsten.aspx*
[306] L. M. Ward and P. E. Greenwood, "1/f noise", *Scholarpedia, Vol.* 2-12, pp. 1537, (2007)
[307] A. Longtin, "Neuronal noise", *Scholarpedia, Vol.* 8-9, pp. 1618, (2013)
[308] J. A. White, J. T. Rubinstein and A. R. Kay, "Channel noise in neurons", *Trends in neurosciences, Vol.* 23-3, pp. 131-137, (2000)
[309] M. Kearns, S. Solla and D. Cohn, "Advances in Neural Information Processing Systems 10", *Cambridge, MA*, (1999)
[310] S. Roy, "The role of noise in living systems", *Universita degli studi di Palermo*, Online: *http://www.unipa.it/daa_erice11/DAA2011_Conference/Speakers_files/Roy.pdf*
[311] T. Markl, "1/f noise, telegraph noise", *Karlsruher Institut für Technologie*, Online: *http://www.phi.kit.edu/noise/abbildungen/Noise-03_Non-Thermal_Noise_1_over_f_Noise.pdf*
[312] A. Destexhe and M. Rudolph-Lilith, "Neuronal noise", Vol. 8, *ed. Springer*. (2012)
[313] H. Feldwisch-Drentrup, A. B. Barrett, M. T. Smith and M. C. van Rossum, "Fluctuations in the open time of synaptic channels: An application to noise analysis based on charge", *Journal of neuroscience methods, Vol.* 210-1, pp. 15-21, (2012)
[314] D. A. Stanley, "Synaptic Noise-Like Activity in Hippocampal Interneurons", *University of Toronto*, (2009),
[315] B. Delgutte, "Auditory Nerve Laboratory: What was the Stimulus?", *Massachusetts Institute of Technology* Online: *web.mit.edu/hst.723/www/Labs/ANF%20Lab.ppt*
[316] D. Johnson and N. Kiang, "Analysis of discharges recorded simultaneously from pairs of auditory nerve fibers", *Biophysical journal, Vol.* 16-7, pp. 719-734, (1976)
[317] B. L. Tempel, "The auditory system", *Washington University*,
[318] A. R. Palmer, "The basic physiology of the auditory nerve ", *MRC Institute of Hearing Research, University of Nottingham*, Online: *http://neurobiologyhearing.uchc.edu/Course_Content_Library/Auditory_nerve/PALMER%20Auditory%20Nerve%20Physiology-ARP.pdf*
[319] A. M. Simmons, J. J. Schwartz and M. Ferragamo, "Auditory nerve representation of a complex communication sound in background noise", *The Journal of the Acoustical Society of America, Vol.* 91-5, pp. 2831-2844, (1992)
[320] I. Fukui, T. Sato and H. Ohmori, "Improvement of phase information at low sound frequency in nucleus magnocellularis of the chicken", *Journal of Neurophysiology, Vol.* 96-2, pp. 633-641, (2006)
[321] R. Roeser and M. Valente, "Audiology diagnosis", *ed. Thieme*. (2007)
[322] E. R. Kandel, J. H. Schwartz and T. M. Jessell, "Principles of neural science", Vol. 4, *ed. McGraw-Hill New York*. (2000)
[323] P. Revest, "Neuroscience Methods: A Guide for Advanced Students", *ed. Elsevier*. (1998)
[324] D. C. Johnson and W. R. LaCourse, "Liquid chromatography with pulsed electrochemical detection at gold and platinum electrodes", *Analytical Chemistry, Vol.* 62-10, pp. 589A-597A, (1990)
[325] "Electrophysiology", *wikipedia.org*, (2014), Online: *http://en.wikipedia.org/wiki/Electrophysiology*
[326] B. Singhal, "Drug Analysis: A Perspective of Potentiometric Sensors", *World Journal of Chemistry, Vol.* 6-2, pp. 59-74, (2011)
[327] R. v. Rohr, "Cochlear Implant Impedance Telemetry Measurements and Model Calculations to Estimate Modiolar Currents", *Swiss Federal Institute of Technology Zurich*, (2011),
[328] N. Dillier, W. K. Lai, B. Almqvist, C. Frohne, J. Muller-Deile, M. Stecker and E. Von Wallenberg, "Measurement of the electrically evoked compound action potential via a neural response telemetry system", *Annals of Otology Rhinology and Laryngology, Vol.* 111-5, Part 1, pp. 407-414, (2002)
[329] J. Mitchell, "Conduction/Synapse, Chapter 4, Neurophysiology II courses", *University of Vermont*, Online: *http://www.uvm.edu/~biology/Classes/255/Lab3.pdf*
[330] J. M. Simone Helluy, Jocelyne Dolce, Emily A. Buchholtz, "Lab 9: Conduction Velocity of Nerves in *BISC 111/113: Introductory Organismal Biology*", *OpenWetWare*, (July 2012), Online: *http://openwetware.org/wiki/Lab_9:_Conduction_Velocity_of_Nerves*

[331] Y.-A. Song, R. Melik, A. N. Rabie, A. M. Ibrahim, D. Moses, A. Tan, J. Han and S. J. Lin, "Electrochemical activation and inhibition of neuromuscular systems through modulation of ion concentrations with ion-selective membranes", *Nature Materials, Vol.* 10-12, pp. 980-986, (2011)
[332] F.-G. Zeng, S. Rebscher, W. Harrison, X. Sun and H. Feng, "Cochlear implants: system design, integration, and evaluation", *Biomedical Engineering, IEEE Reviews in, Vol.* 1, pp. 115-142, (2008)
[333] N. S. Lawand, J. van Driel and P. French, "Electric Field Density Distribution for Cochlear Implant Electrodes", *COMSOL Conference*, (2012)
[334] A. Komal, R. Dowell and P. Dawson, "Cochlear Implant Stimulation Rates and Speech Perception", (2012)
[335] B. Somek, S. Fajt, A. Dembitz, M. Ivković and J. Ostojić, "Coding strategies for cochlear implants", *AUTOMATIKA: časopis za automatiku, mjerenje, elektroniku, računarstvo i komunikacije, Vol.* 47-1-2, pp. 69-74, (2006)
[336] "Cochlear implant simulation", *University of Canada*, (2006), Online: *http://www.ugr.es/~atv/web_ci_SIM/en/seccion_4_en.htm*
[337] L. M. Friesen, R. V. Shannon, D. Baskent and X. Wang, "Speech recognition in noise as a function of the number of spectral channels: comparison of acoustic hearing and cochlear implants", *The Journal of the Acoustical Society of America, Vol.* 110-2, pp. 1150-1163, (2001)
[338] C. T. Choi and Y.-H. Lee, "A Review of Stimulating Strategies for Cochlear Implants", *Intechopen*, Online: *http://cdn.intechopen.com/pdfs-wm/36343.pdf*
[339] J. D. Falcone, "Validation of high density electrode arrays for cochlear implants: a computational and structural approach", (2011)
[340] T. Rader, "Speech Perception of Cochlear Implanted Patients with Combined Electric-Acoustic Stimulation", *ed. Verlag Dr. Hut*. (2012)
[341] "FineHearing™ Technology - Med-El", *Med-El*, Online: *http://www.medel.com/data/pdf/20287.pdf*
[342] M. Y. Srinivas, M. P. Darwin and V. Sailja, "Continuous Interleaved Sampled (CIS) Signal Processing Strategy for Cochlear Implants MATLAB Simulation Program", *International Journal of Scientific & Engineering Research, Vol.* 3-12, (2012)
[343] M. Vondrášek, P. Sovka and T. Tichý, "ACE Strategy with Virtual Channels", *Radioengineering, Vol.* 17-4, (2008)
[344] T. Zajdel, "Asynchronous Stimulation for Cochlear Implants", *The Ohio State University*, (2012),
[345] J.-J. Sit and R. Sarpeshkar, "A cochlear-implant processor for encoding music and lowering stimulation power", *Pervasive Computing, IEEE, Vol.* 7-1, pp. 40-48, (2008)
[346] H. P. Wolmarans, "Cochlear implant speech processing, based on the cochlear travelling wave", *University of Pretoria*, (2005),
[347] A. E. Vandali, L. A. Whitford, K. L. Plant and G. M. Clark, "Speech perception as a function of electrical stimulation rate: using the Nucleus 24 cochlear implant system", *Ear and hearing, Vol.* 21-6, pp. 608-624, (2000)
[348] R. Saba, "Cochlear implant modelling: stimulation and power consumption", *University of Southampton*, (2012),
[349] E. D. Marsman, R. M. Senger, G. A. Carichner, S. Kubba, M. S. McCorquodale and R. B. Brown, "DSP architecture for cochlear implants", *ISCAS ed. Citeseer*, (2006)
[350] T. Instrument, "C5000™ Ultra Low Power DSPs Datasheet",
[351] CSEM, "icyflex4 Datasheet", Online: *http://www.capdigital.com/wp-content/uploads/2012/11/icycom_CapDigital_121205-pdf.pdf*
[352] X. L. e. al., "Ultra-Low-Energy Near-Threshold Biomedical Signal Processor for Versatile Wireless Health Monitoring", *IEEE Asian Solid-State Circuits Conference*, (Kobe, Japan)
[353] M. W. Baker and R. Sarpeshkar, "Feedback analysis and design of RF power links for low-power bionic systems", *Biomedical Circuits and Systems, IEEE Transactions on, Vol.* 1-1, pp. 28-38, (2007)
[354] T. Buchegger, G. Ossberger, E. Hochmair, U. Folger, A. Reisenzahn and A. Springer, "An ultra low power transcutaneous impulse radio link for cochlea implants", *Ultra Wideband Systems, 2004. Joint with Conference on Ultrawideband Systems and Technologies. Joint UWBST & IWUWBS. 2004 International Workshop on*, pp. 356-360, (2004)

[355] T. Buchegger, G. Oß, A. Reisenzahn, E. Hochmair, A. Stelzer and A. Springer, "Ultra-wideband transceivers for cochlear implants", *EURASIP Journal on Advances in Signal Processing, Vol.* 2005-18, pp. 3069-3075, (1900)
[356] J.-J. Sit, A. M. Simonson, A. J. Oxenham, M. A. Faltys and R. Sarpeshkar, "A low-power asynchronous interleaved sampling algorithm for cochlear implants that encodes envelope and phase information", *Biomedical Engineering, IEEE Transactions on, Vol.* 54-1, pp. 138-149, (2007)
[357] N. M. Neihart and R. R. Harrison, "Micropower circuits for bidirectional wireless telemetry in neural recording applications", *Biomedical Engineering, IEEE Transactions on, Vol.* 52-11, pp. 1950-1959, (2005)
[358] A. Yodtean and A. Thanachayanont, "A Micropower CMOS Preamplifier for Cochlear Implant System", *ITC-CSCC: International Technical Conference on Circuits Systems, Computers and Communications*, pp. 997-1000, (2008)
[359] Charand and K. Xiong, "Action Potentials", *Hyperphysics and Biology*, Online: *http://hyperphysics.phy-astr.gsu.edu/hbase/biology/actpot.html*
[360] A. Kral, R. Hartmann, D. Mortazavi and R. Klinke, "Spatial resolution of cochlear implants: the electrical field and excitation of auditory afferents"*, Vol.* 121-1-2, pp. 11-28, (1998)
[361] M. C. e. al., "BioInitiative 2012: A Rationale for Biologically Exposure Standards for Low Electromagnetic Radiation", (December 31, 2012)
[362] H. Solmaz, Y. Ülgen and M. Tümer, "Design of A Microcontroller Based Cole-Cole Impedance Meter for Testing Biological Tissues"*, Vol.* 25-7, pp. 488-491, (September 7-12 2009)
[363] P. Glover, "Resistivity theory", *Petrophysics MSc Course Notes*, Online: *http://www2.ggl.ulaval.ca/personnel/paglover/CD%20Contents/GGL-66565%20Petrophysics%20English/Chapter%2017.PDF*
[364] "The Electrical Conductivity of Tissues ",in *The Biomedical Engineering Handbook: Second Edition*, *ed. Joseph D. Bronzino*. (2000)
[365] N. Ida, "9.2 electromagnetic properties of materials",in *Engineering Electromagnetics*, *ed. Springer*. (2003)
[366] "Microtubules and Filaments", *Scitable by Nature education*, Online: *http://www.nature.com/scitable/topicpage/microtubules-and-filaments-14052932*
[367] A. L. Hodgkin and A. F. Huxley, " A quantitative description of membrane current and its application to conduction and excitation in nerve"*, Vol.* 117-4, pp. 500-544, (1952)
[368] M. Wegmuller, "Intra-Body Communication for Biomedical Sensor Networks", *ETH Zurich Library Collection*, (2007), Online: *http://e-collection.library.ethz.ch/eserv/eth:29911/eth-29911-02.pdf*
[369] L. Watts, "Cochlear mechanics: Analysis and analog VLSI", *California Institute of Technology*, (1992),
[370] E. Mancall and D. Brock, "Gray's clinical neuroanatomy", *ed. Elsevier Health Sciences*. (2011)
[371] M. Deol and S. Gluecksohn-Waelsch, "The role of inner hair cells in hearing", *Nature, Vol.* 278, pp. 250-252 (1979)
[372] I. Chen, C. J. Limb and D. K. Ryugo, "The effect of cochlear-implant-mediated electrical stimulation on spiral ganglion cells in congenitally deaf white cats", *Journal of the Association for Research in Otolaryngology, Vol.* 11-4, pp. 587-603, (2010)
[373] R. R. Fay, "Structure and function in sound discrimination among vertebrates",in *The evolutionary biology of hearing*, *ed. Springer*. 229-263, (1992)
[374] "Innervation of the organ of Corti. Afferent fibres arise from nerve cell bodies within the spiral ganglion", Online: *http://dspace.jorum.ac.uk/*
[375] S. Errede, "The Human Ear Hearing, Sound Intensity and Loudness Levels ", *http://courses.physics.illinois.edu*,
[376] D. Purves, G. J. Augustine, D. Fitzpatrick, L. C. Katz, A.-S. LaMantia, J. O. McNamara and S. M. Williams, "The External Ear in *Neuroscience. 2nd edition*", *ed. Sinauer Associates*. (2001)
[377] S. S. Stevens and H. Davis, "Hearing: Its psychology and physiology", *ed. Wiley New York*. (1938)
[378] "All about ears in *Physics of the Human Body - Physics 3110*", *University of Utah*, (2013),
[379] "IV. Functions and pathphysiology of the middle ear", *University of Wisconsin, Departement of Neurophysiology*, (1996),
[380] "Coclia Anatomy and physiology of hearing ", *University of Vermont, College of Medicine*, (2012),

[381] P. Dallos, "Response characteristics of mammalian cochlear hair cells", *The Journal of Neuroscience, Vol.* 5-6, pp. 1591-1608, (1985)
[382] J. Ashmore, "Biophysics of the cochlea–biomechanics and ion channelopathies", *British medical bulletin, Vol.* 63-1, pp. 59-72, (2002)
[383] C. Fielding, "Lecture 007 Hearing II", *Colege of Santa Fe Auditory theory*, Online: *http://www.feilding.net/sfuad/musi3012-01/html/lectures/007_hearing_II.htm*
[384] D. D. Greenwood, "A cochlear frequency-position function for several species—29 years later", *The Journal of the Acoustical Society of America, Vol.* 87, pp. 2592, (1990)
[385] R. Shepherd, S. Hatsushika and G. Clark, "Electrical stimulation of the auditory nerve: the effect of electrode position on neural excitation", *Hearing research, Vol.* 66-1, pp. 108-120, (1993)
[386] K. Cheng, V. Cheng and C.-H. Zou, "A logarithmic spiral function to plot a Cochleaogram", *Trends in Medical Research, Vol.* 3-1, pp. 36-40, (2008)
[387] D. Furness, "Cochlea of the inner ear", *Welcome Images*,
[388] P. Bebis, "Short Time Fourier Transform (STFT)", *University of Nevada, Computer Sciences and Engineering*, Online: *http://cse.unr.edu*
[389] R. G. Osuna, "L6: Short time Fourier analysis and synthesis in *Introduction to Speech Processing*", *Computer Science & Engeneering, Texas A&M University*, Online: *http://research.cs.tamu.edu/prism/lectures/sp/l6.pdf*
[390] T. F. Quatieri, "SHORT-TIME FOURIER TRANSFORM in *Discrete-Time Speech Signal Processing, Principles and Practice. PHI, 2002. (Chapter 7)*", *University of Hong Kong, Department of Electrical and Electronic Engineering*, Online: *http://www.eee.hku.hk/~work3220/Speech%20analysis%20and%20synthesis-2%20STFT.pdf*
[391] R. Bradford, R. Dobson and J. ffitch, "Sliding is smoother than jumping", *University of Bale, Department of Computer Science*, Online: *http://quod.lib.umich.edu/cgi/p/pod/dod-idx/sliding-is-smoother-than-jumping.pdf?c=icmc;idno=bbp2372.2005.086*
[392] I. Shipsey, "Bionic Hearing: the science and the experience", *University of Minnesota*, (2010),
[393] K. Kawamoto, S.-H. Sha, R. Minoda, M. Izumikawa, H. Kuriyama, J. Schacht and Y. Raphael, "Antioxidant gene therapy can protect hearing and hair cells from ototoxicity", *Molecular Therapy, Vol.* 9-2, pp. 173-181, (2004)
[394] M. O'Leary, J. Fayad, W. House and F. Linthicum Jr, "Electrode insertion trauma in cochlear implantation", *The Annals of otology, rhinology, and laryngology, Vol.* 100-9 Part 1, pp. 695-699, (1991)
[395] P. Ndungidi, H. García-Vázquez, J. d. Pino, F. Dualibe and C. Valderrama, "RF specification driven by Multi-Objective Optimization Method", *DCIS*, (2012)
[396] N. Bohr, "On the Constitution of Atoms and Molecules, Part I", *Philosophical Magazine, Vol.* 26-151, pp. 1–24, (1913)
[397] D. T. Marx, "Physics 355, Metals: Free Electron Model", *Department of Physics at Illinois State University*,
[398] E. Y. Tsymbal, "Free Electron Model", *University of Nebralska-Lincoln, Department of Physics and Astronomy*,
[399] L. Kienle, "3.1.1 Polarization and Dielectric Constant", *Institut für Materialwissenschaft, Christian-Albrechts-Universität zu Kiel*,
[400] "Electric Displacement", *The world of David Darling, Encyclopedia of Science*, Online: *http://www.daviddarling.info/encyclopedia/E/electric_displacement.html*
[401] Lavrentovich, "Introduction_to_dielectric_measurments", Online: *http://www.lci.kent.edu/Lavrentovich/Introduction_to_dielectric_measurments2.htm*
[402] R. Nave, "Electricity and Magnetism"*, Georgia State University, Hyperphysics* Online: *http://hyperphysics.phy-astr.gsu.edu/hbase/electric/elefie.html*
[403] "Maxwell Equations: The Displacement Current and the Maxwell Equations", *Ware, MIT Open Courses*, Online: *http://ocw.mit.edu/courses/physics/8-02sc-physics-ii-electricity-and-magnetism-fall-2010/maxwells-equations/the-displacement-current-and-maxwells-equations/MIT8_02SC_notes26to30.pdf*
[404] "Phénomènes de propagation–Equation de d'Alembert", *Classes Préparatoires de Brizeux*, (2014), Online: *http://www.cpge-brizeux.fr/casiers/jnb/cours/physondes/chpo1.pdf*

[405] A. Woslky, "Advanced Electromagnetism (Part2)", *University of Liverpool*, Online: *http://pcwww.liv.ac.uk/~awolski/Teaching/Liverpool/PHYS370/AdvancedElectromagnetism-Part2.pdf*
[406] R. F. Lyon and C. A. Mead, "Cochlear Hydrodynamics demystified", *Caltech University*, (1988),
[407] I. Inc, "Course Syllabus: EEE498 Overview of Electrical Engineering for Non-ME's, Lecture 9: Faraday's Law Of Electromagnetic Induction, Displacement Current, Complex Permittivity and Permeability", *Lect09.ppt - download.intel.nl*,
[408] J. S. Seybold, "Introduction to RF propagation", *ed. Willey and sons*. (2005)
[409] B. Lambert, "Dielectric responses", *University of Southern Misissipi, Research Group of Dr. Kenneth A. Mauritz*, Online: *http://commons.wikimedia.org/wiki/File:Dielectric_responses.svg*
[410] B. S. Wilson and M. F. Dorman, "Cochlear implants: current designs and future possibilities", *Journal of Rehabilitation Research & Development, Vol.* 45-5, (2008)
[411] J. Rouger and e. al., "Evidence that cochlear-implanted deaf patients are better multisensory integrators"*, Vol.* vol. 104-no. 17, pp. 7295-7300, (2007)
[412] J.-C. Breton, "Fondements des Probabilités, de (O;F; P) aux conséquences de la LGN et du TCL", *Université de Rennes 1, L3/M1 Mathématiques*, (Avril 2014),
[413] T. Gallouet, "Chapitre 3: Fonctions mesurables, variables aléatoires", *Aix-Marseille Université*, Online: *http://www.cmi.univ-mrs.fr/~gallouet/licence.d/int/part2.pdf*
[414] T. Gallouet, "Chapter 2: Tribus et mesures", *Aix-Marseille Université*, Online: *http://www.cmi.univ-mrs.fr/~gallouet/tele.d/tele90/envoi1-cours.pdf*
[415] "Correlation in Random Variables, Lecture 11", *Chester F. Carlson, Center for Imaging Science*, (Spring 2002), Online: *http://www.cis.rit.edu/class/simg713/Lectures/Lecture713-11.pdf*
[416] J. F. L. Gall, "Intégration, Probabilités et Processus Aléatoires", *FIMFA*, (Septembre 2006),
[417] I. F. Wilde, "Measure, integration & probability", *King's College London: Mathematics Department*,
[418] V. V. Veeravalli, "Gaussian Random Variables and Vectors", *University of Illinois*, (Fall 2006), Online: *http's://courses.engr.illinois.edu/ece461/handouts/notes1.pdf*
[419] Fan-Gang Zeng, Arthur N. Popper and R. R. Fay, "Cochlear Implants: Auditory Prostheses and Electric Hearing - 437 pages", *ed. Springer*. *U. University of California Irvine*, (21 avr. 2004)
[420] N. Semiconductor, "Power spectra Estimation", (November 1980),
[421] Y. Jin, "Signals and Spectra (3)"*, Jiao Tong University*, (2008-09-19),
[422] I. J. Wassell, "Power and Energy Spectral Density", Online: *www.cl.cam.ac.uk*
[423] C. A. Bouman, " Digital Image Processing", (13 January 2014),
[424] B. Hassibi, "EE160 Handout number 5: The Wiener-Khintchine Theorem", (26 January 2010), Online: *http://www.ee2.caltech.edu*
[425] G. Matz and F. Hlawatsch, "Time-varying power spectra of nonstationary random processes",in *Time-Frequency Signal Analysis and Processing: A Comprehensive Reference*, *ed. B. Boashash, Oxford, UK*. 400–409, (2003)
[426] M. Sandsten, "Time-frequency analysis of non-stationary processes: an introduction", (2013), Online: *Lund University, Center for Mathematical Sciences*
[427] W. Lu and N. Vaswani, "The Wiener-Khinchin Theorem for Non-wide Sense stationary Random Processes", *arXiv preprint arXiv:0904.0602*, (2009)
[428] A. Bruscat and C. M. C. Talo, "Spectral analysis of non stationary processes using the Fourier Transform", *Brazilian Journal of Probability and Statistics, Vol.* 18, pp. 69–102, (2004)
[429] A. Demir, "Analysis and simulation of noise in nonlinear electronic circuits and systems", *University of California, Berkeley*, (1997),
[430] F. Römer, "Some notes on time varying convolution integral", *Technische Universitat Ilmenau*, Online: *http://www2.tu-ilmenau.de/nt/en/private_home/roemer/TimevaryingConvolution.pdf*
[431] C. Fliu, "Chapter 5: Linear system: random process", *Xidian University*, Online: *http://web.xidian.edu.cn/cfliu/files/20121125_153218.pdf*
[432] G. F. Margrave, "Theory of nonstationary linear filtering in the Fourier domain with application to time-variant filtering", *Geophysics, Vol.* 63-1, pp. 244-259, (1998)
[433] A. Moctezuma and J. Tu, "An overview of cochlear implant systems", (2011),
[434] W. A. D. Ham, and D. Ricketts, "Phase noise in oscillators", *ed. Harvard University*.

[435] P. A. Martin, "Mécanique statistique avancée", *Ecole Polytecnique Fédérale de Lausanne*, Online: *http://itp.epfl.ch/webdav/site/itp/shared/import/migration/coursEPFL.pdf*
[436] P. Hanggi and P. Jung, "Colored noise in dynamical systems", *Advances in chemical physics, Vol.* 89, pp. 239-326, (1995)
[437] W. M. Sansen, "Low-noise wide-band amplifiers in bipolar and CMOS technologies", Vol. 117, *ed. Springer*. (1991)
[438] T. G. M. K. a. L. K. J. V. F N Hooge, "Experimental studies on 1/f noise", *Reports on Progress in Physics, Vol.* 44, pp. 1981,
[439] K. Kundert, "the fracpole suite", *designer guide community, version 1.b*, (June 2008),